TÉCNICO LISBOA

UNIVERSIDADE DE LISBOA

INSTITUTO SUPERIOR TÉCNICO

The anticancer potential of the bacterial protein azurin and its derived peptides: mode of action and development of a nanosized drug delivery system for lung cancer therapy

Ana Rita Cebola Garizo

Supervisor: Doctor Arsénio do Carmo Sales Mendes Fialho

Co-supervisor: Doctor Bruno Filipe Carmelino Cardoso Sarmento

Thesis approved in public session to obtain the PhD Degree in Biotechnology and Biosciences

Jury final classification: Pass with Distinction

2021

UNIVERSIDADE DE LISBOA
INSTITUTO SUPERIOR TÉCNICO

The anticancer potential of the bacterial protein azurin and its derived peptides: mode of action and development of a nanosized drug delivery system for lung cancer therapy

Ana Rita Cebola Garizo

Supervisor: Doctor Arsénio do Carmo Sales Mendes Fialho
Co-supervisor: Doctor Bruno Filipe Carmelino Cardoso Sarmento

Thesis approved in public session to obtain the PhD Degree in Biotechnology and Biosciences

Jury final classification: Pass with Distinction

Jury:

Chairperson: Doctor Isabel Maria de Sá Correia Leite de Almeida, Instituto Superior Técnico, Universidade de Lisboa

Members of the Committee:

Doctor Pedro Miguel Ribeiro Viana Baptista, Faculdade de Ciências e Tecnologia, Universidade Nova de Lisboa

Doctor Miguel Augusto Rico Botas Castanho, Instituto de Bioquímica da Faculdade de Medicina, Universidade de Lisboa

Doctor Isabel Maria de Sá Correia Leite de Almeida, Instituto Superior Técnico, Universidade de Lisboa

Doctor Arsénio do Carmo Sales Mendes Fialho, Instituto Superior Técnico, Universidade de Lisboa

Doctor Ilídio Joaquim Sobreira Correia, Faculdade de Ciências da Saúde, Universidade da Beira Interior

Doctor Nuno Filipe Santos Bernardes, Instituto Superior Técnico, Universidade de Lisboa

Funding Institution – Fundação para a Ciência e Tecnologia

2021

Resumo

A azurina é uma proteína bacteriana com propriedades anticancerígenas. Esta característica singular resulta de um conjunto único de características estruturais, que incluem uma estrutura geral em sanduíche β semelhante às imunoglobulinas com um domínio hidrofóbico e uma grande hélice α anfipática, ambas localizadas na superfície desta proteína. Um péptido bioativo derivado da azurina (denominado p28) que abrange a hélice α, tem propriedades de penetração celular e exerce atividade anticancerígena por reconhecimento seletivo de células cancerígenas. Este péptido foi avaliado em dois ensaios clínicos de fase I em humanos. Inicialmente, neste trabalho, o resíduo de fenilalanina$_{114}$ localizado no centro do domínio hidrofóbico exposto da azurina foi substituído por um resíduo de alanina. Com esta substituição de um único aminoácido, foi demonstrado, dependente da dose, que esta região da proteína é importante para a sua entrada preferencial nas células cancerígenas. Além disto, verificou-se que o reconhecimento inicial de células cancerígenas parece ser mediado, pelo menos *em parte*, pela caveolina-1 (Cav-1) e pelo gangliosídeo-1 (GM-1), componentes pertencentes a microdomínios de jangadas lipídicas dispostos nas membranas plasmáticas. Após tratamento com a azurina nativa, foi observada uma diminuição da ordem membranar, ao contrário do tratamento com a proteína mutada. Em segundo lugar, foi estudado o potencial anticancerígeno de um péptido (CT-p19LC) derivado do C-terminal da azurina. Os dados indicaram que este péptido exibe propriedades ativas de membrana e induz a morte de células cancerígenas. Por fim, o p28 foi pela primeira vez associado a um nanosistema de entrega de fármacos para terapia direcionada ao cancro de pulmão. A funcionalização de nanopartículas (NPs) com este péptido, permitiu aumentar a sua internalização em células cancerígenas A549, bem como foi capaz de diminuir a viabilidade destas células, sem qualquer efeito em células não cancerígenas 16HBE14o-. *In vivo*, os estudos com xeno-enxerto subcutâneo de A549 mostraram que NPs funcionalizadas com p28 e carregadas com gefitinib (GEF), um inibidor da atividade tirosina quinase do recetor do fator de crescimento epidérmico (EGFR), frequentemente superexpresso em células de cancro de pulmão, reduziram a carga tumoral primária de A549 e a formação de metástases pulmonares. Assim, foi possível concluir que a seletividade intrínseca do p28 manteve-se mesmo este estando ligado a NPs, sendo esta característica utilizada como uma mais valia neste tipo de aplicações, enquanto que o GEF foi entregue às células-alvo. Com base no trabalho desta tese, considerou-se a azurina, uma fonte de péptidos bioativos anticancerígenos capazes de serem associados

a estratégias de entrega de fármacos para o desenvolvimento de terapias mais eficazes, e possíveis de serem aplicadas a qualquer tipo de cancro.

Palavras chave: azurina; p28; nanosistemas de entrega de fármacos; seletividade; efeito anti-tumoral.

Abstract

Azurin, a protein from bacterial origin, has been found to exhibit anticancer properties. This singular characteristic results from a unique set of structural features, which include an overall immunoglobulin-like β-sandwich scaffold with a hydrophobic patch and a large amphipathic α-helix, both located on the surface of the protein. A bioactive azurin derived peptide (termed p28) encompassing the α-helix has cell penetrating properties and exerts anticancer activity by selective recognition of cancer cells. The p28 peptide is being evaluated in two phase I human clinical trials. Initially, in this work, the phenylalanine$_{114}$ residue located on the center of the exposed hydrophobic patch of azurin was replaced with an alanine residue. With this single amino acid substitution, it was shown that this region of the protein is important for its preferential entry into cancer cells in a dose-dependent manner. In addition, it was found that the initial recognition of cancer cells appears to be mediated, at least *in part*, by caveolin-1 (Cav-1) and ganglioside-1 (GM-1), components belonging to lipid rafts microdomains arranged in plasma membranes. After treatment with wild-type azurin, a decrease in membrane order was observed, unlike treatment with the mutated protein. Secondly, the anticancer potential of a peptide (CT-p19LC) derived from the C-terminal of azurin has been studied. Data indicated that this peptide exhibits membrane-active properties and induces cancer cell death. Lastly, p28 was associated for the first time with a drug delivery nanosystem for targeted lung cancer therapy. The functionalization of nanoparticles (NPs) with this peptide increased its internalization in A549 cancer cells, as well as was able to decrease the viability of these cells, without any effect in 16HBE14o- non-cancer cells. *In vivo*, the studies using A549 subcutaneous xenograft showed that p28-functionalized NPs loaded with gefitinib (GEF), an inhibitor of tyrosine kinase activity of epidermal growth factor receptor (EGFR), often overexpressed in lung cancer cells, reduced A549 primary tumor burden and lung metastases formation. Thus, it was possible to conclude that the intrinsic selectivity of p28 was maintained even though it was linked to NPs, being this characteristic used as an asset in this type of applications, while GEF was delivered to target cells. Based on the work of this thesis, azurin was considered a source of bioactive anticancer peptides capable of being associated with drug delivery strategies for the development of more effective therapies, and possible to be applied to any type of cancer.

Key words: azurin; p28; drug delivery nanosystems; selectivity; anti-tumor effect.

Acknowledgements

This PhD work is the result of a long journey subject to several obstacles, concerns and challenges, but which has contributed a lot to my growth and to the shaping of my thinking. During this time, people who were essential to the realization of this project accompanied me, and to whom I would like to express my sincere thanks.

First of all, I would like to thank my supervisors, Professor Arsénio Fialho and Professor Bruno Sarmento for accepting me in their research groups and giving me the opportunity to develop this work, also for all the support, guidance and help. A special acknowledgment to Professor Pedro Granja and Professor Cristina Barrias (i3S - Instituto de Investigação e Inovação em Saúde da Universidade do Porto) for their interest in this project; to Professor Isabel Sá-Correia, Biological Sciences Research Group (BSRG) leader (IST/IBB - Instituto Superior Técnico/Institute of Biotechnology and Bioengineering) and also member of my “Comissão de Acompanhamento da Tese” for her support.

Secondly, I acknowledge all the co-authors of the manuscripts presented in this dissertation for their scientific contributions, the support provided by the Biointerfaces and Nanotechnology, Translational Cytometry, Biochemical and Biophysical Technologies, and Histology and Electron Microscopy i3S Scientific Platforms as well as by Mónica Rato and Luísa Coimbra, laboratory technicians from BSRG.

I would also like to acknowledge to Fundação para a Ciência e Tecnologia (FCT) for funding both my PhD grant SFRH/BD/122636/2016 and the research project PTDC/BTM-SAL/30034/2017_LISBOA-01-0145-FEDER-030034_POCI-01-0145-FEDER-030034.
Funding received by iBB from FCT (UID/BIO/04565/2020), and through the project PTDC/BTMSAL/31057/2017, and from Programa Operacional Regional de Lisboa 2020 (Project N. 007317) is as well acknowledged.

A particular word of gratitude to Doctor Nuno Bernardes for accompanying me since the master's course and placing great trust in me. For his patience, suggestions, criticism and knowledge transmission, and above all for his friendship.

To the Nanomedicines and Translational Drug Delivery group (NTDD Group of i3S) for having received me at the beginning of my PhD, and for transmitting all of his knowledge indispensable to the development of this work. For all the intense lab meetings, but also for all the fun field trips. And most importantly, the opportunity to meet wonderful people, that I will take with me for life.

To my colleagues and friends at iBB, to whom I thank all the words of encouragement, availability and laughter, especially to Andreia Pimenta, Cláudia Agostinho, Dalila Mil-Homens, Joana Feliciano, Karina Marangoni, Luís Almeida, Luís Martins, Margarida Palma, Mafalda Cavalheiro, Miguel Fuzeta, Sara Gomes, Tânia Sousa and Tiago Pita.

To my favorite group of researchers. We met while we were developing our master's thesis, and we have remained together. Lígia Coelho, Marcelo Ramires, Marília Silva, Rui Martins and Soraia Guerreiro were a great pillar for me on this journey.

To my two "adoptive" families, Sousa and Borges, who received me for two years in Porto, and who shared with me my frustrations and the joys of this work; to the friends Thiago Silva, Joel Laia and Sílvia Henriques for the good times dedicated to photography, and for sometimes putting up with my “bad mood”.

Last but not least, I want to thank my family and my old friends, who are always with me, and who make me feel like the richest person on earth.

I would like to end this section of acknowledgements to dedicate this work to my parents and my grandmother, because to them I owe them everything I am, they will always be my safe haven and be with me, in my thought and heart.

Table of Contents

Resumo i
Abstract iii
Acknowledgements v
Table of Contents vii
List of Figures xi
List of Tables xiv
List of Acronyms xv
I. INTRODUCTION 1
I.1. The etiology of cancer 2
I.2. The anticancer potential of the bacterial protein azurin 3
I.2.1. The discovery of p28 and its domains 6
I.2.2. p28 preclinical pharmacokinetic studies and clinical trials 9
I.2.3. Combination of p28 with anticancer drugs 11
I.2.4. p28 as a transport anticancer agent 12
I.3. Cell-penetrating peptides for cancer therapy 15
I.4. Nanomedicine in cancer 16
I.4.1. Delivery nanosystems 18
I.4.2 Poly (lactic-co-glycolic acid) nanoparticles and their application in cancer therapy 26
I.4.3 Nano-therapy in lung cancer 32
I.4.4 Future perspectives of NDDSs application in cancer therapy 43
I.5. Thesis aims and outline 45
II. AZURIN INTERACTION WITH THE LIPID RAFT COMPONENTS GANGLIOSIDE GM-1 AND CAVEOLIN-1 INCREASES MEMBRANE FLUIDITY AND SENSITIVITY TO ANTI-CANCER DRUGS 47
II.1. Abstract 48
II.2. Introduction 48
II.3. Materials and Methods 50
II.3.1. Human cancer cell lines and cell cultures 50
II.3.2. Hydrophobic surface analysis of azurin 50
II.3.3. Construction of a site-directed mutation in the azurin gene of *Pseudomonas aeruginosa* PAO1 50
II.3.4. Bacteria growth, over-expression, extraction and purification of wild-type azurin or mutated protein 51
II.3.5. Protein extraction and western blot analysis 51

II.3.6. GM-1 inhibition with Cholera Toxin Subunit B 52
II.3.7. Confocal microscopy-Cholera Toxin Subunit B 52
II.3.8. SiRNA transfection of human cancer cells lines 53
II.3.9. Interaction between Cav1-CSD and azurin: FRET measurements 54
II.3.10. Two-Photon excitation microscopy – Generalized polarization determination 54
II.3.11. MTT cell viability assay 55
II.3.12. Statistical analysis 56
II.4. Results 56
II.4.1. F114A substitution alters the uptake rate of azurin in cancer cells 56
II.4.2. Blocking GM-1 ganglioside reduces the penetration of azurin in cancer cells 58
II.4.3. Silencing of caveolin-1 inhibits cell entry of WT azurin 60
II.4.4. Azurin binds to caveolin-1 scaffolding domain *in vitro* 60
II.4.5. Azurin leads to a decrease in caveolin-1 total protein levels 61
II.4.6. Azurin decreases plasma membrane order 62
II.4.7. Azurin enhances the activity of chemotherapeutic drugs 64
II.5. Discussion 65
III. THE AZURIN-DERIVED PEPTIDE CT-P19LC EXHIBITS MEMBRANE-ACTIVE PROPERTIES AND INDUCES CANCER CELL DEATH 73
III.1. Abstract 74
III.2. Introduction 74
III.3. Materials and Methods 76
III.3.1. Azurin-derived peptides 76
III.3.2. Circular dichroism spectroscopy 77
III.3.3. Human cancer cell lines and cell culture conditions 77
III.3.4. MTT cell proliferation assays 78
III.3.5. LDH release assays 78
III.3.6. Quantitative cellular interaction 78
III.3.7. CT-p19LC cellular uptake 79
III.3.8. Apoptosis assay 79
III.3.9. Zeta potential measurements of live A549, MCF-7, HeLa, HT-29 cancer cells, and 16HBE14o-, MCF10A non-cancer cells in the presence of CT-p19LC 80
III.3.10. GP determination for membrane order evaluation 80
III.3.11. Statistical analysis 81
III.4. Results and Discussion 81
III.4.1. CT-p26 peptide effect on cell viability confirms the anticancer potential of C-terminal azurin 81

III.4.2. CT-p19 peptide decreases cancer cell viability and has selective property .. 83

III.4.3. The newly designed CT-p19LC peptide reduces proliferation and induces cell death in cancer cell lines 84

III.4.4. CT-p19LC peptide targets cellular plasma membrane 86

III.5. Conclusions 89

IV. P28-FUNCTIONALIZED PLGA NANOPARTICLES LOADED WITH GEFITINIB REDUCE TUMOR BURDEN AND METASTASES FORMATION ON LUNG CANCER 91

IV.1. Abstract 92

IV.2. Introduction 92

IV.3. Materials and Methods 94

IV.3.1. Materials 94

IV.3.2. Methods 95

IV.4. Results 102

IV.4.1. Preparation and characterization of p28-functionalized PLGA nanoparticles loaded with gefitinib 102

IV.4.2. Colloidal stability of nanoparticles in cell culture medium 104

IV.4.3. Payload release profile 104

IV.4.4. Cell-Nanoparticles interaction studies 105

IV.4.5. Effect of p28-functionalized PLGA nanoparticles loaded with gefitinib on metabolic activity 107

IV.4.6. p28-functionalized PLGA nanoparticles loaded with gefitinib decrease A549 tumor progression 109

V.4.7. p28-functionalized PLGA nanoparticles loaded with gefitinib reduce lung metastasis burden 112

IV.5. Discussion 113

IV.6. Conclusion 118

V. FINAL DISCUSSION AND FUTURE PERSPECTIVES 121

V.1. Final Discussion 122

V.2. Future perspectives 128

VI. PUBLICATIONS AND COMUNICATIONS 131

VII. REFERENCES 135

VIII. APPENDIX 163

VIII.1. AZURIN INTERACTION WITH THE LIPID RAFT COMPONENTS GANGLIOSIDE GM-1 AND CAVEOLIN-1 INCREASES MEMBRANE FLUIDITY AND SENSITIVITY TO ANTI-CANCER DRUGS (Supplementary information of Chapter II) 164

VIII.2. P28-FUNCTIONALIZED PLGA NANOPARTICLES LOADED WITH GEFITINIB REDUCE TUMOR BURDEN AND METASTASES FORMATION ON LUNG CANCER (Supplementary information of Chapter IV) 170

VIII.3. P28-FUNCTIONALIZED PLGA NANOPARTICLES LOADED WITH ERLOTINIB: DEVELOPMENT, CHARACTERIZATION AND *IN VITRO* EVALUATION OF THEIR LUNG ANTICANCER ACTIVITY 174

VIII.3.1. Material and methods 174

VIII.3.2. Results 175

List of Figures

Figure I.1-1: Worldwide distribution of new cases and deaths caused by different types of cancer……...2

Figure I.2-1: Summary of the anticancer activity of the bacterial protein azurin……..……..5

Figure I.2-2: p28 protein transduction domain (PTD) of azurin, its domains and respective activities……7

Figure I.2-3: Control of cancer proliferation by p28 via p53 pathway……..……8

Figure I.2-4: Summary of the potential anticancer of the p28……..……..15

Figure I.4-1: Scheme of nanosized drug delivery system (NDDS)……17

Figure I.4-2: Nanosized drug delivery systems (NDDSs) administration routes, their advantages and disadvantages, as well as associated barriers……17

Figure I.4-3: Comparison of nanoscale sizes……..18

Figure I.4-4: Schematic representation of passive and active targeting approaches…….25

Figure I.4-5: Poly(lactic-co-glycolic acid) polymer (PLGA) chemical structure……26

Figure I.4-6: Comparison of clinical trials in the field of cancer nanomedicine with the number of published reports……44

Figure II.4-1: Point mutation of phenylalanine$_{114}$ delays azurin entry in cancer cells…….57

Figure II.4-2: Phenylalanine$_{114}$ is important for interaction with GM-1……..……...59

Figure II.4-3: Phenylalanine$_{114}$ is important for interaction with Cav-1……..……..62

Figure II.4-4: Impact of WT or F114A mutant azurin protein on the membrane fluidity of cancer cell lines MCF-7, HeLa and HT-29……64

Figure II.4-5: The effect of the combination of WT or F114A mutant azurin proteins with chemotherapeutic agents [paclitaxel (P) and doxorubicin (D)] was determined by MTT assay……..66

Figure III.4-1: Comparison of cell viability after treatment with p28 and CT-p26 peptides (0 to 100 µM) on A549 (lung) and MCF-7 (breast) cancer cells incubated during 48 h……83

Figure III.4-2: Viability decrease (100% of proliferation in untreated condition – % of proliferation for each treatment condition) of A549 (lung) and MCF-7 (breast) cancer cells, and 16HBE14o- (bronchial) and MCF10A (mammary gland) non-cancer cells, when incubated with different concentrations of CT-p19 peptide (0 to 100 µM), during 48 h……84

Figure III.4-3: Cytotoxic effect of newly designed CT-p19LC peptide……..86

Figure III.4-4: CT-p19LC membrane-active properties……..89

Figure IV.1-1: Graphical abstract……..92

Figure IV.4-1: Scheme of the p28 peptide to the PLGA-PEG-Mal polymer conjugation by Maleimide-Thiol click chemistry with a conjugation efficiency around 74±12% determined by indirect method HPLC (n=8)…….103

Figure IV.4-2: Physico-chemical characterization and *in vitro* release of p28-NPs-GEF……..105

Figure IV.4-3: Cell-NPs interaction/internalization……107

Figure IV.4-4: Metabolic activity of 16HBE14o- non-cancer cells and A549 cancer cells when incubated with different concentrations of free GEF, empty nanoparticles (NPs-0), functionalized unloaded NPs (p28-NPs), GEF loaded NPs (NPs-GEF), and p28-functionalized GEF-loaded NPs (p28-NPs-GEF) during 72h……...108

Figure IV.4-5: Effect of p28-NPs-GEF in A549 tumor progression (subcutaneous treatment)……110

Figure IV.4-6: Effect of p28-NPs-GEF in A549 tumor progression (intravenous treatment)……111

Figure IV.4-7: Effect of p28-NPs-GEF in lung metastasis……113

Figure V.1-1: Summary of previous results published by others and the results presented in this thesis about the anticancer potential of the bacterial protein azurin and its derived peptides: mode of action and development of a nanosized drug delivery system (NDDS) for cancer therapy……...127

Figure VIII.1-1: Full-lenght western blot images. Conditions described in main text……164

Figure VIII.1-2: Full-length western blot images. Conditions described in main text……165

Figure VIII.1-3: Fluorescence spectra of the donors Atto390-WT **A)** or Atto390-F114A **B)** acquired with 390 nm excitation and measured over the emission wavelength range of 400 to 470 nm, since no acceptor (FITC-labeled CSD peptide) emits there……..166

Figure VIII.1-4: Full-length western blot images. Conditions described in main text……167

Figure VIII.1-5: Full-length western blot images. Conditions described in main text……168

Figure VIII.1-6: Full-length western blot images. Conditions described in main text……169

Figure VIII.1-7: Entry of azurin WT and F114A mutant in MCF-7, HeLa and HT-29 cells……..169

Figure VIII.2-1: Elementary analysis of functionalized unloaded NPs (p28-NPs) and p28-functionalized GEF-loaded NPs (p28-NPs-GEF)……..173

Figure VIII.2-2: Metabolic activity of A549 cancer cells upon treatment with different empty nanoparticles (NPs-0) concentrations for 72 h……...173

Figure VIII.3.2-1: Physico-chemical characterization and *in vitro* release of p28-NPs-ERL……..178

Figure VIII.3.2-2: Metabolic activity of 16HBE14o- non-cancer cells and A549 cancer cells when incubated with different concentrations of free ERL, empty nanoparticles (NPs-0), functionalized unloaded NPs (p28-NPs), ERL loaded NPs (NPs-ERL), and p28-functionalized ERL-loaded NPs (p28-NPs-ERL) during 72h……179

Figure VIII.3.2-3: Metabolic activity of A549 cancer cells upon treatment with different empty nanoparticles (NPs-0) concentrations for 72 h……180

List of Tables

Table I.4-1: Advantages and disadvantages of various types of soft solids nanosystems, and some commercial products for cancer clinic……..20

Table I.4-2: Advantages and disadvantages of various types of hard solids nanosystems, and some commercial products for cancer clinic……..21

Table I.4-3: Most common PLGA nanosystems production methods……...28

Table I.4-4: Examples of targeted and loaded Poly(lactic-co-glycolic acid) (PLGA) nanoparticles (NPs)……..29

Table I.4-5: List of drugs approved by the Food and Drug Administration (FDA) for lung cancer treatment……...35

Table I.4-6: Types of NDDSs approved by the FDA or in various stages of clinical trials for the lung cancer treatment……42

Table III.4-1: Overview of the characteristics of azurin and its derived peptides……82

Table IV.4-1: Physico-chemical properties of empty nanoparticles (NPs-0), functionalized unloaded NPs (p28-NPs), gefitinib (GEF) loaded NPs (NPs-GEF), and p28-functionalized GEF-loaded NPs (p28-NPs-GEF) and their association efficiency (AE) and drug loading (DL). Energy-dispersive X-ray spectra (EDS) analysis (average atomic) of p28-NPs and p28-NPs-GEF detect the presence of sulfur (S)……104

Table VIII.2-1: Physico-chemical properties of nf-NPs and p28-NPs with different percentages of PLGA-PEG and PLGA-PEG-Mal polymers, their conjugation efficiency (CE) and energy-dispersive X-ray spectra (EDS) analysis (average atomic)……170

Table VIII.2-2: Gefitinib (GEF) loaded PLGA NPs (NPs-GEF) production design……171

Table VIII.2-3: Physico-chemical characteristics, association efficiency (AE) and practical gefitinib (GEF) loading of GEF-NPs based on the established production design……..172

Table VIII.3.2-1: Erlotinib loaded PLGA NPs (NPs-ERL) production design……176

Table VIII.3.2-2: Physico-chemical characteristics, association efficiency (AE) and practical erlotinib loading of ERL-NPs based on the established production design……..177

Table VIII.3.2-3: Physico-chemical properties of empty nanoparticles (NPs-0), functionalized unloaded NPs (p28-NPs), erlotinib (ERL) loaded NPs (NPs-ERL), and p28-functionalized ERL-loaded NPs (p28-NPs-ERL) and their association efficiency (AE) and drug loading (DL)……177

List of Acronyms

5-ALA - 5-aminolevulinic acid

ACN - Acetonitrile

ACPs - AntiCancer Peptides

ADC - Adenocarcinoma

ADH - Adipic acid di-hydrazide

AE - Association Effiency

AFM - Atomic force microscopy

ALK - Anaplastic lymphoma kinase

Anti-CA IX - Anti-carbonic anhydrase IX

APC - Allophycoerythrin

AUC - Area under the curves

AXL - Anexelekto

BBB - Blood-brain barrier

Bcl-2 - B-cell lymphoma 2

BEV - Bevacizumab

bFGF - Basic fibroblast growth factor

BF-NPs - Bifunctional nanoparticles

Cav-1 - Caveolin-1

CD31 - Cluster of differentiation 31

CD - Circular dichroism

CDDP - Cis-diamminedichloroplatinum II

CDK2 - Cyclin-dependent kinase 2

CLB - Catenin Lysis Buffer

COP1 - Constitutive photomorphogenic 1

CPDT - Chemo-photodynamic therapy

CPP - Cell-penetrating peptide

CSCC - Combined small cell carcinoma

CSD - Caveolin-1 Scaffolding Domain

CT - Computed tomography

CTR - Saline control

CTxB - Cholera Toxin Subunit B

DAPI - 4′,6-diamidino-2-phenylindole

DBD - DNA-binding domain

DL - Drug loading

DLS - Dynamic light scattering

DLTs - Dose-limiting toxicities

DMEM - Dulbecco's Modified Eagle Medium

DMF - Dimethylformamide

DMSO - Dimethyl sulfoxide

DNA - Deoxyribonucleic acid

DOX - Doxorubicin

ECL - Enhanced chemiluminescent

EDS - Energy-dispersive X-ray spectra

EGF - Epidermal growth factor

EGFR - Epidermal growth factor receptor

EMA - European Medicines Agency

EMT - Epithelial-to-mesenchymal transition

EPR - Enhanced Permeability and Retention

ERL - Erlotinib

FA - Folic acid

FAK - Focal adhesion kinase

FBS - Fetal Bovine Serum

FDA - Food and Drug Administration

FITC - Fluorescein-5 IsoThioCyanate

FOXM1 - Forkhead box M1

FRA - Folate receptors alpha

FRET - Fluorescence resonance energy transfer

GA - Glycolic acid

GAPDH - Glyceraldehyde 3-phosphate dehydrogenase

GEF - Gefitinib

Geo MFI - Geometric mean fluorescence intensity

GM-1 - Ganglioside-1

GP - Generalized polarization

GST - Glutathione S-transferase

HA - Hyaluronic acid

HPLC - High-performance liquid chromatography

HPV - Human papillomavirus

HuR - Human antigen R

IARC - International Agency for Research on Cancer

IFN-γ - Interferon-gamma

IPTG - Isopropyl β-d-1-thiogalactopyranoside

K-ras - Kirsten rat sarcoma virus

LA - Lactic acid

LCC - Large cell carcinoma

LDA - Laser doppler anemometry

LMWP - Low molecular weight cell-penetrating peptide

LPH NPs - Lipid-polymer hybrid nanoparticles

Mal - Maleimide

MDR - Multi-drug resistance

MDSCs - Myeloid-derived suppressor cells

MEM - Minimum Essential Medium with Earle's salt

mPEG-P(LG-co-LC) - Methoxy poly(ethyleneglycol)–poly(L-glutamic acid-co-L-cystine

mPEG-P(LP-co-LC) - Poly(ethylene glycol)–poly(L-phenylalanine-co-L-cystine)

MPS - Mononuclear phagocyte system

mRNA - Messenger ribonucleic acid

MTD - Maximum-tolerated dose

Mw - Molecular weight

MWCO - Molecular weight

Myr - Myricetin

NC - Negative control

NDDSs - Nanosized drug delivery systems

NF-κB - Nuclear factor kappa-light-chain-enhancer of activated B cells

nf-NPs - Non-functionalized

NIH - National Institutes of Health

NIR - Near infrared

NLM - National Library of Medicine

NOAEL - No observed adverse effect level

NPs-0 - Empty nanoparticles

NPs - Nanoparticles

NPs-GEF - Nanoparticles loaded with gefitinib

NSCLC - Non-small cell lung cancer

OCC - Oat cell cancer

O/W - Oil in water

p28-NPs - Nanoparticles functionalized with p28

p28-NPs-GEF - p28-functionalized gefitinib-loaded PLGA nanoparticles

PAMAM - Poly(amidoamine)

PBS - Phosphate-buffered saline

PBS-T - PBS containing 0.5% (v/v) Tween-20

PC - Positive control

PCEC - Poly(e-caprolactone)-poly(ethylene glycol)-poly(e-caprolactone)

PDI - Polydispersity index

PD-L1 - Programmed death/ligand 1

PDT - Photodynamic therapy

PEG - Polyethylene glycol

PFA - paraformaldehyde

PFS - Progression-free survival

PGA - Poly(glycolic acid)

PLA - Poly(lactic acid)

PLGA - Poly(lactic-co-glycolic acid)

POM - Polarized optical microscopy

PSMA - Prostate-Specific Membrane Antigen

PTD - Protein transduction domain

PTEN - Phosphatase and tensin homolog

PTX - Paclitaxel

R&D - Research and Development

RES - Reticuloendothelial system

RNA - Ribonucleic acid

ROI - Regions of Interest

ROS - Reactive oxygen species

ROS1 - ROS proto-oncogene receptor tyrosine kinase

RT-PCR - Reverse transcription polymerase chain reaction

SCC - Squamous cell carcinoma

SCLC - Small cell lung cancer

SD - Standard deviation

SDS-PAGE - Sodium dodecyl sulphate-polyacrylamide gel electrophoresis

SEM - Scanning electron microscopy

siAXL - Anti-anexelekto siRNA

siRNA - Small interfering ribonucleic acid

SVM - Support vector machine

TAT - Transactivator of transcription

TCEP- Tris(2-carboxyethyl) phosphine

TEM - Transmission electron microscopy

TFA - Trifluoroacetic acid

TGN - 12-mer peptide

TKIs - Tyrosine kinase inhibitors

TNF-α - Tumor necrosis factor alpha

TPL - Triptolide

UV - Ultraviolet

VCR - Vincristine sulfate

VEGF - Vascular endothelial growth factor

VEGFR-2 - Vascular endothelial growth factor receptor 2

VOCs - Volatile organic compounds

W/O/W - Water in oil in water

WT - Wild-Type

XDR - X-ray diffraction

Z-average - Average size

ζ-potential - Zeta-potential

I. INTRODUCTION

I.1. The etiology of cancer

In the 21st century, cancer is expected to become the leading cause of death, being a barrier to increasing life expectancy worldwide. Each year, more than 18 million cases are diagnosed and 10 million deaths occur (Bray *et al.,* 2018). The International Agency for Research on Cancer (IARC) forecasts predict that by 2040 there will be more than 29 million new cases and 16 million deaths (Wild *et al.,* 2020). Lung cancer is one of the most commonly diagnosed cancer (11.4% of the total cases) and the leading cause of cancer death (18.0% of the total cancer deaths), closely followed by female breast cancer (11.7%), colorectal cancer (10.0%) and prostate cancer (7.3%) for incidence, and colorectal cancer (9.4%), stomach cancer (7.7%) and liver cancer (8.3%) for mortality (Figure I.1-1; GLOBOCAN, 2020).

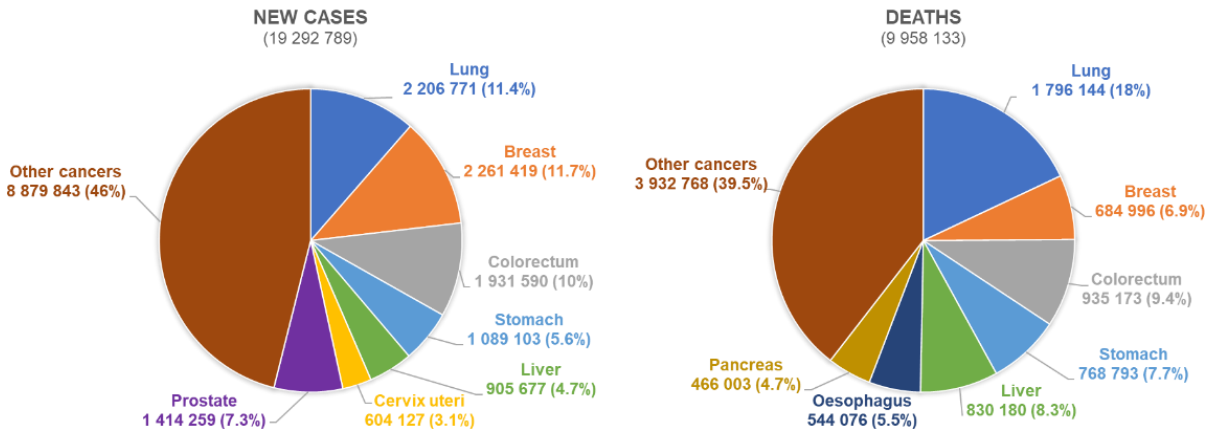

Figure I.1-1: Worldwide distribution of new cases and deaths caused by different types of cancer. Source: GLOBOCAN, 2020.

This rising problem is mostly due to rapid growth and an aging population. Also, societal, economic and lifestyle changes related to human development may contribute to the increase in scale, and alter the profile of cancer in the next years. Only 5-10% of all cancers are owing to highly penetrant inherited mutations (Fidler *et al.,* 2018; Wild, 2019).

The most developed countries have the highest cancer incidence, while low-income and middle-income countries have the bigger cancer mortality rate (Bray *et al.,* 2012; Wild *et al.,* 2020). This is explained by the limited access to prevention, early detection, treatment and care in these countries (Fidler *et al.,* 2018; Wild, 2019).

The cancer hallmarks include sustaining proliferative signaling, evading growth suppression, avoiding immune destruction, enabling replicative immortality, resisting apoptosis, deregulating cellular energetics, inducing angiogenesis, and activating invasion

and metastasis (Wild *et al.,* 2020). Frequently, this occurs due to the activation of oncogenes and/or deactivation of tumor suppressor genes leading to uncontrolled cell cycle progression and inactivation of apoptotic events. Mechanisms such as mutations, chromosomal translocations or deletions, and dysregulated expression or activity of signaling pathways are involved in these genetic and cellular changes. Studies also suggest that epigenetic alterations can cause cancer due to its role in the generation of cancer progenitor cells (Sarkar *et al.,* 2013).

The complexity and heterogeneity of the carcinogenesis hampers the development of a single effective therapy. Currently, surgical intervention, radiotherapy and chemotherapy are the three most common treatments of this disease. Although these treatments have saved many lives, they have major limitations, including the risk of damaging healthy tissues owing to their non-specific targeting, inadequate drug concentration at the lesion site, high toxicity (hepatic, renal, bone marrow, pulmonary, gastrointestinal and cardiac toxicities), multi-drug resistance (MDR) development, and not being able to effectively eradicate the disease (Damyanov *et al.*, 2018; Gurunathan *et al.,* 2018).

Thus, due to the lack of specificity and effectiveness of conventional treatments, the investigation and development of new anti-tumor approaches has gained extreme importance in the cancer therapy field. Immunotherapy, nanotechnology based-targeting therapy, microbial based-therapy including the use of bacterial products as scaffolds for novel anticancer drugs, are some of the examples currently being studied (Attia *et al.*, 2019; Bernardes *et al.*, 2010; Byrne *et al.*, 2008; Inthagard *et al.*, 2019; Martínez-Montiel *et al.*, 2016).

I.2. The anticancer potential of the bacterial protein azurin

Azurin is a bacterial periplasmic copper-containing small protein (14 kDa; 128 amino acids; Figure I.2-1), remarkably stable and water-soluble, belonging to the cupredoxin family, a group of type I redox proteins. This is produced by *Pseudomonas aeruginosa*, and in this organism is involved in the electron transfer during the denitrification process (Baker, 1994; De Rienzo *et al.*, 2000; Fialho *et al.*, 2016; Van de Kamp *et al.*, 1990; Yamada *et al.*, 2009). In addition to its biological function, azurin has therapeutic characteristics probably associated with its structure. This protein is structurally similar to several immunoglobulins' domains, demonstrating a single antibody-like structure composed by one α-helix and eight β-sheets, forming a β-barrel motif. The unique structural features of azurin allows it to mediate high-affinity interactions with various unrelated mammalian proteins relevant in

cancer, being azurin considered a non-antibody scaffold (Figure I.2-1; Fialho *et al.*, 2007). Normally, non-antibody scaffolds are small single-domain proteins with recognition properties that reveal immunoglobulin-like binding features as is the case of certain domains of albumin and fibronectin (Hey *et al.*, 2005; Škrlec *et al.*, 2015). The ability to bind many different proteins makes it more difficult to trigger resistance, habitually observed with the successive application of other drugs (Bernardes *et al.*, 2013a; Bernardes *et al.*, 2014; Fialho *et al.*, 2007). The bindings result mainly from electrostatic and hydrophobic interactions, and occur specifically through distinct binding regions on its surface: one face with two charged clusters (one large negative nearby to one small positive), and a prominent neutral aromatic-rich hydrophobic patch centered on phenylalanine$_{114}$, occupying a region around the copper ion (Fialho *et al.*, 2016; Yanagisawa *et al.*, 2006).

Azurin has been considered a potential anticancer agent due to its preferential entry into cancer cells, as it is able to exert *in vitro* cytotoxicity effects against numerous cancer cell lines, promotes tumor regression in *in vivo*, and inhibits cancer-induced angiogenesis. The selectivity of this protein appears to be dependent on the cholesterol-enriched microdomains, named lipid rafts and generally overexpressed in cancer cells (Figure I.2-1; Mehta *et al.*, 2011; Punj *et al.*, 2004; Taylor *et al.*, 2009; Yamada *et al.*, 2004; Yamada *et al.*, 2002a; Zaborina *et al.*, 2000).

It has also been shown that this protein can interact and stabilize the levels of the tumor-suppressor protein p53, as well as increase the pro-apoptotic genes expression, preventing cell proliferation and triggering apoptosis (Figure I.2-1; Punj *et al.*, 2003; Yamada *et al.*, 2004; Yamada *et al.*, 2005). Azurin binds to the NH_2-terminal domain of p53 with nanomolar affinity in a 4:1 stoichiometry, as well to the deoxyribonucleic acid (DNA)-binding domain of this protein through a copper-independent mechanism of action (Apiyo and Wittung-Stafshede, 2005; Goto *et al.*, 2003; Taranta *et al.*, 2009; Yamada *et al.*, 2005). In fact, studies supported by site-directed mutagenesis propose that a region of azurin constituted by amino acids Met-44 to Met-64, located in its hydrophobic patch, is important for the interactions with p53. The substitutions performed led to a change in the formation of this complex, showing the dependence of this interaction with the hydrophobic character of azurin (Goto *et al.*, 2003; Yamada *et al.*, 2002b; Yamada *et al.* 2009).

In addition, it is known that the azurin treatment leads to an up-regulation of genes associated with cellular processes, like membrane organization, endocytosis, vesicle transport and pathways associated with lysosomes in cancer cells. This protein also

causes a down-regulation of an important number of genes coding for cell surface receptors that frequently sustain cell proliferation and aberrant constitutive signaling (Figure I.2-1; Bernardes *et al.*, 2014). This was verified in the case of EGFR, normally overexpressed in several types of cancer (Bernardes *et al.*, 2016; Cadranel *et al.*, 2013; Nakamura *et al.*, 2006). Besides this, it was also verified that azurin is able to decrease the cellular invasion, a crucial step in the cancer progression. After its treatment, this protein can modulate the levels of P-cadherin and β1-integrin, two adhesion proteins, limiting communication between cancer cells, thus disturbing their ability to invade (Figure I.2-1; Bernardes *et al.*, 2013a; Bernardes *et al.*, 2014; Bernardes *et al.*, 2016). Furthermore, the matrix metalloproteases activity and the activation of the intracellular non-receptor tyrosine kinases focal adhesion kinase (FAK) and Src, that regulate a wide number of signaling pathways involved in cell spreading, adhesion, migration, invasion, survival, proliferation, differentiation and angiogenesis were also affected by azurin action (Bernardes *et al.*, 2013a; Bernardes *et al.*, 2014).

The anticancer potential of azurin has also been combined with anticancer drugs, and a synergistic effect has been documented (Figure I.2-1; Bernardes *et al.*, 2016; Bernardes *et al.*, 2018; Choi *et al.*, 2011). A possible explanation for this phenomenon is that after the treatment with this protein, changes in the biophysical properties of the plasma membranes of cancer cells occur, such as increased elasticity, which possibly will facilitate the entry of co-administered drugs, facilitating its action on intracellular targets (Bernardes *et al.*, 2016).

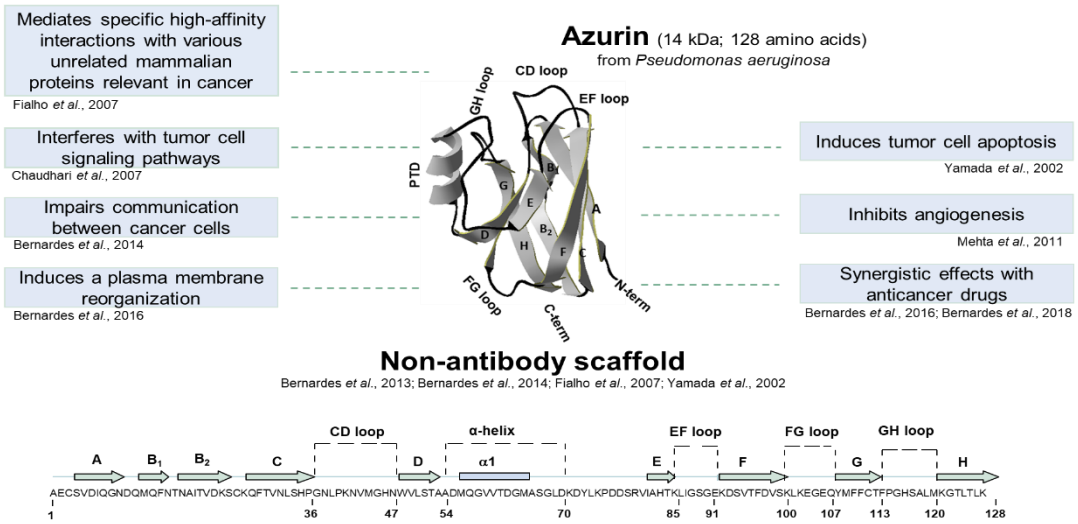

Figure I.2-1: Summary of the anticancer activity of the bacterial protein azurin.

In turn, based on the characteristics of its regions, azurin has been explored in the form of anticancer bioactive peptides. From C-terminal, several peptides were prepared and shown to be able to bind to ephrin tyrosine kinases receptors, often overexpressed in

cancer, preventing the binding of their ephrinB2 ligand, interfering with their phosphorylation at the tyrosine residue, inhibiting cell signaling and cancer growth. This action translates into an advantage in therapeutic terms, since the commercially available drugs that target these receptors bind to the ATP binding pockets kinases, and this is often unspecific due to the inhibition of other receptors with tyrosine kinase domains unrelated to cancer, leading to toxicity (Chaudhari *et al.*, 2007). In addition, one of these peptides was also linked to a radiotherapeutic compound called nicotinamide, and the combination increased the effectiveness of radiotherapy (Micewicz *et al.*, 2011).

Beyond this, the exposed amphipathic α-helix of azurin (azurin 50-77 amino acids) has also been extensively studied in the form of a peptide called p28, which also presents anti-tumor activity, and enters preferentially in cancer cells (Taylor *et al.*, 2009).

I.2.1. The discovery of p28 and its domains

In 2005, Yamada *et al.* conducted a study with 8 fragments of azurin fused with glutathione S-transferase (GST) to find out if any of them had the ability to promote the entry into cancer cells. These fragments were tested on a number of types of cancer cells, and found that one of these fragments, consisting of 28 amino acids, was more internalized than the others, and able to translocate the cargo protein. This fragment was termed p28, and it has been shown to be identified in cancer cells 3-6-fold higher than in normal ones (Figure I.2-2; Taylor *et al.*, 2009; Yamada *et al.*, 2005).

p28 is a cell-penetrating peptide (CPP), also known a protein transduction domain (PTD), which is, *in part*, responsible for mediating the entrance of the azurin protein into cells (Figure I.2-2). This peptide has an overall net negative charge, and forms an extended amphipathic α-helix with both hydrophobic amino acids (azurin 50-66) in its N-terminal domain, and hydrophilic amino acids in its C-terminal domain (azurin 67-77; Figure I.2-2; Yamada *et al.*, 2005). In 2009, Taylor *et al.* studied these domains separately. In a first phase, they refined the N-terminal domain, calling it p18, and applied it to five types of human cancer cells (melanoma, prostate, colon, lung, and ovarian), as well as in their normal tissue matches. The results showed that this minimal fragment can be more translocated to the inside of cancer cells than normal ones. Beyond this, it has also been described that the penetration of both p28 and p18 is dependent on temperature, presenting a slower entry at 4 ºC than at 22 and 37 ºC, as well as being translated into a saturable process, where possibly receptors, cell surface proteins or specific residues may be responsible, at least *in part*, for the initial entry of them. In addition, proliferation studies

exhibited that p28 inhibited cell survival, but p18 did not cause any cytotoxic effect. Regarding the C-terminal domain, it was also refined and referred to as p12. The application of this fragment demonstrated that its interaction with cells was less than that obtained with p18 and p28, suggesting that the hydrophilicity of this domain contributes to the decrease of selectivity of cell penetration. Beyond this, since p28 has anticancer activity, responsible for cell cycle inhibition and apoptotic activity, and p18 does not, p12 is then considered responsible for this. Thus, it was defined that the N-terminal domain of p28 influences the preferential entry of azurin into cancer cells and its C-terminal domain, its anti-proliferative activity (Figure I.2-2; Taylor *et al.*, 2009; Yamada *et al.*, 2005).

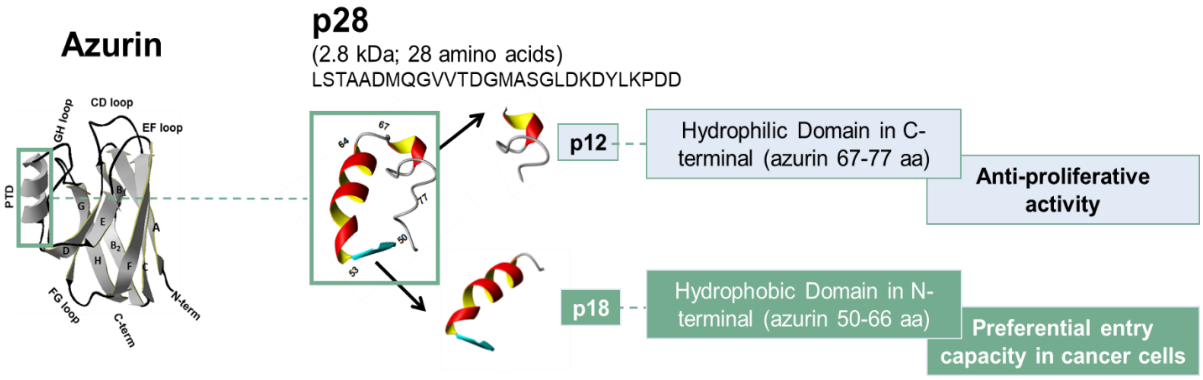

Figure I.2-2: p28 protein transduction domain (PTD) of azurin, its domains and respective activities.

I.2.1.1. Preferred mechanism of entry into cancer cells

p28 is also a tumor-homing peptide, but most of the mechanisms that promote its preferential entry remain to be unveiled. The penetration of this peptide into cells is dependent on the amount of cholesterol in the plasma membranes, on a type of lipid rafts with unique characteristics and biological properties called *caveolae*, as well as on the activity of late endosomes and lysosomes (Taylor *et al.*, 2009). In fact, it has been shown that the entire protein and p28 bind to components such as Golgi apparatus as well as Cav-1 protein and GM-1, which are overexpressed in *caveolae* (Bernardes *et al.*, 2018; Parton, 2018; Taylor *et al.*, 2009). These evidences suggest that p28 penetrates the plasma membrane, *in part*, via *caveolae*-mediated endocytic pathway. In addition, the levels of lipid rafts are increased in several types of cancers (Irwin *et al.*, 2011; Murai, 2015), which suggests that the p28 preferential entry is related to higher proportion of these lipid domains on the surface of cancer cells than in normal ones. However, this should not be the only basic principle used by the protein and its derived peptide, since fibroblasts and some types of normal cells also have a significant number of *caveolae* in their plasma membranes (Parton and Richards, 2003). A study with inhibitors of energy-

dependent transport mechanisms, also demonstrated that the p28 penetration was not inhibited suggesting non-endocytic pathways might also be involved in this process. Beyond this, the entry of p28 is not dependent on membrane bound glycosaminoglycans or clathrins. In a first phase of recognition, it is assumed that N-glycosylated cell surface proteins are involved (Taylor *et al.*, 2009; Yamada *et al.*, 2009). It has also been shown that D-amino acid substitutions within the α-helical backbone changes the p28 chirality that may be critical to its entry, but not for its selectivity (Yamada *et al.*, 2015).

I.2.1.2. Control of cancer proliferation

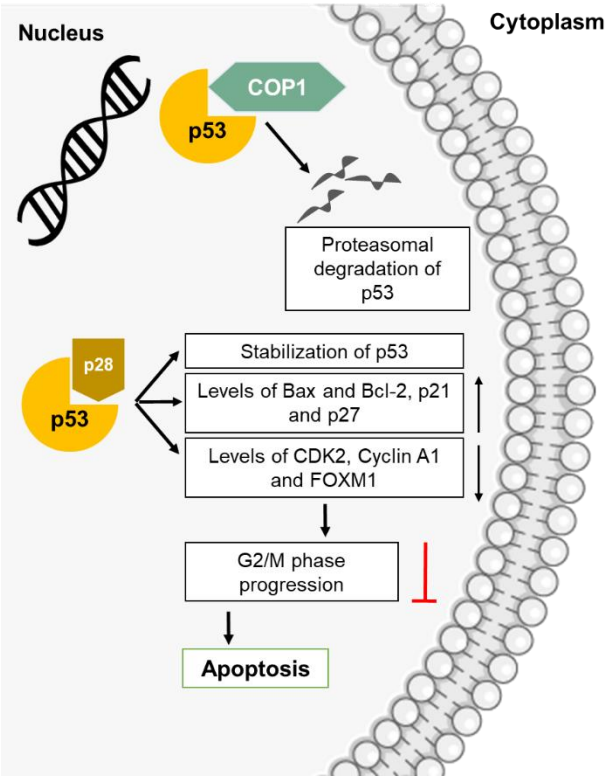

Figure I.2-3: Control of cancer proliferation by p28 via p53 pathway.

Upon entering in cancer cells, p28 promotes the inhibition of tumor growth by interfering with tumorigenesis-related signaling pathways. One of these pathways is based on the action of the tumor-suppressor protein p53, which is involved in many cellular processes, including the promotion of apoptosis (Dornan *et al.*, 2004). p28 competes with the E3 ubiquitin ligase constitutive photomorphogenic 1 (COP1), which is overexpressed in several types of cancer (Figure I.2-3; Li *et al.*, 2012), for the DNA-binding domain (DBD) of p53. When p28 and p53 form a complex, this protein escapes the ubiquitination promoted by its assembly with COP1 (Santini *et al.*, 2011; Yamada *et al.*, 2009; Yamada *et al.*, 2013a; Yamada *et al.*, 2013b). It was also discovered that the binding of p28 to the DBD of p53 is partial, allowing this domain to be available for functional interactions and controlling cell proliferation (Bizzarri *et al.*, 2019). Thus, there is a post-translational increase of p53 in the cytoplasm and nucleus, that therefore rise the cyclin-dependent kinase inhibitors p21 and p27 levels, which in turn reduces the intracellular amounts of cyclin-dependent kinase 2 (CDK2) and cyclin A1, important proteins in the mitotic process, as well as forkhead box M1 (FOXM1), a transcription factor for G2/M phase progression. Subsequently, the decrease in the levels of CDK2, cyclin A1 and FOXM1, and the increased expression of pro-apoptotic genes like

Bax and Bcl-2 leads to apoptosis (Figure I.2-3; Yamada *et al.,* 2009). Studies have also shown that p28 is also able to interact and bind with p53 mutants, and with other members of its family, namely p63 and p73 (Bizzarri *et al.*, 2011; Coppari *et al.*, 2014; Signorelli *et al.*, 2017; Yamada *et al.*, 2013b).

p28 also has an anti-angiogenic effect, essentially related to the inhibition of vascular endothelial growth factor receptor 2 (VEGFR-2) tyrosine kinase activity, and basic fibroblast growth factor (bFGF)-induced migration, capillary tube formation and neo-angiogenesis. This translates into a therapeutic advantage, since anti-angiogenic treatment in many cancers involves the vascular endothelial growth factor (VEGF)/VEGFR2 pathway inhibition. Moreover, the p28 application leads to a downstream phosphorylation of FAK and Akt that typically are responsible for cellular repositioning of the cytoskeletal, focal adhesion, and cell to cell junction. All this enables the reduction of motility, migration, matrix attachment and cell survival (Mehta *et al.*, 2011).

I.2.2. p28 preclinical pharmacokinetic studies and clinical trials

Pharmacokinetic studies play a fundamental role in the development of new drugs (Nishant *et al.*, 2011). In this sense, the pharmacokinetic and metabolic profiles of p28 in mouse, dog, non-human primates and human serum and hepatic microsomes were investigated (Jia *et al.*, 2011). In a first evaluation, the stability of p28 in serum was determined. They found that this peptide is stable at 4 ºC for 48 h, but at 37 ºC a degradation of about 45%, 45%, 79%, and 65% was found in the mouse, dog, non-human primates and human serum, respectively. These results suggested that p28 metabolism is temperature dependent, namely due to enzymatic processes. Regarding the stability of this peptide in hepatic microsomes, it was determined that it is more stable in human hepatic microsomes (41%) than in mouse and non-human primates microsomes (19% and 10%, respectively). *In vitro* and *in vivo* studies were also carried out to determine the metabolites of p28. *In vitro*, after 2 h of incubation, the main metabolite was loss of the N-terminal leucine from p28 that appeared 63%, 63%, and 12% in mouse, monkey and human hepatic microsomes, respectively. The same metabolite was lost on day 1, in the *in vivo* study. It should be noted that both degradation and metabolism of p28 are less accelerated in human hepatic microsomes (Jia *et al.*, 2011). In addition, it was also determined that although p28 is eliminated almost exclusively by the kidneys, this peptide distributes extensively in the species under study, and the entry of p28 into cancer cells is quite rapid, reaching its maximum level after 2 h of exposure (Jia *et al.*, 2011; Taylor *et al.*, 2009; Yamada *et al.*, 2009). The findings also suggest that p28 does not exhibit toxicity (non-

toxic peptide), nor does it trigger immune responses (non-immunogenic peptide). The no observed adverse effect level (NOAEL) for mice was 120 mg/kg/dose, and for monkey following intravenous administration of p28 at 30, 60, and 120 mg/kg three times per week for four consecutive weeks was 120 mg/kg. In relation to the maximum-tolerated dose (MTD), in a mouse was ≥240 mg/kg/dose, and in a monkey was ≥120 mg/kg (Jia *et al.*, 2011). These data were useful to predict therapeutic dose levels in clinical trials. The authors propose that a 10 mg/kg (3.4 μmol/L) dose of p28 offers an initial point for efficacy in a human trial in patients with solid tumors (Jia *et al.*, 2011).

To date, two phase I clinical trials with p28 were performed, both demonstrated that p28 is a safe therapeutic compound for human cancer patients. The first study (NCT00914914) involved 15 adult patients with progressive, refractory or recurrent solid tumors (seven melanomas, two sarcomas, four colon, one pancreatic and one prostate carcinomas), that received at least one dose level of p28 (intravenous administration) as a short infusion 3x per week for 4 weeks (followed by 2 weeks of rest) for a minimum total of 12 doses (Warso *et al.*, 2013). None of the patients presented dose-limiting toxicities (DLTs), significant side effects or showed an immune response to the peptide, consistent with animal models (Jia *et al.*, 2011; Warso *et al.*, 2013). Thus, the NOAEL and MTD were determined above the highest single (50 mg/kg/dose) and cumulative (140 mg/kg/dose) doses studied. The response to the target lesions and survival evaluation demonstrated that one patient had a complete response, three patients had a partial response, seven patients had stable disease, and the median overall survival was 28 weeks. In addition, after administration, the p28 pharmacokinetic behavior confirmed a rapid tissue uptake, an improved terminal phase half-life, a low interpatient variability, and also recommend a dose of 30 mg/kg of this peptide for phase II clinical trials (Warso *et al.*, 2013). In this study, it was also verified that there is no relationship between p53 expression and patient response or survival after treatment with p28 (Bizzarri *et al.*, 2011; Warso *et al.*, 2013; Yamada *et al.*, 2009).

The other clinical trial (NCT01975116) was performed in 12 children (age 3 to 19) with progressive central nervous system malignancies (Lulla *et al.*, 2016), based on the fact that p28 can cross the blood-brain barrier (BBB) and saturates the brain parenchyma in a dose-related manner (Hong *et al.*, 2010). After p28 intravenous administration, the results exhibited that this drug was safe and well tolerated, since the most common side effects were flushing, hot flashes, dizziness, headache and changes in blood pressure, which are events that are usually short and rarely require medical intervention. However, one patient with metastatic pineoblastoma showed evidence of neutropenia and thrombocytopenia. In

addition, the pharmacokinetic study demonstrated profiles similar to those obtained in adult patients (Lulla *et al.*, 2016). Thus, this study led the Food and Drug Administration (FDA) to approve p28 as an orphan drug for the treatment of brain tumor glioma (Fialho *et al.*, 2016; Lulla *et al.*, 2016). Beyond this, although the authors have also shown that the anticancer activity of p28 is independent of the status of p53, as in the first phase I clinical trial (Warso *et al.*, 2013), they argue that p28 as a single cytostatic agent is not probable to be effective against progressive central nervous system malignancies developed by pediatric patients. For this reason, they suggest combining p28 with other therapeutic strategies, such as the one presented in the next section (Lulla *et al.*, 2016).

I.2.3. Combination of p28 with anticancer drugs

The combination of the p28 with anticancer drugs has proved to be a promising combinatorial strategy for cancer treatment (Lulla *et al.*, 2016).

Yamada *et al.*, 2016 simultaneously applied p28 with low concentrations of DNA-damaging drugs (doxorubicin [DOX], dacarbazine, temozolamide) and anti-mitotic agents (paclitaxel [PTX] and docetaxel) in various cancer cell types expressing wild-type or mutated p53 (prostate cancer [LNCaP, DU145 and PC-3], breast cancer [ZR-75 and MDA-MB-231], glioblastoma [U87 and LN229], melanoma [Mel-29 and Mel-23], and neuroblastoma [IMR-32 and SK-N-BE2] human cell lines). Through proliferation assays, the authors concluded that the combined treatment reflected a more pronounced decrease in proliferation rate when the cells were treated with p28 and drug than when the cells were treated with only p28. By pull-down assays, it was further shown that the chemotherapeutic agents' application in combination with p28 did not alter the interaction of this peptide with p53. In addition, the results of *in vivo* assays showed that inhibition of tumor growth was more effective after combined treatment than each of these compounds alone. All this was clearly associated with an increase in p53 and p21 levels, as revealed in western blot analysis. In this case, it was concluded that this combined treatment improved the cytotoxic effect of the drugs due to the enhancer action of p28 on p53/p21/CDK2 pathway, leading to apoptosis (Yamada *et al.*, 2016). Overall, this combinatorial strategy allows to overcome the limitations associated with the higher doses and consecutive administration of anticancer drugs, such as the MDR development and the associated toxicity (Damyanov *et al.*, 2018; Yamada *et al.*, 2016).

I.2.4. p28 as a transport anticancer agent

Due to its property of preferential entry into cancer cells (Taylor *et al.*, 2009), as well as the internalization advantages associated with the fact that it is also CPP, p28 has been considered as a possible cell-penetrating transport peptide. Similar to the first work carried out by Yamada *et al.*, where they used fusion proteins and imaging agents to define which portion of the azurin would be responsible for its entry (Yamada *et al.*, 2005), several studies also suggest that p28 can be fused with proteins/peptides or other interest compounds, and is able to delivery and direct them to cancer cells (Jia *et al.*, 2011; Noei *et al.*, 2019; Raber *et al.*, 2020; Shahbazi and Bolhassani, 2018; Soleimani *et al.*, 2019).

The first study documented in this context proposed the fusion of p28 CPP with the HPV16 E7 oncoprotein as an antigenic model (Shahbazi and Bolhassani, 2018). The HPV16 E7 is expressed constitutively by human papillomavirus (HPV)-infected cells, and was determined as a therapeutic vaccine target. The HPV is related to most cervical cancers, and the existing vaccines have some limitations, namely the weak ability to promote the penetration of proteins and DNA constructs (Yang *et al.*, 2016a). This study demonstrated that p28 complexed with HPV16 E7 allowed its effective and controlled delivery to cancer cells, both *in vitro* and *in vivo*, eliciting immune responses with highest levels of interferon-gamma (IFN-γ) and Granzyme B secretion, and eradicating them. In addition, this immune activity promoted complete tumor-free protection and maintenance after >60 days of treatment. Thus, these findings proposed that p28 is a promising protein delivery system for development of HPV therapeutic vaccines (Shahbazi and Bolhassani, 2018).

Beyond this, p28 was combined with the NRC peptide, an antimicrobial peptide with cytotoxic effect *in vitro* and *in vivo* on various breast cancer cell lines (Soleimani *et al.*, 2019). The main mechanism of action of this peptide is mitochondrial membrane damage (Hilchie *et al.*, 2011). The findings displayed that the treatment with this chimeric protein promoted significant cytotoxicity in a dose-dependent manner with the IC_{50} value of about 2 μM on the breast cancer cell lines, while the IC_{50} of the p28 treatment was about 23 μM. It was also verified that the cell death mechanism was via apoptosis, and through real-time reverse transcription polymerase chain reaction (RT-PCR) was demonstrated a significantly increase in the expression of pro-apoptotic genes, and a decrease in anti-apoptotic genes. In addition, it was possible to define that the cytotoxic effects of p28-NRC protein were caused by mitochondrial caspase-dependent and –independent apoptotic pathways. Finally, the cytotoxicity caused by this chimeric protein was different between

non-cancer and cancer cells, indicating that the use of p28 in this construction is an asset, promoting a selective mechanism (Soleimani *et al.*, 2019).

A similar study was performed with p28 fused to apoptin, a protein that can induces apoptosis in a large number of human cancer cells in a p53-independent manner, and acts in a concentration-dependent manner (Noei *et al.*, 2019). However, it is questioned if the apoptin action occurs in both cancer and non-cancer cells (Tavassoli *et al.*, 2005). Thus, with this combination (≈19 kDa), the authors defend a tumor-targeting strategy (Noei *et al.*, 2019). Initially, a bioinformatics analysis was performed, which allowed the development of a model of this chimeric protein, where a cleavable linker including furin cleavage sites was inserted. This linker can be recognized and cleaved by furin that is expressed in the microenvironment of several types of cancer cells. With this action they predict that the two moieties can separate from each other, being able to carry out their independent intracellular action. Based on this analysis, a plasmid vector was constructed, which was expressed in *Escherichia coli* BL21(DE3), and the chimeric protein obtained through purification steps. Treatment with the p28-apoptin complex demonstrated higher cytotoxicity in the breast cancer cells under study than in the HEK-293 non-cancer cell line, which suggests that p28, despite being linked to another component, did not lose its your selection property. In addition, this decrease in cell proliferation was more pronounced when the cells were treated with the chimeric protein than when treated with apoptin alone, suggesting a synergistic effect (Noei *et al.*, 2019).

More recently, p28 was combined with a photosensitizer (EcFbFP) to be tested as a possible photodynamic therapy (PDT). This study thus described the first genetically engineered hybrid fusion of a short CPP with high cancer cell specificity and a protein photosensitizer. The new compound was called Azulitox (≈19 kDa), and it was obtained through the transformation of competent cells like *Escherichia coli* BL21(DE3) with a plasmid containing a synthetic gene consisting of fused gene sequences of EcFbFP and p28. In a first approach, the authors found that the fusion of p28 to the photosensitizer did not affect the functionality of this compound, and then proved a more efficient uptake of the construction, compared to the observed uptake of EcFbFP alone, with internalization occurring quickly in the first incubation hour. The findings also demonstrated that Azulitox uptake depends principally on *caveolae*-mediated endocytosis as p28 uptake, which suggested that p28 transport domain was fully intact and functional in the fusion complex. Overall, the results indicated that p28 was able to specifically direct and translocate the fused EcFbFP into cancer cells. In addition, the excitation of this photosensitizer after the

application of light led to the production of reactive oxygen species (ROS), which induced a decrease in cell viability of about 90%, compared to the extracellular application of the same photosensitizer (Raber *et al.*, 2020). Based on this research, it becomes clear that similar combinations can be studied with other types of photosensitizers and drugs that can be better tolerated by each of the patients.

Thus, these strategies validated the possibility of developing new and promising therapeutic delivery approaches based on the use of p28, taking advantage of its tumor-targeting capacity, since all these studies indicated that a chimeric protein can be produced, without affecting the biological function of each of the moieties. It was also possible to verify that the use of bioinformatics tools for the design of these compounds can be applied allowing to reduce the consumption time, and it is less laborious and expensive (Agrawal *et al.*, 2020).

In summary, the use of p28 bacterial peptide is a promising strategy in the cancer treatment. This CPP has been shown to have essential features that make it a potential anticancer agent, namely its preferential cell internalization (tumor-homing peptide) and its anticancer activity (Figure I.2-4). These properties are associated with the hydrophobic domain located at the N-terminal, and with the hydrophilic domain located at the C-terminal of this peptide, respectively. Moreover, studies suggest that p28 combined with other compounds, is also an anticancer transporter and enhancer (Figure I.2-4). The first allows p28 to transport a specific cargo to the target cancer site, and the second enhances the cytotoxic effects of drugs administered together. Finally, two phase I clinical trials confirmed the safety and anticancer property of this peptide in human cancer patients (Figure I.2-4). Taking into account everything that is already known, the application of p28 may overcome some of the limitations associated with conventional therapies, making them more effective and efficient.

In the future, as has been done for p28, it will also be interesting to continue the study of other azurin domains, which have already indicated that they also have anticancer properties, and which may prove to be even more powerful.

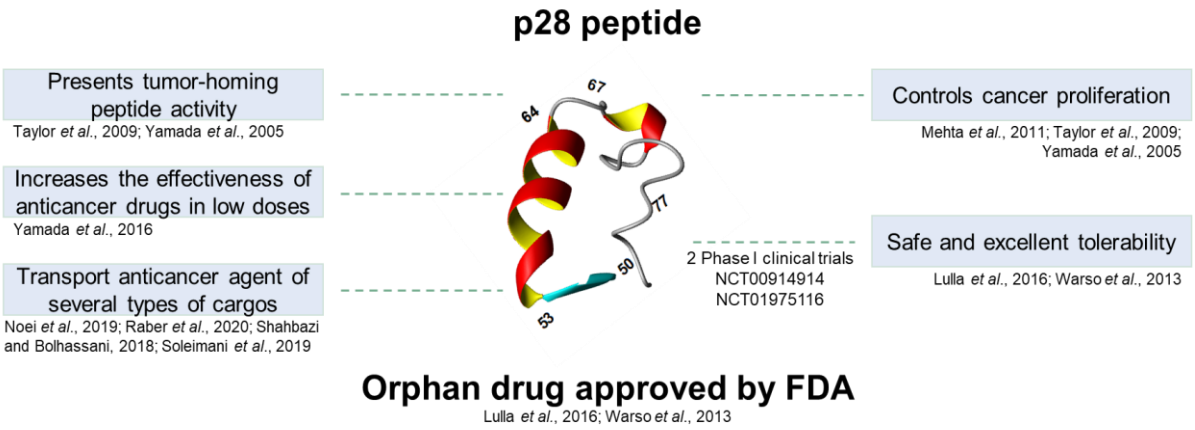

Figure I.2-4: Summary of the p28 potential anticancer.

I.3. Cell-penetrating peptides for cancer therapy

CPPs, also recognized as PTDs, are short peptides (≈5-40 amino acids) with amphipathic or cationic motifs that have the ability to cross the cell membrane efficiently without compromising their integrity (Kurrikoff *et al.*, 2021; Lundberg and Langel, 2003; Vale *et al.*, 2020). These small peptides possess high cellular permeability rates and translocate into a wide spectrum of cell types. Typically, they have a low cell toxicity associated with no immunological response (Lundberg and Langel, 2003). The exact mechanism of CPPs still remains unknown, since this process depending on the several conditions such as the membrane curvature, alterations in membrane domain architecture, non-bilayer disorder, fusion of vesicles and/or lipid flip-flop processes. Nevertheless, biophysical studies elucidated in detail the mechanisms of permeation of lipid bilayer and suggested that different intracellular targets in transmembrane transport are involved, and endocytosis could represent the main entry route for many CPPs (Silva *et al.*, 2018; Silva *et al.*, 2019). Moreover, they are versatile, simple to synthesize, functionalize and characterize (Habault and Poyet, 2019).

Currently, 1855 CPPs are described in the CPPsite 2.0 database, several with the potential to be transport agents for a diversity of cargoes, promoting the access of therapeutic molecules into the cells. In this context, 58% of which deliver fluorophores (imaging agents), 16% nucleic acids and 10% proteins, the remaining 16% distributed by delivery of NPs, peptides, and drugs (CPPsite 2.0, 2021; Kurrikoff *et al.*, 2021). In the case of cancer therapy, CPPs were initially studied to deliver chemotherapeutic drugs to cells (Tan *et al.*, 2006) as well as pro-apoptotic proteins (Johansson *et al.*, 2008). However, there are some limitations to the exclusive application of CPPs as delivery tools. As these peptides are passive and frequently non-selective, CPPs-cargo constructions for cancer diagnosis

or treatment must be combined with a targeting moiety, for example a biomolecule that recognize a membrane receptor of cancer cells (Derakhshankhah and Jafari, 2018; Gessner and Neundorf, 2020; Kurrikoff *et al.*, 2021; Vale *et al.*, 2020). Furthermore, although the number of clinical trials that applied CPPs has increased in recent years, to date, no CPP-conjugated drug has been approved by the FDA (Falanga *et al.*, 2020; Habault and Poyet, 2019; Xie *et al.*, 2020a; Vale *et al.*, 2020).

Nowadays, the study of the application of CPPs in cancer clinical approaches focuses on its use as an adjuvant potentiators of other delivery systems such as NPs (Vale *et al.*, 2020). These peptides promote the internalization of nanosized drug delivery systems (NDDSs), increasing their capacity for intracellular delivery of therapeutic compounds, with low toxicity and high stability (Silva *et al.*, 2019).

I.4. Nanomedicine in cancer

Nanomedicine relies upon the collaboration of several areas such as nanoscience, nanoengineering, imaging, physics, biology, chemistry and medicine to understand how nanomaterials, nanosystems and nanodevices can be applied in prevention, diagnosis (nano-diagnosis) and treatment of various diseases (nano-therapy), as well as in regenerative medicine and in tissue engineering (Iqbal *et al.*, 2018).

The nanomedicine application has demonstrated its value in improving and developing new cancer diagnosis and treatment strategies by modulating the biodistribution of imaging agents/chemotherapeutic drugs and their accumulation in the target sites (Woodman *et al.*, 2020). This is only possible due to the great innovation of nanotechnology: the NDDSs (Figure I.4-1), that have made it possible to respond to unresolved medical needs, such as the ability to explore multiple mechanisms of action (multi-functionality), to integrate effective compounds that conventionally administered in treatments would produce high toxicity with low bioavailability, and resistance to physiological and cellular barriers, the ability to achieve and enter the target tissue, and finally the acquisition of a theranostic potential (diagnosis and therapy combination in the same system; Li and Zhang, 2019; Soares *et al.*, 2018).

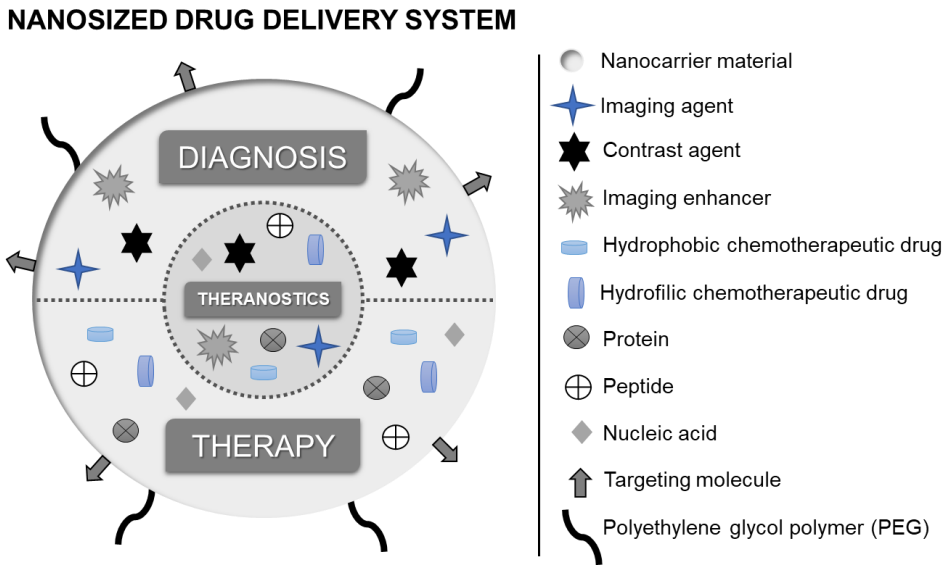

Figure I.4-1: Scheme of nanosized drug delivery system (NDDS).

The NDDSs can be administered by transdermal, parenteral, oral or inhalation routes. After their administration, these nanocarriers encounter some biological, chemical and physical barriers, depend on the route of administration as well as the patient's disease type and progression, through which they have to pass in order to reach their target (Figure I.4-2; Rizvi and Saleh, 2018). For this, effective design of an ideal delivery nanosystem is the key foundation to overcome these barriers.

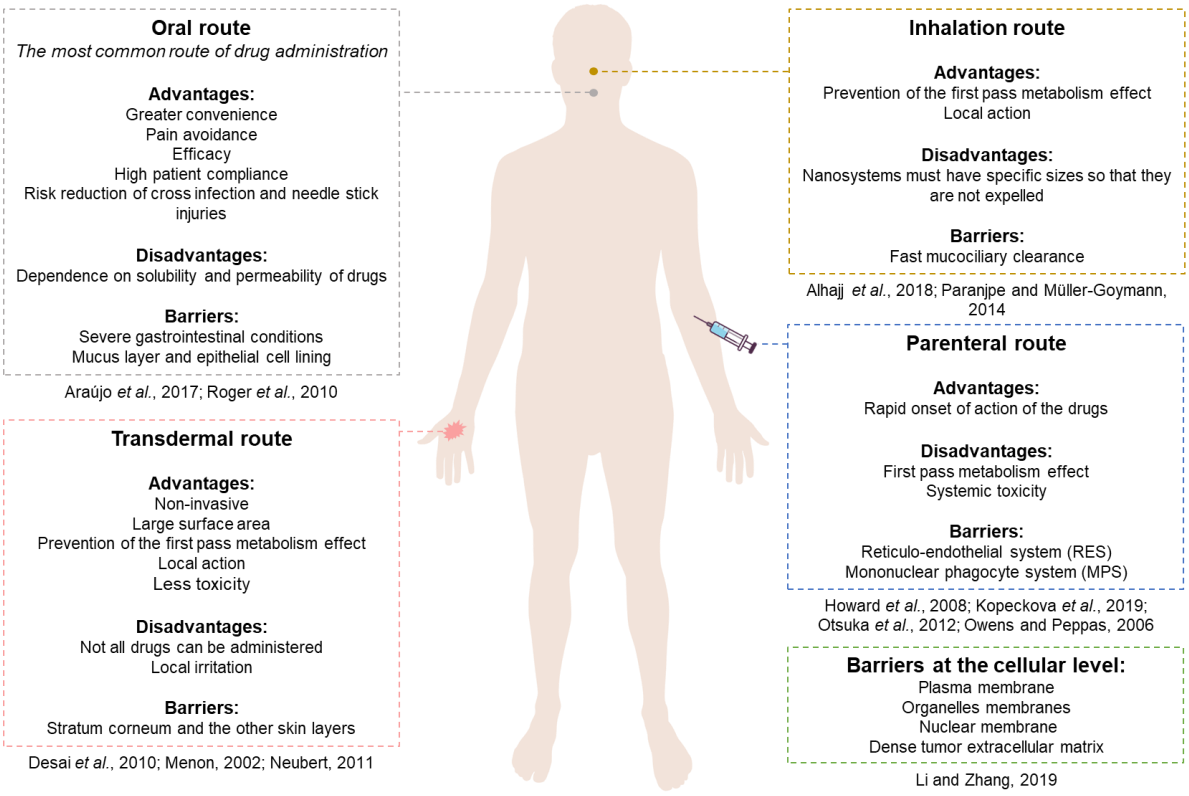

Figure I.4-2: Nanosized drug delivery systems (NDDSs) administration routes, their advantages and disadvantages, as well as associated barriers.

I.4.1. Delivery nanosystems

Although smaller when compared to the average cell size (Figure I.4-3), the NDDSs are large enough to encapsulate many small molecule compounds like chemotherapeutic drugs, nucleic acids, proteins, peptides and hormones (Cryer and Thorley, 2019), which can have poor water solubility, improper size and surface area, and a low therapeutic index by facing elevated biodistribution and targeting challenges (Jahan *et al.*, 2017). The encapsulation of these compounds in nanosystems, helps to avoid their degradation by protecting them from rapid catabolism by detoxification enzymes and body clearance. As a consequence, it helps improving their plasma half-life, increasing their bioavailability, thereby regulating their pharmacokinetic/pharmacodynamic profile, sustaining drug release kinetics, reducing their side effects by decreasing their dosage which can also lead to lower treatment costs. Thus, this technology may offer many advantages compared to administering the drug only (Da Silva *et al.*, 2017; Jahan *et al.*, 2017; Su *et al.*, 2018).

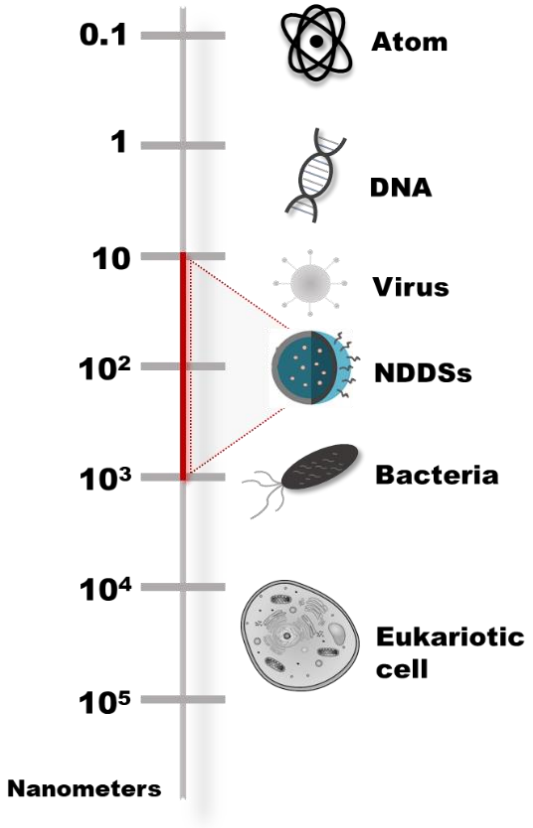

Figure I.4-3: Comparison of nanoscale sizes. **NDDSs:** nanosized drug delivery systems.

In addition to drug carriers, these nanosystems may also be used to encapsulate contrast agents for use in *in vivo* magnetic resonance imaging for diagnostic purposes (Chen *et al.*, 2011).

NDDSs can be constructed from a wide range of nanomaterials (Iqbal *et al.*, 2018), and are classified according to their physical and chemical properties into two main categories: soft and hard solids. The use of each type of NDDSs has associated advantages and drawbacks (Tables I.4-1 and -2; Bor *et al.*, 2019; Su *et al.*, 2018).

Soft solids (Table I.4-1) are based on organic materials that may consist of natural and synthetic biodegradable polymers being able to form dendrimers, nanogels/hydrogels and polymeric NPs (Bor *et al.*, 2019; Cryer and Thorley, 2019; Kamaly *et al.*, 2016); proteins

(Molino and Wang, 2014); lipids that can produce solid liposomes, micelles and lipid NPs (Allen and Cullis, 2013); or carbon structures that can form nanotubes, fullerenes and nanodiamonds (Chen *et al.*, 2015; Yang *et al.*, 2016b). This type of solids can largely depend on environmental factors like temperature, pH, ionic strength or medium characteristics (Su *et al.*, 2018).

On the other hand, the hard solids (Table I.4-2) can be produced by non-biodegradable and non-bio-persistent materials (Bor *et al.*, 2019), made up of inorganic matter such as metals (metallic NPs) like gold, silver, iron (Dreaden *et al.*, 2012; Mahmoudi *et al.*, 2011); silica (Yang *et al.*, 2012); rare-earth elements (Chen *et al.*, 2014) and quantum dots (Zhang *et al.*, 2013).

Furthermore, there are still carriers made up of viral components which do not fall into either hard or soft solids (Yildiz *et al.*, 2011).

Due to all this diversity of nanomaterials that can be used to construct nanosystems, their physico-chemical properties such as size, shape, surface charge, surface roughness and deformability can be tuned and adjusted to control their *in vitro* and *in vivo* behavior (Albanese *et al.*, 2012).

The most used NDDSs in oncology field are protein-based nanocarriers, liposomes, polymeric NPs, dendrimers, hydrogels, carbon nanotubes, gold and silver NPs (Sevastre *et al.*, 2019). To date, even though there has been a huge number of studies related to nanoformulations, only a few of such NDDSs have progressed to market-related assessment and have been commercialized (Tables I.4-1 and -2; Farjadian *et al.*, 2019).

For a rapid and effective clinical translation, the NDDS should have (Attia *et al.*, 2019; Montané *et al.*, 2020):

- Satisfactory physico-chemical properties, including high solubility, high stability and small size;
- Ability to load both hydrophobic and hydrophilic drugs;
- Ability to protect the loaded drug from degradation in physiological fluids;
- Ability to escape from the reticuloendothelial system (RES) clearance and not captured by mononuclear phagocyte system (MPS);
- Accurate and targeted drug delivery to cancer cell without interactions with healthy cells;
- High absorption rate/cellular uptake;
- Acceptable safety in exposure to blood and cell components;
- High manufacturability;
- Sufficient shelf-life during storage.

Table I.4-1: Advantages and disadvantages of various types of soft solids nanosystems, and some commercial products for cancer clinic.

TYPES OF SOFT SOLIDS	ADVANTAGES	DRAWBACKS	COMMERCIAL PRODUCTS FOR CANCER CLINIC	REFERENCES
Dendrimers 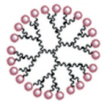	- Well-defined structures - Biodegradable and biocompatible - Water-soluble - Low immunogenicity - Large surface area - High long-term stability	- High cost - Complex synthetic route	- Taxotere®	Duncan and Izzo, 2005; Eftekhari *et al.*, 2019; Gurunathan *et al.*, 2018; Kim, 2007; Montané *et al.*, 2020; Tomalia *et al.*, 1985
Nanogels 	- Biodegradable and biocompatible - Highly porous structure results in controlled pharmacokinetic of the delivery system	- High cost	———	Eftekhari *et al.*, 2019; Prasad *et al.*, 2018
Polymeric NPs 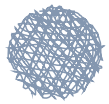	- Biodegradable and biocompatible - Low immunogenicity - Wide payload spectrum of agents - Controlled drug release - Low cost - High long-term stability - Multiple administration routes - Prolonged circulation time	- Insufficient toxicology assessment - Aggregation	- Eligard® - Neulasta® - Oncaspar®	Din *et al.*, 2017; Farjadian *et al.*, 2019; Kahraman *et al.*, 2017; Kopeckova *et al.*, 2019; Masood, 2016; Prasad *et al.*, 2018; Ventola, 2017; Wu *et al.*, 2019
Protein-based Nanocarriers 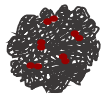	- Easy preparation - Biodegradable and biocompatible - Low immunogenicity - High binding capacity for various drugs - Prolonged circulation time - Versatility	- Easy degradation - Low drug loading efficiency	- Abraxane® - Ontak®	Farjadian *et al.*, 2019; Gou *et al.*, 2018; Montané *et al.*, 2020; Senapati *et al.*, 2018; Ventola, 2017
Liposomes 	- Biodegradable and biocompatible - Low immunogenicity - High intracellular transfection - Easy surface functionalization - Extremely versatile - High-throughput synthesis	- Physically and chemically unstable - Batch to batch variability - High cost - Insufficient drug loading - Slow drug release - Hydrophilic drug leakage	- Doxil®/Caelyx® - DaunoXome® - DepoCyt® - Onivyde® - Myocet® - Mepact® - Marqibo® - Vyxeos®	Akbarzadeh *et al.*, 2013; Attia *et al.*, 2019; Eftekhari *et al.*, 2019; Farjadian *et al.*, 2019; Forssen *et al.*, 1996; Glantz *et al*., 1999; Guaglianone *et al*., 1994; Hubert *et al*., 2000; Immordino and Cattel, 2006; Jaeckle *et al.*, 2002; Judson *et al.*, 2001; Montané *et al.*, 2020; Park *et al.*, 2004; Prasad *et al.*, 2018; Soares *et al.*, 2018; Ventola, 2017
Carbon Nanotubes 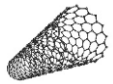	- Large surface area - Exceptional cell membrane permeability - Efficient drug loading - Remarkable optical and electronic properties	- Poor-water solubility - High toxicity - Low biodegradability	———	Din *et al.*, 2017; Madani *et al.*, 2011; Montané *et al.*, 2020; Ng *et al.*, 2016

Table I.4-2: Advantages and disadvantages of various types of hard solids nanosystems, and some commercial products for cancer clinic.

TYPES OF HARD SOLIDS	ADVANTAGES	DRAWBACKS	COMMERCIAL PRODUCTS FOR CANCER CLINIC	REFERENCES
Metallic NPs 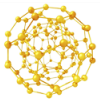	- Physically and chemically stable - Facile synthesis - Easy surface functionalization - Versatility - Exceptional optical and electronic properties	- High toxicity - Non-biodegradable - Coating required	_____	Gurunathan *et al.*, 2018; Montané *et al.*, 2020; Su *et al.*, 2018; Ventola, 2017
Mesoporous Silica NPs 	- Biodegradable and biocompatible - Low immunogenicity - Large surface area - Highly porous structure results in controlled pharmacokinetic of the delivery system - Good thermal and chemical stability	- Surface density of silanol groups interacts with the surface of the phospholipids of the red blood cell membranes resulting in hemolysis - Metabolic changes induced by mesoporous silica NPs leading to melanoma promotion	_____	Bharti *et al.*, 2015; Li *et al.*, 2017; Senapati *et al.*, 2018; Slowing *et al.*, 2008
Quantum Dots 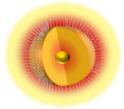	- Biocompatible - Large surface area - Uniform size - Highly tunable photoluminescence property	- Aggregation - Non-specific adsorption - Non-biodegradable - Induction of oxidative stress	_____	Bilan *et al.*, 2016; Senapati *et al.*, 2018; Zhang *et al.*, 2008

I.4.1.1. Nanosystems physico-chemical properties

In order to obtain efficient biological outcomes, a careful design of the NDDSs is necessary, taking into account their physical and chemical properties. These influence the pharmacokinetics of these nanosystems, especially absorption, distribution, metabolism and excretion. In addition, it is important to consider them to analyze possible toxic properties, as well as the persistence of these nanocarriers in the environment and in the human body, and to assess the crossing of biological barriers (Soares *et al.*, 2018).

The size of the NDDSs is one of the most critical design parameter, since this feature can affect their biodistribution, retention time and cellular uptake (Biswas *et al.*, 2014). This characteristic range from 10 nm to 1000 nm (colloidal particles; Da Silva *et al.*, 2017). Nanosystems smaller than 500 nm can penetrate the bloodstream, and larger than 300 nm cannot be absorbed by intestinal cells (Kopeckova *et al.*, 2019). It was reported that 100 nm NPs exhibited a 2.5-fold greater uptake compared to 1 µm diameter particles and a 6-fold higher uptake than a 10 µm particles (Desai *et al.*, 1997). It is also described that smaller NPs (less than 6 nm) are eliminated through the renal filtration system and larger ones (more than 500 nm) are absorbed by the MPS present mainly in the liver and spleen (Gaumet *et al.*, 2008). Thus, from the literature evaluation, the NP optimal size range is around 20-200 nm. Size is also central for the permeation and retention in the tumor areas, and thus is limited by the fenestrations in tumor vessels (Attia *et al.*, 2019). In addition, particle size influences the type of uptake routes. Normally, NPs with a diameter higher than 1 µm internalize through phagocytosis and/or macropinocytosis, while nanosystems with approximately 120 nm, 90 nm or 60 nm preferentially enter the cells by clathrin-mediated endocytosis, clathrin and caveolin-independent endocytosis, and caveolar-mediated endocytosis, respectively. The size of nanosystems can be determined using the following techniques: x-ray diffraction (XDR), scanning electron microscopy (SEM), transmission electron microscopy (TEM), atomic force microscopy (AFM) and dynamic light scattering (DLS; Kim *et al.*, 2019; Kopeckova *et al.*, 2019).

The shape of the nanosystems is another parameter that must be taken into account when approaching the topic of drug delivery. There is a wide range of shapes from spherical to cylindrical, from cubes to ellipsoids and even in disk form. However, it has been found that spherical NPs are more rapidly and uniformly internalized because of their symmetry (Li and Zhang, 2019). In addition, the shape also influences the trafficking of nanomaterial inside the cells. For example, hexagonal shapes are retained in the cytoplasm, while the rod-like ones are moved towards the nucleus by microtubules. This property can be

analyzed using the following techniques: polarized optical microscopy (POM), SEM and TEM (Ping *et al.*, 2008).

In addition to size and shape, the surface charge of these nanosystems also plays a key role in the circulation time and cell internalization. Regarding the circulation time of the nanosystems, hydrophobic or charged systems are rapidly opsonized by the MPS, so it is necessary to make their surface “look like water” as hydrophilic and neutral, or slightly anionic (Attia *et al.*, 2019). About the cell internalization, due to the negatively charged character of the cell plasma membrane, cationic nanocarriers are internalized more efficient than neutral and anionic (Biswas *et al.*, 2014). Furthermore, positively charged nanosystems seem to be able to escape from lysosomes after being internalized and exhibit perinuclear localization, whereas the negatively charged and neutral nanocarriers prefer to colocalize with lysosomes (Danhier *et al.*, 2012). Nevertheless, the cationic ones were susceptible to be opsonized and cleared by RES during blood circulation (Peng *et al.*, 2020). In terms of therapeutic activity and efficacy, it is known that neutral or up to ±10 mV surface charge-based NPs exhibit an enhanced circulation by comparison with high negative or positive charges (Jahan *et al.*, 2017; Wilhelm *et al.*, 2016). This property can be analyzed by zeta-potential (ζ-potential) measurements, which is estimated by laser doppler anemometry (LDA). Colloidal solutions with high ζ-potential (negative or positive) are electrically stabilized while emulsions with low ζ-potential tend to coagulate or flocculate, possibly leading to poor physical stability. In general, when the ζ-potential of an emulsion is high, the repulsive forces exceed the attractive forces, resulting in a relatively stable system (Kumar and Dixit, 2017). With these data, it can be concluded that the chemical properties of nanosystem surfaces play an important role in their interaction with each other, with their surrounding environment, and with cells (Biswas *et al.*, 2014).

However, in spite of all the developments in nanomedicine, combining these factors to define the best characteristics of a nanosystem to be applied in novel therapies remains a challenge (Biswas *et al.*, 2014).

I.4.1.2. Biological targeting

For a high therapeutic efficacy, it is important to considered the five steps of the CAPIR cascade: blood Circulation, Accumulation and Penetration in the tumor, interaction and Internalization with the targeted tumor cells, and finally the intracellular Release of the drug (Fernández *et al.*, 2020).

Nanocarriers loaded with one or more therapeutic compounds can accumulate in the neoplastic tissue by passive targeting (Figure I.4-4). This mechanism depends on the Enhanced Permeability and Retention (EPR) effect (Jahan *et al.*, 2017) described by Matsumura and Maeda in 1986. It is known that in typical tumor conditions of inflammation/hypoxia, the endothelium of blood vessels becomes more permeable than in the healthy mode. This EPR effect occurs due to the fact that tumor tissues present a disorganized and leaky vasculature with enlarged inter-endothelial gaps around 100 nm to 2 μm depending upon the tumor type. In addition, these tumor sites produce a variety of vascular permeability factors and have an ineffective lymphatic drainage (interstitial pressure is higher at the center of tumors than at the periphery). These characteristics facilitate the permeability and retention of nanosystems in tumor areas. It should be noted that this effect varies from tumor to tumor and from patient to patient owing to the intrinsic tumor biology that each one can present, namely in the angiogenesis and lymph-angiogenesis degrees, in the degree of perivascular tumor growth and the density of the stromal response, and in the intratumor pressure. On the other hand, the normal vasculature is permeable only to molecules that are smaller than 2-4 nm, whereby nanosystems are not largely internalized by healthy cells. In addition, reports have shown that the EPR effect provides that about 10 to 15% of the injected nanosystems are able to accumulate at the tumor site compared to the administration of free drugs that reaches up to 0.1% (Albanese *et al.*, 2012; Attia *et al.*, 2019; Bazak *et al.*, 2014; Byrne *et al.*, 2008; Matsumura and Maeda, 1986; Mitchell *et al.*, 2020).

Despite all the knowledge about the EPR effect, some criticisms question its value. Some nanomedicine researchers argue that this effect exists only in mice and not in humans, but it is generally agreed that passive accumulation definitely occurs, despite being highly heterogeneous (Meel *et al.*, 2019). However, others report that this passive targeting does not occur due to the inter-endothelial gaps in the tumor area (passive process), but by an active process through the binding of nanosystems to endothelial cells and transport through them inside vesicles, or transport through transcellular channels that are formed through connecting vesicles, or any other mechanisms that have not yet been discovered (Sindhwani *et al.*, 2020).

In addition to the ability of nanocarriers to penetrate the tumor areas due to passive targeting, it is also possible to increase their internalization in cancer cells through an active targeting (Figure I.4-4). Since these NDDSs comprise a relatively large surface area in relation to the volume due to their small size, they can also be used to bind biological

targeting agents (functionalization process) such as small molecules, DNA or ribonucleic acid (RNA) strands, proteins, peptides, aptamers or antibody fragments. This specifically direct them towards a component of the tumor or the surrounding microenvironment (Byrne *et al.*, 2008; Soares *et al.*, 2018). A crucial requirement to reach an optimal target specificity is ligand attachment in a stable, oriented, and dense manner thus conserving the binding capacity of the ligand to its target (Thalhauser and Breunig, 2020). Ligands can bind to the surface of the nanosystems with or without cross-linking agents through various bonding methods such as covalent methods (like carbodiimide or click chemistries) and physical adsorption methods (electrostatic interactions; Jahan *et al.*, 2017). They have advantages such as rational size, high stability, low-cost, facile conjugation, low immunogenic effects and favorable physicochemical properties that made them a successful targeting approach for engineered nanosystems (Li and Zhang, 2019). Beyond this, the nature of these compounds can be important to improve the circulation time, cellular uptake, affinity, extravasation, aggregation and stability of the NDDSs (Byrne *et al.*, 2008; Rizvi and Saleh, 2018).

In theory, these products lead to a favorable biodistribution to which a higher drug concentration is delivered in the intra-tumoral region. In comparison to conventional therapy, this would lead to a reduction in the amount of drug administered capable of eliciting an effective therapeutic response, without causing side effects, dose limiting toxicities, and acquisition of MDR, improving the patient quality of life as well as the survival (Byrne *et al.*, 2008; Cryer and Thorley, 2019; Li and Zhang, 2019).

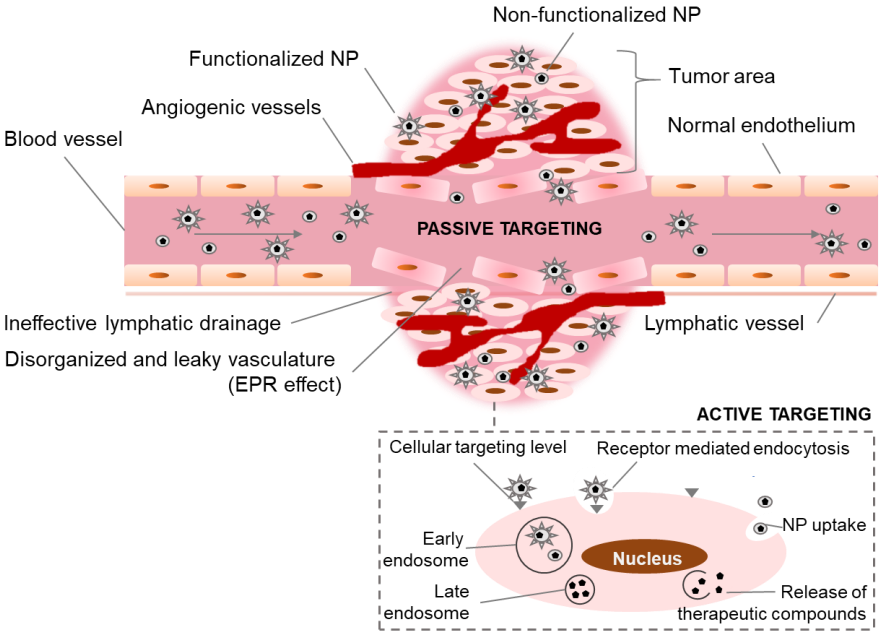

Figure I.4-4: Schematic representation of passive and active targeting approaches.
EPR effect: Enhanced Permeability and Retention effect; **NP:** Nanoparticle.

I.4.2 Poly (lactic-co-glycolic acid) nanoparticles and their application in cancer therapy

When starting the study of a new nanosystem for medical applications mainly, it has to be taken into account the toxicity it may have associated. The compounds chosen to be part of these vehicles must be biodegradable and biocompatible which can be degraded *in vivo*, via enzymatic or non-enzymatic routes, producing by-products further eliminated by common metabolic pathways and with this, it induces a minor inflammatory response. This is the case of poly (lactic-co-glycolic acid) (PLGA) synthetic polymer, typically produced by a catalyzed ring-opening copolymerization of lactic acid (LA; 2-hydroxypropanoic acid) and glycolic acid (GA; 2-hydroxyethanoic acid) monomers. This polymer has been the most promising material showing potential to be used as carrier in drug delivery, having been approved by the FDA and the European Medicines Agency (EMA) for parenteral administration, diagnostics and other applications of basic and clinical research (Figure I.4-5; Calzoni *et al.*, 2019; Kim *et al.*,2019; Martins *et al.*, 2018; Mir *et al.*, 2017).

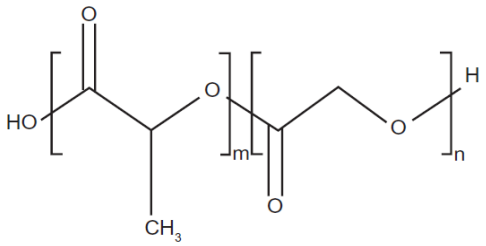

Figure I.4-5: Poly (lactic-co-glycolic acid) polymer (PLGA) chemical structure; **m:** number of units of lactide acid (LA); **n:** number of units of glycolic acid (GA). From Dinarvand *et al.*, 2011.

Upon hydrolysis, the constituents of this polymer, lactate and glycolate linked by an ester bond, can be integrated into metabolic pathways. LA is converted into CO_2, excreted by the breathing process or converted to pyruvate, which enters the Krebs cycle. On the other hand, GA is either directly excreted through the renal system or can be oxidized to glyoxylate, which is afterward further converted into glycine, serine, and pyruvate, which also enters the Krebs cycle (Danhier *et al.*, 2012; Silva *et al.*, 2015).

Poly (lactic acid) (PLA) is more hydrophobic than poly (glycolic acid) (PGA) due to the presence of a side methyl group present in the first one. With this, the PLGA degradation properties can be controlled by tuning the ratio between PLA and PGA units. For example, with an increase in the LA/GA ratio, the overall PLGA hydrophobicity increases, which leads to lower degradation, and thus slower drug release rate. However, it is reported that the 50:50 ratio shows the fastest degradation rate around two months *in vivo* (Calzoni *et al.*, 2019; Kim *et al.*, 2019; Mir *et al.*, 2017). In addition, it is demonstrated that *in vitro*

degradation of PLGA is highly dependent on pH, where strongly alkaline media stimulates and accelerates PLGA hydrolysis (Martins *et al.*, 2018). Beyond this, the polymer molecular weight (Mw) also influences its degradation rate. The lower the Mw, the higher the degradation rate of this polymer and consequently, the higher the drug release rate. Typically, Mw in range of 5-150 kDa is used for controlled drug delivery systems (Fredenberg *et al.*, 2011).

The most used techniques that allow the production of PLGA NPs are single (oil in water [O/W]) or double/multiple (water in oil in water [W/O/W]) emulsification (most frequently used method), nanoprecipitation, spray drying and microfluidics. Depending on the technique chosen, these nanosystems will present certain shapes, sizes, size distributions and stabilities. All these methods have their pros and cons, and the chosen one must take into account the NPs physico-chemical properties that are desired and possible interactions between the drug that is intended to be encapsulated with the polymer, the solvents and surfactants used in each one (Table I.4-3). The formation of these nanosystems is usually driven by supramolecular self-assembly. The driving force is typically intermolecular non-covalent interactions, including hydrophobic interaction, electrostatic interaction, hydrogen bonding, host-guest interaction, and π−π stacking (Mir *et al.*, 2017).

Over time, PLGA NPs have proven their NDDS potential for numerous therapeutic agents such as antibiotics, chemotherapeutic, antiseptic, anti-inflammatory and antioxidant drugs, or proteins (Danhier *et al.*, 2012).

Another advantage of using this polymer is that it can be chemically modified, after or before NPs production, to give biofunctionality. These chemical modifications are provided by functional groups that allow the binding of compounds of interest to the NPs surface. These compounds of interest can be hydrophilic molecules such as polyethylene glycol (PEG) or targeting moieties like folic acid (FA), aptamers, antibodies and CPPs, which in the first case will allow to prolong the circulation time in the bloodstream, since it will be possible to escape the RES, and in the second case are specifically recognized by receptors that are overexpressed or are unique in tumor cells or tumor vasculature, or are attracted to the tumor environment, resulting in increased penetration of these nanosystems into tumor cells (Kim *et al.*, 2019).

Several examples of multifunctional PLGA NPs have been developed and studied, and have shown promising strategies for use in cancer therapy (Table I.4-4).

Table I.4-3: Most common Poly (lactic-co-glycolic acid) (PLGA) nanosystems production methods.

PRODUCTION METHOD	PROCEDURE	PROS	CONS	REFERENCES
Single, double or multiple emulsifications	In the single emulsion, PLGA polymer and hydrophobic drugs are dissolved in water-immiscible organic solvents, and added to an aqueous phase containing surfactant. The mixture is homogenized using a homogenizer or ultrasonic probe. Then, the organic phase is evaporated through simple stirring, under a gentle nitrogen gas stream or in a vacuum state. The NPs are obtained by centrifugation, washed to remove the surfactant and lyophilized for later storage. In the double emulsion an aqueous phase containing hydrophilic drugs is added to the organic phase containing the PLGA, and they are homogenized by vigorous stirring. This is added to the aqueous phase containing the surfactant, and the procedure is the same as for the single emulsion. This procedure can be repeat to produce multiple emulsions.	- Suitable for hydrophobic (single emulsion) and lipophilic (double or multiple emulsions) drugs encapsulation - NPs size can vary from nano to micrometers - Ease scale-up	- High shear stress - Partial elimination of organic solvent and surfactant - Batch-to-batch variance - Polydispersity of particle size - Inaccurate loading/dosing - Unpredictable drug release kinetics	Ding and Zhu, 2018; Kim *et al.*, 2019; Rezvantalab *et al.*, 2018; Swider *et al.*, 2018
Nanoprecipitation	The most common technique used to encapsulate hydrophobic drugs. The organic phase is usually injected at a constant flow into the aqueous phase under magnetic mild stirring. During this step, rapid diffusion of the organic solvent occurs through the aqueous phase, leading to the polymer precipitation which instantly leads to the self-assembly of core–shell-like spheres. In addition, drugs are entrapped within the polymeric core. Then, the organic phase is evaporated at room temperature or with a rotavapor. Ultracentrifugation, ultrafiltration or freeze drying are three methods that could be employed in next step to eliminate the surfactant and the drug that was not encapsulated.	- Simplest method - Instantaneous NPs formation - Stable produced formulations - One-step procedure - Quick process - Profitability - Good/high reproducibility - Safety - Low energy input - Ease scale-up	- Not suitable for lipophilic drugs encapsulation - Partial elimination of organic solvent and surfactant - Need to control the speed of phase mixing for the size distribution of NPs can be controlled	Almoustafa *et al.*, 2017; Bilati *et al.*, 2005; Kamaly *et al.*, 2016; Kim *et al.*, 2019; Nagavarma *et al.*, 2012; Rivas *et al.*, 2017; Tao *et al.*, 2019; Werengowska-CieTwierz *et al.*, 2015
Spray-Drying	NPs are prepared by spraying solid in oil (s/o) dispersion or water in oil (w/o) emulsion in a stream of heated air.	- Suitable for hydrophobic and lipophilic drugs encapsulation - High entrapment efficiency - One-step procedure - Quick process - Good/high reproducibility - Ease scale-up	- NPs adhesion to the walls - Difficulty in control of size - Diversity in particle shape - High pumping power	Booysen *et al.*, 2013; Ding and Zhu, 2018; Kim *et al.*, 2019; Swider *et al.*, 2018
Microfluidics	There are two types of systems: the flow-focusing and the co-flowing systems. In the first one, the dispersed phase flows through a narrow capillary and the continuous phase flows from the two side channels with the vertical direction of the dispersed phase. In the second one, the dispersed phase flows inside the capillary and the continuous phase flows outside the capillary in the same direction.	- Precise of processing parameters - NPs production with narrow size distribution - Precisely controlled size and shape - Prevention of an initial burst release	- Limited production scale and scale-up - Microchannel clogging and fouling	Ding and Zhu, 2018; Kim *et al.*, 2019; Rezvantalab *et al.*, 2018; Swider *et al.*, 2018

NPs: Nanoparticles; **PLGA:** Poly (lactic-co-glycolic acid)

Table I.4-4: Examples of targeted and loaded Poly (lactic-co-glycolic acid) (PLGA) nanoparticles (NPs).

TARGETING MOIETY	LOADED DRUG	APPLICATION	REFERENCE
Epidermal growth factor	5-fluorouracil and Perfluorocarbon	Colon cancer	Wu *et al.*, 2020
GE11 peptide	Curcumin		Akl *et al.*, 2019
Chondroitin sulfate	Camptothecin		Zu *et al.*, 2019
SP94 peptide	Cryptotanshinone	Hepatocellular carcinoma	Nie *et al.*, 2020
CD-340 antibody	Doxorubicin	Breast cancer	Mondal *et al.*, 2019
Heparanase aptamer	Paclitaxel		Duan *et al.*, 2019
Cholesterol-PEG	Doxorubicin and Indocyanine green		Chen *et al.*, 2019
Sialyl-Lewis A antibody	5-fluorouracil and Paclitaxel	Gastric cancer	Fernandes *et al.*, 2019
Cholera toxin subunit B	Paclitaxel	Glioblastoma	Guan *et al.*, 2019
Aptamer	Doxorubicin	Lung cancer	Saravanakumar *et al.*, 2019
Folic acid	Gefitinib and Capsaicin		Parashar *et al.*, 2019
Cholic acid	Ent-11α-hydroxy-15-oxo-kaur-16-en-19-oic acid	Liver cancer	Gong *et al.*, 2019
α-tocopherol	5-fluorouracil	Oral squamous cell carcinoma	Srivastava *et al.*, 2019
C2NP aptamer	Doxorubicin	Anaplastic large cell lymphoma	Luo *et al.*, 2019
Carcinoembryonic antigen	-	Colorectal cancer	Sousa *et al.*, 2019
v6-specific antibody fragment	Bevacizumab		Baião *et al.*, 2020

The uptake and intracellular trafficking dynamics of PLGA-NPs is also an important topic for studying the therapeutic effectiveness of this nanosystem. Studies have shown that these NPs are taken up by macropinocytic, *caveolae*- and clathrin- mediated endocytic pathways, but the passive diffusion is also a significant contributory pathway in cellular uptake of NPs. In addition, their uptake is concentration- and time-dependent, and the rate and extent of uptake differs in relation to the cell type under study due to the inherent regulatory mechanisms. Beyond this, it was recently discovered that an active exocytosis process is mainly responsible for extrusion of NPs from the cells (Baidya *et al.*, 2020; Cartiera *et al.*, 2009; Qaddoumi *et al.*, 2004; Sahin *et al.*, 2017; Xiong *et al.*, 2011). Studies suggest that after exposure and after a short period of time, PLGA-NPs are co-located in early endosomes, and that over time they escape from this compartment and will interact with exocytic organelles of the cell: the RES, the Golgi apparatus, and secretory vesicles. In addition, these NPs are not highly co-localized with late endosomes or lysosomes relative to the other compartments, which leads to the conclusion that those nanosystems may largely escape endo-lysosomal degradation (Cartiera *et al.*, 2009; Panyam *et al.*, 2002).

About the toxicity effects of PLGA NPs, they have been determined on an extensive variety of cell lines showing very little or no toxicity *in vitro*. These types of nanosystems have also been tested for their *in vivo* toxicity on visceral organs, and a minimal toxicity in intestine and liver and no toxicity in kidney, brain and lung were observed (Mir *et al.*, 2017).

For the clinical translation of developed PLGA NPs, the following problems should be overcome (Danhier *et al.*, 2012; Sadat *et al.*, 2014):

- In spite of high drug encapsulation efficiency, poor drug loading (DL) capacity (around 1% which means that NPs content is 1 mg of active ingredient per 100 mg of polymer);
- High initial burst release rate of drug. The drug might not be able to reach the target tissue or cells, leading to a loss of efficacy. Generally, the rapid initial, or burst release is attributed to adsorbed drug to the NPs surface;
- Finally, nanotoxicology studies and regulations are needed in order to fully define the biocompatibility of these NPs in humans. In most of case, *in vitro* studies provide encouraging results. Unfortunately, these results are often far away from reality *in vivo*. In the same line, animal models routinely used in preclinical trials are far from being representative for the clinical situation.

However, some PLGA-based nanosystems have succeeded to overcome the previously described hurdles, and are being evaluated in clinical trials such as Docetaxel loaded PEG-PLA-Prostate-Specific Membrane Antigen (PSMA)-targeted NPs (research product of Bind Biosciences, Inc. and named as BIND-014), which is in clinical trial phase II and is being studied to treat metastatic or advanced cancer (ClinicalTrials.gov identifier: NCT01792479).

I.4.2.1 Poly (lactic-co-glycolic acid) nanoparticles functionalized with cell-penetrating peptides

The conjugation of CPPs to PLGA NPs is a promising approach to increase the internalization of them, thus, facilitating the design of efficient delivery nanosystems with accuracy and therapeutic activity. Nevertheless, their combination with nanocarriers is extremely complex, starting with the chosen conjugation method that plays a fundamental role, which can compromise the biological action of these CPPs (Gessner and Neundorf, 2020).

The potential of CPP-functionalized PLGA NPs as chemotherapeutic drug delivery systems has been studied on a large scale over the past decade.

Li *et al.*, 2011 report the production of PEG-PLGA NPs with a CPP called 12-mer peptide (TGN) that is capable of directing these coumarin-6 loaded nanosystems to the brain. These were able to overcome the blood-brain barrier, central for maintenance of brain homeostasis and protection against organisms and toxins, and thus served as a diagnostic device, since they were able to recognize glioblastoma cells. This targeting was 3.6-fold times higher than this type of NP without functionalization (Li *et al.*, 2011).

Chen *et al.*, 2012 tried a new approach to treat breast cancer by producing PEG-PLGA NPs functionalized with a CPP designated R7 and FA, and with encapsulated vincristine sulfate (VCR). These bifunctional NPs (BF-NPs) showed favorable particle size and zeta potentials, promising DL and entrapment efficiency. The cellular uptake of BF-NPs was found to be higher than that of the NPs merely modified by FA or R7. *In vitro* cytotoxicity, cell apoptosis and cell cycle arrest studies also revealed that BF-NPs were more potent than those of the NPs merely modified by FA or R7. Therefore, the results demonstrated that BF-NPs developed in this study could be a potential vehicle for delivering chemotherapeutic agents such as VCR for breast cancer therapy (Chen *et al.*, 2012).

MDR is a major challenge for cancer therapy. For this reason, Wang *et al.*, 2014 developed the simple yet effective system, CPP-assisted PLGA NPs for improving DOX delivery and overcoming this problem. They selected the naturally derived low molecular weight CPP (LMWP) to coat PLGA NPs surface for enhanced DOX delivery. This delivery nanosystem could boost intracellular and intranuclear delivery, thus avoiding drug efflux. Importantly, enhanced uptake and penetration within the tumor was found in mice given LMWP-based NPs. In addition, LMWP-PLGA NPs effectively arrested growth in mice harboring drug-resistant breast tumors, thereby improving treatment outcomes without detectable toxicities. These data suggest that this nanosystem could provide effective yet safe anti-MDR cancer therapy based on a synergistic, multipronged drug-delivery strategy (Wang *et al.*, 2014).

In the area of hepatocarcinomas, some studies with this type of nanocarrier have shown good results. This is the case of Zhang's work demonstrating that trans-activator of transcription (TAT) of human immunodeficiency virus CPP functionalized PLGA NPs efficiently deliver epirubicin, an anticancer drug that acts against hepatic cancer and neuroblastoma cell lines. The construct demonstrated a sustainable release of about 38% in 48 h and intravenous administration of 4 µg/mL resulted in inhibition of tumor growth after 15 days of treatment (Zhang *et al.*, 2015).

The study of Sims *et al.*, 2019 proposed a formulation constituted of PEG-PLGA functionalized with a CPP called MPG and encapsulated DOX. In this case, the effectiveness of this formulation depended on the type and morphology of the cervical tumor. Longer-term, this information may help guide the design of NPs mediated strategies to maximize efficacy based on patient specific cervical tumor origin and characteristics (Sims *et al.*, 2019).

These advances and innovations have revealed that CPP conjugation with PLGA-NPs presents outstanding therapeutic delivery potential as non-toxic compounds that can be applied in the near future for cancer diagnosis and treatment.

I.4.3 Nano-therapy in lung cancer

In recent years, lung cancer is the most incident and the leading cause of cancer death worldwide, being considered a global health problem (Figure I.1-1). It is estimated that from 2018 to 2040, the incidence increases from 2.1 million cases to 3.6 million new

diagnosed cases, and mortality increases from 1.8 million to 3.1 million deaths (Wild *et al.*, 2020).

There are two types of lung cancer: non-small cell lung cancer (NSCLC; 85% of cases) and small cell lung cancer (SCLC; 15% of cases; Pirker, 2020), which differ from each other in the histological profiles and locations of their cells. NSCLC is further subdivided into adenocarcinoma (ADC), squamous cell carcinoma (SCC), large cell carcinoma (LCC) and other less differentiated variants. The first two are the most common subtypes, 60% and 15% of cases, respectively. As these types have different morphological features, molecular characterization and etiology, they give rise to particular conditions of the tumor microenvironment, contributing to the difficult treatment of NSCLC (Alhajj *et al.*, 2018; Cryer and Thorley, 2019; Travis *et al.*, 2015). In the case of SCLC type, this is an aggressive, fast growing lung cancer, and can be classified into oat cell cancer (OCC) and combined small cell carcinoma (CSCC; Sher *et al.*, 2008).

Tobacco smoking, and about 29 agents such as asbestos, silica, radon and several heavy metals have been recognized to cause this disease, depending on the exposure time to these compounds. Besides these, certain foods, alcohol, a sedentary lifestyle and outdoor air pollution were also considered risk factors (Wild *et al.*, 2020). However, the genetic component also has its relevance in this disease. It is estimated that the heritability of lung cancer is about 18%, and that having a first-degree relative with this disease increases the risk of lung cancer by 1.25-1.5-fold in never-smokers (Coté *et al.*, 2012).

Genetic changes in cells can occur in response to risk factors, leading to the formation of cancer (Alhajj *et al.*, 2018). Genomic characterizations demonstrated a very high average tumor mutation burden of about 8-9 somatic mutations per megabase (Wild *et al.*, 2020), most of which involve cell signaling pathways including the ErbB protein family (EGFR/HER1-4) and the Kirsten rat sarcoma virus GTP-ase (K-ras) gene (Groot *et al.*, 2018). Typically, these mutations can trigger molecular biological changes in cells. An example of these changes can involve receptors overexpression on their surfaces or inside them (Alhajj *et al.*, 2018). The EGFR overexpression is one of those cases. This receptor is a transmembrane peptide with a ligand binding extracellular segment for the epidermal growth factor (EGF), and an intracellular segment characterized by tyrosine kinase activity. EGFR is expressed moderately on alveolar epithelial cells surface and intensively on bronchial epithelial cells. When the gene of this receptor mutates, it begins to be overexpressed in cancer cells and promotes angiogenesis, proliferation, invasion and metastasis. In the case of lung cancer, this receptor is associated with 85% of NSCLC, of

which 60% are expressed in SCC and 40% in ADC and LCC. In the case of SCLC, no expression of EGFR has been detected (Cadranel *et al.*, 2013; Nakamura *et al.*, 2006). Finally, other genetic and epigenetic variations can origin inactivation of tumor suppressor genes for example the p53, p16 and phosphatase and tensin homolog (PTEN; Groot *et al.*, 2018).

The diagnosis and treatment of lung cancer have become two important areas in research due to the disease's increased morbidity and mortality in the last years.

In the case of diagnosis, for an early detection, methods such as spiral computed tomography (CT) scanning, PCR sputum assay and fluorescence bronchoscopy are expensive, fairly time consuming and relatively invasive. In fact, the most usual procedures are biopsy, bronchoscopy and sputum cytology, which occasionally fail to detect the tumor owing to the nodule size (Woodman *et al.*, 2020). With the advances in molecular biology, diagnostic methods have also been evolved with the identification of specific biomarkers. These are substances produced by tumor cells or induced by tumor cells from non-tumor cells that allow molecular profile analysis for the application of a personalized therapeutic strategy (Cryer and Thorley, 2019). More recent, exhaled volatile organic compounds (VOCs) have been considered non-invasive biomarkers that are indicative of mutations and pathophysiological processes of lung cancer. These diagnostic methods are intended to achieve early detection, screening for therapeutic targets, profiling cancer panel, monitoring therapeutic effectiveness and early recurrence detection (Li *et al.*, 2020).

The lung cancer treatment requires multidisciplinary co-operation, and is based on surgery, radiofrequency ablation, chemo-targeted therapies, radiotherapy, immunotherapy and palliative therapy. The treatment depends on tumor characteristics, tumor stage and patient-related factors (Pirker *et al.*, 2020; Woodman *et al.*, 2020). In most cases, surgical resection is the first to be applied. However, due to the advanced stage or metastatic spread of this disease at the time of diagnosis, this modality may not be effective. Thus, radiotherapy and chemotherapy can also be applied, individually or in combination, as a neoadjuvant or adjuvant therapies. Radiotherapy is usually performed through the administration of high dose radiation specifically to the tumor delineated by advanced techniques such as four-dimensional CT, positron emission tomography-CT or image guided radiotherapy. Regarding chemotherapy, drugs have been developed that act on the products of mutated genes identified in this disease, such as EGFR, anaplastic lymphoma kinase (ALK), K-ras, ROS proto-oncogene receptor tyrosine kinase 1 (ROS1), VEGFR genes (Table I.4-5; Cryer and Thorley, 2019).

Table I.4-5: List of drugs approved by the Food and Drug Administration (FDA) for lung cancer treatment. Sources: NATIONAL CANCER INSTITUTE, 2020 and FOOD AND DRUG ADMINISTRATION, 2020.

LUNG CANCER TYPE	ANTICANCER DRUG	BRAND NAME	FIRST APPROVAL
Non-Small Cell Lung Cancer (NSCLC)	Afatinib Dimaleate	Gilotrif®	2013
	Alectinib	Alecensa®	2015
	Atezolizumab	Tecentriq®	2016
	Bevacizumab	Avastin®; Mvasi™	2004; 2017
	Brigatinib	Alunbrig™	2017
	Carboplatin	Paraplatin®	2003
	Ceritinib	Zykadia®	2014
	Crizotinib	Xalkori®	2011
	Dabrafenib Mesylate	Tafinlar	2013
	Dacomitinib	Vizimpro®	2018
	Dexrazoxane Hydrochloride	Totect® Zinecard®	2007 1995
	Docetaxel	Taxotere	1996
	Durvalumab	Imfinzi®	2017
	Entrectinib	Rozlytrek™	2019
	Erlotinib	Tarceva®	2004
	Everolimus	Afinitor®; Afinitor Disperz®; Zortress®	2009
	Gefitinib	Iressa®	2015
	Gemcitabine Hydrochloride	Gemzar	1996
	Lorlatinib	Lorbrena®	2018
	Methotrexate	Rheumatrex	1953
	Necitumumab	Portrazza	2015
	Nivolumab	Opdivo	2014
	Osimertinib Mesylate	Tagrisso™	2015
	Paclitaxel	Taxol®	2002
	Pembrolizumab	Keytruda®	2014
	Pemetrexed Disodium	Alimta®	2004
	Ramucirumab	Cyramza	2014
	Trametinib	Mekinist®	2013
	Vinorelbine Tartrate	Navelbine®	1994
Small Cell Lung Cancer (SCLC)	Atezolizumab	Tecentriq®	2016
	Dexrazoxane Hydrochloride	Totect® Zinecard®	2007 1995
	Durvalumab	Imfinzi®	2017
	Etoposide Phosphate	Etopophos®	1983
	Everolimus	Afinitor®; Afinitor Disperz®; Zortress®	2009
	Methotrexate	Rheumatrex	1953
	Nivolumab	Opdivo	2014
	Pembrolizumab	Keytruda®	2014
	Topotecan Hydrochloride	Hycamtin®	1996

This treatment can be administered intravenously or orally, but the major disadvantage is that it presents a non-specific systemic distribution, causing serious side effects. This limits the dose to be administered, which does not allow an effective therapy to be achieved (Alhajj *et al.*, 2018). Another problem is the development of resistance to this modality which limits the treatment options (Woodman *et al.*, 2020).

Despite all the knowledge that has been acquired about this disease, it does not correspond to our ability to treat it (Cryer and Thorley, 2019). Currently, new approaches have emerged as an alternative to conventional therapies to advance cancer diagnosis and treatment with the ability to specifically recognize the tumor site while bypassing normal tissues (Li and Zhang, 2019). Over the last century, this idea has been studied based on the Paul Ehrlich's immunotherapy work, who defends the concept of “magic bullets” to allow the development and application of a rational and targeted strategy against this disease (Strebhardt and Ullrich, 2008). This proposal probably now has the potential to be realized with the emergence of nanotechnology/nanomedicine.

Over the past few years, nanosystems of various types have been developed for the treatment of lung cancer as summarized in the examples described below.

Poly (amidoamine) (PAMAM) dendrimers are NDDS capable of being functionalized with numerous biomolecules due to the availability of numerous free amino groups in their structure, and can incorporate hydrophilic and/or hydrophobic drugs (Prasad *et al.*, 2018; Woodman *et al.*, 2020). For this reason, Amreddy *et al.*, 2018 used this type of nanosystem to co-administered cis-diamminedichloroplatinum II (CDDP), a platinum-based anticancer drug that is commonly used for the treatment of lung cancer, and human antigen R (HuR) small interfering RNA (siRNA; Amreddy *et al.*, 2018). HuR is an RNA-binding protein overexpressed in this type of cancer, which induces tumor growth and the appearance of metastasis (Muralidharan *et al.*, 2015). The decrease in its expression can be obtained through RNAi-based gene silencing methods, such as the use of siRNA. In addition, this nanosystem has been conjugated with FA that allows targeted folate receptors alpha (FRA), which are also overexpressed in lung cancer cells (Leamon and Low, 2001). Thus, the effectiveness of this nanosystem was tested *in vitro*. It was found that this exhibited improved cytotoxicity compared to non-targeted nanosystem, and that this toxicity was negligible towards normal MRC9 lung fibroblast cells. In addition, the nanosystem treatment had a significantly greater therapeutic effect than did individual therapeutics. In short, the FA-conjugated PAMAM dendrimer-based NP system for co-delivery of siRNA against HuR messenger RNA (mRNA) and CDDP has proven to be a suitable carrier for targeted co-delivery of siRNA and chemotherapy agents in lung cancer cells. However, these studies need to be validated in *in vivo* assays using lung tumor xenograft models (Amreddy *et al.*, 2018).

Another type of nanosystem that has been developed and applied in lung cancer therapy is the nanogel, which has a strong core-shell structure with a high DL capacity (Prasad *et*

al., 2018). Niu *et al.*, 2019 developed reduction-sensitive polypeptide nanogels formulations, that could suppress lung carcinoma cell proliferation at low dose and decrease side effects (Niu *et al.*, 2019). These platforms were composed of methoxy poly(ethylene glycol)–poly(L-phenylalanine-co-L-cystine) (mPEG–P(LP-co-LC)) and methoxy poly(ethyleneglycol)–poly(L-glutamic acid-co-L-cystine) (mPEG–P(LG-co-LC)) to take advantage of its reducing potential at low pH, often found in tumor microenvironments (Biswas *et al.*, 2014; Li and Zhang, 2019). In addition, this nanosystem carried a chemotherapy agent, the DOX. Niu *et al.*, 2019 demonstrated that these nanogels were stable at neutral pH, and in acidic condition they were easily degraded, releasing DOX in a controlled manner. In addition, *in vitro* studies revealed a greater uptake of nanogels in comparison with the free drug. *In vivo* assays in the Lewis lung carcinoma grafted nude mouse model have also shown efficient antitumor effects, with the visualization of an increase in necrotic areas in tumor tissues, as well as a reduction in the systemic side effects associated with treatment with free DOX. In conclusion, these reduction-responsive polypeptides based nanogels are a promising nanodrug delivery platform for the future of lung carcinoma chemotherapy (Niu *et al.*, 2019).

Many NDDS developed not only allow to overcome the challenges related with chemotherapy but can also be combined with other therapies, such as PDT, which has been used in lung cancer for about 20 years. In this therapeutic method, molecules called photosensitizers are used, which, when excited after light irradiation, produce ROS that promote apoptosis (Sibata *et al.*, 2000). A recent study combined polymeric NPs constituted by PLGA loaded GEF anticancer drug with the application of a common photosensitizer called 5-aminolevulinic acid (5-ALA) promoting a chemo-PDT (CPDT) with external laser light irradiation. The effects of this therapy were explored on A549 cells (adenocarcinomic human alveolar basal epithelial cells) and on primary lung cancer rats after intratracheal administration. Although single therapies were effective, there was an extraordinary synergistic effect of CPDT with high anti-lung cancer effects, such as high anti-angiogenesis effect, associated with a decrease in the presence of some typical lung cancer markers like cluster of differentiation 31 (CD31), VEGF, nuclear factor kappa-light-chain-enhancer of activated B cells (NF-κB) p65 and B-cell lymphoma 2 (Bcl-2). In addition, this treatment was able to moderate inflammation with the down-regulation of tumor necrosis factor alpha (TNF-α), as well as increase apoptosis. With this, it is possible to understand that the combination of pulmonary NDDS and PDT is a promising approach for treatment of lung cancer (Zhang *et al.*, 2020).

Liposomes have also been tested in the treatment of NSCLC after design, synthesis and characterization of these nanosystems with the triptolide (TPL) anticancer drug encapsulated, and functionalized simultaneously with an anti-carbonic anhydrase IX (anti-CA IX) antibody and a CPP33 tumor lineage-homing CPP. Assays in 3D tumor spheroids demonstrated an increase in tumor penetration and inhibition of tumor growth. Furthermore, pharmacokinetic studies in rats that received these formulations by endotracheal administration showed a reduced concentration of TPL in systemic circulation which leads to less systemic toxicity. This dual-ligand modified liposomal vehicle is an innovative system that allows targeted delivery of anticancer drugs to improve their efficacy (Lin *et al.*, 2018).

The production of solid lipid NPs has also been developed in this context, as an example, the production of solid lipid NPs loaded with berberin and rapamycin, two anticancer drugs with synergistic effect, and functionalized with lactoferrin and hyaluronic acid (HA), which target the CD44 and lactoferrin receptors overexpressed by lung cancer cells. *In vivo* assays have shown that inhalation of these nanosystems induced a decrease in lung weight, a reduction in tumor size and in the levels of angiogenic markers compared with the inhalation of free drugs (Kabary *et al.*, 2018).

Another study proposed the development of HA decorated, pH sensitive lipid-polymer hybrid NPs (LPH NPs) to co-deliver Erlotinib (ERL) anticancer drug and bevacizumab (BEV), a recombinant monoclonal antibody that targets VEGF or VEGFR, for targeting and suppressing NSCLC. The ERL-BEV combination has already been tested in phase II clinical trials, which demonstrated a statistically significant and clinically meaningful prolongation of progression-free survival (PFS) compared with ERL alone. However, severe toxicity was found in the results of these trials (Kato *et al.*, 2018; Seto *et al.*, 2014), which promotes the study of a novel delivery nanosystem capable of encapsulating the ERL and the BEV to promote the reduction of these side effects, and increase their therapeutic effects. In this nanosystem preparation, the sensitivity to pH comes from the existence of pH sensitive nanomaterials such as adipic acid di-hydrazide (ADH) associated with HA, which promotes a rapid drug release at pH 5.5 compared to pH 7.4. After 21 days of LPH NPs treatment administration, the tumor volume decreased significantly from 1126.3 ± 39.4 mm^3 to 229.2 ± 13.1 mm^3 with a tumor inhibition rate of 79.7 ± 3.2%. A higher tumor tissue accumulation concentration (25 µg/mL) of these nanosystems was also verified. Thus, this treatment could be a good alternative to conventional therapies (Pang *et al.*, 2020).

MDR is one of the major obstacles that cancer therapy faces. In the case of NSCLC associated with overexpression of the tyrosine kinase receptors, standard treatment includes the tyrosine kinase inhibitors (TKIs) therapies, which in most patients are not effective due to resistance development to these drugs after 9-14 months after initial treatment (Ishii *et al.*, 2015). Studies with biomarkers have shown that this resistance in 80% of cases is owing to amplifications or gene mutations. In the remaining 20%, it was determined that it is due to the anexelekto (AXL) kinase bypass signaling through interaction with EGFR (Byers *et al.*, 2013). The AXL kinase is a member of the tyrosine kinase family of growth receptors, which is overexpressed after an epithelial-to-mesenchymal transition (EMT) that gives rise to the metastasis process. It was found that the inhibition of this receptor with pharmacologic inhibitors leads to a subsequent drug-sensitization, but the problem with this treatment is that in addition to inhibiting the intended pathway, it inhibits other multiple pathways signaling (Hojjat-Farsangi, 2014). A possible solution that has been studied is the use of siRNAs for selective suppression of AXL gene in resistant cells. However, siRNAs are inherently unstable and often need a carrier system for safe delivery (Aagaard and Rossi, 2007). To overcome these challenges, Suresh *et al.* developed a nanosystem composed of gelatin functionalized with Cetuximab (EGFR antibody) conjugated to an anti-AXL siRNA (siAXL) to apply in NSCLC cell lines. This antibody has excellent transport capabilities and can further aid in overcoming entrapment. The application of these NPs demonstrated a down-regulation of the AXL mRNA of about 70-80%, which in turn led to a decrease in EMT signaling with concomitant increase in p53 expression. Hence, the AXL silencing sensitizes the NSCLC cell lines to TKI (Suresh *et al.*, 2019). Thus, similar works may be useful to revert the numerous mechanisms developed for MDR, and a nanosystem that acts at that level can be administered simultaneously carrying drugs that until now could not perform their action.

In the scope of the production of nanosystems composed of inorganic matter, a recent study on a mouse lung cancer model reveals that the specialized nanoplatform, composed of copper sulfide nanocarriers that enclose the Norvaline and Sunitinib prodrug complexes can be applied as a “photothermal immunotherapy”. It is known that immunosuppressive chemoresistance is a major barrier in lung cancer treatment associated with the existence of myeloid-derived suppressor cells (MDSCs), which inhibit T-cell sensitization to tumor antigens. With the application of this nanoplatform capable of distributing two anticancer drugs with different actions, there was an increase in drug circulation time as well as a greater accumulation in lung and peripheral tissues, which allowed to control MDSCs immunosuppressive signaling. Thus, tumor regression was verified after near infrared

(NIR) exposure. In conclusion, this innovation allowed the reversal of the tumor immunosuppression and the reactivation of the immune system's mechanisms (Domvri *et al.*, 2020).

In addition to all these types of NDDS previously described, the mesoporous silica NPs have also been studied as an alternative to conventional therapeutic modalities. Recently, Song *et al.*, 2020 developed myricetin (Myr)-loaded mesoporous silica NPs combined with MDR protein (MRP-1) siRNA. Myr is a bioactive compound normally found in vegetables and fruits, which has anticancer properties, but its poor solubility and consequently bioavailability limit its effectiveness (Zhang *et al.*, 2014). MRP-1 is associated with drug resistance, and its expression can be inhibited with the application of siRNA (Cole, 2014). Thus, Myr and MRP-1 siRNA can be protected by being encapsulated, increasing their bioavailability and therapeutic efficacy. In addition, these NPs were functionalized with FA, which allowed a greater uptake of this nanosystem in lung cancer cells compared with that of the non-targeted NPs. In this study, a sustained release of Myr and MRP-1 siRNA occurred in the physiological conditions. *In vitro* assays have shown a marked reduction in cell viability and increased apoptosis in lung cancer cell lines under study. *In vivo* fluorescence results demonstrated that this NPs could specifically accumulate at tumor sites, and were more effective at suppressing tumor growth with non-significant toxicity. Overall, this nanosystem could provide an ideal platform for the lung cancer treatment (Song *et al.*, 2020).

However, despite the numerous studies performed in this area, few are those that reach clinical trials and are approved by FDA (Table I.4-6).

Some of the approved formulations have been combined with other treatments to allow the evaluation of a possible synergy, capable of increasing the efficiency of the treatments involved when applied together.

This is the case of Abraxane®, a nanoformulation of PTX incorporated in albumin NPs as the carrier, which was approved by the FDA in 2005 for the clinical treatment of breast, non-small cell lung and pancreatic cancers (Table I.4-6). The use of this nanoformulation brought advantages by comparison with the administration of the drug alone as it increased the delivery of this drug to the target sites, reducing the associated toxicity (Green *et al.*, 2006; Weissig *et al.*, 2014). Abraxane® has been combined with immunotherapy and chemotherapy evaluated on lung cancer. In two phase III clinical trials (ClinicalTrials.gov identifier: NCT02367781; NCT02367794) it was demonstrated that the

combined administration of atezolizumab with Abraxane® and carboplatin anticancer drug significantly increased median overall survival compared to treatment with this nanosystem and carboplatin only. Atezolizumab is a monoclonal antibody against programmed death/ligand 1 (PD-L1). PD-L1 expressed by cancer cells inhibited the activity of T-cells that expressed PD-1 on its surface, terminating immune responses by inhibiting cytotoxic/effector T-cell function and delivering anti-apoptotic signals to tumors. When PD-L1 is blocked by antibodies, it allows T-cells to find and perform their immune action on cancer cells. The use of this type of antibodies is associated with a significant increase in the survival rate in patients with solid tumors and in advanced stages. Carboplatin drug causes DNA damage. This combination regimen has very recently been approved by the FDA for metastatic non-squamous NSCLC (Shi, 2020; West *et al.*, 2019). A similar study, also in a phase III clinical trial (ClinicalTrials.gov identifier: NCT02775435), combined Abraxane® with carboplatin as well, but with pembrolizumab antibody, which performs the same function as atezolizumab, and the results were similar to the studies mentioned above, where the chemo-immunotherapy combination with this nanoformulation demonstrated benefits in relation to individual treatments (Garon *et al.* 2016).

The study of the nano-therapy in lung cancer treatment still has many challenges to face, but overcoming these obstacles is believed to have a promising future.

Table I.4-6: Types of nanosized drug delivery nanosystems (NDDSs) approved by Food and Drug Administration (FDA) or in various stages of clinical trials for the lung cancer treatment.

NDDS TYPE	LOADED PRODUCT	INDICATION	PRODUCT NAME	PHASE/FIRST APPROVAL	REFERENCES
Protein-based nanocarriers	Paclitaxel	**Non-small cell lung cancer**; Breast cancer; Pancreatic cancer	Abraxane®	Approved (2005)	Green *et al.*, 2006; Weissig *et al.*, 2014
	NY-ESO-1 + MAGE C1 + 4MAGE C2 + TPGB, Survivn + MUC1	**Non-small cell lung cancer**	RNActive® CV9201	Phase II	Fiedler *et al.*, 2016
Polymeric micelles	Paclitaxel	**Non-small cell lung cancer**; Breast cancer; Ovarian cancer	Genexol®PM	Approved (2007)	Pillai, 2014
	Cisplatin	**Non-small cell lung cancer**; Pancreatic cancer; Head and neck cancers; Bladder cancer	Nanoplatin™ NC-6004	Phase III	Duan *et al.*, 2016
Liposomes	Paclitaxel	**Non-small cell lung cancer**; Breast cancer; Ovarian cancer; Gastric cancer; Head and neck cancers	Lipusu®	Approved (2006)	Zhao *et al.*, 2018
	Cisplatin	**Non-small cell lung cancer**	Lipoplatin™	Phase III	Stathopoulos *et al.*, 2010; Stathopoulos *et al.*, 2011
	MUC1 antigen	**Non-small cell lung cancer**	Tecemotide	Phase III	Wurz *et al.*, 2014
	Irinotecan	**Small cell lung cancer**	Onivyde®	Phase II	Zhang, 2016
	Doxorubicin + Carboplatin	**Non-small cell lung**	-	Phase II	Numico *et al.*, 2002
	Lurtotecan + Cisplatin	**Non-small cell lung cancer**; Head and neck cancers; Ovarian cancer	-	Phase I	MacKenzie *et al.*, 2004
Polymeric nanoparticles	Camptothecin	**Small cell lung cancer**; Renal cancer; Ovarian cancer	CRLX101	Phase II	Weiss *et al.*, 2013
	Camptothecin	**Small cell lung cancer; Non-small cell lung cancer**	XMT1001	Phase I	Sausville *et al.*, 2010
	Docetaxel + Prostate-Specific Membrane Antigen (PSMA)	**Non-small cell lung cancer**; Cholangiocarcinoma; Cervical cancer; Bladder cancer; Head and neck cancers	Accurin™ BIND-014	Phase II	Hrkach *et al.*, 2012
Metallic nanoparticles	Tumour Necrosis Factor (TNF)	**Non-small cell lung cancer**	CYT-6091	Phase I	Libutti *et al.*, 2010
	Ferumoxytol	**Non-small cell lung cancer**; Triple negative breast cancer; Colorectal cancer; Pancreatic cancer; Ovarian cancer; Gastric cancer; Head and neck cancers; Lymph node cancer; Prostate cancer; Bladder cancer; Kidney cancer; Thyroid cancer	Feraheme®	Phase II	Zanganeh *et al*., 2016
	-	**Lung cancer**; Head and neck cancers	AuroLase®	Phase I	Singh *et al.*, 2018

NDDS: Nanosized drug delivery system

I.4.4 Future perspectives of NDDSs application in cancer therapy

In the future, nanotechnology-based cancer therapy will face numerous challenges. It is necessary to acquire more knowledge on this matter through a multidisciplinary approach that will allow the development and production of a complex multifunctional nanosystem capable of simultaneous transporting and delivering a wide range of diagnostic and therapeutic agents. With these nanoformulations serving as theranostic platforms, it will be possible to track their delivery and localization to the targeted area of treatment, monitor disease progression, predict the treatment efficacy and enhance local treatment effectiveness in real time. For this development, it must respond to certain key issues such as finding multiple carcinogenic receptors to know the necessary and effective modifications to be made to the nanosystems surface so that they can reach the targets, choose the DLs indicated for each case (a pharmacologically effective concentration will have to be achieved, without the need to increase the amount of the carrier material that can lead to side effects), take into account the toxicity associated with each type of nanosystem, and understand the nanocarriers stability after their storage, prior to being applied in cancer diagnosis and treatment (Attia *et al.*, 2019; Meel *et al.*, 2019).

In addition, it is also described that the delivery efficiency that is defined as the percentage of administered nanoformulations that actually reach a solid tumor, is less than 1%. This conclusion has led to discussions about the usefulness of nanomedicine in the cancer treatment. However, pharmacological parameters such as peak drug concentration, clearance rate and elimination half-life are not so low, and these should be considered with identical importance. Also, these results come from *in vivo* studies in mouse models, so the fundamental interaction of nanosystems may be different when in contact with the human body and the associated biological barriers (McNeil, 2016; Wilhelm *et al.*, 2016).

Besides this, in future studies, it is of paramount importance to gain a comprehensive insight into the physiological and pathophysiological variabilities among patients with an attempt of exploring their impacts on the behavior of the administrated nanomaterials. This will guide the design of precision nanomedicines toward personalized cancer treatments improving patients' quality of life (Bor *et al.*, 2019).

It has become clear that the use of NDDSs has a great value in providing an evolution of theranostic responses if used properly and if the toxicological issues that arise from them are fully clarified.

In many cases, the nanotoxicology resulting from the application of these nanoformulations is not fully understood (Farjadian *et al.*, 2019). This is multifactorial and depends on the size and shape of the NDDSs, on their physico-chemical characteristics, surface properties, constituent leaching and triggering of immune reactions. Even nanosystems of the identical material can exhibit completely different behavior due to, for example, slight alterations in surface coating, charge or size. This makes the categorization of NP behavior, when in contact with biological systems, complex and thus NP hazard identification is not straightforward (Elsaesser and Howard, 2012). With this, it is essential to consider the risk/benefit ratio in order to assess the NDDSs application in cancer therapy. This will certainly help to implement safe drug delivery (Farjadian *et al.*, 2019).

Moreover, in an ideal situation, academic institutions should be working together with industry partners, regulatory and funding agencies to bring advanced nanomedicines to clinical practice and commercialization. In the literature it is possible to identify a considerable number of publications in nanomedicine, but that is not comparable to the number of clinical trials (Figure I.4-6). This is due to the Research and Development (R&D) costs and time taken by a clinical trial, the lack of batch-to-batch reproducibility and long-term stability of some products, complexity of the manufacturing processes and maintenance of sterile conditions (Bor *et al.*, 2019; Martins *et al.*, 2020).

New strategies must be devised for nanomedicine to continue to revolutionize the health system by improving our ability to diagnose and treat cancer.

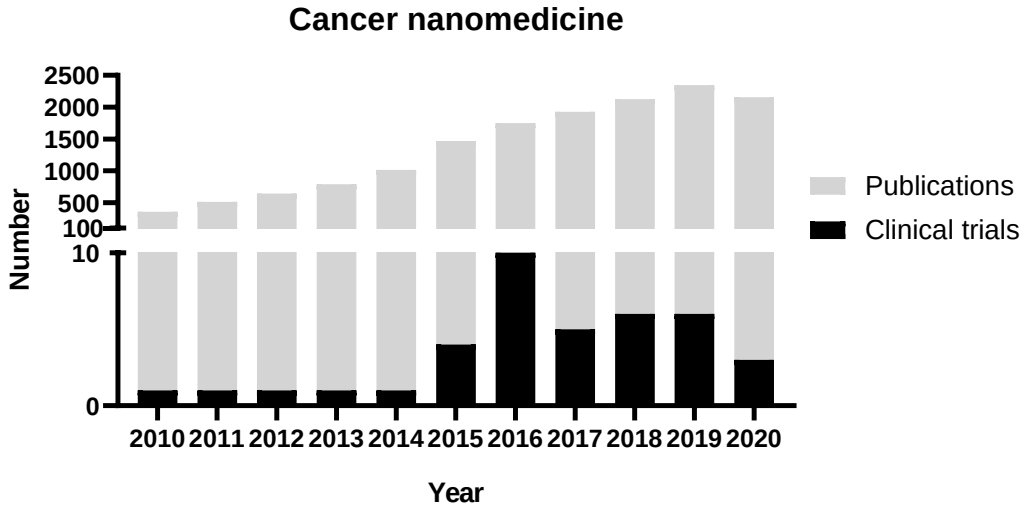

Figure I.4-6: Comparison of clinical trials in the field of cancer nanomedicine with the number of published reports. Source: Pubmed, 2021a; Search keyword: cancer nanomedicine, Filter: Clinical trials.

I.5. Thesis aims and outline

Azurin is a small bacterial protein that has been shown to have anticancer potential. Its structural characteristics allow it to interact with several proteins involved in the tumorigenesis, avoiding the possibility of developing MDR (Fialho *et al.*, 2007). It also presents preferential uptake in cancer cells, and is able to control cell proliferation, trigger apoptosis, and inhibit cancer-induced angiogenesis (Mehta *et al.*, 2011; Taylor *et al.*, 2009; Yamada *et al.*, 2004). In recent years, azurin has been combined with several anticancer drugs enhancing their therapeutic activity (Bernardes *et al.*, 2016; Bernardes *et al.*, 2018; Choi *et al.*, 2011). However, what drives the preferential entry and its molecular mechanisms are not completely understood, so further studies are needed to completely unravel this essential key point for the establishment of an effective therapy.

In addition, several domains of azurin have been studied in the form of linear peptides, also showing anticancer activity (Chaudhari *et al.*, 2007, Taylor *et al.*, 2009). This protein can thus be considered a source of anticancer bioactive peptides.

Taking advantage of the anticancer potential of these peptides, it is possible to design new drug delivery strategies, overcoming the issues related with the individual administration of drugs such as the appearance of severe side effects (Damyanov *et al.*, 2018). This approach has been studied with the p28 peptide derived from azurin, which has been described as a transporter agent for proteins/peptides/photosensitizers, demonstrating selective and effective delivery of its cargos to tumor sites (Noei *et al.*, 2019; Raber *et al.*, 2020; Shahbazi and Bolhassani, 2018; Soleimani *et al.*, 2019).

Thus, in this work, a set of specific aims were pursued in order to i) add relevant information about the azurin uptake, ii) evaluate the *in vitro* anticancer potential of peptides derived from this protein, which were previously studied through an *in silico* bioinformatic analysis, and iii) develop an innovative drug delivery nanosystem of based on the targeting capacity of p28. The work developed so far will be presented and organized in four main chapters:

Chapter I is a detailed literature review of the anticancer potential of azurin and its p28-derived peptide, considered a CPP. The application of this type of peptides in cancer therapy is also addressed, emphasizing its association with NDDS, in particular with a type of polymeric NPs. Finally, several examples of NDDS applied specifically in lung cancer therapy are reported.

Chapter II elucidates the impact of azurin treatment at the level of the membrane order and lipid packing on cancer cells, as well as confirms its interaction with components

present in characteristic lipid microdomains of the plasma membrane, identifying a new region of this protein responsible, at least *in part*, for its uptake.

Chapter III comprises an *in vitro* evaluation of the anticancer potential of CT-p26, CT-p19 and CT-p19LC peptides derived from the C-terminal region of azurin previously designed by our group using bioinformatic tools. The results confirmed the anticancer potential predicted *in silico*, and demonstrated that CT-p19LC, in addition to having an improved anti-tumor activity and maintaining the selectivity in relation to cancer cells, also has membrane-active properties.

Chapter IV addresses for the first time the association of p28 with a polymeric nanosystem with encapsulated TKIs as a NDDS for the lung cancer treatment. In this study, the production of NPs was initially optimized, followed by their physico-chemical characterization. These nanosystems were then tested in *in vitro* and *in vivo* to assess their anti-lung cancer therapeutic activity.

II. AZURIN INTERACTION WITH THE LIPID RAFT COMPONENTS GANGLIOSIDE GM-1 AND CAVEOLIN-1 INCREASES MEMBRANE FLUIDITY AND SENSITIVITY TO ANTI-CANCER DRUGS

Journal Paper

Bernardes N, Garizo AR, Pinto SN, Caniço B, Perdigão C, Fernandes F, Fialho AM. 2018. Azurin interaction with the lipid raft components ganglioside GM-1 and caveolin-1 increases membrane fluidity and sensitivity to anti-cancer drugs. *Cell Cycle* **17**: 1649-1666

| DOI: 10.1080/15384101.2018.1489178

Garizo AR performed experiments and analyzed data (Protein extraction and purification, GM-1 inhibition, SiRNA transfection, western blot, GP images analysis and MTT cell viability assays)

II.1. Abstract

Membrane lipid rafts are highly ordered microdomains and essential components of plasma membranes. In this work, we demonstrate that azurin uptake by cancer cells is, *in part*, mediated by Cav-1 and GM-1, lipid rafts' markers. This recognition is mediated by a surface exposed hydrophobic core displayed by azurin since the substitution of a phenylalanine residue in position 114 facing the hydrophobic cavity by alanine impacts such interactions, debilitating the uptake of azurin by cancer cells. Treating of cancer cells with azurin leads to a sequence of events: alters the lipid raft exposure at plasma membranes, causes a decrease in the plasma membrane order as examined by Laurdan two-photon imaging and leads to a decrease in the levels of Cav-1. *Caveolae*, a subset of lipid rafts characterized by the presence of Cav-1, are gaining increasing recognition as mediators in tumor progression and resistance to standard therapies. We show that azurin inhibits growth of cancer cells expressing Cav-1, and this inhibition is only partially observed with mutant azurin. Finally, the simultaneous administration of azurin with anticancer therapeutic drugs (PTX and DOX) results in an enhancement in their activity, contrary to the mutated protein.

II.2. Introduction

Azurin is a protein from bacterial origin (*Pseudomonas aeruginosa*) which in the last years has been studied as an anticancer agent. We and others have identified different modes of action that account for the therapeutic effects of both the entire protein and one lead peptide, p28 (Bernardes *et al.*, 2016; Mehta *et al.*, 2011; Taylor *et al.*, 2009; Yamada *et al.*, 2002a; Yamada *et al.*, 2009). The 28 amino acid sequence was first identified as the domain responsible for the penetration of azurin into cancer cells (Yamada *et al.*, 2005) and further studied as an anticancer peptide. Indeed, p28 has already completed two phase I clinical trials in both adult patients with various tumors and in children with tumors of the central nervous system (Lulla *et al.*, 2016; Warso *et al.*, 2013). Both trials ended with positive indications in relation to the possible use of this peptide as an anticancer agent.

Mechanistically, the uptake of azurin or the peptide was suggested as being energy-dependent, with no observable loss of membrane integrity, independent of membrane-bound glycosaminoglycans, dependent on the cholesterol within the cell membrane and strongly associated with *caveolae* (Taylor *et al.*, 2009). The depletion of cholesterol from plasma membranes using methyl-β-cyclodextrin; the disruption of microtubules with

nocodazole; or the inhibition of late endosomes/lysosomes activity with monensin, all led to a decrease in the penetration of p28 (Taylor *et al.*, 2009; Yamada *et al.*, 2009).

Caveolae are a subset of lipid rafts with unique physical and biological properties. These membrane microdomains are enriched in glycosphingolipids (including sphingomyelin, ceramide and gangliosides, like GM-1) and cholesterol that can act as lipid-ordered platforms within the plasma membrane (Martinez-Outschoorn *et al.*, 2015; Mollinedo and Gajate, 2015). In particular, *caveolae* are defined as wide pits in the plasma membrane that contain Cav-1 in oligomers of 140-150 proteins. Cav-1 and *caveolae* in general are now recognized as important mediators for signal transduction, plasma membrane organization and composition. Additionally, they have been associated with the phenomenon of drug resistance in cancer either by contributing to altered membrane lipid and protein composition, higher membrane order and altered signaling pathways (Lavie *et al.*, 2001; Quest *et al.*, 2013).

Research with azurin or the derived peptide in the past years have demonstrated that a number of signaling pathways associated with tumor progression and angiogenesis, such as FAK/Src or PI3K/Akt signaling are attenuated after treatment in several cancer models (Bernardes *et al.*, 2013a; Bernardes *et al.*, 2016; Mehta *et al.*, 2011). Also, functional evidences associated to adhesion to extracellular matrices, invasion and migration of cells are also weakened (Bernardes *et al.*, 2014; Bernardes *et al.*, 2016), linking the cellular responses to azurin to its possible effects at lipid rafts, which may act as the main gate of azurin to cancer cells. Moreover, binding to both Cav-1 and GM-1, structural components of *caveolae*/lipid rafts, is strongly associated to hydrophobic enriched regions in the binding partners (Pang *et al.*, 2004; Vihanto *et al.*, 2006), and azurin harbours in its tertiary structure two sheets arranged around an hydrophobic core region with the particular characteristic of being exposed and available for interactions (Bernardes *et al.*, 2013b). As such, in this work we evaluated the impact that azurin treatment has at the membrane level, particularly at the lipid raft organization level in terms of membrane order and lipid packaging, and identified a new region of azurin outside p28 that is also involved, at least *in part*, in the uptake of this protein by cancer cells.

II.3. Materials and Methods

II.3.1. Human cancer cell lines and cell cultures

Three human cancer cell models have been used: the MCF-7 breast cancer cell line, the HeLa cervical cancer cell line and the HT-29 colon cancer cell line. These cell lines were purchased from European Collection of Authenticated Cell Cultures. All of them were cultured in Dulbecco's Modified Eagle Medium (DMEM; Gibco® by Life Technologies), supplemented with 10% of heat-inactivated Fetal Bovine Serum (FBS; Gibco® by Life Technologies), 100 IU/mL penicillin and 100 mg/mL streptomycin (PenStrep, Invitrogen). These cell lines were passed between 2 to 3 times per week, by chemical detaching with 0.05% of trypsin. Cells were grown at 37 ºC in a humidified chamber containing 5% of CO_2 (Binder CO_2 incubator C150).

II.3.2. Hydrophobic surface analysis of azurin

Surface properties of azurin from *Pseudomonas aeruginosa* PAO 1 (PDB entry 1jzg) were evaluated using the program PyMol. This program was used to identify and score clusters of hydrophobic atoms (named as hydrophobic patches). Swiss-Pdb Viewer (Deep View) was used to produce azurin 3D structure cartoons.

II.3.3. Construction of a site-directed mutation in the azurin gene of *Pseudomonas aeruginosa* PAO1

The pWH844 vector with azurin-encoding gene from *Pseudomonas aeruginosa* PAO 1 (Bernardes *et al.*, 2013a), was extracted using the ZR Plasmid MiniprepTM-Classic kit (ZymoResearch), according to manufacturer's instructions. The Quick Change II site-directed mutagenesis kit (Agilent Technologies) was used for the site-directed mutagenesis. Forward and reverse primers used for the substitution of phenylalanine at position 114 by alanine were respectively: 5´-GTA CAT GTT CTT CTG CAC CGC GCC GGG CCA CTC CGC GCT G-3´ and 5´-CAG CGC GGA GTC GCC CGG CGC GGT GCA GAA GAA CAT GTA C-3´. PCR was carried out in a 50 µL mixture using 30 ng template plasmid DNA from the plasmid pWH844 with the WT azu gene, 5 µL of 10x Reaction Buffer, 1.25 µL of each primer (at 10 µM), 1 µL of dNTP mix and double-distilled water (ddH_2O) to a final volume of 50 µL. After that, 1 µL of PfuTurbo DNA polymerase (2.5 U/µL) was added to the mixture.

II.3.4. Bacteria growth, over-expression, extraction and purification of wild-type azurin or mutated protein

The continuous production of azurin was performed as described in Bernardes *et al.*, 2013a. For the mutated protein F114A, a final concentration of 0.5 mM of isopropyl β-d-1-thiogalactopyranoside (IPTG) was added to induce protein overexpression.

II.3.5. Protein extraction and western blot analysis

For protein extraction, plates with incubated cells, after the desired incubation times with the azurin proteins, were placed on ice and wells were washed twice with phosphate-buffered saline (PBS) 1x. Then, cells lysed in 100 µL of Catenin Lysis Buffer (CLB; 1% Triton X-100, 1% Nonidet-P40 in deionized PBS) supplemented with 1:7 proteases inhibitor (Roche Diagnostics GmbH) and 1:100 phosphatases inhibitor (Cocktail 3, Sigma Aldrich) for 10 min at 4 ºC. Then, the cells were scratched, collected and vortexed three times (10 sec each), centrifuged (14000 rpm, 4 ºC, 10 min; B. Braun Sigma-Aldrich 2K15) and the pellet was discarded, collecting the supernatant containing proteins. Total protein quantification was done using by a Quantification Protein Kit (Bradford, BioRad). 10-20 µg of total protein per sample were prepared with Laemmli buffer. Proteins were transferred onto nitrocellulose membranes (BioRad) using Trans-Blot TurboTM system (BioRad). Membranes were blocked with 5% (w/v) non-fat dry milk in PBS containing 0.5% (v/v) Tween-20 (PBS-T) for 1 h, incubated with different primary antibodies: β-actin (1:1000, sc-1616) or glyceraldehyde 3-phosphate dehydrogenase (GAPDH) (G-9) (1:1000, sc-365062) were used as loading controls; Cav-1 (N-20) (1:1000, sc-894). In order to evaluate azurin expression, an anti-azurin antibody was produced through immunization of one goat with purified azurin, obtained as described above (1:1000 dilution). The resulting immunized serum was then purified by protein A affinity chromatography (SicGen, Portugal) and purity was checked by SDS-PAGE. All the membranes were incubated overnight at 4 ºC and then washed three times for 5 min with PBS-T. These were then incubated for 1 h with secondary antibodies (anti-rabbit, anti-mouse or anti-goat, 1:2000, Santa cruz Biotechnology), conjugated with horseradish peroxidase Proteins were detected through the addition of enhanced chemiluminescent (ECL) reagent (Pierce) as a substrate and exposed captured the chemiluminescence by Fusion Solo (Viber Lourmat) equipment. When loading controls were necessary, samples were run in the same gels, and after transfer to the membrane, the membranes were cut according to the protein MWs and probed with the antibodies in separate. Three experiments were independently

performed and representative results are shown. Signal quantifications were performed using ImageJ and results are presented as the ratio between the signal intensities in azurin treated samples to untreated cells, both normalized to the respective GAPDH or actin band intensities.

For co-immunoprecipitation experiments, lysed cells were incubated with 10 µL of primary antibody anti-Cav-1 (Cell Signaling, 3238) in an agitator overnight at 4 ºC. The next day, 100 µL of beads (Protein G Agarose, Thermo Scientific) were incubated with the mixture of lysate and antibodies, in an agitator during 2 h at room temperature. After that time, 500 µL of IP buffer (Thermo Scientific) were added, in order to precipitate the mixture, and then it was centrifuged (2500 x*g* during 3 min), 10 times. At every time, the supernatant was discarded. To elute the proteins from the beads, the pellet was incubated twice with 50 µL of Elution Buffer (Thermo Scientific), each time during 5 min, and then it was centrifuged (2500 x*g* during 2 min) and the supernatant was recovered. To neutralize the supernatant, 10 µL of Neutralization Buffer (Thermo Scientific) were added.

To the pellet, that contains the beads, 60 µL of sample buffer were added and to the supernatant with the Neutralization Buffer it was added 30 µL of sample buffer. 20 µL per sample were denatured at 95 ºC during 5 min, and then separated by electrophoresis in a sodium dodecyl sulphate-polyacrylamide gel electrophoresis (SDS-PAGE). Western Blot was performed as previously described.

II.3.6. GM-1 inhibition with Cholera Toxin Subunit B

MCF-7 breast and HT-29 colon cells were plated in 6-well plates with $5x10^5$ cells per well and left to adhere and grow overnight in a CO_2 incubator (5%) at 37 ºC. The following day, medium was collected and cells were treated with 1 µg/mL of Cholera Toxin Subunit B (CTxB; Invitrogen, Alexa Fluor® 488 conjugate) in DMEM during 10 min. After this time, medium was again collected and cells were treated with 50 µM of wild-type (WT) azurin or mutated protein in DMEM. The plates were placed for 30 min at 37 ºC.

II.3.7. Confocal microscopy-Cholera Toxin Subunit B

MCF-7, and HT-29 cell lines were seeded on µ-Slide 8 well IBIDI treated chambers (ibidi®) with $5x10^4$ cells per well. These cells were left to adhere and grow overnight in a CO_2 incubator (5%) at 37 ºC. In the next day, medium was collected and cells were treated with 100 µM of WT azurin or mutated protein in medium containing 10% FBS and 1% PenStrep, for 48 h. After this time, medium was again collected and cells were treated with 1 µg/mL

of CTxB (Invitrogen, Alexa Fluor® 488 conjugate) in DMEM during 10 min. Afterwards, the chambers were rinsed three times with PBS 1x. For fixation, cells in coverslips were immersed in 3.7% formaldehyde for 20 min at room temperature. After seven washing steps in PBS 1x, Vectashield with 4′,6-diamidino-2-phenylindole (DAPI) was added and cells were observed in a Leica TCS SP5 inverted confocal microscope (Leica Microsystems CMS GmbH; model no. DMI6000) with a 63x water (1.2-numerical-aperture) apochromatic objective. For measurement of CTxB-Alexa488 fluorescence, the sample was excited at 488 nm, while emission was collected within the 500-600 nm range. For measurement of DAPI fluorescence, the sample was excited by two-photon excitation at 780 nm with a Ti:sapphire laser (Mai Tai, Spectra-Physics, Darmstadt, Germany), while emission was collected within the 400-450 nm range. Signal intensity was quantified for each cell using the Image J software. In each cell, a mask identifying the plasma membrane was defined and signal from within these pixels was quantified as plasma membrane associated intensity. Next, the signal from the within each cell was also quantified, excluding the nucleus, and defined as the intracellular signal. For each condition, quantifications are presented as ratios between the plasma membrane signal over the intracellular signal. Results were compared by analysis of variance ANOVA (Newman- Keuls Multiple Comparisons, using GraphPad Prism version 6).

II.3.8. SiRNA transfection of human cancer cells lines

MCF-7 and HeLa cell lines were plated in 6-well plates with $5x10^5$ cells per well. These cells were left to adhere and grow overnight in a CO_2 incubator (5%) at 37 ºC. Prior to transfection, 100 nM of Control siRNA (sc-37007, Santa Cruz Biotechnology) and Cav-1 siRNA (sc-29241, Santa Cruz Biotechnology) were mixed with Lipofectamine® 2000 (Thermo Fisher Scientific). For this, 25 µL of each siRNA were added to 225 µL of DMEM and 10 µL of Lipofectamine® 2000 were added to 240 µL of the same medium, according to the manufacturer's instructions. After 5 min, the prepared solutions were mixed gently to form siRNA-lipofectamine complex. This mixture was incubated for 20 min at room temperature and added to 2 mL of DMEM in the respective well. After 6-8 hours in a CO_2 incubator (5%) at 37 ºC, the medium was removed and fresh medium containing 10% FBS and 1% PenStrep was added to each well. The appropriate time for observing the decrease in the Cav-1 protein levels was determined by Western blot, determining that 24 h post-transfection was adequate to perform the azurin entry assay. After this time, cells were treated with 50 µM of WT azurin or mutated protein. The plates were placed for 30

min at 37 ºC. To determine the levels of azurin entry in Cav-1-silenced cells, a Western blot was performed as described above (20 µg of total protein per sample).

II.3.9. Interaction between Cav1-CSD and azurin: FRET measurements

To observe the interaction between the Cav-1 Scaffolding Domain (CSD; amino acids 82-101 of Cav 47) and WT or mutated azurin, we made used of Fluorescein-5 IsoThioCyanate (FITC)-labeled CSD peptide (Pepmic). WT and F114A azurin mutant proteins were labeled with Atto 390 NHS ester (Sigma), according to the manufacturer's instruction. Briefly, 150 µM of each protein was incubated with the dye (molar ratio 2:1), for 2 h at room temperature. Reaction was stopped with by adding a solution of NH_2OH 1.2 M pH 8.5, for 1 h at room temperature. After this, the mixture was centrifuged at 18000 x*g*, 10 min, to remove any precipitated dye, before dialysis against 10 mM phosphate buffer pH 7.4, in slide-A-lyzer 3.5 kDa cut-off, overnight at 4 ºC. For fluorescence resonance energy transfer (FRET) measurements, WT and F114A azurin concentration was 2 µM. The donor (Atto390-WT or Atto390-F114A)-only fluorescence spectra were acquired with 390 nm excitation and measured over the emission wavelength range of 400 to 470 nm, since no acceptor (FITC-labeled CSD peptide) emits there. The FITC-labeled CSD peptide was titrated from 0 to 14 µM. Fluorescence measurements were carried out with a SLMAminco 8100 Series 2 spectrofluorimeter (Rochester) with double excitation and emission monochromators (MC 400), in a right-angle geometry. The light source was a 450-W Xe arc lamp and the reference a Rhodamine B quantum counter solution. Quartz cuvettes (1×1 cm) from Hellma Analytics were used. The FRET efficiency, *E*, was calculated on the basis of the quenching of the donor fluorescence intensity in the FRET complex relative to the donor only emission in the presence of the buffer. *E* was calculated using the following equation: $E = 1-(F_{DA}/F_A)$ after all intensities were normalized to the intensities in the absence of FITC-peptide. All spectra were corrected for background and inner filter effects (Lakowicz, 2006).

II.3.10. Two-Photon excitation microscopy – Generalized polarization determination

MCF-7, HeLa and HT-29 cells were cultured on µ-Slide 8 well IBIDI treated chambers (ibidi®) with 5×10^4 cells and treated with WT azurin or F114A mutated protein (100 µM). After 48 h, medium was collected and cells were washed twice with PBS. After that, DMEM with 5 µM of Laurdan was added and the cells were incubated in a CO_2 incubator at 37 ºC for 20 min. Samples were examined on a Leica TCS SP5 (Leica Microsystems CMS

GmbH, Mannheim, Germany) inverted microscope (model no. DMI6000) with a 63× water (1.2-numerical-aperture) apochromatic objective. Two photon excitation microscopy data was obtained by using Leica TCS SP5 inverted microscope with a Ti:sapphire laser (Mai Tai, Spectra-Physics, Darmstadt, Germany) as the excitation light source. The excitation wavelength was set to 780 nm and the fluorescence emission was collected at 400-460nm and 470-550nm to calculate the generalized polarization (GP) images. Laurdan GP images were obtained through a homemade software based on a MATLAB environment, with the GP value defined as GP = (/400–460 – G. I470-530)/(/400–460 + G. I470- 530), where G is the calibration factor for the experimental setup. G is obtained from imaging Laurdan in dimethyl sulfoxide (DMSO; with the predetermined GP = 0.01) using the same experimental conditions as those set for the measurements in living cells (Owen *et al.*, 2011). Control conditions correspond to untreated cells. Dark counts were subtracted to all intensity values. In the analysis, only Regions of Interest (ROI) corresponding to the plasma membranes in each cell were selected, restricting therefore the analysis to this cellular component. At least 15 independent cells were analyzed per condition and all the experiments were done in independent days. Results were compared by analysis of variance ANOVA (Newman-Keuls Multiple Comparisons, using GraphPad Prism version 6).

II.3.11. MTT cell viability assay

MTT [3-(4,5 dimethylthiazol-2-yl-2,5 tetrazolium bromide)] assays were used to determine the proliferation rate of MCF-7, HT-29 and HeLa human cancer cells lines after they were treated with WT azurin combined with drugs. The drugs used in these assays were PTX, an anti-mitotic agent, and DOX, a DNA-damaging drug (Sigma Life Science). All these cell lines were seeded in 96-well plates (3 replicates) with a density of $2x10^4$ MCF-7 cells per well, $1x10^4$ HeLa cells per well and $2x10^4$ HT-29 cells per well. These cells were left to adhere and grow overnight in a CO_2 incubator (5%) at 37 ºC. In the next day, medium was collected and cells were treated with 50 and 100 µM of WT azurin together with 0.1, 0.5 or 1 nM of PTX or 10 or 50 nM of DOX in medium containing 10% FBS and 1% PenStrep. The plates were placed for 72 h at 37 ºC. After this time, 20 µL of MMT [3-(4,5-dimethylthiazol-2-yl-2,5-diphenyltetrazolium bromide] reagent (5 mg/mL) were added to each well and incubated at 37 ºC for 3.5 h. Reaction was stopped with the addition of 150 µL of a solution 40 mM HCL in isopropanol. MTT formazan formed was spectrophotometrically read at 590 nm in a microplate reader (SpectroStarNano, BMG

LABTECH). Untreated cells were used as control, in order to determine the relative cell viability of treated cells.

II.3.12. Statistical analysis

For Western blot experiments, three independent replicates were performed. All *p*-values were calculated using Student's *t*-test (two-tailed distribution, two-sample equal variance). Values of $p<0.05$ were considered statistically significant (*: $p<0.05$). In MTT cell viability experiments, results were compared by analysis of variance ANOVA (Newman-Keuls Multiple Comparisons, using GraphPad Prism version 6 or Statistica version 13).

II.4. Results

II.4.1. F114A substitution alters the uptake rate of azurin in cancer cells

In order to study the importance of the hydrophobic core in the process of cell uptake by azurin, we first analyzed this aromatic core by a computational analysis. In Figure II.4-1A the residues that contribute most to hydrophobic core are highlighted in blue on the amino acid sequence representation. We analyzed three aromatic residues of the hydrophobic patch (Y108, F111, F114; Figure II.4-1A), and the computational results showed that F114 is facing the central cavity of the hydrophobic core on a loop with the hydrophobic ring exposed in the azurin hydrophobic cavity (Figure II.4-1A, B). This positioning of F114 makes it an ideal place to introduce a mutation in order to study the importance of possible hydrophobic interactions mediated by this region. On the other hand, Y108 and F111 are located on a β-sheet and a mutation there might affect azurin structure and functionality. Furthermore, while previous studies regarding azurin but not related to its anticancer activity had shown that the mutation F114A did not alter significantly the protein structure, the *in silico* prediction of the mutation F114A reveals changes in the hydrophobic core of azurin that reduces the hydrophobicity in the surface of the protein (Figure II.4-1B; Yanagisawa *et al.*, 2006). For all these reasons, we choose to mutate azurin in the F114 residue, replacing it by alanine. The exposure of cells (MCF-7 and HeLa) to 50 and 100 μM of both proteins for 30 min and 2 h clearly demonstrated that the mutant protein is much less efficient in entering the cells when compared to the WT protein (Figure II.4-1C). In parallel, both WT and mutated protein were labeled with the fluorescent molecule Atto 390 NHS ester by coupling it with the amines of proteins. Labeled proteins (10 μM) were mixed with unlabeled protein (to a final concentration of 100 μM) and added to MCF-7 cells for 2 h, after which cells were imaged under the confocal microscope. It is possible to see

that while the WT protein is detected both at the plasma membrane and inside the cells, lower intensity is observed for the mutated protein. This suggests that the F114A mutant protein is less efficient in the processes of recognition and uptake by the cancer cells than the WT protein (Figure II.4-1D).

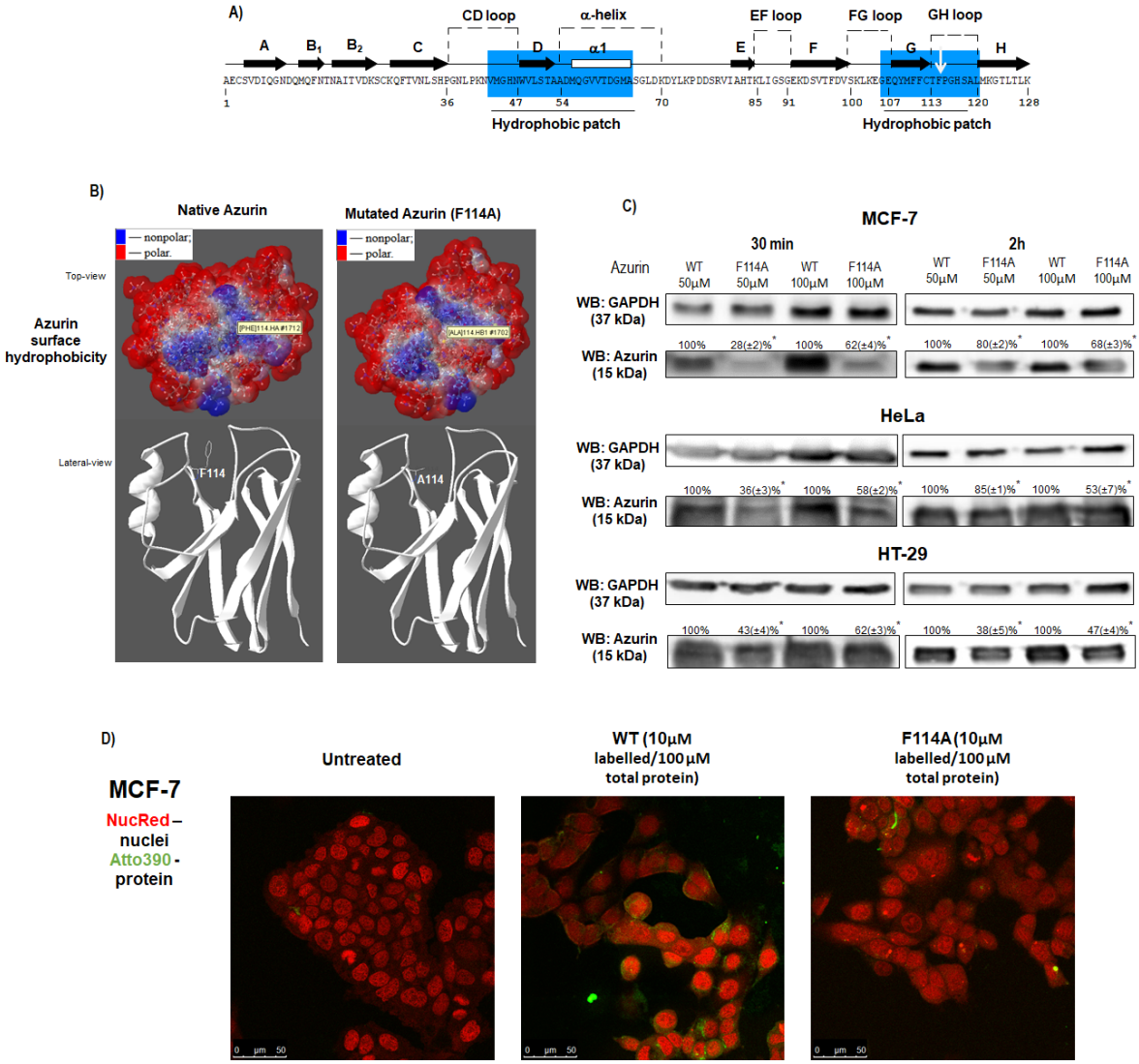

Figure II.4-1: Point mutation of phenylalanine$_{114}$ delays azurin entry in cancer cells. **A)** Amino acids sequence of azurin from *Pseudomonas aeruginosa*. Hydrophobic patches are highlighted in blue. **B)** 3D structural view of azurin depicting surface hydrophobicity (top view) and ribbon 3D structure (lateral view) of both WT azurin (left panel) and F114A mutant azurin (right panel), identifying the structural positioning of phenylalanine amino acid residue side chain. The amino acid change was generated using SPDB Viewer (v4.01). Surface hydrophobicity was generated using PyMol. **C)** Entry of azurin WT and F114A mutant in MCF-7, HeLa and HT-29 cells. Cells were exposed to 50-100 μM of both proteins for 30 min (left) and 2 h (right), after which cells were lysed and protein entry inside cells was determined by western blot. A cropped representative image of western blot is depicted. Full-length western blot images are displayed in Figure VIII.1-1. **D)** Confocal scanning microscopy of Atto 390-labelled WT or F114A azurin proteins. Labeled proteins (10 μM) were mixed to non-labeled proteins (to a final concentration of proteins of 100 μM), and MCF-7 cells were exposed for 2 h before fixing and imaging. Cell nuclei are displayed labelled with NucRed and presented in red, labeled WT and mutated azurin proteins are displayed in green.

II.4.2. Blocking GM-1 ganglioside reduces the penetration of azurin in cancer cells

CTxB, a component of a heat-labile enterotoxin produced by *Vibrio cholerae*, is a probe commonly used to label and/or detect GM-1 which can be used as marker for lipid rafts, since the GM-1 has an abundant localization in these membrane microdomains (Gaus *et al.*, 2003; Owen *et al.*, 2011). GM-1 is important for recognition and trafficking of a great number of protein and viruses. To evaluate the involvement of GM-1 in the recognition and cell entry of azurin in cancer cells (due to the apparent hydrophobic nature involved in this process), we hypothesized that pretreating the cells with CTxB might decrease the availability of GM-1 to mediate the entry of azurin in cancer cells, if this route is used by the protein. MCF-7 and HT-29 cancer cells were exposed to CTxB during 10 min before the addition of 50 μM of WT azurin or the mutated protein (Figure II.4-2A). The controls were the cells exposed to bacterial proteins in the absence of CTxB. In both models, we observed that when cells were firstly subjected to CTxB a decrease in the total levels of WT and F114A azurin inside cancer cells was observed suggesting that availability of GM-1 is important for the entry of azurin in the cells. For the WT protein, a decrease of about 40% was observed, whereas for the mutated protein the decrease was more accentuated (≈50%). Despite it is not possible to rule-out that the effect is due to a change in membrane raft morphology due to lipid-raft cross-linking by CTxB, our results indicate that the intact GM-1/raft morphology is needed for an entirely efficient azurin entry and that the hydrophobicity provided by this phenylalanine aromatic residue and its exposure to the surface of the protein may be important to mediate the entry of the protein by means of its interaction with GM-1. Having determined that the presence of GM-1 is important for the recognition and entry of azurin, we went on to study how both proteins impacted the distribution of GM-1 at the plasma membrane. Using a fluorescence tagged (Alexa488) form of CTxB, cells were treated for both a short (30 min) as well as a longer (48 h) period of time with the different azurin proteins after which cells were labeled with Alexa488-CTxB (10 min), before fixing and observed under the scanning confocal microscope. Overall, we observed that untreated cells have a more selective plasma membrane staining (Figure II.4-2B, upper panel) which upon treatment with the WT protein becomes much more undefined at the membrane level (Figure II.4-2B, middle panel). Our results seem to indicate that the involvement of GM-1 in the entry of azurin dislodges, at least *in part*, this ganglioside from the plasma membrane. As for the F114A azurin mutant, the results seem to be intermediate between the untreated cells and cells treated with the WT protein

(Figure II.4-2B, lower panel). The increase in the intracellular staining appears to be maintained but at a more moderate level, nevertheless there is also a more evident membrane staining than in the cells treated with the WT protein. The signal intensity in the cells was quantified in the plasma membrane and in the cytoplasm in the interior of the cells (excluding the nucleus region), and represented as a ratio of the plasma membrane signal intensity over the cytoplasm intensity signal for the different proteins (Figure II.4-2B). As it is seen, the treatment with the WT protein decreases the ratio of signal in the plasma membrane, contrary to the F114A protein, particularly right after the addition of the proteins (30 min). Being a regularly marker used to assess lipid rafts localization, the displacement here observed suggests that WT azurin may alters the membrane profile of these ordered domains.

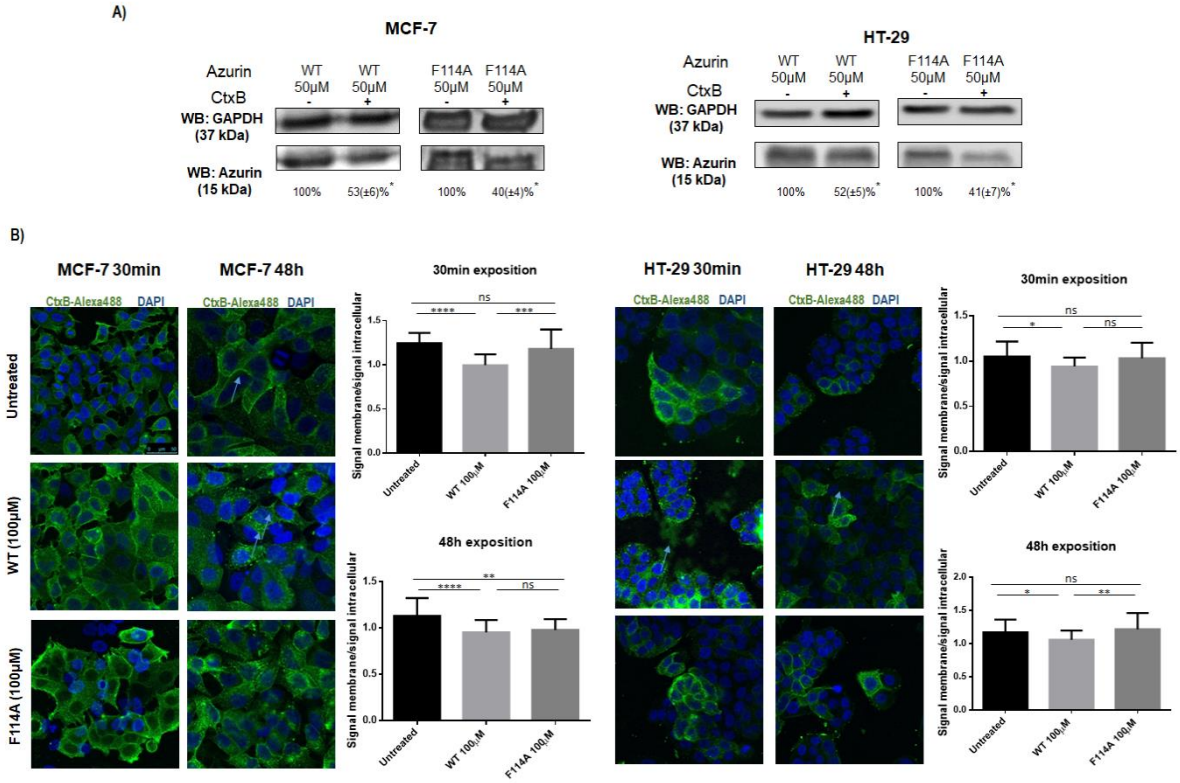

Figure II.4-2: Phenylalanine$_{114}$ is important for interaction with GM-1. **A)** Azurin interacts with GM-1. Blocking GM-1 with CTxB impairs azurin entry for both WT and F114A azurin mutant. GM-1 was blocked by adding CTxB for 10 min, before being treated with 50 μM of WT or the mutated azurin proteins for 30 min, in MCF-7 (left) and HT-29 (right) cells. A cropped representative image of western blot is depicted and results are presented as the ratio of band intensity of target protein between azurin treated samples and control samples, both normalized to their respective GAPDH or actin band intensity (* p<0.05; two-tailed t-student test). Full-length western blot images are displayed in Figure VIII.1-2. **B)** The effects of WT and F114A azurin in the cells' lipid raft organization. Cells were grown and treated with both azurin proteins at 100 μM, 30 min or 48 h. The glycosphingolipid GM-1 of lipid rafts is marked with CTxB-Alexa488 (green) and the nuclei are stained with DAPI (blue). CTxB-Alexa488 was added for 10 min at a final concentration of 1 μg/mL right before cells were fixed in formaldehyde and prepared for visualization under the confocal fluorescence microscope. Fluorescence signal intensity was quantified in Image J software for at least 20 cells from experiments performed in different days, as explained in Material and Methods Section. Results are represented as an average of the ratio between fluorescence intensity signal in the plasma membrane and the intracellular signal, excluding the nucleus, ± SD. Results were compared by analysis of variance ANOVA using GraphPad Prism (version 6).

II.4.3. Silencing of caveolin-1 inhibits cell entry of WT azurin

Previous reports had described that azurin co-localizes with Cav-1 almost immediately after penetration into cells. Cav-1, together with GM-1, is a component of *caveolae*, a particular type of lipid rafts. Being an important mediator of several signaling pathways, numerous studies already indicated that part of the mechanism by which Cav-1 does so is through the binding to several other proteins, therefore controlling part of their signaling activity (del Pozo *et al.*, 2005; Norambuena and Schwartz, 2011; Vihanto *et al.*, 2006). Furthermore, not only Cav-1 is recognized as an important mediator of endocytosis, it has been strongly associated to the entry of azurin in cancer cells (Mehta *et al.*, 2011; Yamada *et al.*, 2009). Therefore, to understand how Cav-1 protein levels in the membrane could also control the velocity of the entry process for azurin, we silenced the CAV1 gene with siRNA to test if under those conditions azurin was less capable to enter in cancer cells. After silencing of CAV1 expression, cells were exposed to 50 μM of WT azurin or the mutated F114A, for 30 min, as for the previous assay. As seen in Figure II.4-3A, we observed a decrease in the levels of WT azurin entry for both MCF-7 and HeLa cells but for F114A mutated azurin, no decrease was observed. The protein levels were normalized by the respective actin level. It is interesting to note that for F114A azurin, the same levels of azurin are detected in the cells non-silenced for Cav-1 (Control siRNA) when compared to the cells subjected to the treatment with WT azurin after silencing Cav-1. In addition, when compared with its own control, no decrease in the entry of the mutant protein was observed, which suggests that the mediation of Cav-1 for azurin entry is more important to the WT protein than for that mutated in the F114 amino acid residue. Nevertheless, when CAV1 gene expression is down-regulated, the entire membrane organization may be altered, for instance *caveolae* that are Cav-1-enriched smooth invaginations of the plasma membrane that form a subset of lipid rafts, can no longer be formed in the absence of Cav-1. Therefore, such inhibition may cause alterations that can explain the differences observed for the F114A mutant protein.

II.4.4. Azurin binds to caveolin-1 scaffolding domain *in vitro*

One particular domain of Cav-1 that is involved in multiple interactions with other proteins is its CSD. In order to study possible interactions between the CSD and WT azurin or F114A azurin, we carried out FRET measurements between WT and F114A mutant azurin labeled with Atto390 NHS and CSD labeled with FITC. We collected fluorescence spectra for WT and mutant azurin labeled proteins in the absence and in the presence of increasing

concentrations of FITC-CSD labeled peptide (Figure VIII.1-3). The occurrence of energy transfer was readily visualized as a decrease in the donor fluorescence of about 35% for the WT for the highest concentration of the FITC-peptide (14 μM). For the mutated protein, we observed a decrease in the intensity of the protein of only about 17%, indicating that in the same experimental conditions, a higher energy transfer occurs for the WT protein than for the F114A mutant, suggesting a higher interaction with the WT protein. The FRET efficiency was, at this concentration, 35% for the WT and only 17% for the F114A mutant protein (Figure II.4-3B).

Furthermore, we also observed that the WT azurin is immunoprecipitated with Cav-1 in much higher levels that the mutated protein after 30 min of exposure to each protein (Figure II.4-3C) in both MCF-7 and HeLa cells, reflecting both the decreased capacity to recognize and enter in cancer cells and a diminished ability of the mutant protein of azurin to bind to Cav-1.

II.4.5. Azurin leads to a decrease in caveolin-1 total protein levels

The mechanism of azurin/p28 cell entry has been associated to Cav-1 and lipid rafts. However, those indications were related mainly to the interactions between the protein and the peptide almost immediately after the cells were exposed to any of them, but no information is available regarding the impact of azurin on the total protein levels of Cav-1. We have demonstrated that azurin causes an increase in endocytosis in breast cancer cells (Bernardes *et al.*, 2014), while in lung cancer cells the exposure to azurin led to a decrease in the membrane stiffness probed by AFM to which alterations at the Cav-1 levels may be related (Bernardes *et al.*, 2016). In this work, azurin treatment of MCF-7 and HeLa cancer cells for 48 h led to a decrease in the levels of Cav-1, in a dose-dependent manner (Figure II.4-3D). Shorter treatment times produced similar results, while onset times for depletion of Cav-1 levels were observed to be cell line dependent (data not shown).

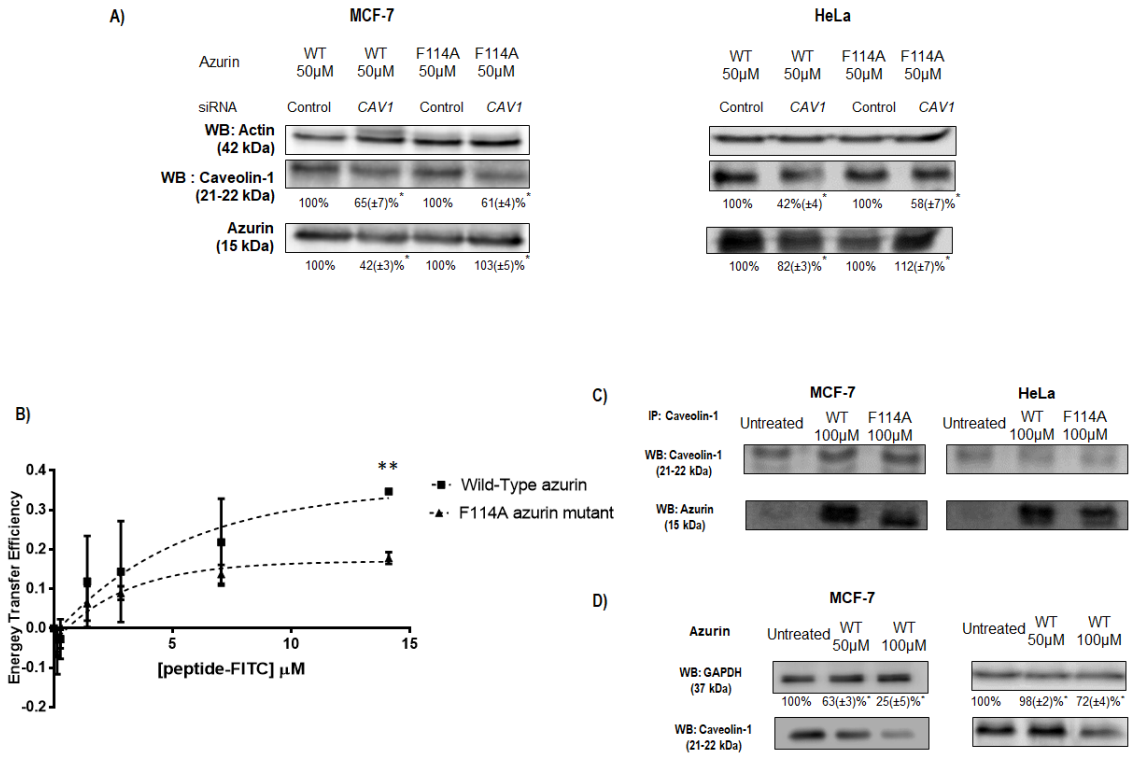

Figure II.4-3: Phenylalanine$_{114}$ is important for interaction with Cav-1. **A)** Entry of WT azurin and mutated F114A azurin upon silencing of Cav-1 by siRNA. Cells were treated with 50 µM of WT or the mutated azurin proteins for 30 min. Control siRNAs with proteins are the control conditions. A cropped representative image of western blot is depicted and results are presented as the ratio of band intensity of target protein between azurin treated samples and control samples, both normalized to their respective GAPDH or actin band intensity (* p<0.05). Full-length western blot images are displayed in Figure VIII.1-4. **B)** Energy transfer efficiencies of WT and F114A mutant azurin proteins labeled with Att0 390 in the presence of FITC-labed CSD (Caveolin Scaffolding Domain) peptide. Values were calculated as described in the Methods section. **C)** Co-immunoprecipitation of Cav-1 and azurin in MCF-7 and HeLa cells treated with azurin 100 µM for 30 min. An antibody to caveolin-1 was incubated with total cell lysates and used to precipitate it from both control and azurin treated total cell lysates. Proteins were separated in SDS-Page gels transferred to membranes which were probed with both anti-Cav-1 and anti-azurin antibodies. Full-length western blot images are displayed in Figure VIII.1-5. **D)** Azurin causes a decrease in the protein levels of Cav-1. A single dose of azurin (50-100 µM) for 48 h leads to a dose-dependent decrease in two different cancer cell types (MCF-7 and HeLa). A cropped representative image of western blot is depicted and results are presented as the ratio of band intensity of target protein between azurin treated samples and control samples, both normalized to their respective GAPDH band intensity (* p<0.05; Figure VIII.1-6).

II.4.6. Azurin decreases plasma membrane order

Having determined that exposition to WT azurin leads to a decreased content of lipid raft components GM-1 and Cav1, we next sought to investigate if the interactions of azurin with caveolar lipid raft components could be associated to changes in the organization of the plasma membrane of the cancer cell lines under study. It has been demonstrated that variations in the order of the plasma membranes in living cells can be detected using the environment-sensitive fluorescent probe Laurdan and two-photon excitation microscopy (Gaus *et al.*, 2003; Owen *et al.*, 2011). Laurdan fluorescence emission spectra is sensitive to changes in membrane order by exhibiting a 50 nm red shift as the order changes from

the liquid-ordered to a liquid disordered state (Parasassi *et al.*, 1991; Parasassi and Krasnowska, 1998). The changes in emission spectra are the result of alterations in the penetration of water molecules within the lipid bilayer and it can be quantified by calculating the GP value as demonstrated in *e.g* (Parasassi *et al.*, 1991). The value of GP can vary between 1 and −1 (complete exposure to bulk water). Therefore, higher GP values are associated to higher membrane ordering and a less fluid plasma membrane.

To determine Laurdan GP values several images were acquired (Figure II.4-4A) and Laurdan fluorescence spectral shifts in the plasma membrane were quantified through the GP function as stated in the Methods section. Laurdan GP measurements were made for exposure times of 30 min and 48 h to both WT and mutant F114A azurin proteins. In both time points, exposure to azurin WT caused a decrease in the GP values measured in the plasma membranes, indicating that exposition to azurin causes a decrease in the plasma membrane order (Figure II.4-4B). On the other hand, the F114A azurin mutant did not altered the GP values when compared to untreated cells, in accordance to what was observed in previous sections. The GP values found in control conditions are in line with published values for these cell lines (Owen *et al.*, 2011).

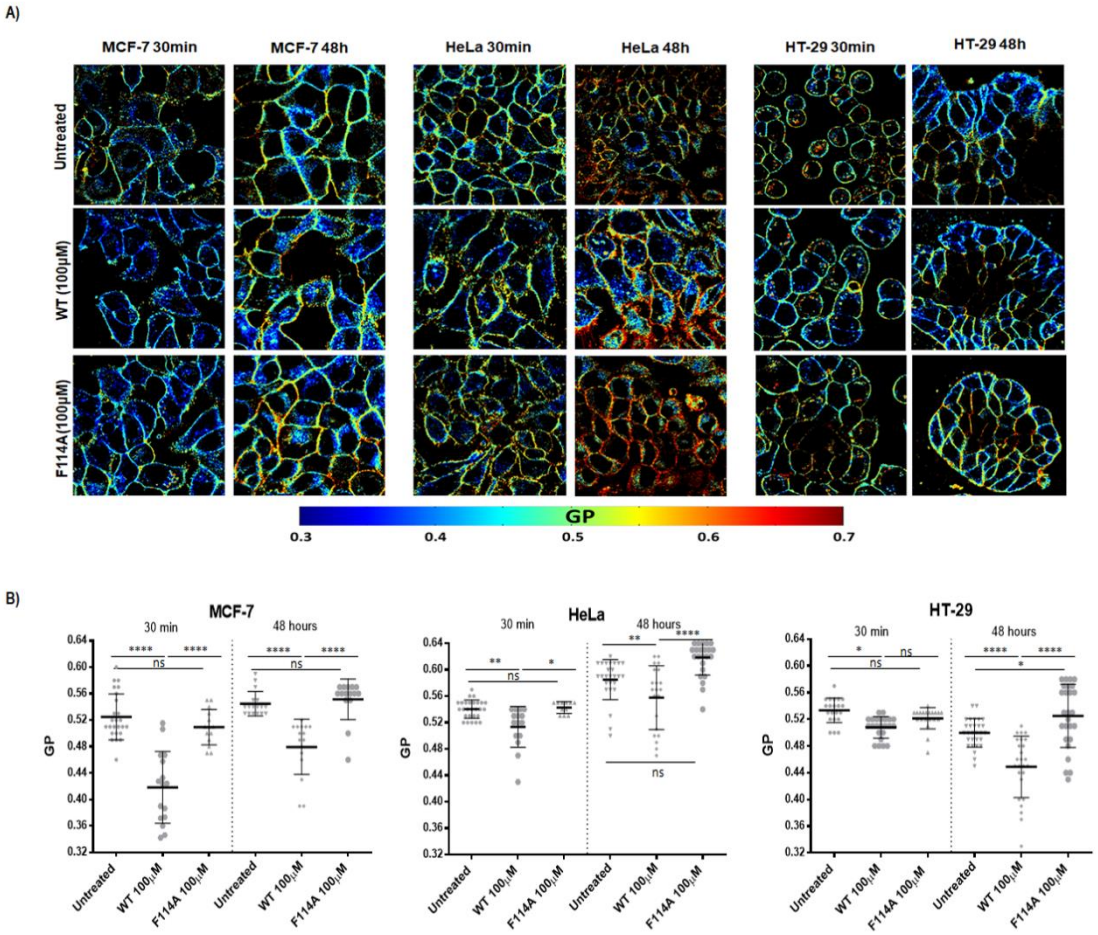

Figure II.4-4: Impact of WT or F114A mutant azurin protein on the membrane fluidity of cancer cell lines MCF-7, HeLa and HT-29. **A)** Cells were loaded with 5 µM of Laurdan after incubation with azurin proteins at 100 µM for 30 min or 48 h. Laurdan GP values were determined as described in Material and Methods. Representative Laurdan GP images are shown. **B)** Average GP values after incubation with azurin proteins are shown for the plasma membranes for the three cell lines. WT azurin causes a decrease in the average GP value in all three cell lines, either from 30 min or 48 h of exposure. Average GP values are expressed as mean ± SD from at least 15 individual cells in each condition. Results were compared by analysis of variance ANOVA using GraphPad Prism (version 6).

II.4.7. Azurin enhances the activity of chemotherapeutic drugs

With the above demonstration of the interaction of azurin with Cav-1 and GM-1 and taking in consideration that Cav-1/lipid rafts are important mediators of numerous cellular processes, including the resistance to anticancer drugs, we determined the degree of cytotoxicity for two chemotherapeutic drugs (PTX and DOX), alone or in the presence of both WT or mutated azurin. Interestingly, in MCF-7 and HeLa cells the proteins alone had different behaviors in terms of cytotoxicity. One single delivery of the WT protein results in a viability loss of about 20% for MCF-7 and 40% for HeLa cells, whereas the F114A mutant did not produce such an effect, causing a lower reduction in cell viability (Figure II.4-5A, B). However, for the HT-29 colon cancer cell line, these differences were not observed

with both proteins showing a similar effect in terms of cytotoxicity. Such a result might be explained by the low expression of Cav-1 in that cell line (Figure VIII.1-7). Overall, for the combined treatments, the results point to the increase in the cytotoxicity observed when the proteins are present, using drug concentrations that inhibit cell proliferation in values close to 20-50% (Figure II.4-5). In MCF-7 and HeLa cells, an increase is seen particularly for PTX at the lower doses tested (0.1 and 1 nM), and the effects are more evident for the WT protein. Indeed, in the case of F114A mutated azurin the values seem to reflect the less pronounced effect demonstrated by the protein in terms of perturbing the organization of lipid rafts. On the other hand, for DOX the effects of the combinations did not produce a significant increment in the action of the drug in these cell lines. However, in both cell lines the WT protein had a more pronounced effect that the F114A mutant. In the HT-29 cell line, the two proteins significantly enhanced the action of both tested drugs, possibly reflecting the higher cytotoxicity that the proteins alone present in these cells.

II.5. Discussion

The microdomains present in the plasma membranes of cells, such as *caveolae*/lipid rafts, are important mediators in signal transduction pathways associated to several cellular phenomena such as membrane trafficking, cytoskeletal organization, motility, polarity and endocytosis (Lingwood and Simons, 2010; Martinez-Outschoorn *et al.*, 2015; Simons and Toomre, 2010). Many of these signaling pathways were in the last years identified as targets of azurin, which has been proposed as a therapeutic protein in anticancer therapies (Bernardes *et al.*, 2013a; Bernardes *et al.*, 2016; Mehta *et al.*, 2011). The entire protein and one lead peptide, p28, target p53 and signaling pathways mediated by VEGF/FAK, Src, PI3K/Akt, and the EGFR signaling, in all cases contributing to their attenuation, therefore altering the capacity of several cancer cell models to progress. Over the years, the mechanisms by which azurin orderly enters in the cells without disrupting the membrane have been identified, pointing to an important interaction with *caveolae*/lipid rafts. Firstly, the p28 amino acid fragment was identified as a mediator of azurin entry (Yamada *et al.*, 2005), but later other domains of azurin were also associated to its anticancer activity, namely the C-terminal region (96-113 amino acids).

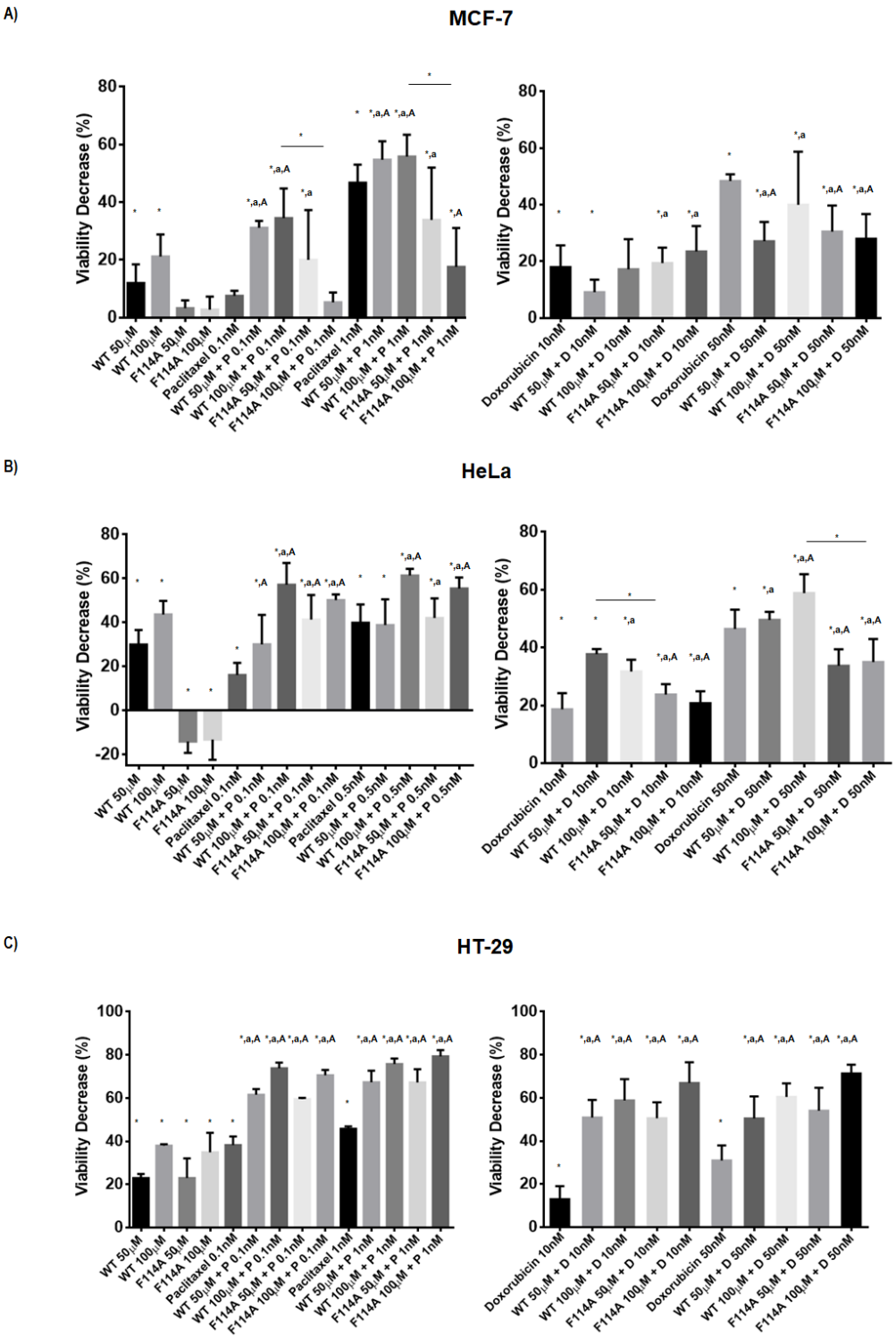

Figure II.4-5: The effect of the combination of WT or F114A mutant azurin proteins with chemotherapeutic agents [paclitaxel (P) and doxorubicin (D)] was determined by MTT assay. Paclitaxel or doxorubicin, WT azurin or F114A mutant azurin were added alone or in combination for 72 h in MCF-7 **A)**, HeLa **B)** and HT-29 **C)** cells. Concentrations are shown above each data point. MTT reagent was added to each well and percentage change in absorbance at 570 nm in treated cells relative to untreated controls. Results are represented as percentage of viability decrease, determined as 100% (control) – % of proliferation for each treatment condition. Values represent the mean ± SD. * p<0.05 each condition vs untreated cells; [a] p<0.05 combination vs protein alone; [A] p<0.05 combination vs drug alone.

This domain has a structural similarity with ephrinB2 at the GH loop, and a peptide composed of these amino acids, demonstrated significant cytotoxicity against the prostate cancer cell line DU142 expressing a functional form of ephrinB2, contrary to the natural ligand (Chaudhari *et al.*, 2007). Azurin-derived peptides comprising this region were also later improved and used to radiosensitize cancer cells (Micewicz *et al.*, 2011). In this work, we propose that the C-terminal region of azurin, which is rich in hydrophobic amino acid residues like phenylalanine and tyrosine, also contributes to the recognition of azurin in cancer cell lines, mainly due to its contribution to hydrophobic favored interactions. We computationally analyzed several point mutations in azurin, replacing three hydrophobic amino acids (Y108, F111 and F114) by alanine, and looked into the alterations that such mutations could cause to the hydrophobicity pattern exhibited at the topological surface of the protein (Figure II.4-1A). From these, the F114 residue demonstrated to be the one with the most impact, since its side chain is exposed to the surface of the protein and its replacement by alanine, led to an alteration in the hydrophobicity displayed at the surface of azurin (Figure II.4-1B). This mutated protein exhibited less effective penetration of cancer cells after exposure for 30 min and 2 h (Figure II.4-1C).

An important component of lipid rafts is GM-1. GM-1 is a glycosphingolipid present in high abundance in lipid rafts (Ichikawa *et al.*, 2009; Pang *et al.*, 2004). Carbohydrate-protein interactions have been vastly studied, and it is known that in some sugars, the clustering of three or more adjacent C-H groups caused by the characteristic steric disposition of hydroxyl groups creates hydrophobic patches on the sugar surface that can establish apolar interactions with hydrophobic epitopes in proteins, most notably the aromatic rings of tryptophan, tyrosine and phenylalanine residues (del Carmen Fernández-Alonso *et al.*, 2012). The aromatic amino acids identified within the C-terminal amino acid sequence of azurin might interact with these sugar components of *caveolae* in the first recognition steps to enter cancer cells. In fact, pre-treatment of cells with tunicamycin which inhibits the N-linked glycosylation significantly reduced the entry of the peptide (Taylor *et al.*, 2009). The demonstration that there is a decrease in the levels of these proteins within cancer cells, when GM-1 is blocked with a powerful ligand such as CTxB reinforces those observations (Figure II.4-2A). It should be noted that there seems to be a greater decrease in the entry of the mutated protein in comparison to the WT protein in all cell lines, when these cells are previously exposed to CTxB. With these results one can infer that one of the mechanisms of azurin recognition by cancer cells acts at the level of GM-1 ganglioside and aromatic amino acids on the azurin structure, being F114 important for that recognition, which seems, according to our results, to occur both in Cav-1 positive and

negative cell lines. Indeed, in cell lines expressing low levels of Cav-1, like HT-29, blocking GM-1 seems to be enough to delay azurin entry. GM-1 is already recognized as a mediator of protein accumulation in lipid membranes in other pathologies like in in Alzheimer´s disease where it facilitates the accumulation of amyloid β-protein and related peptides in neural plasma membrane cells (Evangelisti *et al.*, 2016; Wakabayashi and Matsuzaki, 2009; Yamamoto *et al.*, 2008).

CTxB is also a marker widely used to assess lipid rafts in cancer. An Alexa488-CTxB version was used to assess what happens to these membrane microdomains upon exposure to both proteins. Contrary to untreated cells, where the membrane staining of CTxB is clear, in cells treated with WT protein, GM-1 is dislocated from the plasma membrane within 30 min of exposure, an effect that is maintained for at least 48 h (Figure II.4-2B). For the mutated protein, that observation is less clear than for the WT protein. The membrane staining is maintained to a higher extent than the WT protein, suggesting once again a stronger affinity of WT azurin to GM-1 than the mutated protein. This higher affinity then leads to a higher internalization of this lipid raft marker (Figure II.4-2C).

Interestingly, when we silenced Cav-1 with siRNA, the WT protein was also affected in the entry process, reinforcing that Cav-1 is another important mediator in that process (Figure II.4-3A). Regarding the F114A mutant, its entry was not delayed in the cells in which CAV1 expression was down-regulated; instead, it is close to the WT protein levels, which points to the different behavior of the two proteins in the absence of Cav-1. Nevertheless, when Cav-1 is silenced with siRNA, the molecular organization of the membrane is likely to be altered due to the structural role played by Cav-1, which may lead to different observations when compared to an assay where both proteins are added to the cells for 30 min with no previous changes induced.

The interaction of each protein with the CSD was also analyzed using an FITC-labeled CSD peptide since the interactions of several proteins with Cav-1 and other lipid rafts' components are mainly determined by hydrophobic motifs in the proteins, being the CSD a mediator of such interactions with multiple signaling proteins. We used FRET to determine possible interactions of WT azurin with the FITC-CSD peptide, observing a higher energy transfer efficiency for the WT protein than for the mutant protein which suggests that azurin interacts directly with Cav-1 through this domain. These results also suggest that the WT and mutated azurin show significant differences in affinity for the interaction with Cav-1, offering an additional explanation for the less effective entry of the mutant protein relatively to the WT protein. In the cellular context, after exposition of both

proteins to the cells for 30 min, when Cav-1 is immunoprecipitated, azurin is detected in complex with it, being the WT protein detected in higher levels than the mutant, reflecting the lower levels of the protein that bind to and are up taken by the cells. Furthermore, when the total levels of Cav-1 are analyzed by western blot, after 48 h of exposure to the WT protein, it is possible to see that Cav-1 is less abundant in the cells. Combined with the displacement observed for GM-1, the decrease in the Cav-1 protein suggests that additional changes in the profile of membrane protein composition, mainly within lipid rafts, are altered by azurin, which prompted us to analyze the membrane fluidity of cells treated with azurin.

Lipid rafts are clusters of specific lipids, cholesterol and sphingolipids, forming highly condensed relatively ordered nano-domains, distinctive from the rest of the membrane (Sezgin *et al.*, 2017), very important for the lateral organization of cellular membranes. The complexity of lipid and protein packing, rotation and lateral diffusion gives rise to what is called the cell membrane fluidity (Sengupta *et al.*, 2007). Indeed, the biophysical features of membranes severely impact many of the phenomena they regulate, and may have a huge impact on drug resistance (Peetla *et al.*, 2013). After identifying the molecular changes above mentioned, we assessed the effects of azurin on the organization of plasma membranes, by assessing the membrane fluidity with the fluorescent probe Laurdan. Our results indicate clearly that the fluidity of the plasma membrane increases after exposure to WT azurin, as evaluated from changes in the Laurdan GP values. The entry of azurin preferentially through *caveolae*/lipid rafts, probably removing Cav-1 from the membrane and perturbing the raft organization, seems to cause a structural change in the plasma membrane organization, possibly decreasing the fraction of liquid-ordered membrane/domains (Figure II.4-4). These results are in accordance with the previous results obtained by us and others, in which the exposure to azurin not only attenuates signaling pathways associated to motility, adhesion and invasiveness but also to biophysical changes at the plasma membrane level, effects attributed to the presence of lipid rafts. Indeed, plasma membranes define the boundaries of live cells, playing a major role in all cell functions and in the communications cell establish with the exterior. Being Cav-1 a major integral protein of *caveolae*, the ability to target it can be of extreme importance to establish new therapeutic strategies. Its role in cancer is still controversial, with reports indicating that cancer development and progression can be either associated to an increase in Cav-1 levels or its absence, varying across different models (Bourseau-Guilmain *et al.*, 2016; Chanvorachote *et al.*, 2014; Lee *et al.*, 1998; Logozzi *et al.*, 2009; Nam *et al.*, 2013; Shi *et al.*, 2015). However, it is becoming clear that the development of

the MDR phenomenon is strongly associated to its increase, as well as to the increase in the membrane stiffness, blocking the ability of several drugs to efficiently penetrate into the cells to reach their intracellular targets (Lavie *et al.*, 2001; Quest *et al.*, 2013). In this context, we tested if the alterations caused at the plasma membrane order here observed could be related to an increase in the sensitivity to two chemotherapeutic drugs, PTX and DOX (Figure II.4-5). Indeed, the p28 peptide was very recently associated to such an increase in the sensitivity to these drugs in different cell models (Yamada *et al.*, 2016), mainly due to its effects of p53 stabilization. Therefore, we tested in parallel both the WT and the F114A mutant protein. Interestingly, from the three cell lines tested, in which all of them the delay in F114A entry was observed, in the Cav-1 negative HT-29 cell lines, no significant differences were observed in the toxicity generated by the proteins alone. On the contrary, for Cav-1 expressing MCF-7 and HeLa cells, significant differences were observed, with the mutant displaying much lower cytotoxicity than the WT protein, pointing to the identified decrease in the interaction with the CSD. In terms of potentiating the effects of both drugs, such different effects were also only detected in these cell lines, albeit in HT- 29 the effects were more accentuated in all the combinations tested, indicating maybe that the higher toxicity levels created by the proteins were dominating. In MCF-7 and HeLa cells, the combinations with the WT protein led to a potentiation of the chemotherapeutic drugs, with a statistically significant difference in favor of the WT protein for the highest concentrations of proteins and drugs observed in most cases (Figure II.4-5A, B). Therefore, in these cases, the molecular effects of WT azurin at the membrane level seem to contribute positively to the action of the drugs. Indeed, recently the interaction of DOX with model cell membranes was evaluated to determine how the interaction of the drug alone could impact the organization of the plasma membranes in cancer cells and how it could affect its delivery efficacy and the contribution to chemoresistance. It was seen that this drug has a preference to locate in more ordered microdomains, where for example, P-glycoprotein is also preferentially located. For the authors, this could explain how the drug is available to be a substrate for efflux by this protein which is also located in these structures (Alves *et al.*, 2017). It is then possible that, by decreasing the more ordered domains, one of the mechanisms by which azurin enhances the activity of this drug is by perturbing this preferential localization of the drug reducing its availability to be efflux pumps.

In sum, the combination of azurin with these drugs benefited their cytotoxic effect and statistical differences were observed between the WT and the mutant azurin tested in the lines where Cav-1 is more expressed. A number of recent studies indicate that acting at

the membrane level may be a new strategy to target cancer cells, enhancing the cytotoxicity of chemotherapeutic drugs, and by doing so, to also decrease the severe systemic toxic effects they cause, since lower concentrations are needed to achieve the same therapeutic response. Drugs that target the membrane lipid composition and/or organization are now receiving attention as adjuvants for cancer therapy (Colin *et al.*, 2011; Escribá *et al.*, 2015; Lee *et al.*, 2014; Peetla *et al.*, 2013). In this context, the action of azurin over different cancer cell models is a contribution to the broad anticancer action this protein demonstrates. In particular, it would be interesting in the future to evaluate the effects over drug resistant cells, where the biophysics of the plasma membranes seems to be a major contributor to that phenomenon.

Acknowledgments

The work presented was supported by scientific projects (PTDC/EBBBIO/100326/2008, and FAPESP/20107/2014) financed by the Portuguese Science and Technology Foundation (FCT). FCT also provides a post-doctoral research grants for Nuno Bernardes (SFRH/BPD/98162/2013) and Sandra N Pinto (SFRH/BPD/92409/2013), and PhD grant for Ana Rita Garizo (SFRH/BD/122636/2016). Fabio Fernandes acknowledges financial support from FCT with grant IF/00386/2015. The authors acknowledge the support of the national infrastructure PPBI-Portuguese Platform of BioImaging (supported by POCI-01’0145-FEDER 022122). This work has received funding from European Structural & Investment Funds through the COMPETE Programme and from National Funds through FCT under the Programme grant SAICTPAC/0019/2015. Funding received by iBB-Institute for Bioengineering and Biosciences from FCT (UID/ BIO/04565/2013) and from Programa Operacional Regional de Lisboa 2020 (Project N. 007317) is acknowledged.

III. THE AZURIN-DERIVED PEPTIDE CT-P19LC EXHIBITS MEMBRANE-ACTIVE PROPERTIES AND INDUCES CANCER CELL DEATH

Journal Paper

Garizo AR, Coelho LF, Pinto S, Fernardes F, Bernardes N, Fialho AM. 2021. The azurin-derived peptide CT-p19LC exhibits membrane-active properties and induces cancer cell death. *Biomedicines* **9**: 1194

| DOI:10.3390/biomedicines9091194

Garizo AR performed experiments, analyzed data, writing-review and editing

III.1. Abstract

Peptides have been thoroughly studied as new therapeutic strategies for cancer treatment. In this work, we explored *in vitro* the anticancer potential of three novel peptides derived from the C-terminal of azurin, an anticancer bacterial protein produced by *Pseudomonas aeruginosa*. CT-p26, CT-p19 and CT-p19LC peptides were previously obtained through an *in silico* peptide design optimization process, CT-p19LC being the most promising as it presented higher hydrophobicity and solubility, positive total charge and, most importantly, greater propensity for anticancer activity. Therefore, in this study, through proliferation and apoptosis assays, CT-p19LC was tested in four cancer cell lines-A549, MCF-7, HeLa and HT-29-and in two non-cancer cell lines-16HBE14o- and MCF10A. Its membrane targeting activity was further evaluated with zeta potential measurements and membrane order was assessed with the Laurdan probe. The results obtained demonstrated that CT-p19LC decreases cell viability through induction of cell death and binds to the plasma membrane of cancer cells, but not to non-cancer cells, making them less rigid. Overall, this study reveals that CT-p19LC is an auspicious selective anticancer peptide able to react with cancer cell membranes and cause effective action.

III.2. Introduction

The use of membranolytic anticancer peptides (ACPs) has become a potential strategy for the development of new cancer therapies (Gabernet *et al.*, 2016). ACPs (<10 kDa), either from eukaryotes or of bacterial origin, are small linear or cyclic molecules (5–50 amino acids), rich in cationic and hydrophobic amino acids that give them an overall positive charge (at pH 7) and an amphipathic behavior. These peptides can adopt α-helix or β pleated sheet configurations, but random coil structures have also been described in the literature (Hoskin and Ramamoorthy, 2008).

There are two different classifications for ACPs considering their selectivity properties. The first is the ACP_T class, which includes non-selective peptides with identical activities against several cell types, such as mammalian, bacterial and cancer cells (Gaspar *et al.*, 2013; Harris *et al.*, 2013). The second category, named ACP_{AO}, corresponds to those that selectively target bacterial and cancer cells while showing residual activity against normal cells. The reason for this behavior is not fully clear yet but the differences at the membrane level between normal and cancer cells may explain, at least *in part*, this selectivity. In fact, the plasma membrane of cancer cells is characterized as having some unique features, from which a larger surface area, a net negative charge and an abnormal fluidity stand out.

This may be due to a high number of microvilli, with the negative charge in the outer layer resulting from the abnormal presence of anionic phospholipid phosphatidylserine, O-glycosylated mucins, sialylated gangliosides and heparin sulfate (Bernardes and Fialho, 2018; Gaspar *et al.*, 2013; Harris *et al.*, 2013; Leuschner and Hansel, 2005).

The mechanism of action for ACPs leads to the irreparable disruption of the plasma membrane of tumor cells (Ehrenstein and Lecar, 1977) through the pore formation, followed by cell lysis (direct-acting mechanism; Chiangjong *et al.*, 2020; Hilchie and Hoskin, 2010). Both the structure they adopt when in contact with the plasma membrane of these cells, as well as their intrinsic characteristics, turn these peptides capable of associating with this cellular barrier mainly through electrostatic interactions (Gaspar *et al.*, 2013; Teixeira *et al.*, 2012). Apart from the plasma membrane, other internal membranes may be targeted by the membranolytic effects of ACPs, such as the mitochondrial membrane, where their effects can trigger apoptosis (indirect-acting mechanism; Hetz *et al.*, 2002; Hilchie and Hoskin, 2010).

The development of cancer therapies with the use of ACPs present advantages for clinical applications compared to conventional chemotherapy. In particular, ACPs act both in metabolically active tumor cells and in slow-growing or MDR cancer cells (Xie *et al.*, 2020b). Additionally, ACPs have a relatively high tissue penetration, the cost for producing them is low, and they can be easily modified by solid-phase synthesis technology (Hilchie and Hoskin, 2019).

Currently, the database of the National Library of Medicine (NLM) at the National Institutes of Health (NIH) in the PubMed.gov platform, displays a total of 463 clinical trials with the application of ACPs in several types of cancer being the most common studies in melanomas, breast and lung cancer (Chiangjong *et al.*, 2020; Pubmed, 2021b). As examples, the LTX-3158, a human lactoferrin-derived oncolytic peptide, is currently at phase I clinical trial and the Bryostatin 1, a peptide within the bryostatin family composed of marine natural products, is at phase II (Haug *et al.*, 2016; Wali *et al.*, 2019). In addition to them, there is p28, a CPP derived from the anticancer protein azurin (14 kDa) produced by the bacterium *Pseudomonas aeruginosa* (Yamada *et al.*, 2013a). This peptide has already completed two phase I clinical trials in cancer patients (Lulla *et al.*, 2016; Warso *et al.*, 2013), and received approval as an orphan drug by the FDA (Chakrabarty *et al.*, 2014). Overall, these studies are showing promising results for the treatment of cancer not only as sole drugs but also through combination with other therapeutic approaches (Yamada *et al.*, 2016).

The aim of this study was to evaluate the anticancer potential of new peptides derived from azurin. Evidence from us and others argues that azurin may therapeutically act on cancer cell membranes through a lipid raft/*caveolae*-mediated pathway (Bernardes *et al.*, 2013a; Bernardes *et al.*, 2014; Mehta *et al.*, 2011). By specifically targeting such plasma membrane microdomain sites, azurin promotes a multivalent action accelerating the endocytosis of receptors and the disruption of signaling pathways hyperactivated in cancer cells (Bernardes *et al.*, 2016; Yamada *et al.*, 2009). In addition, it is known that p28 derived from this protein, is a PTD, *in part,* responsible for mediating the entrance of the azurin into cells, and it also has anticancer properties (Taylor *et al.*, 2009; Yamada *et al.*, 2009). Beyond this, it has become clear that the anticancer activity exerted by azurin depends on other domains (azurin C-terminal 88-128 amino acids) besides the p28 domain (azurin 50-77 amino acids). In fact, the C-terminal peptide has anticancer activity through binding with the cell surface EphB2 receptor and interfering in cancer growth promotion, which has been explored to design peptides to improve radiotherapy efficacy in lung cancer (Chaudhari *et al.*, 2007; Micewicz *et al.*, 2011). On the other hand, the phenylalanine residue at position 114 was found to be critical for azurin uptake by cancer cells (Bernardes *et al.*, 2018). Based on this, in a previous study, our group used a region of 26 amino acid residues of azurin close to its C-terminal (CT-p26 peptide) as a template for the discovery of new bioactive peptides against cancer cells. Bioinformatics tools used in peptide design studies have enabled the assessment of the bioactivity of this native peptide. First, by reducing its length, and then by changing some residues in its amino acid sequence, it was possible to improve parameters of solubility, hydrophobicity, overall charge and anticancer potential, giving rise to two new peptides, CT-p19 (shorter than the CT-p26) and CT-p19LC (three amino acid residues altered compared to CT-p19; Coelho, 2017). In the present work, we evaluated *in vitro* the anticancer activity of these peptides and compared it with the anticancer activity of full-length azurin and its derived native peptides.

III.3. Materials and Methods

III.3.1. Azurin-derived peptides

The four azurin-derived peptides used, namely p28, CT-p26, CT-p19 and CT-p19LC, were chemically synthetized by Pepmic Co., Ltd., Suzhou, China, with a minimal purity of 95.0%. CT-p19 and CT-p19LC peptides labeled with 5,6-FAM were commercially synthesized by CASLO ApS, Kongens Lyngby, Denmark. Lyophilized samples of the peptides were

resuspended in 10 mM sodium phosphate buffer (pH 7.4) or in phosphate buffer saline (PBS; pH 7.4), divided into aliquots and stored at -20 ºC.

III.3.2. Circular dichroism spectroscopy

The secondary structure of the CT-p19LC peptide was analyzed through spectroscopic analysis. UV-visible and far-UV circular dichroism (CD) spectra were traced. UV-visible spectra between 250 and 800 nm were obtained using a PharmaSpec UV-1700 (Shimadzu, Kyoto, Japan) UV-visible spectrophotometer. Far-UV CD spectra were traced using a Π*-180 spectropolarimeter from Applied Photophysics using default parameters. Ten measurements were made with an integration time of 1 sec, a cuvette path length of 10 mm, a wavelength ranged of 190 to 250 nm and a step size of 1 nm. The obtained spectra were analyzed using the online DICHROWEB server (http://dichroweb.cryst.bbk.ac.uk/html/home.shtml, accessed on 1 July 2019) to predict the secondary structure of the peptide (Whitmore and Wallace, 2004).

III.3.3. Human cancer cell lines and cell culture conditions

The A549 (lung), MCF-7 (breast), HeLa (cervix) and HT-29 (colorectal) human cancer cell lines (European Collection of Authenticated Cell Cultures (ECACC), Public Health England, Salisbury, United Kingdom), the 16HBE14o- human bronchial cell line (Cozens *et al.*, 1994) and the MCF10A human mammary gland cell line (American Type Culture Collection (ATCC), Manassas, Virginia, United States) were used. The cancer cells were seeded and maintained in Dulbecco's Modified Eagle Medium (DMEM; Gibco® by Life Technologies, Carlsbad, California, United States). The medium was supplemented with 10% heat-inactivated fetal bovine serum (FBS; Gibco® by Life Technologies, Carlsbad, California, United States), 100 IU/mL penicillin and 100 mg/mL streptomycin (Pen-Strep, Invitrogen, Waltham, Massachusetts, United States). The 16HBE14o- cells were grown in MEM medium without earls' salts and supplemented with 10% FBS, 1% L-glutamine and 10000 U/mL penicillin and 10000 mcg/mL streptomycin (PenStrep, Invitrogen, Waltham, Massachusetts, United States). The MCF10A cells were cultured in 50% DMEM/50% F12 nutrient mix, supplemented with 5% equine serum, EGF (20 ng/mL), insulin (10 µg/mL), hydrocortisone (0.5 µg/mL), cholera toxin (100 ng/mL) and 10000 U/mL penicillin and 10000 mcg/mL streptomycin (PenStrep, Invitrogen, Waltham, Massachusetts, United States). The culture conditions for all cell lines were 37 ºC in a humidified chamber containing 5% CO_2 (binder CO_2 incubator C150, Keison products, Chelmsford, United Kingdom).

III.3.4. MTT cell proliferation assays

Cell proliferation after treatment with the peptides was measured by MTT [3-(4,5 dimethylthiazol-2-yl-2,5 tetrazolium bromide)] assay. A549, MCF-7, HeLa and HT-29 human cancer cells were seeded in 96-well plates at a density of 10^4 cells per well (3 replicates), and were left to adhere and grow overnight in a CO_2 incubator (5%) at 37 ºC. The 16HBE14o- and MCF10A cells were seeded at a density of $7.5x10^4$ and $4.5x10^4$ cells per well (3 replicates), respectively, and left to adhere and grow overnight in the same conditions. In the next day, the medium was collected, and cells were treated with the peptides (concentrations from 0 µM to 100 µM). Proliferation was determined after 48 h. Following the incubation period, 20 µL of MTT (5 mg/mL) were added to each well, and incubated at 37 ºC for 3.5 h. The reaction was stopped with the addition of 150 µL of a solution of 40 mM HCL in isopropanol. MTT formazan formed was spectrophotometrically read at 590 nm in a microplate reader (SpectroStarNano, BMG LABTECH, Aylesbury, United Kingdom). Untreated cells were used as control (0% of viability decrease) to determine the relative cell viability of treated cells.

III.3.5. LDH release assays

The Invitrogen™ CyQUANT™ LDH Cytotoxicity Assay Kit (Invitrogen, Waltham, Massachusetts, United States) was used to determine the LDH release of non-cancer cells treated with CT-p19LC, according to the manufacturer's instructions. Briefly, 16HBE14o- and MCF10A cells were seeded at densities of $7.5x10^4$ and $4.5x10^4$ cells per well (three replicates), respectively, and left to adhere and grow overnight in the same conditions. The next day, the medium was collected and the cells were treated with the peptides (100 µM). After 48 h, the medium was collected and analyzed. Untreated cells were used as controls to compare the spontaneous LDH release and to normalize the data. Additional controls used were the maximum LDH activity release by lysing the cells with the lysis buffer provided in the kit, as well as the LDH positive control.

III.3.6. Quantitative cellular interaction

In order to evaluate the cell-peptide interaction, A549, MCF-7, HeLa and HT-29 cell lines were plated in 6-well plates with $5x10^5$ cells per well, respectively, and left to adhere and grow overnight in a CO_2 incubator (5%) at 37 ºC. The following day, the medium was removed, and the cells were washed twice with PBS and treated with 5 µM of CT-p19 and CT-p19LC labeled with 5,6-FAM over 2 h at 37 ºC. After treatment, cells were washed

twice with PBS, detached with TrypLE™ Express (Gibco® by Life Technologies, Carlsbad, California, United States) at 37 ºC and resuspended in medium. Then, cells were collected by centrifugation at 1200 rpm over 3 min, washed once with PBS and re-dispersed in 350 µL of PBS for cytometry analysis. The quantification of the peptides' interaction with the cells was done using a BD Accuri™ C6 Plus Flow Cytometer (BD Biosciences, Devon, England), where peptides were detected through the fluorescein isothiocyanate (FITC) channel (FL1 detector, 533/563 nm; laser configuration of 3-blue 1-red, 640 nm laser). Measurements were carried out in triplicate and 20000-50000 events were acquired in the gated region of the forward-scatter/side-scatter plot per sample. A control based only on cells without treatment was also performed to exclude the possible cellular autofluorescence. The results were analyzed using the software FlowJo v10 by gating out cellular debris and doublets and expressed as the geometric mean fluorescence intensity (Geo MFI).

III.3.7. CT-p19LC cellular uptake

In order to characterize the cellular uptake of CT-p19LC, cells were cultured on µ-Slide 8 well glass-bottom chambers (ibidi®, Munich, Bavaria, Germany) with $5x10^4$ cells per well and left to adhere overnight before being treated with 5 µM of CT-p19LC-5,6-FAM peptide for 2 h. After this time, the medium was collected and the cells were washed twice with phosphate buffer saline (PBS) pH 7.4. Then, Alexa Fluor® 633 WGA (Invitrogen™, Waltham, Massachusetts, United States; 1:200) and Hoechst 33342 (InvitrogenTM, Waltham, Massachusetts, United States; 1:500) were added to stain the plasma membrane and the nucleus, respectively, followed by 15 min of incubation. Finally, the samples were observed on a Leica TCS SP5 (Leica Microsystems CMS GmbH, Mannheim, Germany) inverted confocal microscope (model DMI6000) with a 63.3x water-immersion (1.2-numerical-aperture) apochromatic objective (Pinto *et al.*, 2008).

III.3.8. Apoptosis assay

The FITC-Annexin V Apoptosis Detection Kit I (BD Pharmingen™, BD Biosciences, Devon, England) was used to study the apoptosis of cancer cell lines and non-cancer cell lines under study after treatment with CT-p19LC peptide. Briefly, A549, MCF-7, HeLa, HT-29 and the 16HBE14o- and MCF10A cell lines were plated in 6-well plates with $5x10^5$ and $7.5x10^5$ cells per well, respectively, and left to adhere and grow overnight in a CO_2 incubator (5%) at 37 ºC. The following day, the medium was removed and the cells were washed once with PBS pH 7.4 and treated with 20 µM of CT-p19LC over 48 h at 37 ºC.

After treatment, the cells were washed twice with PBS pH 7.4, detached with Accutase® (Merck KGaA, Darmstadt, Germany) at 37 ºC and resuspended in cell culture medium. After that, $1x10^5$ cell per mL was collected and centrifuged at 1200 rpm for 3 min. The supernatant was discarded, and cells were resuspended in 100 µL of 1X annexin V binding buffer. Then, FITC-annexin and PI (5 µL each) were added, and the cells were incubated at room temperature in the dark for 15 min. Finally, 400 µL of 1X annexin V binding buffer was added, and cells were analyzed on a BD Accuri™ C6 Plus Flow Cytometer (BD Biosciences, Devon, England). Untreated cells were used as a control. Cell death induction was considered by adding quadrant 2 (Q2) to quadrant 4 (Q4). At least 20000 events were acquired and analyzed per sample.

III.3.9. Zeta potential measurements of live A549, MCF-7, HeLa, HT-29 cancer cells, and 16HBE14o-, MCF10A non-cancer cells in the presence of CT-p19LC

Zeta potential measurements through laser Doppler anemometry (LDA) were performed to assess the surface charge density of cancer and non-cancer cells and the electrostatic attraction of CT-p19LC toward them. For this, cells were diluted to $1x10^5$ cells per mL in DMEM and washed with PBS pH 7.4 twice (1200 rpm; 5 min). Then, cellular suspensions were incubated with different peptide concentrations (5, 10 and 20 µM) in serum-free medium for 30 min at 37 ºC and dispensed into disposable zeta cells with gold electrodes. A set of 10 measurements (≈40 runs each) were performed at 37 ºC with a voltage of 48 V (Malvern Instruments Ltd., Worcestershire, United Kingdom). Control values were obtained by measuring the surface charge of each cellular suspension in the absence of CT-p19LC (0 µM, untreated condition).

III.3.10. GP determination for membrane order evaluation

The membrane order evaluation of A549, MCF-7, HeLa and HT-29 human cancer cell lines after CT-p19LC treatment was investigated with the probe Laurdan using two-photon excitation microscopy. Cells were treated for 2 h with 20 µM of CT-p19LC after seeding with $5x10^4$ cells on µ-Slide 8 well glass bottom chambers (ibidi®, Munich, Bavaria, Germany). Subsequently, two washing steps with PBS pH 7.4 were performed followed by incubation at 37 ºC for 15 min with medium containing 5 µM of Laurdan (Owen *et al.*, 2011). Untreated cells were used as control. Following incubation, samples were examined on a Leica TCS SP5 inverted confocal microscope (model DMI6000) with a 63.3x water-immersion (1.2-numerical-aperture) apochromatic objective. Fluorescence microscopy data was obtained by using a titanium-sapphire laser as the excitation light

source (the wave-length was set to 780 nm and the fluorescence emission was collected at 400-460 nm and 470-550 nm to calculate the GP images). Fluorescence imaging data was processed through a homemade software based on a MATLAB environment, with the GP value defined as GP = (/400-460 – G.I470-530)/(/400-460 + G.I470-530). The parameter G is a calibration factor calculated from imaging Laurdan in DMSO (GP = 0.01 in this solvent) using the same experimental conditions.

III.3.11. Statistical analysis

Statistical analysis was performed using GraphPad Prism 8.0.1 (GraphPad Software Inc., San Diego, California). Statistical significance of the difference between two groups was evaluated by with Student's *t*-test. Differences between groups were compared using one-way analysis of variance (ANOVA) and Tukey's multiple comparisons test. Results are expressed as means ± standard deviation (SD) and geometric means with 95% confidence intervals.

III.4. Results and Discussion

III.4.1. CT-p26 peptide effect on cell viability confirms the anticancer potential of C-terminal azurin

CT-p26 peptide comprises amino acid residues 95 to 120 close to the C-terminal region of the bacterial protein azurin (Table III.4-1), which is known to contribute to its anticancer activity as well as to its ability to enter cancer cells (Chaudhari *et al.*, 2007; Micewicz *et al.*, 2011; Bernardes *et al.*, 2018).

Table III.4-1: Overview of the characteristics of azurin and its derived peptides.

PROTEIN /PEPTIDE	STRUCTURE	AMINO ACID SEQUENCE	AZURIN POSITION	HYDROPHOBICITY	CHARGE	ISOELECTRIC POINT	WATER SOLUBILITY	SVM SCORE	VIABILITY DECREASE AFTER 100 µM OF PROTEIN/PEPTIDE TREATMENT	REFERENCES
Azurin		128 aa	n.a.	n.a.	n.a.	n.a.	n.a.	n.a.	20-40%	Bernardes *et al.*, 2018
p28		LSTAADMQGVVTDGMASGLDKDYLKPDD	50-77 aa	n.a.	n.a.	n.a.	n.a.	n.a.	0-25%	Yamada *et al.*, 2016
CT-p26		VTFDVSKLKEGEQYMFFCTFPGHSAL	95-120 aa	−0.03	−0.5	5.3	Poor	0.76	n.a.	Coelho, 2017
CT-p19	n.a.	VSKLKEGEQYMFFCTFPGH	99-117 aa	−0.08	0.5	7.0	Poor	0.90	n.a.	Coelho, 2017
CT-p19LC	n.a.	VSKL**RK**GE**K**YMFFCTFPGH	n.a.	−0.16	3.5	10.0	Good	0.99	n.a.	Coelho, 2017

SVM: Support vector machine score; **aa:** amino acids; **n.a.:** not applicable

Taking this into account, MTT cell proliferation assays were performed to evaluate the effect of this peptide on A549 lung and MCF-7 breast cancer cell lines. Parallel assays, under the same conditions, have also been carried out with the p28 peptide, also derived from azurin and aforementioned for its anticancer properties (Yamada *et al.*, 2009; Yamada *et al.*, 2013; Yamada *et al.*, 2016). These assays were performed with increasing concentrations of both peptides, 0 to 100 µM. As shown in Figure III.4-1, the two peptides exhibited cytotoxic activity against both cancer cell lines, and a dose-response effect is evident in the A549 lung cancer cell line. Moreover, treatment with CT-p26 leads to a higher decrease in cell viability than treatment with p28, of about 2 to 7-fold decrease in the case of A549 cells, and a 1 to 4-fold decrease in the case of MCF-7 cells. These results confirmed that the C-terminal region of the azurin protein can be used as an anticancer functional peptide and thereby making it an interesting lead peptide.

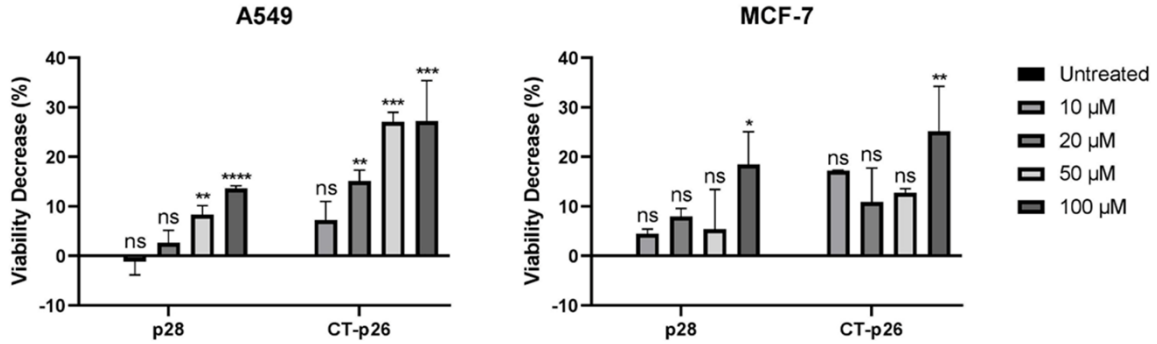

Figure III.4-1: Comparison of cell viability after treatment with p28 and CT-p26 peptides (0 to 100 µM) in A549 (lung) and MCF-7 (breast) cancer cells incubated during 48 h. Untreated condition (control) consisted of cells incubated with medium only. Values represent the mean ± SD, and each condition has at least an n=3. *, **, ***, **** and ns denote a significant difference of p<0.1, p<0.01, p<0.001, p<0.0001 and not statistically significant, respectively, when comparing control with treatments.

III.4.2. CT-p19 peptide decreases cancer cell viability and has selective property

The *in silico* study previously performed by our group allowed to design a new peptide with a shorter length, and with higher propensity to have anticancer activity from the C-terminal peptide (Support vector machine (SVM) score: 0.76 vs 0.90; Table III.4-1; Coelho, 2017). This parameter and the possible selectivity of this peptide, as seen in azurin and the other peptides derived therefrom (Yamada *et al.*, 2005; Yamada *et al.*, 2009), were evaluated through a MTT cell proliferation assay on the cancer cell lines under study, and on two matching-tissue non-cancer cell lines, 16HBE14o- and MCF10A (Figure III.4-2). After treatment with 10, 20, 50 and 100 µM of CT-p19, a decrease in cell viability of 10%, 14%, 22% and 28% was observed in the case of A549 cancer cell line. The same concentrations of CT-p19 induced a decrease of 9%, 9%, 30% and 27% on the viability of MCF-7 cells.

Regarding non-cancer cell lines, the viability decrease did not exceed 3% in 16HBE14o-, and 8% in MCF10A. Thus, the results showed that CT-p19 peptide is able to decrease the viability of cancer cells, but not of non-cancer cells, which demonstrates that this peptide has the desired selectivity. These results provided a smaller version of the CT-p26 peptide maintaining its anticancer activity.

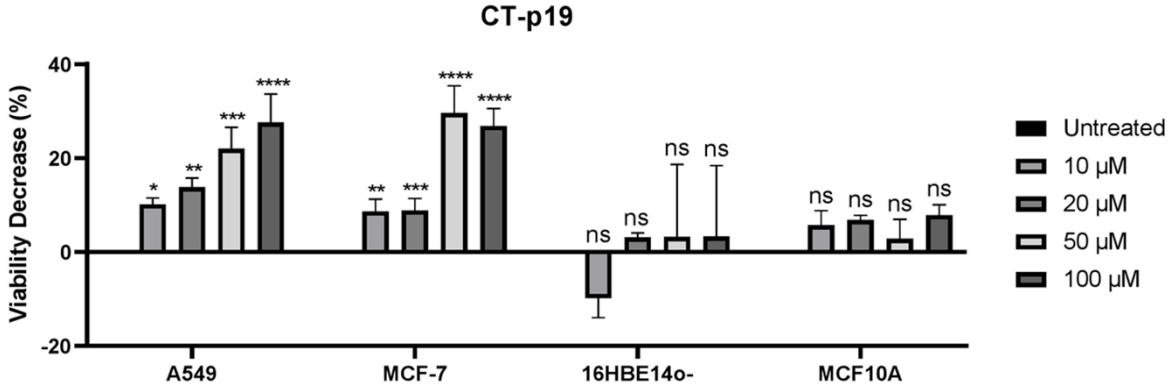

Figure III.4-2: Viability decrease (100% of proliferation in untreated condition – % of proliferation for each treatment condition) of A549 (lung) and MCF-7 (breast) cancer cells, and 16HBE14o- (bronchial) and MCF10A (mammary gland) non-cancer cells, when incubated with different concentrations of CT-p19 peptide (0 to 100 µM), during 48 h. Untreated condition (control) consisted of cells incubated with medium only. Values represent the mean ± SD, and each condition has at least an n=3. *, **, ***, **** and ns denote a significant difference of $p<0.1$, $p<0.01$, $p<0.001$, $p<0.0001$ and not statistically significant, respectively, when comparing control with treatments.

III.4.3. The newly designed CT-p19LC peptide reduces proliferation and induces cell death in cancer cell lines

After the development of CT-p19 *in silico*, our group re-designed a new peptide based on single substitutions of amino acid residues that allowed not only to increase the SVM score to 0.99, but also improved its solubility (Table III.4-1). Thus, this new peptide designated CT-p19LC, contained 19 amino acids (VSKLRKGEKYMFFCTFPGH) and represented an iterative peptide optimization from a region close to the C-terminal of the anticancer protein azurin. It has a molecular weight of 2275.7 g/mol (2.3 kDa), a pI of pH 10 and a net charge of + 3.5 at pH 7 (Table III.4-1; Coelho, 2017).

In this work, circular dichroism (CD) spectral measurements (Figure III.4-3A) indicated that the peptide adopted a randomly coiled structure in solution.

To evaluate the anticancer potential of the CT-p19LC peptide, MTT cell proliferation and apoptosis assays were carried out. For this, the spectrum of cell lines used was expanded by adding the HeLa (cervix) and HT-29 (colorectal) cancer cell lines to the A549 (lung) and MCF-7 (breast) cancer cells, and the 16HBE14o- (bronchial) and MCF10A (mammary gland) non-cancer cell lines.

First, the MTT cell proliferation assays were performed with increasing doses of CT-p19LC (0 to 100 µM; Figure III.4-3B). Comparing it with the CT-p19 treatment that led to a dose-response effect on the lung and breast cancer cell lines (Figure III.4-2), this same effect was only observed at the lowest concentrations of 5, 10 and 20 µM in the case of the CT-p19LC treatment. At higher concentrations of 50 and 100 µM, a stabilization of the decrease in viability was observed. However, we observed that for the concentration of 20 µM of CT-p19LC, the values for the decrease in viability were similar to those obtained with higher concentrations of CT-p19. These results confirmed the anticancer potential predicted *in silico* for CT-p19LC (0.90 vs. 0.99 SVM score; Table III.4-1). The CT-p19LC treatment in the cervix and colorectal cancer cell lines demonstrated that this peptide can exert its anticancer action on a wide spectrum of cancer lines, since a decrease in cell viability of 20-30% was observed (Figure III.4-3B). It is interesting to note that the values of the decrease in viability for the concentration of 20 µM of CT-p19LC in all cancer cell lines were around 20-40%, and to achieve the same decrease with the azurin (Table III.4-1) or p28 peptide treatment (Figure III.4-1), 100 µM would be needed. Furthermore, it was also found that CT-p19LC does not have a cytotoxic effect on the non-cancer cell lines under study (in all concentrations tested, less than a 14% decrease in viability was observed; Figure III.4-3B), which indicates that this peptide also demonstrates selectivity for cancer cells, an important and desired characteristic in the development of new anticancer compounds. The non-toxic effect on non-cancer cells was also supported by the low levels of spontaneous LDH release in cells treated with 100 µM of peptide, in particular for CT-p19LC (Figure III.4-3C)

Second, the apoptosis assays supported the MTT cell proliferation assays. Treating cancer cells with a single dose of CT-p19LC at 20 µM strongly promoted cell death. This concentration was chosen as it corresponded to the maximum anticancer potential, since higher concentrations had no additional impact on cell viability. In A549 cells, there was induction of cell death in 77.8% of the cells, in MCF-7 in 28.8%, in HeLa in 38.5% and in HT-29 in 37.4%, which were comparable to the values in their controls (untreated condition) of 27.4%, 15.7%, 18.4% and 19.2%, respectively (Figure III.4-3D). Importantly, the same was not observed in non-cancer cell lines, since in 16HBE14o- (34.0% control condition vs. 34.2% treatment condition) and MCF10A (7.5% control condition vs. 4.6% treatment condition), cell death was similar to the control condition (untreated), again demonstrating the selectivity of this peptide (Figure III.4-3D). Overall, these results indicate

that CT-p19LC induces a decrease in cell viability *in part* through the induction of cell death.

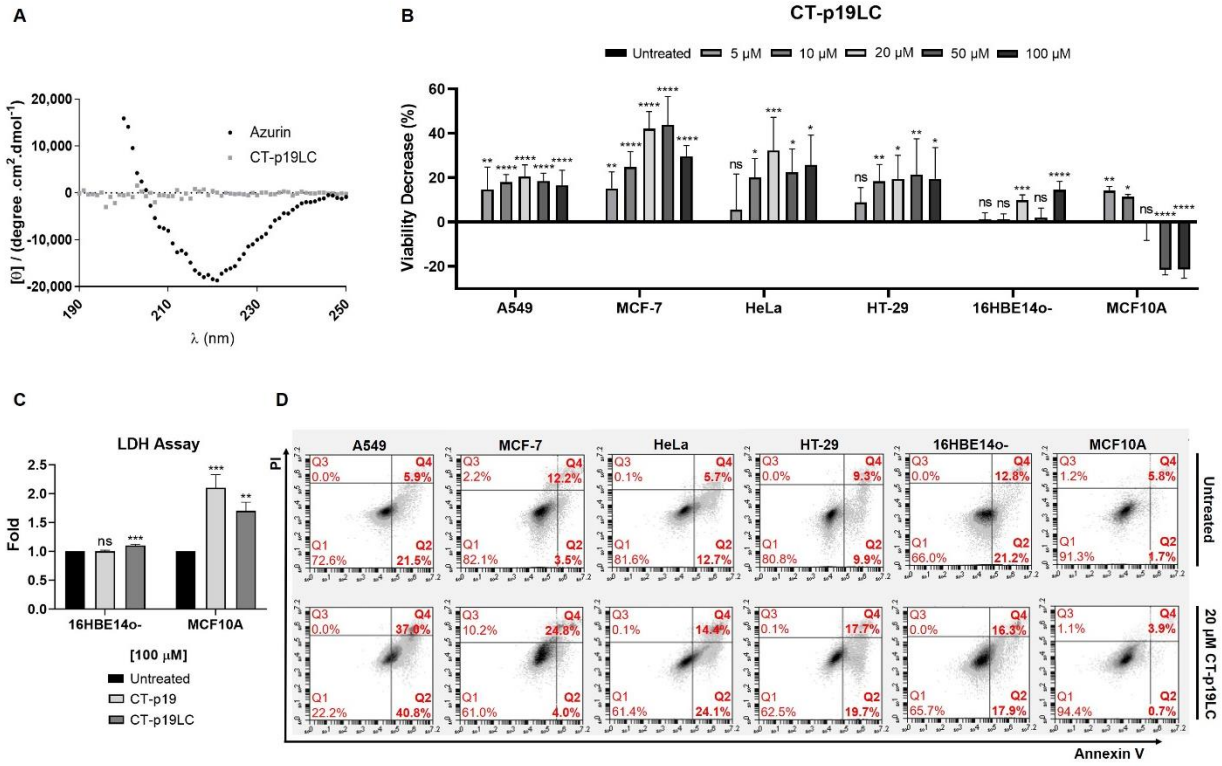

Figure III.4-3: Cytotoxic effect of newly designed CT-p19LC peptide. **A)** Circular dichroism spectra of azurin and CT-p19LC (5 µM) in sodium phosphate buffer 10 mM, pH 7.4, at 25 ºC. **B)** Viability decrease (100% of proliferation in untreated condition - % of proliferation for each treatment condition) of A549 (lung), MCF-7 (breast), HeLa (cervix) and HT-29 (colorectal) cancer cells and 16HBE14o- (bronchial) and MCF10A (mammary gland) non-cancer cells when incubated with different concentrations of CT-p19LC peptide (0 to 100 µM) over 48 h. Untreated condition (control) consisted of cells incubated with medium only. Values represent the means ± SD, and each condition had at least n=3. *, **, ***, **** and ns denote significant differences of p<0.1, p<0.01, p<0.001 and p<0.0001 and differences that were not statistically significant, respectively, when comparing control with treatments. **C)** LDH assay in non-cancer cell lines treated with 100 µM of CT-p19 and CT-p19LC. Values represent the means ± SD (n=3). **, *** and ns denote significant differences of p<0.01 and p<0.001 and differences that were not statistically significant, respectively, when comparing treatments with control. **D)** Apoptosis assay in cancer and non-cancer cells treated with 20 µM of CT-p19LC for 48 h, assessed by flow cytometry. Representative figures showing a population of viable cells in the left lower quadrant (Q1; annexin V-/PI-), early apoptotic cells in the right lower quadrant (Q2; annexin V+/PI-), necrotic cells in the left upper quadrant (Q3; annexin V-/PI+) and advanced apoptotic or necrotic cells in the right upper quadrant (Q4; annexin V+/PI+).

III.4.4. CT-p19LC peptide targets cellular plasma membrane

It is known that the plasma membrane of cancer cells is more anionic at their surface than for non-cancer cells due to its constitution based on negatively charged components (Gaspar *et al.*, 2013; Harris *et al.*, 2013; Leuschner and Hansel, 2005). In addition, one of the mechanisms by which it has been proposed that there is an electrostatic attraction of ACPs towards this cellular barrier of cancer cells is related to the positive charge of these peptides (Gaspar *et al.*, 2013; Teixeira *et al.*, 2012). In the case of the CT-p19LC peptide,

the *in silico* approach established a charge of +3.5 at pH 7 (Table III.4-1; Coelho, 2017). Therefore, we evaluated the capacity of CT-p19 and CT-p19LC to associate to the cancer cell lines using flow cytometry. Cells were treated with 5,6-FAM labeled peptides (5 μM) and left to interact with the cells for 2 h. A stronger association of CT-p19LC was observed for all cell lines compared to CT-p19, which may have contributed to its higher anticancer activity (Figure III.4-4A). We then proceeded to analyze the cellular distribution of this peptide in both cancer and non-cancer cells using fluorescence confocal microscopy (Figure III.4-4B). The peptide was detected both in the plasma membrane and intracellularly distributed, suggesting its capacity to penetrate the plasma membrane and even reach the nucleus, but only in cancer cells. In the non-cancer cell line MCF10A, almost no peptide was detected.

We also evaluated the zeta potential of the live non-cancer and cancer cell lines under study in the presence of increasing concentrations of CT-p19LC peptide (0 to 20 μM). The measurements of the zeta potential allowed the assessment of the electrostatic potential that is triggered after a particle with a certain charge is placed in solution with others (Freire *et al.*, 2011). This concept can be applied to evaluate the interaction of peptides with cell membranes, which results in the alteration of the cell surface electropotential (Domingues *et al.*, 2008). As the concentration of CT-p19LC exposed to cancer cells increased, an increase in the zeta potential was obtained in all cancer cell lines, with this potential reaching positive values for the highest concentration of the peptide (Figure III.4-4C). After treatment with 20 μM of CT-p19LC, the potential of the lung cancer cell line increased from -17.2 ± 2.8 mV to 4.8 ± 7.3 mV; in the case of the breast cancer cell line, it increased from -15.4 ± 4.4 mV to 0.8 ± 5.5 mV; in the cervix cancer cell line, it increased from -15.5 ± 2.2 mV to 1.9 ± 4.8 mV; and, finally, in the colorectal cancer cell line, it increased from -16.6 ± 3.3 mV to 3.0 ± 7.3 mV. These results indicate that this peptide targets the plasma membrane of cancer cells. In the case of the non-cancer cell lines, at the highest concentration used (20 μM), it was found that the potential remained negative and close to the value obtained in the untreated condition (Figure III.4-4C). For 16HBE14o-, before treatment the zeta potential was -11.7 ± 2.9 mV, and it did not change with the treatment (-11.6 ± 4.9 mV). In the case of MCF10A, before treatment the zeta potential was -14.8 ± 3.3 mV, and after treatment it increased only moderately to -9.3 ± 3.2 mV, remaining more negative than that obtained in the same concentration of peptide in cancer cells. Thus, these results show that the CT-p19LC peptide directs itself towards the cancer cell membranes much more strongly than towards non-cancer cell membranes.

To further characterize the effect on the membranes of cancer cells, the membrane order of the plasma membranes subjected to treatment with the CT-p19LC peptide was investigated with the Laurdan probe using two-photon excitation microscopy. To do this, the cancer cells (A549, MCF-7, HT-29 and HeLa) were treated over 2 h with CT-p19LC at 20 µM. To quantify the degree of lipid packing (the measured mean of the GP value) in both conditions (untreated and treated cancer cells), homemade software created in a MATLAB environment was used. The GP value varies between -1 and 1; a GP value higher than 0.5 indicates the existence of very compact and ordered membranes. In contrast, a GP value lower than 0.5 is typically observed for more fluid membranes (Owen *et al.*, 2011; Pinto *et al.*, 2013). As shown in Figure III.4-4D, for the four cancer cell lines the GP values decreased after CT-p19LC treatment, making the cell membranes more fluid (A549: 0.57 to 0.50; MCF-7: 0.53 to 0.48; HeLa: 0.47 to 0.40; HT-29: 0.55 to 0.39). This common pattern indicates that the CT-p19LC peptide acts efficiently at the plasma-membrane level. Fluorescence microscopy images of the cells showed that treated cells suffered a variety of morphological modifications; *i.e.*, the cell shape became irregular and the fragmentation of the plasmatic membrane and the nucleus was visible (Figure III.4-4D).

In general, these results indicate that the CT-p19LC peptide engaged with the plasma membrane, which could trigger the apoptotic events. However, it remains to clarify the possible membrane components that could be targets of CT-p19LC. Further studies with biophysical approaches such as AFM or leakage studies using model membranes (liposomes) are necessary to unravel the mode of action of this peptide against cancer cells.

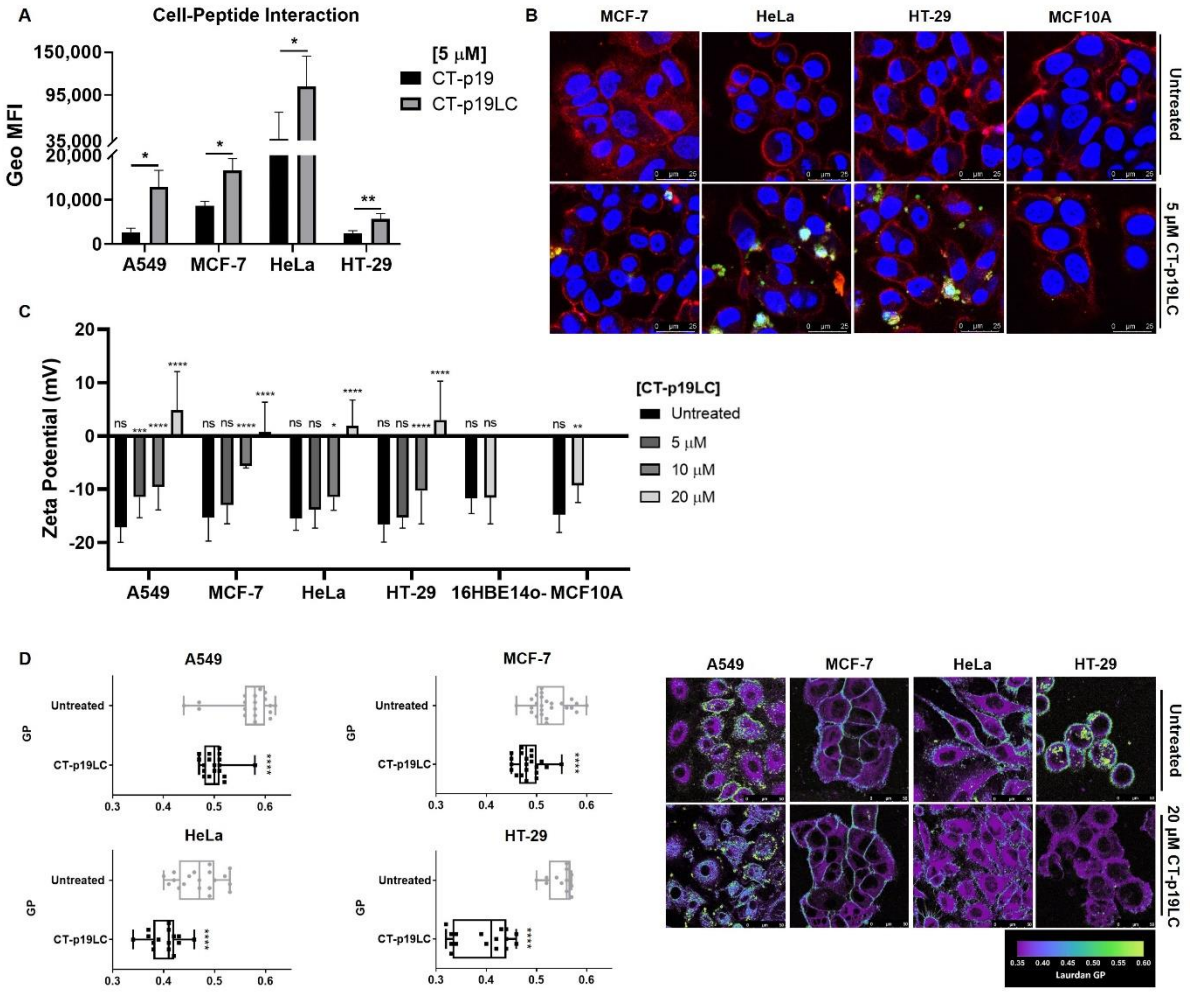

Figure III.4-4: CT-p19LC membrane-active properties. **A)** Flow cytometry quantitative analysis of cancer cell-peptides interaction. Results are reported as the means ± SD, and each condition had at least n=3. * and ** denote significant differences of p<0.1 and p<0.01, respectively, when comparing CT-p19LC treatment with CT-p19 treatment. **B)** Representative confocal microscopy qualitative analysis of CT-p19LC cellular uptake by MCF-7, HeLa and HT-29 cancer cells and MCF10A non-cancer cells incubated with PBS pH 7.4 as control and 5 μM of peptide labeled with 5,6-FAM (green color) for 2 h. WGA Alexa Fluor® 633 and Hoechst 33342, for staining the plasma membrane and nucleus, respectively, are shown in red and blue colors. Scale bars represent 25 μm. **C)** Zeta potential of A549, MCF-7, HeLa and HT-29 cancer cells and 16HBE14o- and MCF10A non-cancer cells in the presence of CT-p19LC peptide. A total of $1.5x10^5$ cells per mL were incubated and stabilized for 30 min at 37 ºC with different peptide concentrations, and the zeta potential was measured. Data are represented as means ± SD. *, **, ***, **** and ns denote significant differences of p<0.1, p<0.01, p<0.001 and p<0.0001 and differences that were not statistically significant, respectively, when comparing the untreated condition (0 μM) with increasing concentrations of CT-p19LC (5, 10 and 20 μM). **D)** The effects of CT-p19LC on the cell's membrane order for A549, MCF-7, HT-29 and HeLa cancer cell lines and their respective GP values. All represented cell lines were seeded on μ-Slide 8-well glass-bottom chambers and treated with 20 μM of CT-p19LC for 2 h. For each condition, 5 μM of Laurdan was used. Untreated cells were used as the control. Homemade software built in a MATLAB environment was used to measure the GP values. Representative Laurdan GP images are shown. Scale bars represent 50 μm. Average GP values are expressed as means ± SD from at least 15 individual cells in each condition. Results are compared to the untreated population with equal variance (****, p<0.0001).

III.5. Conclusions

The CT-p19LC anticancer potential explored in this work reinforces the relevance of studies in other domains of azurin that contain anticancer properties of their own. In an

initial approach, a region of the C-terminal domain of azurin, which was studied in the form of a peptide with 26 residues, CT-p26, was shown to have a similar anticancer potential to the p28 peptide and azurin. From here, the *in silico* redesign of this region made it possible to decrease the length of its peptide chain and increase its anticancer potential, as well as its selectivity for cancer cells through changes in hydrophobicity and net charge, giving rise to a new peptide called CT-p19LC. The results of this work suggest that the CT-p19LC application induced a decrease in the cell viability, *in part* through the triggering of cell death, in all the cancer cell lines under study, without affecting the non-cancer cell lines. In addition to this, it was also demonstrated that this peptide selectively binds to the plasma membranes of cancer cells, since its electrostatic potential is altered, and changes occur at the level of lipid packing. All in all, this study characterizes CT-p19LC as a synthetic ACP with improved and selective anticancer potential and with membrane-active properties.

Acknowledgments

The work was supported by scientific projects PTDC/BTM-SAL/30034/2017_LISBOA-01 0145-FEDER-030034 and SAICTPAC/0019/2015. This work was financed by national funds from Fundação para a Ciência e a Tecnologia (FCT), I.P., in the scope of the projects UIDB/04565/2020 and UIDP/04565/2020 of the Research Unit Institute for Bioengineering and Biosciences (iBB) and the project LA/P/0140/2020 of the Associate Laboratory Institute for Health and Bioeconomy (i4HB). The PPBI-Portuguese Platform of BioImaging (POCI- 01-0145-FEDER-022122) is also acknowledged. Ana Rita Garizo acknowledges a FCT PhD fellowship (SFRH/BD/122636/2016).

IV. P28-FUNCTIONALIZED PLGA NANOPARTICLES LOADED WITH GEFITINIB REDUCE TUMOR BURDEN AND METASTASES FORMATION ON LUNG CANCER

Journal Paper

Garizo AR, Castro F, Martins C, Almeida A, Dias TP, Fernardes F, Barrias CC, Bernardes N, Fialho AM, Sarmento B. 2021. p28-functionalized PLGA nanoparticles loaded with gefitinib reduce tumor burden and metastases formation on lung cancer. *Journal of Controlled Release* **337**: 329-342

| DOI: 10.1016/j.jconrel.2021.07.035

Garizo AR performed experiments, analyzed data, writing-original draft, writing-review and editing

IV.1. Abstract

Lung cancer is still the main cause of cancer-related deaths worldwide. Its treatment generally includes surgical resection, immunotherapy, radiotherapy, and chemo-targeted therapies such as the application of tyrosine kinase inhibitors. Gefitinib (GEF) is one of them, but its poor solubility in gastric fluids weakens its bioavailability and therapeutic activity. In addition, like all other chemotherapy treatments, GEF administration can cause damage to healthy tissues. Therefore, the development of novel GEF delivery systems to increase its bioavailability and distribution in tumor site is highly demanded. Herein, an innovative strategy for GEF delivery, by functionalizing PLGA NPs with p28 (p28-NPs), a cell-penetrating peptide derived from the bacterial protein azurin, was developed. Our data indicated that p28 potentiates the selective interaction of these nanosystems with A549 lung cancer cells (active targeting). Further p28-NPs delivering GEF (p28-NPs-GEF) were able to selectively reduce the metabolic activity of A549 cells, while no impact was observed in non-tumor cells (16HBE14o-). *In vivo* studies using A549 subcutaneous xenograft showed that p28-NPs-GEF reduced A549 primary tumor burden and lung metastases formation. Overall, the design of a p28-functionalized delivery nanosystem to effectively penetrate the membranes of cancer cells while deliver GEF could provide a new strategy to improve lung cancer therapy (Figure IV.1-1).

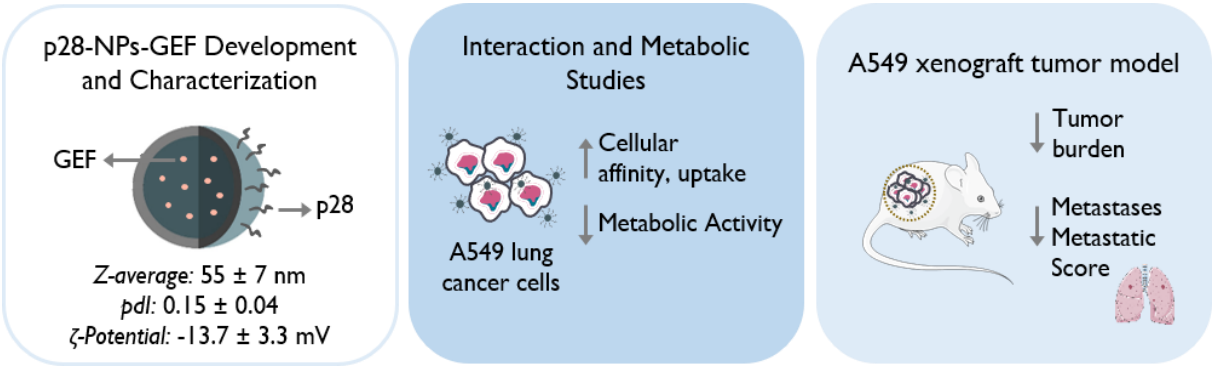

Figure IV.1-1: Graphical abstract.

IV.2. Introduction

Currently, it is recognized that many of the drugs approved for the treatment of numerous diseases, including cancer, may have a low therapeutic efficacy due to their limited ability to reach their target cells, and selectively enter them to achieve their intracellular targets (Silva *et al.*, 2019). This restriction prompted the development of new delivery strategies

for targeted and controlled release of drugs in an attempt to enhance their benefits for patients.

CPPs offer great potential to deliver therapeutic molecules to unreachable intracellular targets, crossing cell membranes without compromising their integrity (Agrawal *et al.*, 2016; Gomes Dos Reis and Traini, 2020; Kalmouni *et al.*, 2019). However, many CPPs are inefficient, and often demonstrate poor bioavailability, low stability, short half-life in *in vivo*, and remain frequently trapped within endosomes with their cargo (Hoffmann *et al.*, 2018). Their conjugation to the surface of NDDSs helps to fill the gap of their individual use for anticancer drug delivery (Silva *et al.*, 2019). These nanosystems can escape endosomal degradation, and may have in their composition hydrophilic polymers, such as PEG, which allows to prolong their plasma circulation time and reduce immunogenicity (Cupic *et al.*, 2019; Davis, 2002; Reissmann, 2014). In addition, the nanosystem itself acts on the form of a passive tumor targeting strategy by the EPR effect. Thus, through the functionalization of these nanocarriers with CPPs, an active tumor targeting strategy is promoted, benefiting of the passive targeting to accumulate into the tumor region, and subsequently binding to the target cells using these biological targeting agents (Danhier *et al.*, 2010). Therefore, this combination potentiates the development of a novel strategy that has greater efficiency, accuracy and therapeutic activity (Silva *et al.*, 2019).

This work proposes the development of a NDDS based on PLGA-NPs functionalized with an azurin-derived peptide termed p28. PLGA is a biodegradable and biocompatible polymer approved by the FDA and the EMA, that can be used for the production of polymeric NPs. Nowadays, polymeric NPs are among the most used NDDSs due to their attractive properties for DL and delivery. PLGA can be chemically modified, before or after NPs production, to give biofunctionality for active targeting (Kim *et al.*, 2019; Martins *et al.*, 2018; Mir *et al.*, 2017). Such biofunctionalization can be carried out, for example, with antibodies, dendrimers, aptamers, carbohydrates and peptides (Mout *et al.*, 2012). Among them, p28 (28 amino acids; 2.8 kDa), a CPP derived from the bacterial protein azurin (128 amino acids; 14 kDa), is an interesting molecule for NDDSs, due to preferential tumor cell internalization (tumor homing peptide) and anticancer activities (Bernardes and Fialho, 2018; Bernardes *et al.*, 2016; Chakrabarty *et al.*, 2014). It is known that the N-terminal of this CPP is responsible for its penetrating capacity in human cancer cells (Taylor *et al.*, 2009; Yamada *et al.*, 2005). When entering the nucleus of cancer cells, p28 can bind to the DNA-binding domain of the tumor-suppressor protein p53, inhibiting its proteasomal degradation, which consequently promotes apoptosis (Yamada *et al.*, 2009; Yamada *et*

al., 2013a; Yamada *et al.*, 2013b). It has also been reported that this peptide can inhibit cancer-induced angiogenesis by reducing the VEGFR-2 tyrosine kinase activity (Mehta *et al.*, 2011). In addition, p28 is an enhancer and anticancer agent transporter. In combination with lower concentrations of anticancer drugs, p28 increased cytotoxicity by activating p53 and its related pathways (Yamada *et al.*, 2016), and can also be fused to other peptides or compounds to form chimeric proteins, emerging as new therapeutic strategies for targeted cancer therapy (Noei *et al.*, 2019; Raber *et al.*, 2020; Soleimani *et al.*, 2019). Importantly, p28 CPP has already finished two phase I clinical trials (NCT00914914; NCT01975116), in adult and pediatric tumors with promising results, being defined by the FDA as an orphan drug (IND 77.754; Lulla *et al.*, 2016; Warso *et al.*, 2013).

In addition, these PLGA NPs were loaded with the TKI GEF (N-[3-chloro-4-fluorophenyl]-7-methoxy-6-[3-morpholin-4-ylpropoxy]quinazolin-4-amine; $C_{22}H_{24}ClFN_4O_3$), which is used to treat various solid tumors expressing the EGFR, such as lung cancer (Pirker, 2020). Approximately 2.1 million people are diagnosed, and about 1.8 million dies from this disease each year (Bray *et al.*, 2018). The lung cancer treatment with commercial tablets of this drug called Iressa® is limited, mainly because of their poor solubility in aqueous medium (logP value of GEF: 4.2), which consequently leads to dose-related adverse effects, such as severe toxicity and development of MDR (Inoue *et al.*, 2003; Yu *et al.*, 2013). The desired bioavailability can be achieved by reducing the size of this compound to a nanoscale when introducing them into NDDSs (Da Silva *et al.*, 2017; Jahan *et al.*, 2017; Su *et al.*, 2018).

In the present study, a nanosystem (p28-NPs-GEF) was developed in which p28 will favor the internalization of the nanosystem in lung cancer cells, where GEF will be released to exert its therapeutic activity. Here, we reported the PLGA NPs preparation and characterization, the ability to interact with A549 lung cancer cell line and 16HBE14o- bronchial non-cancer cell line, and its anti-proliferative effect. A proof-of-concept of the p28-NPs-GEF therapeutic potential was established using the A549 xenograft tumor model.

IV.3. Materials and Methods

IV.3.1. Materials

For the NPs production and characterization, the core PLGA (50:50 LA:GA; 44 kDa; Purasorb® PDLG 5004A) was kindly provided by Corbion; PLGA (30 kDa)-PEG (5 kDa)-

maleimide (PLGA-PEG-Mal) and PLGA labelled with FKR648 or FITC (PLGA-FL) were purchased from Polyscitech/Akina®; GEF from Santa Cruz Biotechnology®, and p28 peptide (Sequence: LSTAADMQGVVTDGMASGLDKDYLKPDDC) from PepMic Co, Ltd; Tween® 80, sodium chloride, ammonium formate, formic acid, tris(2-carboxyethyl)phosphine (TCEP), and diethyl ether from Sigma-Aldrich®; acetonitrile (ACN), Amicon® centrifugal filters (100kDa), LiChrospher 100 RP-18 column (5 µm, 4.6 × 250 mm) and LiChrospher 100 RP-18 guard column from MERCK®; dimethylformamide (DMF) and trifluoroacetic acid (TFA) from Acros Organics. Ultrapure water was prepared in-house with a conductivity of 0.055 µS/cm and a resistivity of 18.2 MΩ.cm, using MilliQ® station from Millipore Corporation.

For the cell culture, T flasks were acquired from Orange Scientific; DMEM, MEM, FBS and TrypLE™ Express from Gibco®, ThermoFisher; penicillin and streptomycin from Invitrogen; L-glutamine from Sigma-Aldrich®.

For the cellular studies, paraformaldehyde (PFA) was purchased from MERCK®; WGA Alexa Fluor® 594 and Hoechst 33342 from ThermoFisher; Resazurin and Triton X-100 from Sigma-Aldrich®.

IV.3.2. Methods

IV.3.2.1. p28 peptide conjugation to the PLGA-PEG-Mal polymer

In order to conjugate the p28 to the PLGA-PEG-Mal polymer, the Maleimide-Thiol click chemistry was selected to covalently link the thiol (SH) group present in the cysteine of the C-terminal p28 peptide to the Mal molecule of the polymer (Werengowska-CieTwierz *et al.*, 2015). This cysteine is not part of the original p28 peptide amino acid sequence, it was inserted during commercial peptide synthesis for this purpose. Briefly, 15 mg of PLGA-PEGMal (35 kDa) was dissolved overnight in 1 mL of anhydrous DMF under an inert atmosphere (N_2). To guarantee the presence of the free SH groups, TCEP was added to the p28 (1:1 M ratio), and incubated for 1 h at room temperature before addition to the polymer. For this, from a 5.2 mM of TCEP stock solution in anhydrous DMF, 127 µL of this solution was added to 663 µM of p28 in anhydrous DMF under an inert atmosphere (N_2). In order to allow the formation of a covalent bond between the free SH group of p28 and free Mal molecule at the terminal distal ends of the cross-linker PLGA-PEG-Mal, the p28 peptide/TCEP solution and the PLGA-PEG-Mal solution (1.5:1 M ratio) were mixed together followed by mild magnetic stirring at 4 ºC overnight under an inert atmosphere (N_2). This polymer was also subjected to this process, but without the addition of p28 as a

control. To remove the non-conjugated peptide, PLGA-PEG-Mal-p28 was precipitated with cold diethyl ether (16 mL) and centrifuged at 3200 x*g* for 5 min. The supernatant was collected, and this was repeated one more time with a sonication (3 min) between each polymer precipitation. In addition, the PLGA-PEG-Mal-p28 was washed three times with MilliQ® ultrapure water (5 mL). Finally, this conjugate was lyophilized and stored at -20 ºC until NPs production.

IV.3.2.1.1. p28 peptide conjugation efficiency

The amount of p28 conjugated to PLGA-PEG-Mal polymer was estimated indirectly. This was calculated by the difference between the total amount of peptide used in the reaction and the amount of peptide detected in the supernatants resulting from the polymer precipitation steps as described in the following equation (das Neves and Sarmento, 2015):

$$Conjugation\ efficiency\ (CE;\ \%) = \frac{Initial\ mass\ of\ p28 - Mass\ of\ recovered\ p28}{Initial\ mass\ of\ p28} x100$$

p28 quantification was determined by reversed-phase high-performance liquid chromatography (HPLC) with ultraviolet (UV) detection using a Hitachi LaChrom Elite® HPLC System (Hitachi High Technologies America, Inc). A LiChrospher 100 RP-18 column (5 µm, 4.6 × 250 mm) with LiChrospher 100 RP-18 guard column was used as stationary phase. Chromatographic runs were performed using a gradient method, according to the peptide's manufacturer instructions. The mobile phase used was ACN:water with 0.1% of TFA. The flow rate was 1 mL/min and sample detection was performed at 220 nm. The column temperature was kept at 25 °C, the run time was 50 min, and the injection volume was 90 µL. A calibration curve of p28 dissolved in water was produced using concentrations from 3 to 400 µg/mL. All samples were run at least in triplicate, and the total area of the peak was used to quantify the p28 peptide mass.

IV.3.2.2. Preparation of p28-functionalized PLGA nanoparticles loaded with gefitinib

p28-functionalized GEF-loaded PLGA NPs (p28-NPs-GEF) were prepared by nanoprecipitation as previously described by Fessi *et al.* 1989. Briefly, the organic phase consisted on 16 mg of PLGA, 4 mg of PLGA-PEG-Mal-p28 and 1.1 mg of GEF dissolved in 3 mL of DMF. To produce the NPs, this phase was directly injected with a needle (25 G)

into the aqueous phase consisting on 10 mL of 1% Tween® 80, under constant magnetic stirring (200 rpm) at room temperature. The final solution was left for 3 h to allow the organic phase evaporation. To remove the non-incorporated drug and the surfactant of the aqueous phase, the obtained colloidal solution was washed three times with MilliQ® ultrapure water and recovered by ultrafiltration (600 x*g*; 4 ºC; Eppendorf Centrifuge 5804R) using Amicon® centrifugal filter units with a molecular weight cut-off (MWCO) of 100 kDa. Finally, this solution was stored at 4 ºC. Empty and non-functionalized NPs (NPs-0) were prepared according to the same procedures in the absence of drugs and p28 functionalized. NPs only loaded with GEF (NPs-GEF) and NPs only functionalized with p28 (p28-NPs) were also produced in the same conditions but with PLGA-PEG-Mal without p28 and without drug encapsulated, respectively. The labeled NPs were also prepared using the same production method, with 2 mg of PLGA-FKR648 (10%) or 6 mg of PLGA FL (30%), adjusting the final composition of the nanosystem to 20 mg of polymer (100%).

IV.3.2.3. Characterization of nanoparticles

IV.3.2.3.1. Average particle size, size distribution and surface charge

All the formulations of NPs were characterized for their average size (Z-average) and polydispersity index (PDI) by DLS, and ζ-potential through LDA, using a Malvern Zetasizer Nano ZS instrument (Malvern Instruments Ltd). For these, samples were diluted (1:100, v/v) in an ionic solution of 10 mM sodium chloride (NaCl) pH 7.4, and three measurements were taken for each of NP formulations. Values reported are the mean ± SD of at least three different formulations batches.

IV.3.2.3.2. Gefitinib association efficiency and drug loading

To determine the association efficiency (AE) and DL of the established nanosystems, the amount of GEF associated to NPs was indirectly estimated. This calculation was made by the difference between the total amount of this drug used to prepare the nanocarriers and the amount of this drug detected in the supernatants resulting from NPs washes. The values of AE and DL were calculated using the following equations (das Neves and Sarmento, 2015):

$$AE\ (\%) = \frac{Initial\ mass\ of\ GEF - Mass\ of\ recovered\ GEF}{Initial\ mass\ of\ GEF} x100$$

$$DL\ (\%) = \frac{Initial\ mass\ of\ GEF - Mass\ of\ recovered\ GEF}{Initial\ mass\ of\ GEF + Total\ mass\ of\ NPs}$$

GEF quantification was determined by reversed-phase HPLC with UV detection using a Hitachi LaChrom Elite® HPLC System (Hitachi High Technologies America, Inc). A LiChrospher 100 RP-18 column (5 µm, 4.6×250 mm) with LiChrospher 100 RP-18 guard column was used as stationary phase. The chromatographic runs were performed using an isocratic method, and the mobile phase used was ACN:40 mM of ammonium formate buffer (30:70, v/v; pH 2.5 adjusted with formic acid) at a flow rate of 1 mL/min. The samples were measured at 248 nm (Sree *et al.*, 2017). The column temperature was kept at 25 °C, the run time was 10 min, and the injection volume was 20 µL. A calibration curve of GEF dissolved in ACN was produced using concentrations from 1 to 100 µg/mL. All samples were run at least in triplicate, and the total area of the peak was used to quantify GEF AE and DL.

IV.3.2.3.3. Morphology and chemical screening

The morphological features of NPs were analyzed by TEM with a JEOL JEM 1 400 microscope (JEOL Ltd) at an accelerating voltage of 120 kV. The energy-dispersive X-ray spectra (EDS) were collected for chemical analysis, namely to identify the sulfur (S) element of the cysteine previously inserted in the peptide chain of p28, and consequently to verify the presence of this peptide. Images were digitally recorded using a Gatan SC 1100 ORIUS CCD camera (Gatan Inc). NPs colloidal solutions were prior diluted thirty times in MilliQ® ultrapure water, and were prepared by dropping 10 µL onto a 300-mesh nickel grid. The excess was wiped out with filter paper, and the samples on the grid were stained with lanthanum.

IV.3.2.3.4. Colloidal stability of nanoparticles

To confirm the stability of these nanosystems in cell culture medium, 4 mg of NPs were dispersed in 1 mL of cell culture medium for 72 h at 37 °C. At each time point (0, 4, 24, 48 and 72 h), samples were collected (200 µL) and diluted in an ionic solution of 10 mM sodium chloride pH 7.4 for measuring Z-average and PDI. ζ-potential was only measured at 0 and 72 h. All the experiments were conducted in triplicates.

IV.3.2.4. Gefitinib *in vitro* release study

In vitro release behavior of GEF from NPs-GEF was performed at 37 ºC under gentle stirring rate of 150 rpm in PBS (pH 10, 7.4, 6.5 and 5) containing 0.1% Tween® 80. Typically, 1 mg/mL of NPs were suspended in release medium in aliquots. At predetermined time intervals (0, 1, 2, 3, 4, 16, 24, 48 and 72 h), aliquots were centrifuged

at 14000 x*g* during 20 min (4 ºC), and the supernatant was used for HPLC, as previously described.

IV.3.2.5. Human cell lines and cell culture

A549 adenocarcinoma human alveolar basal epithelial cancer cell line (European Collection of Authenticated Cell Cultures) and 16HBE14o- human bronchial epithelial cell line (Cozens *et al.*, 1994) were used. A549 cancer cells were cultured in cell culture flasks in DMEM, supplemented with 10% (v/v) of heat-inactivated FBS, 100 IU/mL penicillin and 100 mg/mL streptomycin. 16HBE14o- non-cancer model was maintained in fibronectin-collagen I-coated flasks in MEM supplemented with 10% (v/v) FBS, 0.292 g/L L-glutamine, 100 IU/mL penicillin and 100 mg/mL streptomycin. These cell lines were passed between 2 to 3 times per week, using TrypLE™ Express to detach them from the flasks. Cells were grown at 37 ºC in a humidified chamber containing 5% of CO_2 (Binder CO_2 incubator C150). Mycoplasma detection was routinely performed to ensure no contamination.

IV.3.2.6. Quantitative cellular association

In order to evaluate the cell-NPs interaction, A549 and 16HBE14o- cell lines were plated in 6-well plates with $5x10^5$ and $1x10^6$ cells per well, respectively, left to adhere and grow overnight in a CO_2 incubator (5%) at 37 ºC. The following day, medium was removed, cells were washed once with PBS pH 7.4 and treated with non-functionalized (nf-NPs) and functionalized NPs (p28-NPs) with 10% of PLGA-FKR648 at various concentrations (50, 100, 250 and 500 µg/mL) in serum-free medium during 4 h at 37 ºC. After treatment, cells were washed twice with PBS, detached with TrypLE™ Express at 37 ºC, and resuspended in medium before fixation with 2% of PFA in PBS during 30 min at room temperature. PFA was removed through centrifugation at 1200 rpm during 3 min, after which cells were again washed twice with PBS, re-dispersed in 350 µL of PBS and stored at 4 ºC until sample analysis. To distinguish internalization from NPs association, cells were also washed with an acid wash buffer (0.5 M NaCl, 0.2 M acetic acid) to remove membrane-bound NPs (Costa Verdera *et al.*, 2017). The quantification of NPs interaction to the cells was done using a BD Accuri™ C6 Plus Flow Cytometer (BD Biosciences), where NPs were detected through the allophycoerythrin (APC) channel (FL4 detector, 675/700 nm; laser configuration of 3-blue 1-red, laser 640 nm). Measurements were carried out in triplicate and 50000 events were acquired in the gated region of the forward-scatter/side scatter plot per sample. A control based only on cells without NPs was also performed to exclude the possible cellular autofluorescence. The results were analyzed using the software FlowJo

v10 by gating out cellular debris and doublets, and expressed as the Geo MFI. To compare this treatment between the two cell lines under study, the ΔGeo MFI was calculated and corresponds to the difference between the Geo MFI of p28-NPs treatment and nf-NPs treatment without and with acid wash.

IV.3.2.7. Nanoparticles cellular uptake

In order to characterize the cellular uptake of the p28-NPs, 16HBE14o- or A549 cells were seeded on µ-Slide 8 well glass bottom chambers (ibidi®) with $7.5x10^4$ and $2.5x10^4$ cells per well, respectively. These cells were left to adhere and grow overnight in a CO_2 incubator (5%) at 37 ºC. In the next day, medium was collected, cells were treated with 500 µg/mL of non-functionalized (nf-NPs) and functionalized NPs (p28-NPs) with 30% of PLGA-FL in serum-free medium, and incubated for 4 h and 24 h at 37 ºC. Afterwards, cells were washed with PBS pH 7.4, and Alexa Fluor® 594 WGA (1:200), and Hoechst 33342 (1:2000) were added to stain the plasma membrane and nuclei, respectively, followed by 15 min of incubation. The interaction between NPs and cells was observed in a Leica TCS SP5 confocal inverted microscope (Leica Microsystems CMS GmbH; model no. DMI6000) with a 63.3x water-immersion apochromatic objective (1.2-numerical-aperture). FITC excitation was performed using a 488 nm line of an Argon ion laser and fluorescence emission was collected at 500-575 nm using the tunable system and beam splitter of the Leica TCS SPC5. In relation to Alexa Fluor® 594 WGA fluorescence, the same was performed using a 514 nm line, and the emission was collected at 600-750 nm. For measurement of Hoescht 33342 fluorescence, the sample was excited by two-photon excitation at 780 nm with a Ti:sapphire laser (Spectra-Physics Mai Tai BB, 710e990 nm), while emission was collected within the 400-520 nm range. The laser light intensity was controlled by an acoustic-optical filter system. Images were collected with a resolution of 1024x1024 pixels at a scan rate of 100 Hz per frame.

IV.3.2.8. Cell viability assay

A549 and 16HBE14o- cells were seeded in 96-well plates (n=5 technical replicates x 3 biological replicates) with a density of $1x10^4$ A549 cells per well and $7.5x10^4$ 16HBE14o- cells per well, and left to adhere and grow overnight in a CO_2 incubator (5%) at 37 ºC. In the next day, medium was collected and cells were treated with various types of NPs in complete medium in increasing drug doses. A negative control (NC), consisting on cells incubated with 1% of Triton X-100 in medium (0% of metabolic activity), and a positive control (PC), consisting on cells incubated only with medium (100% of metabolic activity),

were also prepared and treated similarly to the sample wells. The plates were placed for 72 h at 37 ºC. After this incubation, the medium was removed, 10% (v/v) of Resazurin reagent in serum-free medium were added to each well and incubated at 37 ºC for 1.5 h. The fluorescence levels following resazurin reduction into resorufin were measured at an excitation wavelength of 530 nm and an emission wavelength of 590 nm, using the FilterMax™ F5 Multi-Mode Microplate Reader (Molecular Devices LLC). Metabolic activity is expressed based on the following equation:

$$Metabolic\ Activity\ (\%) = \frac{Fluorescence\ signal\ of\ treated\ cells - Fluorescence\ signal\ of\ NC}{Fluorescence\ signal\ of\ PC - Fluorescence\ signal\ of\ NC} x100$$

IV.3.2.9. *In vivo* studies

All animal experiments were performed in strict accordance with the recommendations of the European Union Directive 2010/63/EU, following a protocol previously approved by the i3S Ethics Committee and Direção-Geral Alimentação e Veterinária (reference 2017_10) concerning the humane endpoints, appropriate husbandry and protection of experimental animals. At the defined endpoints, mice were euthanized by cervical dislocation by trained personal, certified by the Portuguese Direção-Geral de Alimentação e Veterinária, to minimize animal suffering.

N:NIH(S(II-nu/nu) mice were developed by successive crossings and backcrossings between athymic nu/nu mice, on an N:NIH(S) background, and female CBA/N mice that have an X-linked immune defect in B-lymphocyte function (Azar *et al.*, 1980). Female N:NIH(S(II-nu/nu) mice aged 4-6 weeks and weighing 16-20 g were breed and cared at the i3S Animal Facility (Porto, Portugal). To generate tumor xenografts, animals were subcutaneously injected into the right flank of the mice, with $2.5x10^6$ A549 cells, resuspended in 100 µL serum-free DMEM in Matrigel matrix (1:1) (Corning). When the tumor volumes reached 133.3 ± 27.1 mm^3, A549 xenograft mice were randomized into 5 groups (n=6 per group) and treated with 100 µL of (a) saline (CTR); (b) p28-NPs (2 mg/mL); (c) NPs-GEF (2 mg/mL); (d) p28-NPs-GEF (2 mg/mL) or free GEF at the same concentration as encapsulated in NP (11 µg/mL; total dose: 0.33 mg/kg mice). Animals were subcutaneously or intravenously injected at the tumor site, 6 times along 2 weeks. Tumor volume was measured using a caliper and calculated as (length x width x width)/2 (mm^3) and was normalized considering its volume prior to any treatment.

IV.3.2.10. Histology

Lungs were fixed for 24-48 h in formalin at room temperature. Afterwards, these organs were embedded in paraffin, sectioned into 3 µm thickness sections, and stained with hematoxylin and eosin. The metastatic score was made along the initial plans of the distinct lung lobules. Such score considered the presence or absence of metastatic foci and their size as: absence of foci (score I), small foci (score II), intermediate foci areas (score III) and large metastasized areas (score IV). 5-6 animals per group were analyzed.

IV.3.2.11. Statistical analysis

Statistical analysis was performed using the GraphPad Prism 8.0.1 (GraphPad Software Inc). Statistical significance of the difference between two groups was evaluated by the Student's *t* test. Differences between more than two groups were compared using one-way analysis of variance (ANOVA) Tukey's multiple comparisons test. Results are expressed as mean ± SD and geometric means with 95% confidence intervals. For *in vivo* studies, nonparametric unpaired Kruskal Wallis test followed by Dunn's multiple comparison test was used for non-paired comparisons of more than two groups. For tumor growth kinetic curves, two-way ANOVA with Geisser-Greenhouse correction, followed of Tukey´s multiple comparison test was performed. Statistical significance was considered when *p<0.05, **p<0.01, ***p<0.001, ****p<0.0001. Survival curve analysis was performed by Log Rank (Mantel-Cox) test.

IV.4. Results

IV.4.1. Preparation and characterization of p28-functionalized PLGA nanoparticles loaded with gefitinib

In a first approach, for the preparation of p28-NPs, we initially produced the PLGA NPs, and then proceeded to their functionalization with p28 through Maleimide-Thiol click chemistry. However, the CE of a control made up of NPs without the Mal molecule (PLGA-PEG) demonstrated that p28 adsorption occurred on the NPs surface, since the CE values of these nanosystems reached 50-60% (Table VIII.2-1). This result indicated that, in the case of NPs with the Mal molecule (PLGA-PEG-Mal), there may not be a covalent bond that favors the intended orientation of the functionalized peptide on its surface. Thus, it was stablished that p28 was first conjugated to the PLGA-PEG-Mal polymer through

Maleimide-Thiol click chemistry, and then NPs was produced. The reaction efficiency of p28 to PLGA-PEG-Mal was around 74 ± 12% (Figure IV.4-1).

For the p28-NPs-GEF production, nanoprecipitation was chosen because it is the most common technique used to encapsulate hydrophobic drugs (logP value of GEF: 4.2) in polymeric matrices (Figure IV.4-2A; Rivas *et al.*, 2017). A NPs-GEF production design was performed to achieve the highest possible AE and DL with appropriate physico-chemical characteristics (Tables VIII.2-2 and -3). Upon this optimization process, the p28-NPs-GEF

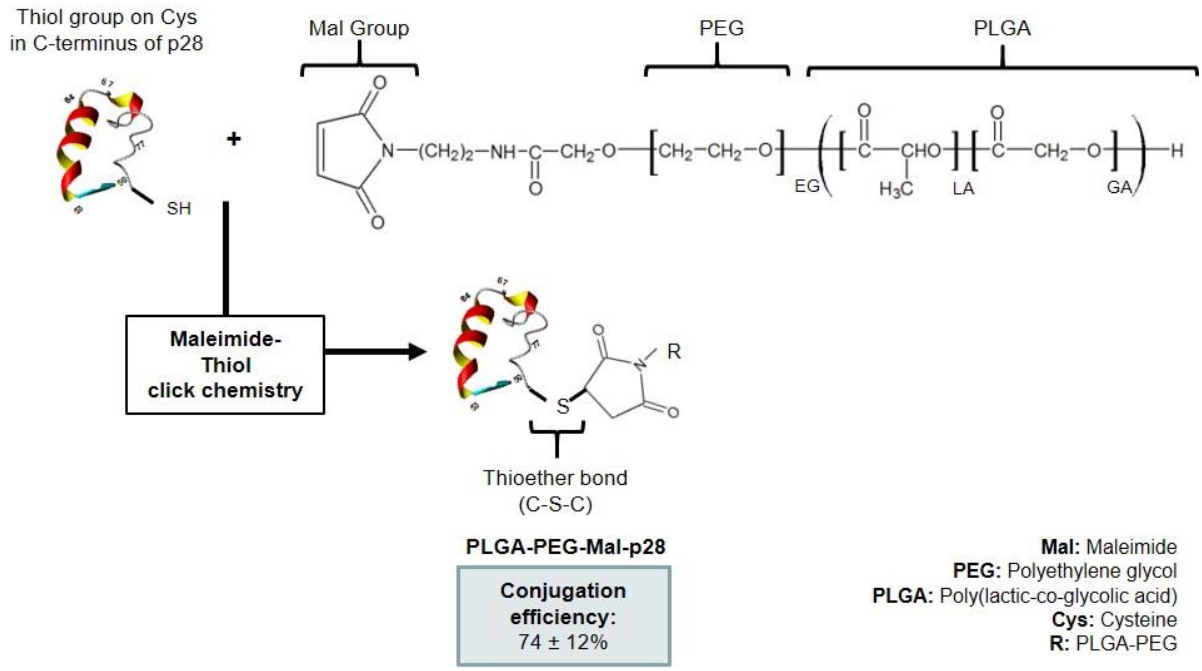

Figure IV.4-1: Scheme of the p28 peptide to the PLGA-PEG-Mal polymer conjugation by Maleimide-Thiol click chemistry with a conjugation efficiency around 74 ± 12% determined by indirect method HPLC (n=8).

were formulated, and the critical physico-chemical properties such as Z-average size, PDI and surface charge (ζ-potential), AE and DL were evaluated (Table IV.4-1), and their morphology was analyzed (Figure IV.4-2B). The Z-average size was 55 ± 7 nm, the small PDI showed a narrow size distribution (0.15 ± 0.04), and ζ-Potential possessed a net negative charge on their surface (-13.7 ± 3.3 mV), owing to deprotonated carboxylic acid groups of PLGA polymer. It is interesting that in the case of NPs with encapsulated GEF there was a decrease tendency in their particle size compared to the NPs-0. AE and DL were determined indirectly by HPLC and the results are shown in Table IV.4-1. The AE and DL of NPs-GEF and p28-NPs-Gef were 74 ± 5% and 75 ± 11%, and 4 ± 0% and 4 ± 1%, respectively. TEM revealed spherical shaped particles with relatively smooth surfaces, and a uniform size distribution in all samples (Figure IV.4-2B). The EDS analysis detected the S element, present in the cysteine of the p28 C-terminal, in p28-NPs and p28-NPs-

GEF samples (S average atomic: 0.48 ± 0.03 % and 0.32 ± 0.12%, respectively; Table IV.4-1; Figure VIII.2-1). These results confirmed the presence of p28 on the developed p28-NPs and p28-NPs-GEF.

Table IV.4-1: Physico-chemical properties of empty nanoparticles (NPs-0), functionalized unloaded NPs (p28-NPs), gefitinib (GEF) loaded NPs (NPs-GEF), and p28-functionalized GEF-loaded NPs (p28-NPs-GEF) and their association efficiency (AE) and drug loading (DL). Energy-dispersive X-ray spectra (EDS) analysis (average atomic) of p28-NPs and p28-NPs-GEF detect the presence of sulfur (S). Values are presented as mean ± SD (n=3), na: not applicable.

Sample	Z-average (nm)	PDI	ζ-Potential (mV)	AE (%)	DL (%)	S average atomic (%)
NPs-0	74 ± 8	0.11 ± 0.03	-14.5 ± 2.5	na	na	na
p28-NPs	73 ± 6	0.10 ± 0.02	-13.8 ± 2.5	na	na	0.48 ± 0.03
NPs-GEF	59 ± 5	0.13 ± 0.04	-11.6 ± 2.6	74 ± 5	4 ± 0	na
p28-NPs-GEF	55 ± 7	0.15 ± 0.04	-13.7 ± 3.3	75 ± 11	4 ± 1	0.32 ± 0.12

IV.4.2. Colloidal stability of nanoparticles in cell culture medium

Colloidal stability evaluation in cell culture medium (DMEM, supplemented with 10% (v/v) of heat-inactivated FBS, 100 IU/mL penicillin and 100 mg/mL streptomycin) during 72 h at 37 ºC demonstrated that when the NPs were added to medium, in all cases the Z-average size remained almost constant and PDI showed slight variations over time, which may be associated with the aggregation of NPs (Figure IV.4-2C). The ζ-potential of p28-NPs-GEF was -15.5 ± 2.9 mV at the beginning of the assay (t=0), and after 72 h was -14.4 ± 0.9 mV.

IV.4.3. Payload release profile

In vitro GEF release study reported a biphasic pattern consisting of an initial burst release (60-80% in the first hour) followed by a sustained release phase over 72 h in both cases (Figure IV.4-2D). The pH's chosen represent a faster hydrolysis of PLGA (pH 10; Martins *et al.*, 2018), the physiological pH (pH 7.4), the pH of the lung cancer tumor environment (pH 6.5; Hao *et al.*, 2018), and the lysosomal pH (pH 5), but regardless of the pH used, no important differences in the release of this drug were observed.

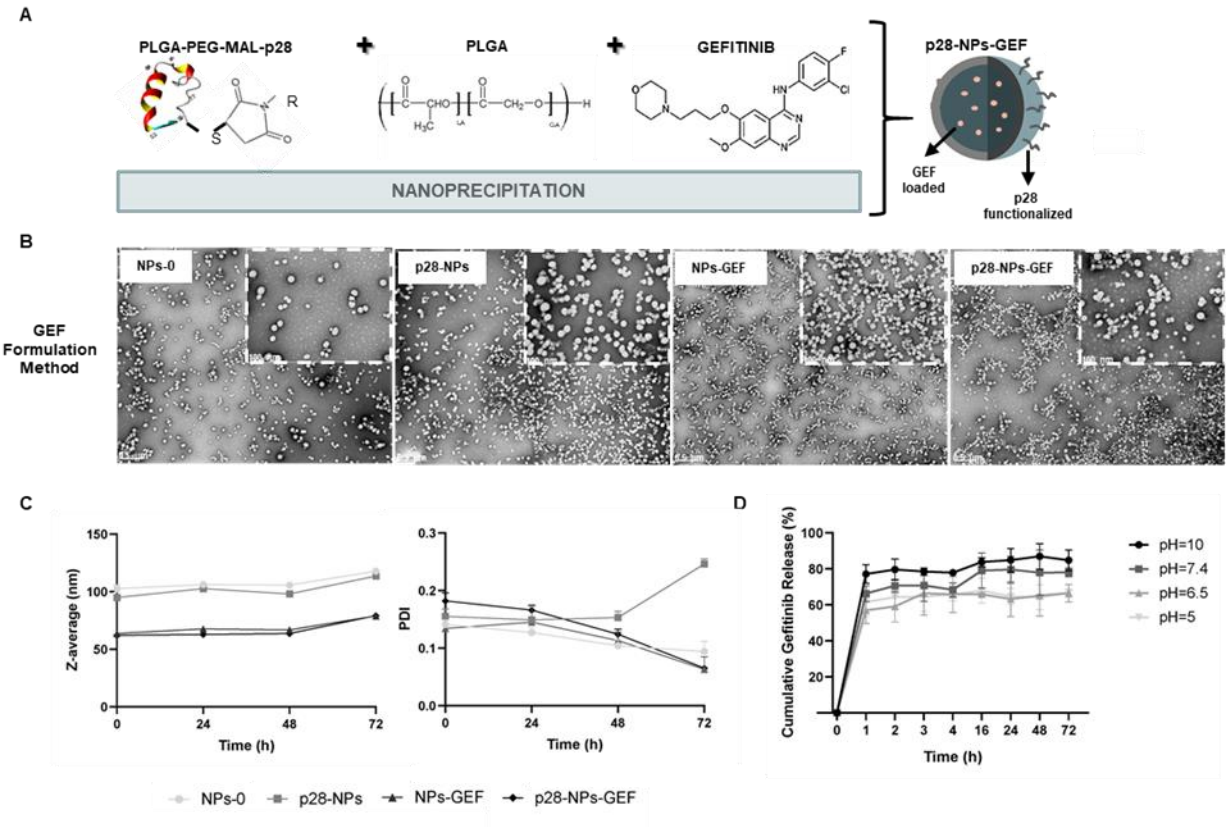

Figure IV.4-2: Physico-chemical characterization and in vitro release of p28-NPs-GEF. **A)** Compounds of p28-NPs-GEF produced by nanoprecipitation. **B)** TEM images of empty nanoparticles (NPs-0), functionalized unloaded NPs (p28-NPs), GEF loaded NPs (NPs-GEF), and p28-functionalized GEF-loaded NPs (p28-NPs-GEF). Scale bars represent 0.5 µm and 100 nm. **C)** Stability of empty nanoparticles (NPs-0), functionalized unloaded NPs (p28-NPs), GEF-loaded NPs (NPs-GEF), and p28-functionalized GEF-loaded NPs (p28-NPs-GEF) in cell culture medium at 37 ºC for 72 h. The size and PdI of the nanosystems were measured over time. **D)** *in vitro* release profile of GEF from PLGA NPs in PBS pH 5, pH 6.5, pH 7.4 and pH 10 added with 0.1% Tween® 80 (v/v) at 37 ºC during 72 h. All measurements were done in triplicate and results are presented as mean ± SD.

IV.4.4. Cell-Nanoparticles interaction studies

The interaction between nf-NPs or p28-NPs with A549 cancer cells and 16HBE14o- non-cancer cells was quantitatively studied through flow cytometry. Cells were treated with increasing NPs concentrations (50, 100, 250 and 500 µg/ml) and incubated for 4 h. These concentrations were established from an A549 cell viability assay that demonstrated that NPs made up only of the PLGA polymer became cytotoxic after treatment with 1 mg/mL of NPs (Figure VIII.2-2). The results of cell-NPs interaction studies were expressed as Geo MFI values, as represented in Figure IV.4-3A. We verified that nf-NPs and p28-NPs can interact with both cell lines, but the cells incubated with p28-NPs had higher Geo MFI values than nf-NPs in all concentrations (Figure IV.4-3A), which means that p28-NPs were more efficient in to interact with cells. As shown in Figure IV.4-3B which represents the

results in each cell line through the ΔGeo MFI (difference between the MFI value of treatment with p28-NPs and nf-NPs), it was found that cell-NPs interaction was always more accentuated in the case of A549 cancer cell line. In addition, it was shown that the interaction was dependent on the NPs concentration applied. The results obtained in the control constituted by the mixture of the free p28 with nf-NPs were similar to the results from treatment with nf-NPs, indicating that the binding of p28 to NPs was essential for them to be directed to cells (Figure IV.4-3A). However, this cytometry study does not distinguish between association of NPs on the cell surface and internalization. Thus, to investigate the NPs internalization, after treatment with these nanosystems, cells were washed with an acid solution of low concentration of acetic acid that allowed the NPs associated by electrostatic and hydrophobic interactions to dissociate, without affecting the signal coming from the NPs that were able to internalize. The results showed, a general decrease in Geo MFI values, but this fluorescence correspond to the NPs internalized, and the same conclusions were reached. Overall, p28-NPs were more internalized (Figure IV.4-3A), and this internalization was higher in the case of cancer cell line (Figure IV.4-3B).

In addition to quantitative analyzes, qualitative analyzes of the interaction of nf-NPs and p28-NPs with A549 cancer cell line and 16HBE14o-non-cancer cell line were also performed by confocal laser scanning microscopy (Figure IV.4-3C). Cells were treated with 500 μg/ml of FITC-labeled NPs and incubated for 4 h and 24 h. An intracellular localization of nf-NPs and p28-NPs was verified, in both cell lines under study. Beyond this, the confocal images seem to show a higher internalization of p28-NPs in cancer cells, which corroborates the above results from flow cytometry studies. Nevertheless, it was not possible to assess if it increases over time.

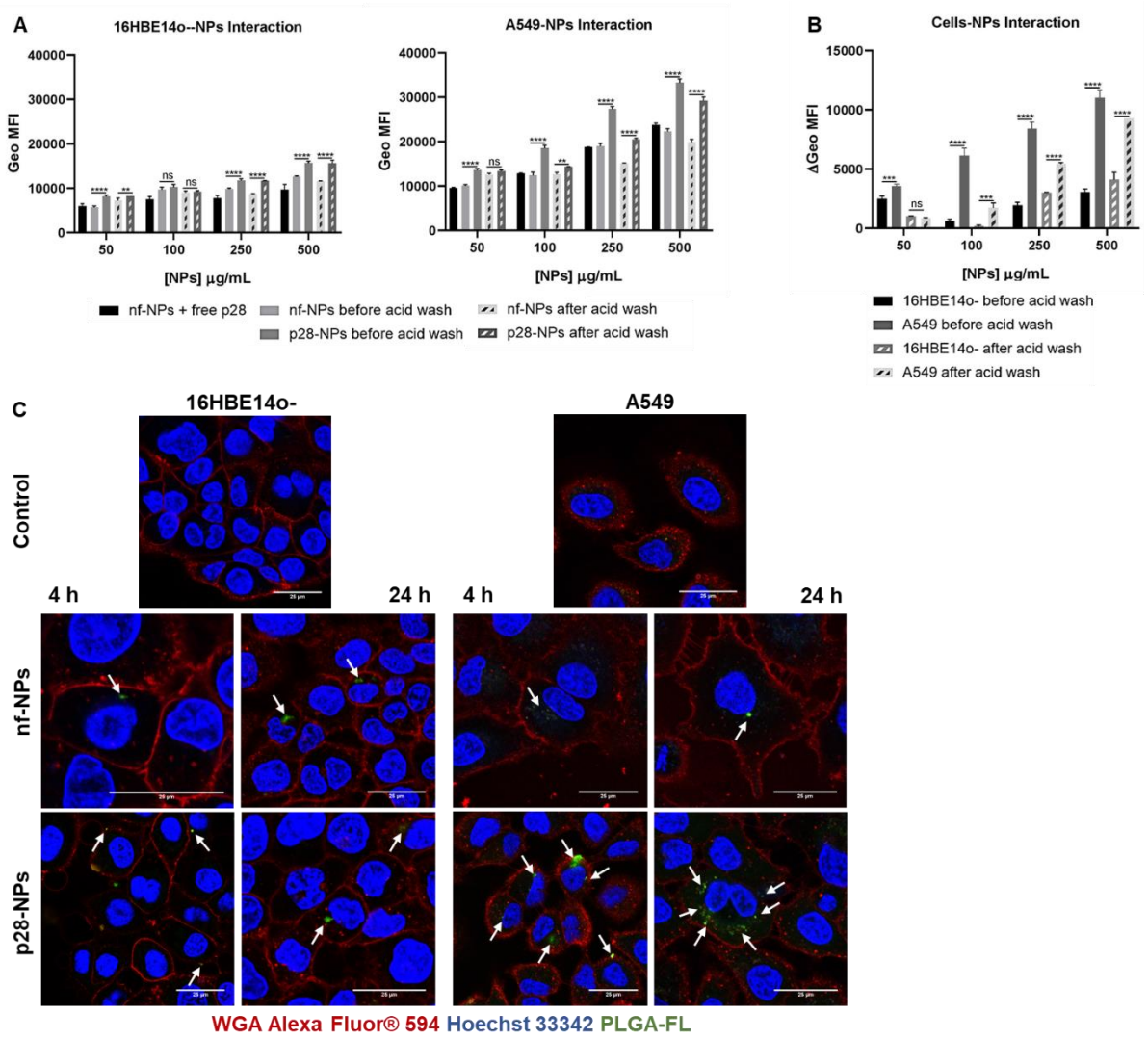

Figure IV.4-3: Cell-NPs interaction/internalization. **A)** Flow cytometry quantitative analysis of cellular association and uptake of non-functionalized NPs (nf-NPs) and p28-functionalized NPs (p28-NPs) by 16HBE14o- cells and A549 cancer cells before and after acid wash. **B)** ΔGeo MFI corresponds to the difference between the mean fluorescence intensity of p28-NPs and nf-NPs without and with acid wash. Results reported the mean ± SD, and each condition has at least an n=3. **, ***, **** and ns denote a significant difference of $p<0.01$, $p<0.001$, $p<0.0001$ and not statistically significant, respectively, when comparing p28-NPs with nf-NPs. **C)** Confocal microscopy qualitative analysis of cellular uptake of non-functionalized NPs (nf-NPs) and p28-functionalized NPs (p28-NPs) by 16HBE14o- cells and A549 cancer cells incubated with PBS pH 7.4 as control and 500 µg/mL of nf-NPs or p28-NPs FITC-labeled (green color) for 4 h and 24 h. WGA Alexa Fluor® 594 and Hoechst 33342 for staining the plasma membrane and nucleus are shown in red and blue colors, respectively. White arrows evidence NPs interaction with cells.

IV.4.5. Effect of p28-functionalized PLGA nanoparticles loaded with gefitinib on metabolic activity

In vitro cell viability evaluation was assessed through a Resazurin assay in A549 cancer cell line and 16HBE14o- non-cancer cell line (Figure IV.4-4). A range of concentrations, in relation to the drug, from 0.01 µM to 5 µM of free GEF, NPs-0, p28-NPs, NPs-GEF and p28-NPs-GEF were tested (in the case of NPs concentration, cells were treated with a maximum of 0.02 mg/mL). The results obtained demonstrated that none of the treatments

in 16HBE14o- non-cancer cells had an effect on their metabolic activity. On the other hand, the treatment in A549 cancer cells revealed a decrease in metabolic activity with increasing concentrations of free GEF (dose-response treatment), exceeding the IC_{50} of this drug after treatment with 5 μM. The treatments with 1.8 μM of free p28 (concentration corresponding to that obtained in the functionalization process), NPs-0 and p28-NPs did not alter the metabolic activity in this cell line. The results obtained from the treatment of the mixture with the free drug and peptide (free p28+GEF) compared to the condition of only free drug, demonstrate similar values of metabolic activity, which again indicated that the treatment with 1.8 μM of free p28 has no influence on this parameter. Regarding the value of the metabolic activity obtained after treatment with the highest concentration of free drug with NPs-0, it was found that this was identical to that obtained in the highest concentration of encapsulated drug, without functionalization. An identical metabolic activity profile was observed in free GEF and NPs-GEF treatments. Lastly, when comparing the p28-NPs-GEF functional nanosystem treatment with NPs-GEF treatment or with free p28+GEF treatment, a significant decrease in metabolic activity (p<0.05) was found in most cases, having registered the biggest decrease of about 37% and 59% in the highest drug concentration applied (5 μM of GEF), respectively (Figure IV.4-4).

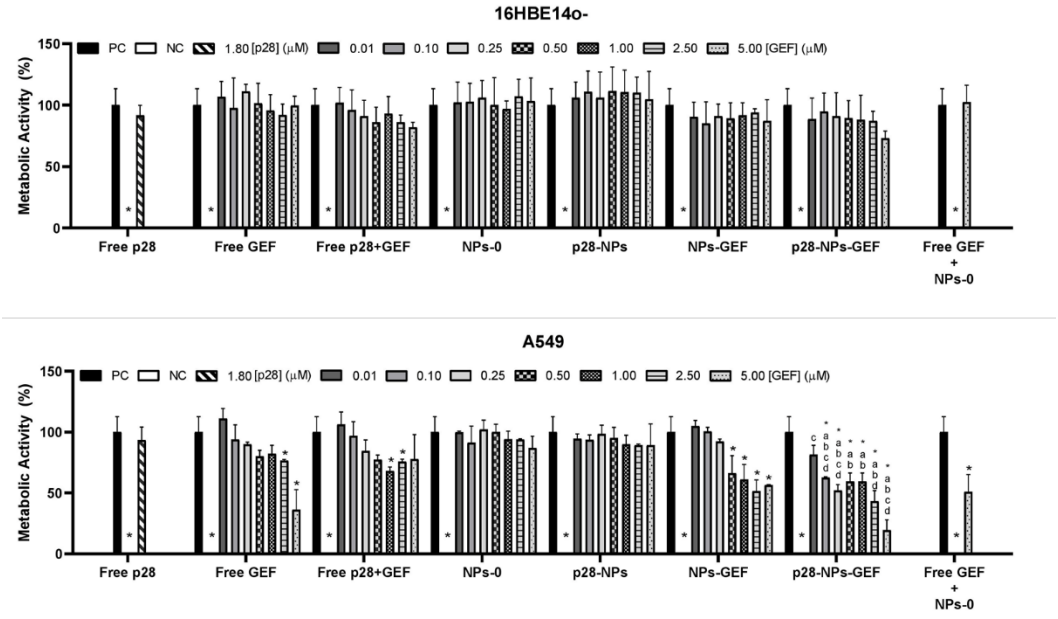

Figure IV.4-4: Metabolic activity of 16HBE14o- non-cancer cells and A549 cancer cells when incubated with different concentrations of free GEF, empty nanoparticles (NPs-0), functionalized unloaded NPs (p28-NPs), GEF loaded NPs (NPs-GEF), and p28-functionalized GEF-loaded NPs (p28-NPs-GEF) during 72h. Negative Control (NC) and Positive Control (PC) consisted on cells incubated with 1% of Triton X-100 in medium, and only with medium, respectively. Values represent the mean ± SD, and each condition has at least an n=3. * denotes a significant difference of p<0.05 between each condition and PC; a, b, c and d represent a significant difference of p<0.05 between p28-NPs-GEF treatment vs empty NPs, p28-NPs, NPs-GEF and Free p28+GEF treatments, respectively.

IV.4.6. p28-functionalized PLGA nanoparticles loaded with gefitinib decrease A549 tumor progression

Taking in consideration the *in vitro* results, we hypothesized that p28-NPs-GEF could have a potential therapeutic effect on lung cancer progression *in vivo*. Therefore, we performed A549 xenograft lung tumor model, previously described by others (Liang *et al.*, 2019). A549 cells were subcutaneously injected in the right flank of 4-6 weeks old N:NIH(S(II-nu/nu) mice. After 17 days of tumor cells inoculation, when tumors reached 133.3 ± 27.1 mm^3, animals were subcutaneously treated with saline (CTR), p28-NPs, NPs-GEF, p28-NPs-GEF and free GEF, three times/week, along two weeks (Figure IV.4-5A). The free GEF, at the same concentration as encapsulated in NPs (11 µg/mL, 0.33 mg/kg mice), was well tolerated. No significant weight loss was observed in the mice in any treatment (Figure IV.4-5B). Regarding the therapeutic efficacy, while tumors from CTR group grew progressively, the tumor growth of treated animals was delayed (Figure IV.4-5C). The groups treated with p28-NPs (685.6 ± 67.0%) and NPs-GEF (662.0 ± 94.44%) exhibited a significant decrease on tumor growth comparing to CTR animals (1058.0 ± 172.2%) (p<0.01), as shown by the tumor growth curves (%; Figure IV.4-5C). Further, free GEF (484.1 ± 76.4%) and p28-NPs-GEF (462.7 ± 22.9%) significantly reduced the A549 tumor growth comparing to CTR group (p<0.0001), and presented a higher tumor growth inhibition in comparison with NPs-p28 and NPs-GEF. Importantly, p28-NPs-GEF potentiating the effect of the single NPs (p28-NPs and NPs-GEF) in 21% and 19%, respectively, suggesting a synergistic action of p28 and GEF. These results were corroborated by the results observed through the calculation of the area under the curves (AUC; Figure IV.4-5D). Nevertheless, p28-NPs-GEF treatment presented similar tumor growth kinetics that obtained with free GEF. Further, survival time is depicted in Figure IV.4-5E. While the mean survival of mice from CTR group was (60.6 ± 5.6 days), animals from free GEF and p28-NPs-GEF presented 68.0 ± 15.0 and 71.1 ± 13.4 days, respectively. Overall, no statistically significant difference in survival between CTR and treated groups was found.

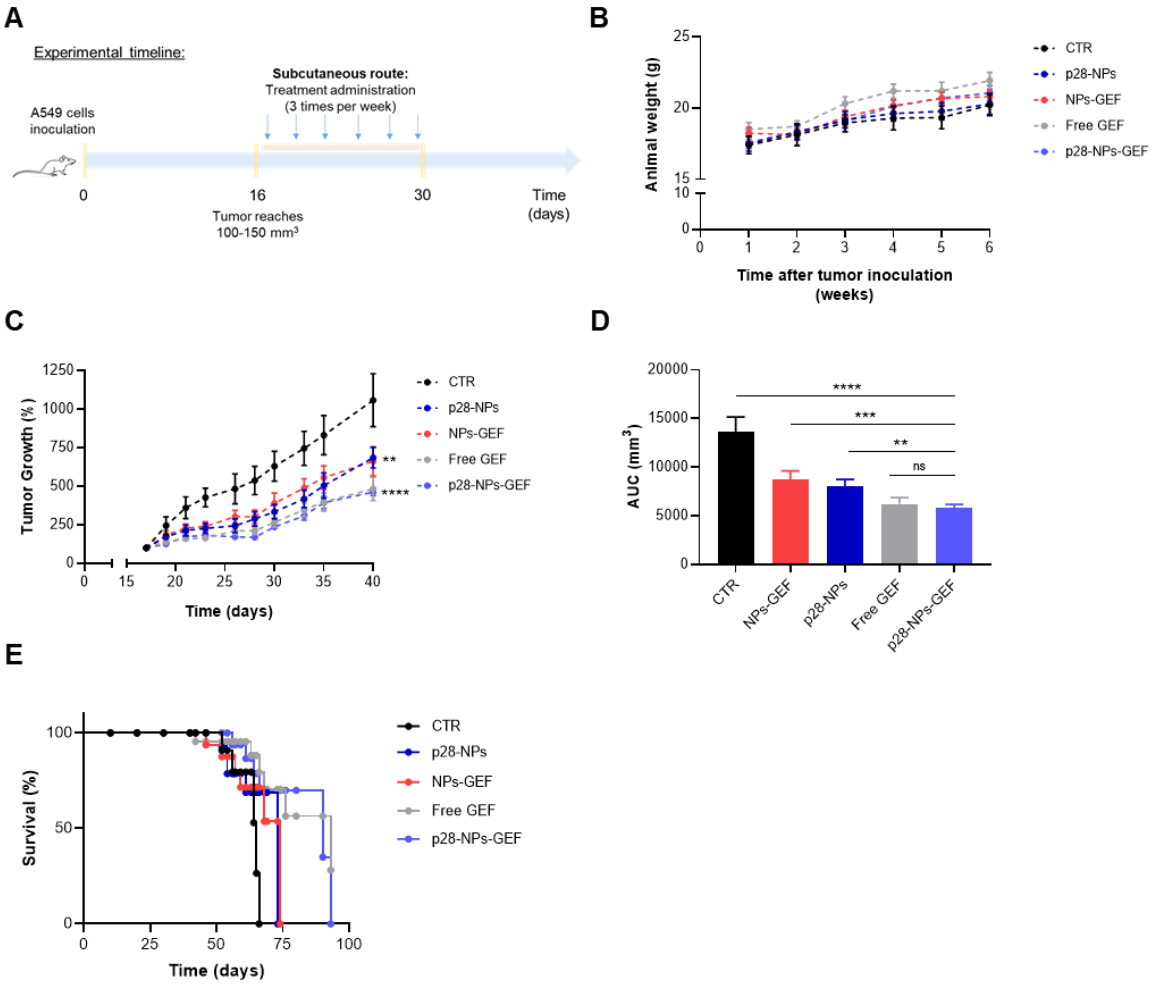

Figure IV.4-5: Effect of p28-NPs-GEF in A549 tumor progression (subcutaneous treatment). **A)** Experimental timeline. N:NIH(S(II-nu/nu) mice were injected with human lung cancer A549 cells into the right flank of the mice. After 17 days of tumor inoculation, animals were subcutaneously treated with p28-NPs, NPs-GEF, p28-NPs-GEF and free GEF, three times/week, along two weeks. Saline-treated animals were used as experimental control (CTR). After 40 days, animals were maintained for survival curve. **B)** Animal body weight was evaluated every week for 6 weeks, after tumor cells inoculation. **C)** Tumor volume (mm^3) was measured using a caliper and the % of tumor growth was obtained by normalizing each value to the initial tumor volume for each animal, before any treatment. **D)** Area under the curve (AUC) in mm^3 was calculated to measure kinetics of tumor growth. Values represent the average tumor growth of 5-6 animals and flags represent standard mean error values. **E)** Survival curves of tumor bearing mice. n=5-6 animals; ***p*<0.01, *** *p*<0.001 and ****p*<0.0001.

Upon the establishment of a proof-of concept that p28-NPs-GEF have a therapeutic effect when locally administrated at the tumor and considering that these NPs were designed to be administrated intravenously, we evaluated the impact of free GEF and p28-NPs-GEF by intravenous route administration. Animals were treated with saline, free GEF and p28-NPs-GEF, three times/week, along two weeks (Figure IV.4-6A). Regarding the animal weight, no alterations were observed upon treatment administration (Figure IV.4-6B). Animals treated with free GEF and p28-NPs-GEF exhibited a significantly delayed tumor growth, 705.5 ± 116.3% and 421.4 ± 39.0%, respectively comparing to CTR group (1058.0 ± 172.2%; Figure IV.4-6C). These results were supported through the calculation of the

AUCs (Figure IV.4-6D), where the p28-NPs-GEF presented the lowest AUC (5417.0 ± 302.2 mm^3) and almost reached statistical significance to free GEF (7543.0 ± 715.2 mm^3; p<0.058). Regarding survival curve, animals from p28-NPs-GEF group presented an increased median survival (78 days) comparing to free GEF and CTR groups (65 and 66 days, respectively). Overall, p28-NPs-GEF exhibited therapeutic effects by decreasing A549 primary tumor growth.

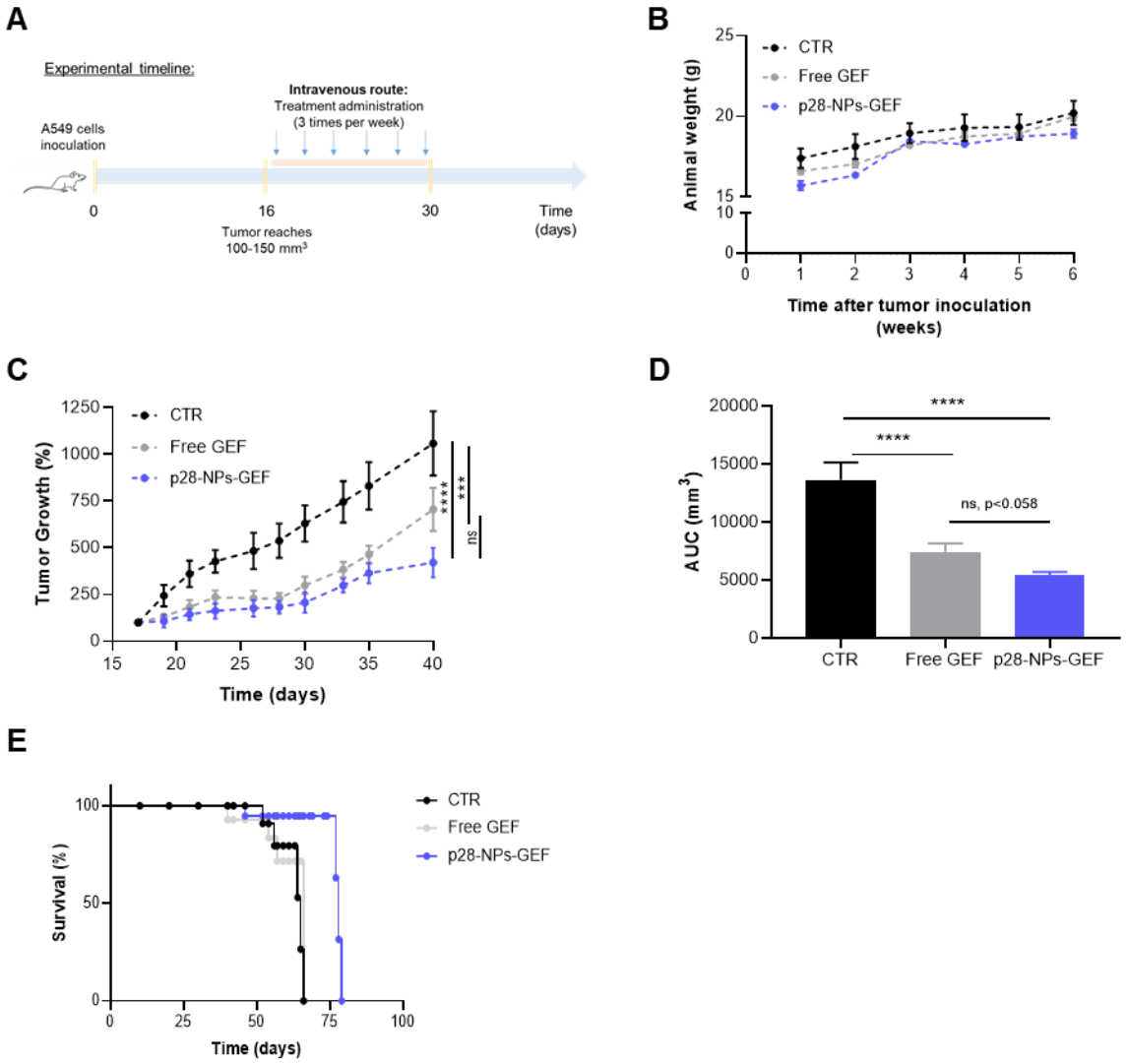

Figure IV.4-6: Effect of p28-NPs-GEF in A549 tumor progression (intravenous treatment). **A)** Experimental timeline. N:NIH(S(II-nu/nu) mice were injected with human lung cancer A549 cells into the right flank of the mice. After 17 days of tumor inoculation, animals were intravenously treated with p28-NPs-GEF and free GEF, three times/week, along two weeks. Saline-treated animals were used as experimental control (CTR). After 40 days, animals were maintained for survival curve. **B)** Animal body weight was evaluated every week during 6 weeks, after tumor cells inoculation. **C)** Tumor volume (mm^3) was measured using a caliper and the % of tumor growth was obtained by normalizing each value to the initial tumor volume for each animal, before any treatment. **D)** Area under the curve (AUC) in mm^3 was calculated to measure kinetics of tumor growth. Values represent the average tumor growth of 5-6 animals and flags represent standard mean error values. **E)** Survival curves of tumor bearing mice. n=4-5 animals; ***p<0.001 and ****p<0.0001.

V.4.7. p28-functionalized PLGA nanoparticles loaded with gefitinib reduce lung metastasis burden

To evaluate the impact of the p28-NPs-GEF on potential lung metastases formation, we performed hematoxylin and eosin staining of the lungs of treated and non-treated animals. Accordingly to our previous studies (Castro *et al*., 2020), we established a metastatic score considering the absence or presence of metastatic foci and their size as: absence of foci (score I), small foci (score II), intermediate foci areas (score III) and larger metastasized areas (score IV; Figure IV.4-7A). We found that A549 cells, subcutaneously inoculated in the mice, were able to establish lung metastases (Figure IV.4-7B). Despite all treatments decreased the number of metastatic foci in the lungs, only p28-NPs-GEF reached statistical significance comparing to CTR ($p<0.05$; Figure IV.4-7B). Further, we observed the largest lung metastasized areas (score III and IV) in CTR animals (Fig. 7C). On animals subjected to p28-NPs and NPs-GEF treatments, the metastatic score was similar, having essentially intermediate and larger metastases (5/6 animals), while free-GEF and p28-NPS-GEF-treated animals presented 50% of the animals with no foci or small lesions (3/6 animals; Figure IV.4-7C). Regarding the outcome of the animals treated through intravenous route, it was possible to observe that both treatments decreased the lung metastatic foci, however only free GEF reached statistical significance ($p<0.03$; Figure IV.4-7D). Nevertheless, the animals from p28 NPs-GEF presented a lower metastatic score, with 60% of animals having small foci of metastases (score II) while 60% of animals from free GEF group presented intermediate or larger areas (score III and IV) metastasized (Figure IV.4-7E). Overall, p28-NPs-GEF were able to attenuate lung metastases formation.

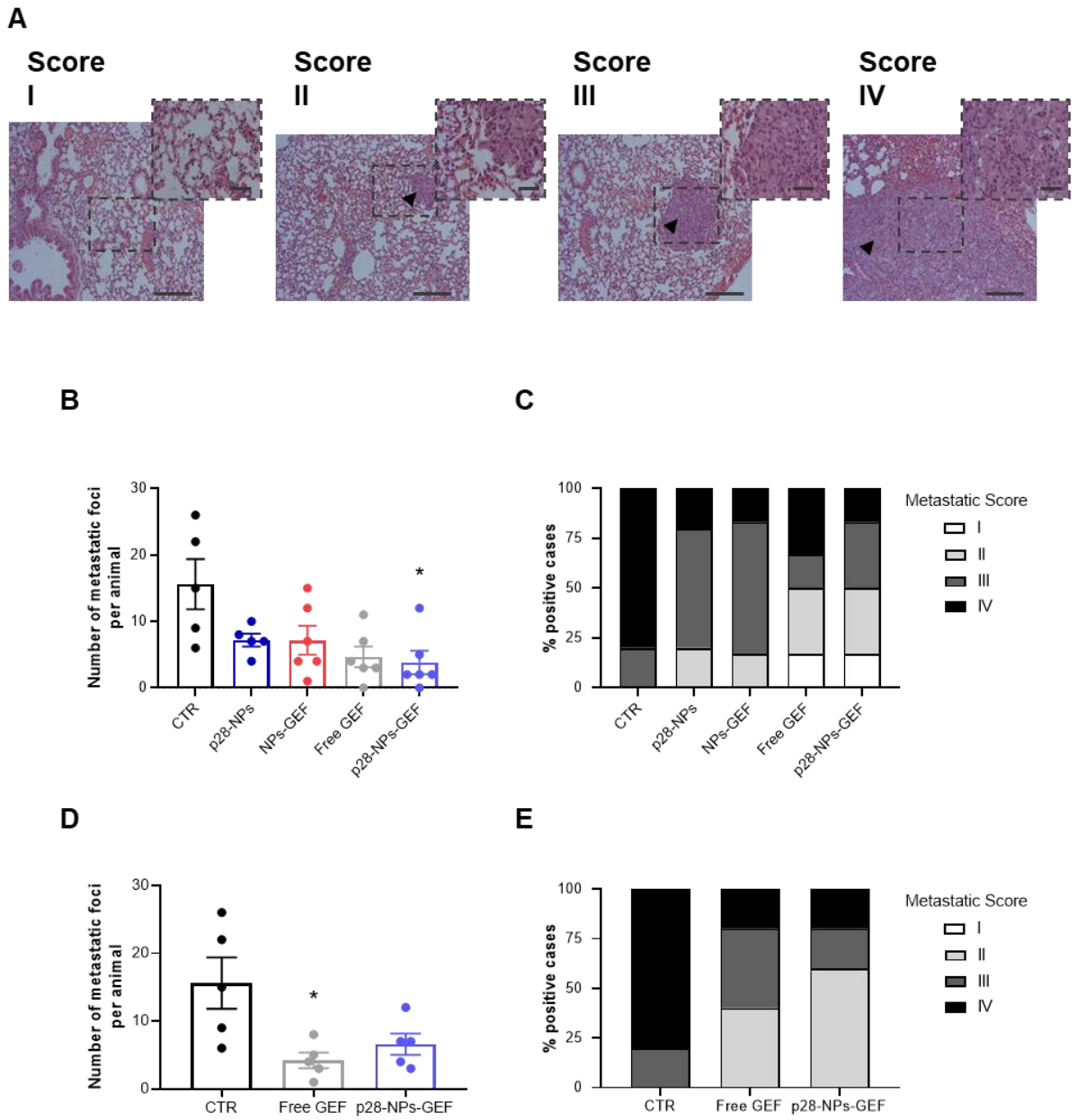

Figure IV.4-7: Effect of p28-NPs-GEF in lung metastasis. **A)** Lungs were stained with hematoxylin and eosin, and scored in accordance to the presence or absence of metastatic foci and their size: absent of foci (score I), small metastatic foci (score II), intermediate areas metastasized (score III) and larger areas metastasized (score IV). Arrows indicate metastatic foci. Magnification: 200x, scale bar: 100 µm; magnification: 600x, scale bar: 30 µm. **B)** Quantification of the number of metastatic foci in each animal treated subcutaneously with p28-NPs, NPs-GEF, p28-NPs-GEF and free GEF. **C)** Experimental subcutaneous treatments and respective metastatic score. **D)** Quantification of the number of metastatic foci in each animal treated intravenously with p28-NPs-GEF and free GEF. **E)** Experimental intravenous treatments and respective metastatic score. Data show the mean ± SEM and it is representative of 5-6 animals, **p*<0.05 relative to CTR.

IV.5. Discussion

The development of functional nanosystems has been widely studied due to the attractive advantages associated with their use as drug delivery strategies in cancer treatment when compared to the delivery of free drugs. Some of the advantages include the improvement

of the half-life plasma and bioavailability of the drugs, which will allow to reduce the doses administrated, and consequently may lead to a reduction in their side effects and treatment costs (Da Silva *et al.*, 2017; Jahan *et al.*, 2017; Su *et al.*, 2018). In this work, we produced p28-functionalized PLGA NPs loaded with GEF (p28-NPs-GEF) to be applied in lung cancer treatment. We intended to improve the drug bioavailability, and combine it to the preferential entry into cancer cells provided by p28, taking advantage of the peptide intrinsic characteristics (Taylor *et al.*, 2009; Yamada *et al.*, 2005).

The conjugation of the p28 to the PLGA-PEG-Mal polymer was established with high CE value determined by HPLC (Figure IV.4-1), suggesting that the insertion of a cysteine residue in the C-terminal of this peptide allowed its linkage to the polymer's Mal molecule, freeing the N-terminal. Therefore, after NPs production with this conjugated polymer, there will be exposure of the N-terminal on their surface, allowing it to perform its preferential entry property (Taylor *et al.*, 2009; Yamada *et al.*, 2005).

In relation to the NPs production method for GEF encapsulation (Figure IV.4-2A), the use of the nanoprecipitation is innovative, since the literature presents its encapsulation in PLGA NPs using only the single emulsification (o/w) solvent evaporation technique, which is not specific for the encapsulation of hydrophobic drugs (Kaur and Tikoo, 2013). The physico-chemical characterization and morphology of p28-NPs-GEF exhibited ideal characteristics for their effective use as NDDSs (Table IV.4-1). Compared with the NPs-0 (74±8 nm), NPs-GEF and p28-NPs-GEF presented a smaller Z-average (59±5 nm and 55±7 nm, respectively), which may be owing to the increased cohesive forces that formed smaller cores resulting from the interactions between the drug and the polymer (Shen *et al.*, 2020). Regarding the PDI values, all formulations presented PDI <0.15, frequently accepted for polymer-based NP materials (Danaei *et al.*, 2018). The negative surface charge of these NPs was not very marked, which may contribute to an enhanced circulation (Jahan *et al.*, 2017). In addition, no significant differences in these physico-chemical parameters were identified between NPs-0 and p28-NPs. This is also reported when other peptides are conjugated to the surface of this type of nanosystems (Martínez-Jothar *et al.*, 2018). However, the DL of these NPs might be improved to avoid the administration of higher doses that consequently will be associated to the presence of non-therapeutic excipients resulting from the NPs production process, which can cause side effects (Liu *et al.*, 2020). Therefore, the optimization of this process is considered. In relation to NPs shape (Figure IV.4-2B), these nanosystems present a spherical shape that

is documented as the one that promotes faster and more uniform internalization (Li and Zhang, 2019).

As part of this study, we also performed *in vitro* assays that involved the use of cell culture medium that can affect the stability of these NPs and their interaction with cells (Moore *et al.*, 2015). Thus, their colloidal stability was evaluated and demonstrated small variations in the physico-chemical characteristics of these nanosystems (Figure IV.4-2C). The observed stability may be due to the presence of 10% FBS, which has been reported to improve NP colloidal stability in various cellular media (Moore *et al.*, 2015).

The *in vitro* GEF release study described a biphasic pattern with an initial burst release, and then a sustained release phase over time (Figure IV.4-2D). This type of kinetic profile is described in other studies using PLGA NPs. The initial release step can be related to the dissolution of entrapped drug molecules near or attached to particles surface, and the second with drug slow diffusion process from the PLGA matrix and/or by the erosion/swelling of PLGA in release medium (Ding and Zhu, 2018). However, these data come from the forced *in vitro* analytical assay which may not necessarily translate into such a dramatic burst release in *in vivo* conditions.

Cell-NPs interaction studies demonstrated that p28-NPs interacted more with cells than nf-NPs, in a dose-dependent manner, and more pronounced in the A549 cells (Figures IV.4-3A, B). Consequently, one can assume that the conjugated peptide on the surface of these nanosystems, continues performing its tumor cell-homing action (Taylor *et al.*, 2009; Yamada *et al.*, 2005). In addition, upon treatment with p28-NPs followed by an acid washing step to remove particles that may be weakly bound to surface of the cells, it was possible to distinguish between the NPs that were associated with the cells, and those that had actually been internalized (Figures IV.4-3A, B). After acid washing, in A549 cells treated with p28-NPs occurred a decrease in the Geo MFI values, which may indicate that a fraction of the NPs was associated with them. This effect is possibly explained by the fact that p28-NPs interact more with cancer cells, and therefore there was probably a saturation of the entry pathways which could result in an accumulation in the surface of these cells. Actually, the mechanisms that promote the preferential entry of this peptide are still unknown, but it is assumed that it is dependent on the cholesterol existing in the plasma membranes, on the *caveolae* which is a type of lipid rafts with unique characteristics, and also on the activity of endosomes and lysosomes (Taylor *et al.*, 2009). In addition, it has been revealed that both azurin and p28 bind to components that are overexpressed in *caveolae*, such as Cav-1 and GM-1. This proposes that p28 penetrates

the plasma membrane via *caveolae*-mediated endocytic pathways (Bernardes *et al.*, 2018; Parton, 2018; Taylor *et al.*, 2009). Our results also confirmed an intracellular localization of these nanosystems by confocal imaging, in both cell lines under study, with a higher concentration of p28-NPs in cancer cells being also observed (Figure IV.4-3C). These findings can be compared to studies that suggest p28 as an anticancer agent transporter. In fact, these studies have shown that this CPP fused to other peptides or compounds, is able to target them through its tumor-homing capacity and translocate them through the plasma membrane of cancer cells, increasing their anticancer potential *in vitro* and *in vivo* (Noei *et al.*, 2019; Raber *et al.*, 2020; Soleimani *et al.*, 2019). As an example, a recent study showed for the first time that p28 can be combined with a photosensitizer for photodynamic therapy, enhancing its therapeutic effects (Raber *et al.*, 2020). For the current work, an optimization of the p28 modulation on the surface of these nanosystems is still necessary to establish the optimal amount of peptide that will provide the best response based on this anticancer action. Beyond this, little is known about the entry mechanisms of this peptide into cells, so more studies in this area can provided important knowledge to allow the development of a more effective nanosystem, and consequently, an improved therapy.

Resazurin assays were also carried out on A549 cancer cell line, and on its non-cancer match tissue cells (16HBE14o-) to analyze the effect of p28-NPs-GEF on metabolic activity (Figure IV.4-4). The results obtained showed that the cellular growth of 16HBE14o- cells is not dependent on EGFR signaling, since treatment with free GEF did not cause a decrease in the metabolic activity, regardless of the concentration of this drug used. In addition, there was no significant decrease in the metabolic activity after treatment with the 4 types of nanosystems produced (NPs-0, p28-NPs, NPs-GEF, and p28-NPs-GEF). The same does not happen with A549 cancer cells, since the treatment with free GEF produced a dose-dependent decrease in the metabolic activity. In fact, these tumor cells have a constitutively active subpopulation of EGFR, which promotes and maintains cell proliferation even in the absence of extracellular ligands (Bollu *et al.*, 2015). Regarding the treatment with 1.8 µM of free p28, the metabolic activity did not change, which is in accordance with what has been described. It is cited that at least 100 µM of this peptide is required for a decrease in cell viability to occur (Yamada *et al.*, 2016). As observed in the treatment with the free peptide, the functionalization of p28 to NPs also did not provide a decrease in metabolic activity. The metabolic activity related to NPs-0 showed that the polymeric matrix made up of PLGA is potentially safe and non-toxic. It is also possible to observe a similar metabolic activity profile when comparing treatments with free GEF and

NPs-GEF. These results, as in the *in vitro* release assay, suggests that part of the drug is associated with the surface of the nanosystem, but a small improvement seems to be observed upon drug encapsulation which may be related to some residual amount of drug that has been encapsulated, and that is being released in a controlled manner. Finally, the results indicated that treatment with the functional nanosystem caused a significant decrease in metabolic activity compared to the application of NPs-GEF or with the two free components, which suggests that when encapsulating GEF and functionalizing p28 in a nanosystem promotes a more efficient and effective delivery of this drug. All of these results indicate that p28 functionalized in PLGA NPs allows a greater interaction of them with cancer cells than with non-cancer cells, increasing their internalization. This study once again demonstrates the potential of CPP-functionalized PLGA NPs as NDDSs that have been studied for the past decade (Chen *et al.*, 2012; Jin *et al.*, 2018; Li *et al.*, 2011; Sims *et al.*, 2019; Wang *et al.*, 2014; Zhang *et al.*, 2015).

Regarding their therapeutic potential, subcutaneous p28-NPs-GEF were able to decrease A549 tumor growth as free GEF (Figure IV.4-5C). The lack of tumor vessels to support the drug distribution may have compromised a potential increased therapeutic effect promoted by a subcutaneous administration. Nevertheless, animals treated with p28-NPs-GEF presented the lowest number of lung metastatic foci and a better metastatic score (Figures IV.4-7B, C). Interestingly, this functionalized nanosystem seems to potentiate the individual anticancer effects of p28-NPs and NPs-GEF, suggesting a synergistic effect. These results are in agreement with previous studies that evidenced that p28 when combined with DNA-damaging drugs (DOX, dacarbazine, temozolamide) or antimitotic drugs (PTX and docetaxel) in a variety of cancer cells expressing wild-type or mutated p53, enhanced their sensitivity to these drugs (Yamada *et al.*, 2016). Nevertheless, we cannot exclude the action of p28 on endothelial cells, which can also contribute for a reduced tumor growth, by inhibiting tumor angiogenesis (Mehta *et al.*, 2011). Further, p28 has been explored as protein and gene delivery systems for human papillomavirus (HPV) therapeutic vaccines (Shahbazi and Bolhassani, 2018).

The results from intravenous administration reinforce the importance of GEF encapsulation (Figure IV.4-6), since its therapeutic effect was potentiated comparing to free GEF (p<0.058), which is in accordance with lower bioavailability of free GEF in circulation (Bergman *et al.*, 2007). Accordingly, animals treated with p28-NPs-GEF presented a lower metastatic score still with increased metastatic foci (Figures IV.4-7D, E). The full interpretation of this outcome should be accompanied by the histopathology of

the lesion, the inflammation index as well as the animal welfare. Nevertheless, the increased median survival of p28-NPs-GEF-treated animals is an important indication that this nanoformulation could bring in the future, an improved therapeutic index for the patients. Despite these modest results, this therapeutic combination has never been explored before, and the current data provide the proof-of-concept that p28-functionalized NPs offer a therapeutic alternative for GEF deliver. At the same time, other groups also reported other type of NPs to deliver this drug. For example, Ni *et al.*, described that GEF-loaded poly(ecaprolactone)-poly(ethyleneglycol)-poly(e-caprolactone) (PCEC) NPs reduced A549 tumor growth and decreased systemic adverse effects associated to free GEF administration (Ni *et al.*, 2017). These results were obtained with a higher dose of GEF (20 mg/kg) while in our study a small amount of GEF was sufficient to observe therapeutic effects (0.33 mg/kg). Further, PCEC NPs were non-targeted and the potential effects on lung metastases formation were not explored. Also, Jeannot and colleagues reported hyaluronan-based copolymer targeting CD44 receptors to encapsulate both GEF and vorinostat for effective combinational lung cancer treatment. To avoid possible hepatic toxicity due to their liver accumulation, drug-loaded hyaluronan NPs were intrapulmonary administrated and had a stronger inhibition of orthotopic lung tumor growth compared to free drugs (Jeannot *et al.*, 2018). More recently, PLGA NPs embedded in carboxymethyl β-glucan porous microcapsules were also described as an alternative to deliver GEF, resulting in a significant improvement in the cytotoxicity of encapsulated GEF compared with the free drug *in vitro* (Li *et al.*, 2019). Despite several competing systems to deliver GEF have been already reported, the advantage and novelty of our system is while p28 penetrate tumor cells, GEF is delivered at the tumor cells *in vitro*, resulting to a tumoricidal synergistic effect *in vivo*.

IV.6. Conclusion

In summary, we developed an innovative formulation for tumor-targeted GEF delivery based on the functionalization using a bacterial peptide, the p28, previously reported by its anticancer properties. This is was the first time that this CPP was combined with a nanosystem. p28-functionalized NPs were capable of loading hydrophobic GEF and provide active targeting mediated by p28. Further, p28-NPs-GEF decreased metabolic activity of A549 cells, and conferred better antitumor effects *in vivo*, by decreasing A549 primary tumor growth as well as lung metastatic burden when compared to free drug condition after intravenous administration. Both therapeutic schedules adopted (3 times/ week, along 2 weeks) and GEF dose was sufficiently to strongly decreased tumor growth

and was well tolerated. Further trials will be needed to optimize the concentrations of encapsulated drug, as well the combination with chemotherapeutic agents, in order to obtain the best therapeutic efficacy.

This pioneer NDDS opens new perspectives for exploring advanced delivery systems with higher loading capacity and minimum adverse effects founded on tumor-homing property of p28, offering in the future a tumor targeted therapy to be applied in different types of cancer.

Acknowledgments

This paper is dedicated to the memory of Professor Ananda M Chakrabarty, who first discovery the anticancer properties of the bacterial protein and its derived peptide (p28). The work presented was supported by scientific project (PTDC/BTM-SAL/30034/2017_LISBOA-01-0145-FEDER-030034_POCI-01-0145-FEDER-030034) financed by the FCT. Funding received by iBB-Institute for Bioengineering and Biosciences from the FCT (UID/BIO/04565/2020), by Programa Operacional Regional de Lisboa 2020 (Project N. 007317) and by Portuguese Platform of BioImage (PPBI-POCI-01-0145-FEDER-022122) is also acknowledged. Ana Rita Garizo (SFRH/BD/122636/2016), Andreia Almeida (SFRH/BD/118721/2016) and Cláudia Martins (SFRH/BD/137946/2018) acknowledge PhD fellowships. Flávia Castro also acknowledges POCI-01-0145-FEDER-030034 financial support.

The authors acknowledge the support of the Biointerfaces and Nanotechnology, Translational Cytometry, Biochemical and Biophysical Technologies and Histology and Electron Microscopy i3S Scientific Platforms.

The authors would also like to express their gratefulness to Marco Araújo (i3S, Portugal) for insightful feedback on the design of experiments, Prof. José Farinha (IST, Portugal) for access to the DLS platform, and Dr Vasco Bonifácio at BSIRG-iBB for providing access to several equipments.

V. FINAL DISCUSSION AND FUTURE PERSPECTIVES

V.1. Final Discussion

Increasingly, research in the field of cancer therapy focuses on the development of new approaches to replace conventional treatments, or at least, combine them in smaller doses to minimize their severe side effects. Of these, one of the most relevant drawbacks is the toxicity developed in healthy tissues due to the lack of selectivity causing an ineffective delivery of drugs into cancer cells, which also lowers the drugs' therapeutic capacity (Chari, 2008). Among the novel strategies for cancer treatment, the application of natural microbial-based products that are able to interfere with tumorigenesis has been widely studied (Fialho *et al.*, 2012). This is the case of azurin, a bacterial protein secreted by *Pseudomonas aeruginosa*, with high therapeutic potential in this field (Yamada *et al.*, 2002a; Yamada *et al.*, 2002b). The results presented throughout this thesis evidence the importance of certain portions of this protein, showing the possibility of azurin for being a source of bioactive peptides not only with direct anti-tumor activity but also promising for the purpose of developing novel drug delivery strategies.

Azurin acts with increased specificity on cancer cells by inhibiting their proliferation, as well as inducing apoptosis (Yamada *et al.*, 2002a; Yamada *et al.*, 2002b). In addition, it could also prevent angiogenesis in endothelial cells, and attenuated several signaling pathways involved in tumor progression (Figure V.1-1; Bernardes *et al.*, 2013; Bernardes *et al.*, 2014; Bernardes *et al.*, 2016; Chaudhari *et al.*, 2007; Metha *et al.*, 2011).

However, the mechanisms associated with its endocytosis are still not completely understood. Evidences point to the uptake through the penetration of the plasma membrane via *caveolae*-mediated endocytic pathway, co-localized with Cav-1, one of the main structural constituents of *caveolae* (Figure V.1-1; Fujimoto *et al.*, 2000; Taylor *et al.*, 2009). This type of lipid rafts is frequently overexpressed in cancer (Irwin *et al.*, 2011; Murai, 2015), proposing the hypothesis that the protein uptake by cancer cells is influenced by the high quantity of these microdomains on their surface. Nevertheless, some types of non-cancer cells also contain a high number of *caveolae* in their plasma membranes (Parton and Richards, 2003), evidencing that this should not be the only route of entry for this protein. In addition, it is known that one of the regions of azurin, the one that corresponds to its α-helix and that has been studied in the form of the p28 peptide, is partly responsible for mediating its entry into cancer cells. This peptide also binds mainly to Cav-1 to achieve its penetration (Taylor *et al.*, 2009). Since binding to this structural membrane protein is often related with hydrophobic regions in the binding partners (Vihanto *et al.*,

2006), and azurin has in its constitution a strong hydrophobic patch, part in the p28 region, and other part in the region of its C-terminal (Bernardes *et al.*, 2013), it was proposed in one of the chapters of this thesis (Chapter II; Figure V.1-1), that in addition to p28, this terminal region of azurin arranged in a hydrophobic core centered on phenylalanine$_{114}$ could also be partly involved in the uptake of this protein. The results showed that the alteration of the central phenylalanine$_{144}$ by an alanine, a less hydrophobic amino acid, led to a decrease in the penetration of azurin in cancer cells and in its anticancer potential associated with a lower affinity with Cav-1. In addition, the knowledge about glycosphingolipids such as GM-1, expressed in abundance in *caveolae* (Pang *et al.*, 2004) and the carbohydrate-protein interactions that they can establish with hydrophobic regions of proteins, mainly through phenylalanine residues (del Carmen Fernández-Alonso *et al.*, 2012), also led to question whether in the first recognition steps to enter cancer cells, azurin could interact with this caveolar component. The findings demonstrated that after inhibition of GM-1, the intracellular levels of azurin decreased associated with a lower entry, as occurred with the inhibition of N-linked glycosylation in a previous study (Taylor *et al.*, 2009). This was even more evident after treatment with the mutated protein. Also in this work, we confirmed a reduction in the total levels of Cav-1 after azurin treatment, and there was a GM-1 relocation from the plasma membrane to the cytosol. These events could then be related with changes in the biophysical status of the plasma membrane of cancer cells, such as an increased membrane fluidity, also documented in previous studies performed by our group. This effect can be interesting to explore therapies for drug resistant cancers, since in these cases the accumulation of anticancer drugs against intracellular targets is limited by the rigid nature of the plasma membranes (Bernardes *et al.*, 2016). Thus, with this treatment, in addition to facilitating the diffusion of the drugs, it may be that membrane receptors, efflux pumps, among others involved in MDR development, can also be relocated from the plasma membrane, as is the case of GM-1, potentiating the cytotoxic effect of co-administration of drugs. This effect at the membrane protein composition of drug resistant cancers is still to be confirmed.

The combination of anticancer drugs with azurin or its p28 derived peptide has already been evaluated, and like what happened in those studies, in this work we could confirm that there was also an improvement in the therapeutic activity of the drugs. On the other hand, the combination with the mutated protein showed less effect on cell viability related to its lower affinity with Cav-1, and consequently less changes at the membrane level that could provide greater efficacy of the intracellular activity of the applied drugs. Thus, all the results obtained in this study contributed to unveil a new region of azurin, which due to its

hydrophobic properties exposed in a core available to interact, is not only responsible for the recognition of this protein by cancer cells, but also partly mediates its uptake (Figure V.1-1).

The anticancer potential shown by the C-terminal region of azurin, was also supported by Chaudhari *et al.* 2007, that produced peptides derived from this region, and after treatment with them, they verified significant cytotoxicity effects in cancer cells (Chaudhari *et al.*, 2007). In this sense, the study of this region continued by our group through an *in silico* analysis with bioinformatic peptide optimization tools (Figure V.1-1; Tyagi *et al.*, 2013), which allowed the initial assessment of a peptide with 26 residues, corresponding to a region close to the C-terminal of azurin, called CT-p26. The re-design of this sequence created a peptide with a lower number of amino acids termed CT-p19. Then, the alteration of some residues of its sequence allowed the production of a promising peptide called CT-p19LC with greater hydrophobicity, a positive net charge, and more importantly, with a high propensity to exhibit enhanced anticancer activity (Coelho, 2017). As part of this thesis (Chapter III; Figure V.1-1), the bioactivity of these peptides was evaluated *in vitro*. The initial results demonstrated that CT-p26 had more marked cytotoxic effects than p28, the peptide compromising amino acids outside the C-terminal region. Similar results showed CT-p19, also confirming its preferential action on cancer cells. Finally, the CT-p19LC with the greatest anticancer potential demonstrated *in silico*, was also proven *in vitro*. The application of a lower concentration of this peptide showed an anti-tumor and selectivity similar to that observed with the application of higher concentrations of CT-p19, as well as of azurin and p28, already documented in the literature. In addition, *in silico*, the charge of this peptide has been increased making it positive, and *in vitro* it has been proven that this characteristic is essential for the interaction of this peptide with plasma membranes of cancer cells, which have a more anionic membrane potential than non-cancer cells (Harris *et al.*, 2013; Leuschner and Hansel, 2005). As studied with the application of azurin and the mutated protein, the membrane order was also assessed after treatment with CT-p19LC. Similar to what was observed with the treatment with azurin, this peptide was also able to make the membrane of cancer cells more fluid, indicating that it also acts at the membrane level. However, in this case, the possible membrane components involved in its targeting capacity were not investigated (Figure V.1-1). In general, these results contributed to the confirmation of the anticancer potential of the C-terminal region of azurin, as well as showing the relevance of the study of other regions of azurin that may be useful for the discovery of other new bioactive anticancer peptides.

In the Chapter IV of this thesis (Figure V.1-1), for all that has been described about the p28 CPP derived from azurin, its properties were explored in the design of a new drug delivery strategy. This peptide was chosen for this purpose, mainly due to its CPP properties, as well as its high and specific internalization in cancer cells associated to its hydrophobic N-terminal (first 18 amino acids; Taylor *et al.*, 2009). In the literature, there are several examples of CPPs associated with various types of nanosystems by the existing conjugation methods for drug delivery application, but few have the potential for tumor-homing peptide presented by p28 (Gessner and Neundorf, 2020; Silva *et al.*, 2019; Vale *et al.*, 2020). Thus, in this thesis, an innovative polymeric formulation based on PLGA, functionalized with p28 oriented so that its N-terminal was exposed and available to interact, and with anticancer drugs that inhibit EGFR receptors encapsulated was produced to be applied in lung cancer therapy. Initially, it was demonstrated that these nanosystems were capable of interacting more with lung cancer cells than with their tissue-match non-cancer cells, with a greater internalization in the first ones. However, the nature of this interaction is not yet known. With this, it was possible to conclude that the action of p28 was maintained, even when conjugated to the NPs. Even so, the modeling of this peptide on the surface of this nanosystems must be considered, in order to achieve the maximum possible interaction/internalization effect of the p28-NPs. After that, the treatment of these NPs *in vitro* proved to be effective and selective, since the cytotoxic effects observed were higher than when the cancer cells were treated with NPs without this peptide on their surface, and moreover, these effects were not seen in non-cancer cells. What happens to these NPs after internalization is still unknown. Thus, it was assumed that there could be an accumulation of these NPs at tumor sites due to the documented EPR effect in drug delivery systems, and then the functionalization with p28 would allow the NPs to interact more specifically with the cancer cells leading to their internalization, thus providing a greater amount of drugs inside these cells. These effects were corroborated *in vivo*, where a reduction in primary tumor burden and formation of pulmonary metastases has been recorded after application of this functional nanosystem (Figure V.1-1). Overall, these results confirm the importance of p28 as a transporter agent for therapeutic compounds, for the first time associated with a NDDS. In addition to this nanosystem carrying chemotherapeutic drugs, it would also be interesting, taking advantage of its functionalization with p28, to associate it with siRNA or photodynamic therapies. In fact, p28 has already been fused directly to a photosensitizer, and the results have shown that combined application has brought greater benefits than its individual application (Raber *et al.*, 2020). Importantly, the decoration of the NPs with p28, whatever

the applied therapy, will allow the combination of several therapeutic strategies may improve their effects compared to their individual use.

In summary, the content of this thesis opens new horizons for the application of azurin, demonstrating the relevance of studying the several regions of this protein for obtaining bioactive anticancer peptides that can be more powerful than their source, capable of being applied in new promising delivery strategies of drugs in the fight against various types of cancer.

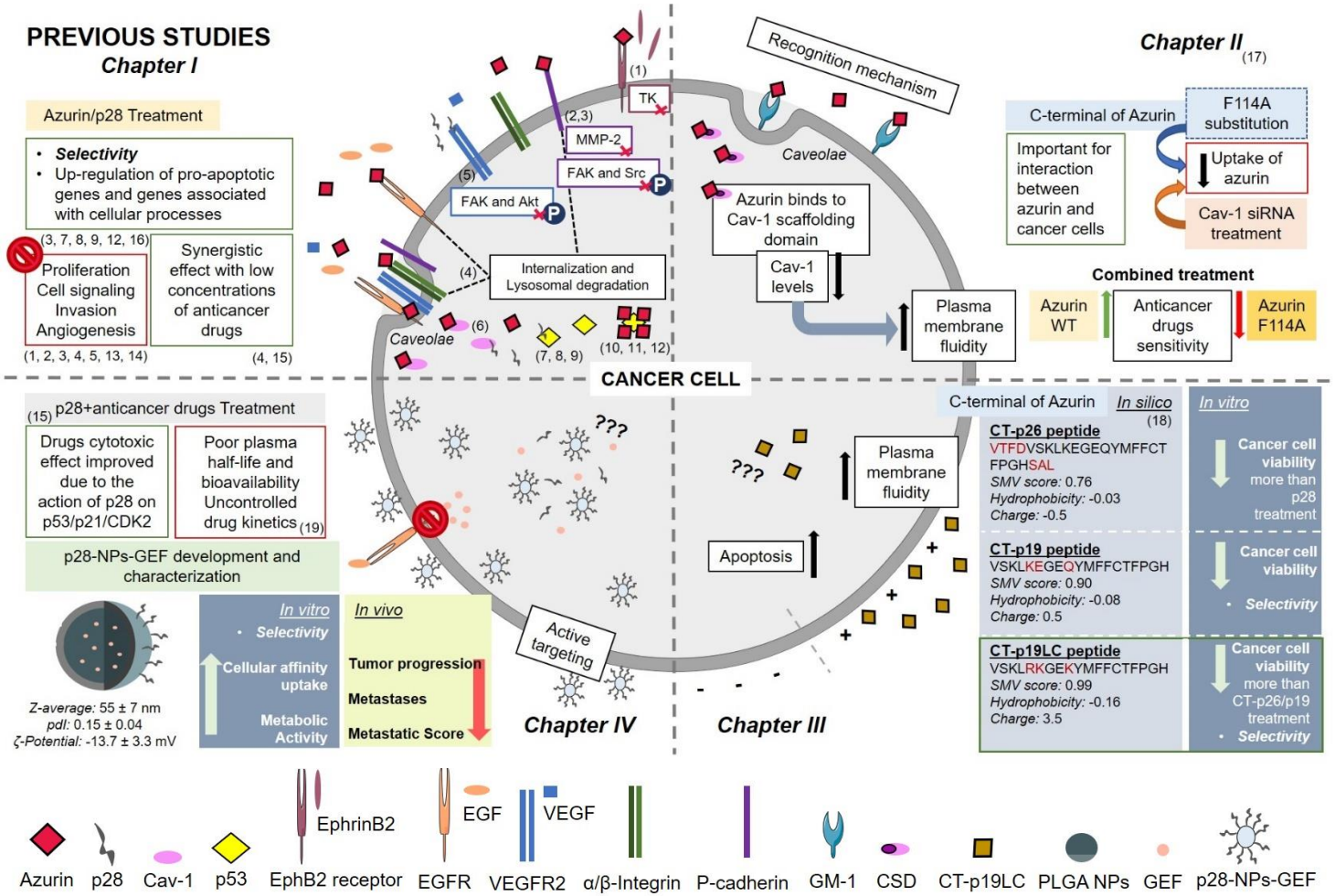

Figure V.1-1: Summary of previous results published by others and the results presented in this thesis about the anticancer potential of the bacterial protein azurin and its derived peptides: mode of action and development of a nanosized drug delivery system (NDDS) for cancer therapy. (1) Chaudhari *et al.*, 2007; (2) Bernardes *et al.*, 2013; (3) Bernardes *et al.*, 2014; (4) Bernardes *et al.*, 2016; (5) Mehta *et al.*, 2011; (6) Taylor *et al.*, 2009; (7) Yamada *et al.*, 2009; (8) Yamada *et al.*, 2013a; (9) Yamada *et al.*, 2013b; (10) Apiyo and Wittung-Stafshede, 2005; (11) Taranta *et al.*, 2009; (12) Yamada *et al.*, 2005; (13) Yamada *et al.*, 2002a; (14) Yamada *et al.*, 2002b; (15) Yamada *et al.*, 2016; (16) Punj *et al.*, 2003; (17) Bernardes *et al.*, 2018; (18) Coelho, 2017.

V.2. Future perspectives

So far, discoveries about the application of azurin and its derived peptides as potential anticancer agents have undoubtedly highlighted their selectivity, acting specifically on cancer cells, with none or minimal cytotoxic effects on non-cancer cells (Taylor *et al.*, 2009; Yamada *et al.*, 2013). The question that arises is which or what are the mechanisms of action that allow this selection and specificity. It has long been known that azurin and p28 enter through the plasma membrane through *caveolae*-mediated endocytic pathways (Taylor *et al.*, 2009), the non-planar lipid raft strongly overexpressed in various types of cancer (Irwin *et al.*, 2011; Murai, 2015). In addition, the confirmation that azurin and p28 co-localize with the Cav-1 membrane protein (Taylor *et al.*, 2009), a major constituent of *caveolae* (Fujimoto *et al.*, 2000), seems to indicate the answer to the explanation of the selectivity of these compounds. However, it is shown that some types of normal cells also have a high content of these membrane microdomains in their constitution (Parton and Richards, 2003). Besides this, a study by our group showed that azurin is also able to interact with planar lipid rafts in cancer cells with a reduced amount of *caveolae* (unpublished work). All of this suggests that azurin and its derived peptides possibly enter through more than one entry pathway, and their ability to select is also involved with other membrane constituents. In fact, it has been shown that azurin is capable of interacting with several receptors and adhesion proteins, overexpressed in various types of cancer, and usually involved with abnormal proliferation and aberrant constitutive signaling (Bernardes *et al.*, 2013a; Bernardes *et al.*, 2014; Bernardes *et al.*, 2016). The continued identification of possible targets of this protein in cancer cells will allow to elucidate both its selectivity and to determine all possible routes of entry. It is therefore suggested that this study be carried out through the inhibition of possible targets by gene silencing through siRNA, in contrast to what has been used with chemical inhibitors that eliminate cholesterol from the plasma membrane, or that lead to the disruption of the membrane to the level of *caveolae* (Taylor *et al.*, 2009), affecting possible membrane constituents, which may be specific targets for this protein and its peptides.

After azurin or p28 internalization, it is known that they can reach late endosomes and lysosomes (Taylor *et al.*, 2009; Mehta *et al.*, 2011), but how they manage to escape these constituents also remains to be clarified. Indeed, in the future, the transient silencing with siRNA of genes involved in several endocytic pathways and/or constituents of such early/late endosomes may be used to identify proteins with a relevant role on the uptake

and endosomal escape of p28 or its associated cargo that make it available for intracellular therapies.

In addition, studies show that treatment with azurin or its derived peptides lead to biophysical changes in the plasma membranes of cancer cells, making them less rigid, more fluid and elastic, and possibly disrupting lipid rafts (Bernardes *et al.*, 2016; Bernardes *et al.*, 2018). This phenomenon may be interesting in a study with patient-derived drug resistance models, which become less permeable to these due to the development of membrane rigidity and the establishment of efflux pumps.

In this thesis, the association of p28 for the first time with a NDDS demonstrated its importance for lung cancer therapy. However, some points need to be optimized such as increasing the drug efficiency encapsulation, and modeling the amount of p28 on nanosystems surface, in order to decrease the necessary administration doses. After the internalization of these nanosystems, their intracellular pathway is also unknown, and some therapeutic potential could be extracted from these future discoveries. In addition, the molecular analysis of the expression of potential tumor marker genes, after application of these functional nanosystems, will reveal which signaling pathways may be affected with this treatment and which benefit may result from this effect. To enrich all this knowledge, it would also be interesting to evaluate by biophysical analyzes such as AFM, the possible bindings that these nanosystems may establish with specific areas of the cell membrane such as lipid rafts, the changes that may occur in terms of the biophysical properties of the membrane and its influence on cell adhesion, as was done after azurin/p28 treatment (Bernardes *et al.*, 2016; Bernardes *et al.*, 2018). Finally, given the selectivity of azurin, as well as its derived peptides, one should also consider the possibility of associating them with other types of nanosystems, combining them with other anticancer drugs, and gene and photodynamic therapies, to achieve a level of universal therapeutic efficacy for any type of cancer.

The clarification of the arguments mentioned above would be an added value for the production of efficient and innovative drug delivery strategies, applied to each type of cancer and patient, being able to achieve a personalized therapy.

VI. PUBLICATIONS AND COMUNICATIONS

Scientific publications:

- Bernardes N, Garizo AR, Pinto SN, Caniço B, Perdigão C, Fernandes F, Fialho AM. 2018. Azurin interaction with the lipid raft components ganglioside GM-1 and caveolin-1 increases membrane fluidity and sensitivity to anti-cancer drugs. *Cell Cycle* **17**: 1649-1666. DOI: 10.1080/15384101.2018.1489178.

- Garizo AR, Coelho LF, Pinto S, Fernardes F, Bernardes N, Fialho AM. 2021. The azurin-derived peptide CT-p19LC exhibits membrane-active properties and induces cancer cell death. *Biomedicines* **9**: 1194. DOI:10.3390/biomedicines9091194.

- Garizo AR, Castro F, Martins C, Almeida A, Dias TP, Fernardes F, Barrias CC, Bernardes N, Fialho AM, Sarmento B. 2021. p28-functionalized PLGA nanoparticles loaded with gefitinib reduce tumor burden and metastases formation on lung cancer. *Journal of Controlled Release* **337**: 329-342. DOI: 10.1016/j.jconrel.2021.07.035.

In preparation:

- Garizo AG, Bernardes N, Fialho AM. p28, an anticancer cell penetrating peptide derived from bacterial protein azurin. (Review - In preparation).

Book chapter:

- Garizo AR, Bernardes N, Chakrabarty AM, Fialho AM. 2019. The Anticancer Potential of the Bacterial Protein Azurin and Its Derived Peptide p28, *Microbial Infections and Cancer Therapy*, ed Ananda M Chakrabarty and Arsenio M Fialho, Pan Stanford Publishing Pte. Ltd. Singapure: ISBN 978-981-4774-86-4.

Poster communication:

- Bernardes N, Garizo AR, Pinto SN, Caniço B, Perdigão C, Fernandes F, Fialho AM. 2018. Modulation of membrane properties and interaction with lipid rafts components GM-1 and caveolin-1 in cancer cells by azurin increases membrane fluidity and sensitivity to anti-cancer drugs, 3th Associação Portuguesa de Investigação em Cancro (ASPIC) internacional congress.

- Garizo AR, Bernardes N, Martins C, Barrias CC, Sarmento B, Fialho AM. 2019. Azurin peptide-decorated gefitinib-loaded nanoparticles: development, characterization and *in vitro* evaluation of their anti-lung cancer activity, 1st iBB Workshop: “Fostering Collaborative Research”.

- Garizo AR, Bernardes N, Martins C, Barrias CC, Sarmento B, Fialho AM. 2020. p28-functionalized gefitinib-loaded PLGA nanoparticles: development and *in vitro* characterization of anti-cancer activity, Liga Portuguesa Contra o Cancro: “Cancer Biology: from Basic to Translational Research” webinar.

VII. REFERENCES

Aagaard L, Rossi JJ. 2007. RNAi therapeutics: principles, prospects and challenges. *Adv Drug Deliv Rev* **59**(2-3): 75-86.

Agrawal P, Bhagat D, Mahalwal M, Sharma N, Raghava GPS. 2020. AntiCP 2.0: an updated model for predicting anticancer peptides. *Brief Bioinform* **6**: bbaa153.

Agrawal P, Bhalla S, Usmani SS, Singh S, Chaudhary K, Raghava GP, Gautam A. 2016. CPPsite 2.0: a repository of experimentally validated cell-penetrating peptides. *Nucleic Acids Res* **44**(D1): D1098-103.

Akbarzadeh A, Rezaei-sadabady R, Davaran S, Joo SW, Zarghami N. 2013. Liposome: classification, preparation and applications. *Nanoscale Res Lett* **8**: 102-111.

Akl MA, Kartal-Hodzic A, Suutari T, Oksanen T, Montagner IM, Rosato A, Ismael HR, Afouna MI, Caliceti P, Yliperttula M, Samy AM, Mastrotto F, Salmaso S, Viitala T. 2019. Real-Time Label-Free Targeting Assessment and *in vitro* Characterization of Curcumin-Loaded Poly-lactic-co-glycolic Acid Nanoparticles for Oral Colon Targeting. *ACS Omega* **4**(16): 16878-16890.

Albanese A, Tang PS, Chan WCW. 2012. The Effect of Nanoparticle Size, Shape, and Surface Chemistry on Biological Systems. *Annu Rev Biomed Eng* **14**: 1-16.

Alhajj N, Chee CF, Wong TW, Rahman NA, Abu Kasim NH, Colombo P. 2018. Lung cancer: active therapeutic targeting and inhalational nanoproduct design. *Expert Opin Drug Deliv* **15**(12): 1223-1247.

Allen TM, Cullis PR. 2013. Liposomal drug delivery systems: From concept to clinical applications. *Adv Drug Deliv Rev* **65**: 36-48.

Almoustafa HA, Alshawsh MA, Chik Z. 2017. Technical aspects of preparing PEG-PLGA nanoparticles as carrier for chemotherapeutic agents by nanoprecipitation method. *Int J Pharm* **533**: 275-284.

Alves AC, Magarkar A, Horta M, Lima JLFC, Bunker A, Nunes C, Reis S. 2017. Influence of doxorubicin on model cell membrane properties: insights from *in vitro* and in silico studies. *Sci Rep* **7**(1): 6343.

Amreddy N, Babu A, Panneerselvam J, Srivastava A, Muralidharan R, Chen A, Zhao YD, Munshi A, Ramesh R. 2018. Chemo-biologic combinatorial drug delivery using folate receptor-targeted dendrimer nanoparticles for lung cancer treatment. *Nanomedicine* **14**(2): 373-384.

Apiyo D, Wittung-Stafshede P. 2005. Unique complex between bacterial azurin and tumor-suppressor protein p53. *Biochem Biophys Res Commun* **332**: 965-968.

Araújo F, das Neves J, Martins JP, Granja PL, Santos HA, Sarmento B. 2017. Functionalized materials for multistage platforms in the oral delivery of biopharmaceuticals. *Prog Mater Sci* **89**: 306-344.

Attia MF, Anton N, Wallyn J, Omran Z, Vandamme TF. 2019. An overview of active and passive targeting strategies to improve the nanocarriers efficiency to tumour sites. *J Pharm Pharmacol* **71**(8): 1185-1198.

Azar HA, Hansen CT, Costa J. 1980. N:NIH(S)-nu/nu mice with combined immunodeficiency: a new model for human tumor heterotransplantation. *J Natl Cancer Inst* **65**(2): 421-430.

Baião A, Sousa F, Oliveira V, Oliveira C, Sarmento B. 2020. Effective intracellular delivery of bevacizumab via PEGylated polymeric Nanoparticles targeting CD44v6 receptor in colon cancer cells. *Biomater Sci* **8**: 1-10.

Baidya G, Tiwary R, Mudassir M, Singh N, Saha S, Chosdol K, Sinha S, Chattopadhyay P. 2020. Passive internalization and active extrusion determines PLGA-nanoparticle concentration in cancer cell lines. *Nanomedicine (Lond)* **15**(23): 2229-2239.

Baker EN. 1994. Copper proteins with type 1 sites, King RB, ed.; Encyclopedia of inorganic chemistry: Chichester, UK, pp. 883-923.

Bazak R, Houri M, Achy SEL, Hussein W, Refaat T. 2014. Passive targeting of NPs to cancer: A comprehensive review of the literature. *Mol Clin Oncol* **2**: 904-908.

Bergman E, Forsell P, Persson EM, Knutson L, Dickinson P, Smith R, Swaisland H, Farmer MR, Cantarini MV, Lennernäs H. 2007. Pharmacokinetics of gefitinib in humans: the influence of gastrointestinal factors. *Int J Pharm* **341**(1-2): 134-142.

Bernardes N, Abreu S, Carvalho FA, Fernandes F, Santos NC, Fialho AM. 2016. Modulation of membrane properties of lung cancer cells by azurin enhances the sensitivity to EGFR-targeted therapy and decreased β1 integrin-mediated adhesion. *Cell Cycle* **20**: 1-10.

Bernardes N, Chakrabarty AM, Fialho AM. 2013b. Engineering of bacterial strains and their products for cancer therapy. *Appl Microbiol Biotechnol* **97**(12): 5189-5199.

Bernardes N, Fialho AM. 2018. Perturbing the Dynamics and Organization of Cell Membrane Components: A New Paradigm for Cancer-Targeted Therapies. *Int J Mol Sci* **19**(12): 3871.

Bernardes N, Garizo AR, Pinto SN, Caniço B, Perdigão C, Fernandes F, Fialho AM. 2018. Azurin interaction with the lipid raft components ganglioside GM-1 and caveolin-1 increases membrane fluidity and sensitivity to anti-cancer drugs. *Cell Cycle* **17**: 1649-1666.

Bernardes N, Ribeiro AS, Abreu S, Mota B, Matos RG, Arraiano CM, Seruca R, Paredes J, Fialho AM. 2013a. The bacterial protein azurin impairs invasion and FAK/Src signaling in P-cadherin-overexpressing breast cancer cell models. *PLoS One* **8**(7): e69023.

Bernardes N, Ribeiro AS, Abreu S, Vieira AF, Carreto L, Santos M, Seruca R, Paredes J, Fialho AM. 2014. High-Throughput Molecular Profiling of a P-Cadherin Overexpressing Breast Cancer Model Reveals New Targets for the Anti-Cancer Bacterial Protein Azurin. *Int J Biochem Cell Biol* **50**: 1-9.

Bernardes N, Seruca R, Chakrabarty AM, Fialho AM. 2010. Microbial-based therapy of cancer: current progress and future prospects. *Bioeng Bugs* **1**: 178-190.

Bharti C, Nagaich U, Pal AK, Gulati N. 2015. Mesoporous silica nanoparticles in target drug delivery system: A review. *Int J Pharm Investig* **5**: 124-133.

Bilan R, Nabiev I, Sukhanova A. 2016. Quantum Dot-Based Nanotools for Bioimaging, Diagnostics, and Drug Delivery. *Chembiochem* **17**: 2103-2114.

Bilati U, Allémann E, Doelker E. 2005. Development of a nanoprecipitation method intended for the entrapment of hydrophilic drugs into nanoparticles. *Eur J Pharm Sci* **24**: 67-75.

Biswas AK, Islam MR, Choudhury ZS, Mostafa A, Kadir MF. 2014. Nanotechnology based approaches in cancer therapeutics. *Adv Nat Sci Nanosci Nanotechnol* **5**: 1-11.

Bizzarri AR, Moscetti I, Cannistraro S. 2019. Interaction of the anticancer p28 peptide with p53-DBD as studied by fluorescence, FRET, docking and MD simulations. *Biochim Biophys Acta Gen Subj* **1863**(2): 342-350.

Bizzarri AR, Santini S, Coppari E, Bucciantini M, Di Agostino S, Yamada T, Beattie CW, Cannistraro S. 2011. Interaction of an anticancer peptide fragment of azurin with p53 and its isolated domains studied by atomic force spectroscopy. *Int J Nanomedicine* **6**: 3011-3019.

Bollu LR, Katreddy RR, Blessing AM, Pham N, Zheng B, Wu X, Weihua Z. 2015. Intracellular activation of EGFR by fatty acid synthase dependent palmitoylation. *Oncotarget* **6**(33): 34992-35003.

Booysen LL, Kalombo L, Brooks E, Hansen R, Gilliland J, Gruppo V, Lungenhofer P, Semete-Makokotlela B, Swai HS, Kotze AF, Lenaerts A, du Plessis LH. 2013. *In vivo/in vitro* pharmacokinetic and pharmacodynamic study of spray-dried poly-(dl-lactic-co-glycolic) acid nanoparticles encapsulating rifampicin and isoniazid. *Int J Pharm* **444**(1-2): 10-17.

Bor G, Diana I, Azmi M, Yaghmur A. 2019. Nanomedicines for cancer therapy: current status, challenges and future prospects. *Ther Deliv* **10**: 113-132.

Bourseau-Guilmain E, Menard JA, Lindqvist E, Indira Chandran V, Christianson HC, Cerezo Magaña M, Lidfeldt J, Marko-Varga G, Welinder C, Belting M. 2016. Hypoxia regulates global membrane protein endocytosis through caveolin-1 in cancer cells. *Nat Commun* **7**:11371.

Bray F, Ferlay J, Soerjomataram I, Siegel RL, Torre LA, Jemal A. 2018. Global Cancer Statistics 2018: GLOBOCAN Estimates of Incidence and Mortality Worldwide for 36 Cancers in 185 Countries. *CA Cancer J Clin* **68**(6): 394-424.

Bray F, Jemal A, Grey N, Ferlay J, Forman D. 2012. Global cancer transitions according to the Human Development Index (2008-2030): a population-based study. *Lancet Oncol* **13**(8): 790-801.

Byers LA, Diao L, Wang J, Saintigny P, Girard L, Peyton M, Shen L, Fan Y, Giri U, Tumula PK, Nilsson MB, Gudikote J, Tran H, Cardnell RJG, Bearss DJ, Warner SL, Foulks JM, Kanner SB, Gandhi V, Krett N, Rosen ST, Kim ES, Herbst RS, Blumenschein GR, Lee JJ, Lippman SM, Ang KK, Mills GB, Hong WK, Weinstein JN, Wistuba II, Coombes KR, Minna JD, Heymach JV. 2013. An epithelial-mesenchymal transition gene signature predicts resistance to EGFR and PI3K inhibitors and identifies Axl as a therapeutic target for

overcoming EGFR inhibitor resistance. *Clin Cancer Res* **19**(1): 279-290.

Byrne JD, Betancourt T, Brannon-Peppas L. 2008. Active targeting schemes for nanoparticle systems in cancer therapeutics. *Adv Drug Deliv Rev* **60**: 1615-1626.

Cadranel J, Ruppert AM, Beau-Faller M, Wislez M. 2013. Therapeutic strategy for advanced EGFR mutant non-small-cell lung carcinoma. *Crit Rev Oncol Hematol* **88**(3): 477-493.

Calzoni E, Cesaretti A, Polchi A, Michele A Di, Tancini B, Emiliani C. 2019. Biocompatible Polymer NPs for Drug Delivery Applications in Cancer and Neurodegenerative Disorder Therapies. *J Funct Biomater* **10**: 1-15.

Cartiera MS, Johnson KM, Rajendran V, Caplan MJ, Saltzman WM. 2009. The uptake and intracellular fate of PLGA nanoparticles in epithelial cells. *Biomaterials* **30**(14): 2790-2798.

Castro F, Pinto ML, Pereira CL, Serre K, Barbosa MA, Vermaelen K, Gärtner F, Gonçalves RM, De Wever O, Oliveira MJ. 2020. Chitosan/γ-PGA nanoparticles-based immunotherapy as adjuvant to radiotherapy in breast cancer. *Biomaterials* **257**: 120218.

Chakrabarty AM, Bernardes N, Fialho AM. 2014. Bacterial Proteins and Peptides in Cancer Therapy: Today and Tomorrow. *Bioengineered* **5**(4): 234-242.

Chanvorachote P, Pongrakhananon V, Halim H. 2015. Caveolin-1 regulates metastatic behaviors of anoikis resistant lung cancer cells. *Mol Cell Biochem* **399**(1-2): 291-302.

Chari RV. 2008. Targeted cancer therapy: conferring specificity to cytotoxic drugs. *Acc Chem Res* **41**(1): 98-107.

Chaudhari A, Mahfouz M, Fialho AM, Yamada T, Granja AT, Zhu Y, Hashimoto W, Schlarb-Ridley B, Cho W, Das Gupta TK, Chakrabarty AM. 2007. Cupredoxin-cancer interrelationship: azurin binding with EphB2, interference in EphB2 tyrosine phosphorylation, and inhibition of cancer growth. *Biochemistry* **46**(7): 1799-810.

Chen D, Dougherty CA, Zhu K, Hong H. 2015. Theranostic applications of carbon nanomaterials in cancer: Focus on imaging and cargo delivery. *J Control Release* **210**: 230-245.

Chen G, Qiu H, Prasad PN, Chen X. 2014. Upconversion NPs: Design, Nanochemistry, and Applications in Theranostics. *Chem Rev* **114**: 5161-5214.

Chen HH, Lu IL, Liu TI, Tsai YC, Chiang WH, Lin SC, Chiu HC. 2019. Indocyanine green/doxorubicin-encapsulated functionalized nanoparticles for effective combination therapy against human MDR breast cancer. *Colloids Surf B Biointerfaces* **177**: 294-305.

Chen J, Li S, Shen Q. 2012. Folic acid and cell-penetrating peptide conjugated PLGA-PEG bifunctional NPs for vincristine sulfate delivery. *Eur J Pharm Sci* **47**: 430-443.

Chen T, Shukoor MI, Wang R, Zhao Z, Yuan Q, Bamrungsap S, Xiong X and Tan W. 2011. Smart multifunctional nanostructure for targeted cancer chemotherapy and magnetic resonance imaging. *ACS Nano* **5**: 7866-7873.

Chiangjong W, Chutipongtanate S, Hongeng S. 2020. Anticancer peptide:

Physicochemical property, functional aspect and trend in clinical application (Review). *Int J Oncol* **57**(3): 678-696.

Choi JH, Lee MH, Cho YJ, Park BS, Kim S, Kim GC. 2011. The bacterial protein azurin enhances sensitivity of oral squamous carcinoma cells to anticancer drugs. *Yonsei Med J* **52**: 773-778.

Coelho LF. 2017. Anticancer activity of CT-p19LC, a synthetic peptide derived from the bacterial protein azurin. Master of science degree in Microbiology, Instituto Superior Técnico, University of Lisbon (Portugal).

Cole SPC. 2014. Targeting multidrug resistance protein 1 (MRP1, ABCC1): past, present, and future. *Annu Rev Pharmacol Toxicol* **54**: 95-117.

Colin D, Limagne E, Jeanningros S, Jacquel A, Lizard G, Athias A, Gambert P, Hichami A, Latruffe N, Solary E, Delmas D. 2011. Endocytosis of resveratrol via lipid rafts and activation of downstream signaling pathways in cancer cells. *Cancer Prev Res (Phila)* **4**(7): 1095-1106.

Coppari E, Yamada T, Bizzarri AR, Beattie CW, Cannistraro S. 2014. A nanotechnological, molecular-modeling, and immunological approach to study the interaction of the anti-tumorigenic peptide p28 with the p53 family of proteins. *Int J Nanomedicine* **9**:1799-1813.

Costa Verdera H, Gitz-Francois JJ, Schiffelers RM, Vader P. 2017. Cellular uptake of extracellular vesicles is mediated by clathrin-independent endocytosis and macropinocytosis. *J Control Release* **266**: 100-108.

Coté ML, Liu M, Bonassi S, Neri M, Schwartz AG, Christiani DC, Spitz MR, Muscat JE, Rennert G, Aben KK, Andrew AS, Bencko V, Bickeböller H, Boffetta P, Brennan P, Brenner H, Duell EJ, Fabianova E, Field JK, Foretova L, Friis S, Harris CC, Holcatova I, Hong YC, Isla D, Janout V, Kiemeney LA, Kiyohara C, Lan Q, Lazarus P, Lissowska J, Le Marchand L, Mates D, Matsuo K, Mayordomo JI, McLaughlin JR, Morgenstern H, Müeller H, Orlow I, Park BJ, Pinchev M, Raji OY, Rennert HS, Rudnai P, Seow A, Stucker I, Szeszenia-Dabrowska N, Dawn Teare M, Tjønnelan A, Ugolini D, van der Heijden HF, Wichmann E, Wiencke JK, Woll PJ, Yang P, Zaridze D, Zhang ZF, Etzel CJ, Hung RJ. 2012. Increased risk of lung cancer in individuals with a family history of the disease: a pooled analysis from the International Lung Cancer Consortium. *Eur J Cancer* **48**(13): 1957-1968.

Cozens AL, Yezzi MJ, Kunzelmann K, Ohrui T, Chin L, Eng K, Finkbeiner WE, Widdicombe JH, Gruenert D. 1994. CFfR Expression and Chloride Secretion in Polarized Immortal Human Bronchial Epithelial Cells. *Am J Respir Cell Mol Bio* **10**: 38-47.

CPPsite 2.0, 2021. CPPsite 2.0 database of Cell-Penetrating Peptides. Available: https://webs.iiitd.edu.in/raghava/cppsite/stats1.php. Accessed on: 15th April 2021.

Cryer AM, Thorley AJ. 2019. Nanotechnology in the diagnosis and treatment of lung cancer. *Pharmacol Ther* **198**: 189-205.

Cupic KI, Rennick JJ, Johnston AP, Such GK. 2019. Controlling endosomal escape using nanoparticle composition: current progress and future perspectives. *Nanomedicine (Lond)* **14**(2): 215-223.

Damyanov CA, Maslev IK, Pavlov VS, Avramov L. 2018. Conventional Treatment of Cancer Realities and Problems. *Ann Complement Altern Med* **1**(1): 1002.

Danaei M, Dehghankhold M, Ataei S, Hasanzadeh Davarani F, Javanmard R, Dokhani A, Khorasani S, Mozafari MR. 2018. Impact of Particle Size and Polydispersity Index on the Clinical Applications of Lipidic Nanocarrier Systems. *Pharmaceutics* **10**(2): 57.

Danhier F, Ansorena E, Silva JM, Coco R, Le Breton A, Préat V. 2012. PLGA-based NPs: an overview of biomedical applications. *J Control Release* **161**: 505-522.

Danhier F, Feron O, Préat V. 2010. To exploit the tumor microenvironment: Passive and active tumor targeting of nanocarriers for anti-cancer drug delivery. *J Control Release* **148**(2): 135-146.

Da Silva CG, Peters GJ, Ossendorp F, Cruz LJ. 2017. The potential of multi-compound NPs to bypass drug resistance in cancer. *Cancer Chemother Pharmacol* **80**: 881-894.

das Neves J, Sarmento B. 2015. Precise engineering of dapivirine-loaded nanoparticles for the development of anti-HIV vaginal microbicides. *Acta Biomater* **18**: 77-87.

Davis FF. 2002. The origin of pegnology. *Adv Drug Deliv Rev* **54**(4): 457-458.

del Carmen Fernández-Alonso M, Díaz D, Berbis MÁ, Marcelo F, Cañada J, Jiménez-Barbero J. 2012. Protein-carbohydrate interactions studied by NMR: from molecular recognition to drug design. *Curr Protein Pept Sci* **13**(8): 816-830.

del Pozo MA, Balasubramanian N, Alderson NB, Kiosses WB, Grande-García A, Anderson RG, Schwartz MA. 2005. Phospho-caveolin-1 mediates integrin-regulated membrane domain internalization. *Nat Cell Biol* **7**(9): 901-908.

Derakhshankhah H, Jafari S. 2018. Cell penetrating peptides: A concise review with emphasis on biomedical applications. *Biomed Pharmacother* **108**: 1090-1096.

De Rienzo F, Gabdoulline RR, Menziani MC, Wade RC. 2000. Blue copper proteins: a comparative analysis of their molecular interaction properties. *Protein Sci* **9**(8): 1439-1454.

Desai MP, Labhasetwar V, Walter E, Levy RJ, Amidon GL. 1997. The mechanism of uptake of biodegradable microparticles in Caco-2 cells is size dependent. *Pharm Res* **14**: 1568-1573.

Desai P, Patlolla RR, Singh M. 2010. Interaction of nanoparticles and cellpenetrating peptides with skin for transdermal drug delivery. *Mol Membr Biol* **27**(7): 247-259.

Dinarvand R, Sepehri N, Manoochehri S, Rouhani H, Atyabi F. 2011. Polylactide-co-glycolide NPs for controlled delivery of anticancer agents. *Int J Nanomedicine* **6**: 877-895.

Din F, Aman W, Ullah I, Qureshi OS, Mustapha O, Shafique S, Zeb A. 2017. Effective use of nanocarriers as drug delivery systems for the treatment of selected tumors. *Int J Nanomedicine* **12**: 7291-7309.

Ding D, Zhu Q. 2018. Recent advances of PLGA micro/nanoparticles for the delivery of biomacromolecular therapeutics. *Mater Sci Eng C Mater Biol App* **92**: 1041-1060.

Domingues MM, Santiago PS, Castanho MA, Santos NC. 2008. What can light scattering spectroscopy do for membrane-active peptide studies? *J Pept Sci* **14**(4): 394-400.

Domvri K, Petanidis S, Anestakis D, Porpodis K, Bai C, Zarogoulidis P, Freitag L, Hohenforst-Schmidt W, Katopodi T. 2020. Dual photothermal MDSCs-targeted immunotherapy inhibits lung immunosuppressive metastasis by enhancing T-cell recruitment. *Nanoscale* **12**(13): 7051-7062.

Dornan D, Bheddah S, Newton K, Ince W, Frantz GD, Dowd P, Koeppen H, Dixit VM, French DM. 2004. COP1, the negative regulator of p53, is overexpressed in breast and ovarian adenocarcinomas. *Cancer Res* **64**: 7226-7230.

Dreaden EC, Alkilany AM, Huang X, Murphy CJ, El-Sayed MA. 2012. The golden age: gold NPs for biomedicine. *Chem Soc Rev* **41**: 2740-2779.

Duan T, Xu Z, Sun F, Wang Y, Zhang J, Luo C, Wang M. 2019. HPA aptamer functionalized paclitaxel-loaded PLGA nanoparticles for enhanced anticancer therapy through targeted effects and microenvironment modulation. *Biomed Pharmacother* **117**: 109121.

Duan X, He C, Kron SJ, Lin W. 2016. Nanoparticle formulations of cisplatin for cancer therapy. *Wiley Interdiscip Rev Nanomed Nanobiotechnol* **8**(5): 776-791.

Duncan R, Izzo L. 2005. Dendrimer biocompatibility and toxicity. *Adv Drug Deliv Rev* **57**: 2215-2237.

Eftekhari RB, Maghsoudnia N, Samimi S, Zamzami A, Dorkoosh FA. 2019. Co-Delivery Nanosystems for Cancer Treatment: A Review. *Pharm Nanotechnol* **7**(2): 90-112.

Ehrenstein G, Lecar H. 1977. Electrically gated ionic channels in lipid bilayers. *Q Rev Biophys* **10**: 1-34.

Elsaesser A, Howard CV. 2012. Toxicology of NPs. *Adv Drug Deliv Rev* **64**: 129-137.

Escribá PV, Busquets X, Inokuchi J, Balogh G, Török Z, Horváth I, Harwood JL, Vígh L. 2015. Membrane lipid therapy: Modulation of the cell membrane composition and structure as a molecular base for drug discovery and new disease treatment. *Prog Lipid Res* **59**: 38-53.

Evangelisti E, Cascella R, Becatti M, Marrazza G, Dobson CM, Chiti F, Stefani M, Cecchi C. 2016. Binding affinity of amyloid oligomers to cellular membranes is a generic indicator of cellular dysfunction in protein misfolding diseases. *Sci Rep* **6**: 32721.

Falanga A, Lombardi L, Galdiero E, Genio VD, Galdiero S. 2020. The world of cell penetrating: the future of medical applications. *Future Med Chem* **12**(15): 1431-1446.

Farjadian F, Ghasemi A, Gohari O, Roointan A, Karimi M, Hamblin MR. 2019. Nanopharmaceuticals and nanomedicines currently on the market: challenges and opportunities. *Nanomedicine (Lond)* **14**(1): 93-126.

Fernandes E, Ferreira D, Peixoto A, Freitas R, Relvas-Santos M, Palmeira C, Martins G, Barros A, Santos LL, Sarmento B, Ferreira JA. 2019. Glycoengineered nanoparticles

enhance the delivery of 5-fluoroucil and paclitaxel to gastric cancer cells of high metastatic potential. *Int J Pharm* **570**: 118646.

Fernández VA, Viñuela AL, Velasco PJ, Hernández AP, Perez AO, Román RM, Gongora R, Fuentes M. 2020. Nanomedicine and Onco-Immunotherapy: From the Bench to Bedside to Biomarkers. *Nanomaterials (Basel)* **10**(7): 1274.

Fessi H, Puisieux F, Devissaguet J, Ammoury N, Benita S. 1989 Nanocapsule formation by interfacial polymer deposition following solvent displacement. *Int J Pharm* **55**: 1-4.

Fialho AM, Bernardes N, Chakrabarty AM. 2016. Exploring the anticancer potential of the bacterial protein azurin. *AIMS Microbiology* **2**: 292-303.

Fialho AM, Salunkhe P, Manna S, Mahali S, Chakrabarty AM. 2012. Glioblastoma multiforme: novel therapeutic approaches. *ISRN Neurol* **2012**: 642345.

Fialho AM, Stevens FJ, Das Gupta TK, Chakrabarty AM. 2007. Beyond host-pathogen interactions: microbial defense strategy in the host environment. *Curr Opin Biotechnol* **18**: 279-286.

Fidler MM, Bray F, Soerjomataram I. 2018. The global cancer burden and human development: A review. *Scand J Public Health* **46**(1): 27-36.

Fiedler K, Lazzaro S, Lutz J, Rauch S, Heidenreich R. 2016. MRNA Cancer Vaccines. *Recent Results Cancer Res* **209**: 61-84.

FOOD AND DRUG ADMINISTRATION, 2020. Drug Approval Package. Available: https://www.fda.gov/. Accessed on: 6th May 2020.

Forssen EA, Lee MJA, Schmidt PG, Krasieva TB, Shimizu S. 1996. Fluorescence Imaging Studies for the Disposition of Daunorubicin (DaunoXome) within Tumor Tissue. *Cancer Res* **56**: 2066-2076.

Fredenberg S, Wahlgren M, Reslow M, Axelsson A. 2011. The mechanisms of drug release in poly (lactic-co-glycolic acid)-based drug delivery systems — A review. *Int J Pharm* **415**: 34-52.

Freire JM, Domingues MM, Matos J, Melo MN, Veiga AS, Santos NC, Castanho MARB. 2011. Using zeta-potential measurements to quantify peptide partition to lipid membranes. *Eur Biophys J* **40**: 481-487.

Fujimoto T, Kogo H, Nomura R, Une T. 2000. Isoforms of caveolin-1 and caveolar structure. *J Cell Sci* **19**: 3509-3517.

Gabernet G, Müller AT, Hiss JA, Schneider G. 2016. Membranolytic anticancer peptides. *Med Chem Commun* **7**(12): 1-14.

Garon EB, Halmos B, Rina H, Leighl N, Lee SS, Walsh W, Dragnev K, Piperdi B, Rodriguez LP-A, Shinwari N, Wei Z. 2016. Phase III study of carboplatin-paclitaxel/nab-paclitaxel chemotherapy with or without pembrolizumab for first-line metastatic, squamous non-small cell lung carcinoma: kEYNOTE-407. *J Immunother Cancer* **4**(Suppl 1): P138.

Gaspar D, Veiga AS, Castanho MARB. 2013. From Antimicrobial to Anticancer Peptides.

A Review. *Front Microbiol* **4**: 1-16.

Gaumet M, Vargas A, Gurny R, Delie F. 2008. NPs for drug delivery:The need for precision in reporting particle size parameters. *Eur J Pharm Biopharm* **69**: 1-9.

Gaus K, Gratton E, Kable EP, Jones AS, Gelissen I, Kritharides L, Jessup W. 2003. Visualizing lipid structure and raft domains in living cells with two-photon microscopy. *Proc Natl Acad Sci USA* **100**(26): 15554-15559.

Gessner I, Neundorf I. 2020. Nanoparticles Modified with Cell-Penetrating Peptides: Conjugation Mechanisms, Physicochemical Properties, and Application in Cancer Diagnosis and Therapy. *Int J Mol Sci* **21**(7): 2536.

Glantz MJ, Jaeckle KA, Chamberlain MC, Phuphanich S, Recht L, Swinnen LJ, Maria B, Lafollette S, Schumann GB, Cole BF, Howell SB. 1999. A Randomized Controlled Trial Comparing Intrathecal Sustained- release Cytarabine (DepoCyt) to Intrathecal Methotrexate in Patients with Neoplastic Meningitis from Solid Tumors. *Clin Cancer Res* **5**: 3394-3402.

GLOBOCAN, 2020. Cancer today. Available: https://gco.iarc.fr/today/home. Accessed on: 7th February 2021.

Gomes Dos Reis L, Traini D. 2020. Advances in the use of cell penetrating peptides for respiratory drug delivery. *Expert Opin Drug Deliv* **17**(5): 647-664.

Gong X, Zheng Y, He G, Chen K, Zeng X, Chen Z. 2019. Multifunctional nanoplatform based on star-shaped copolymer for liver cancer targeting therapy. *Drug Deliv* **26**(1): 595-603.

Goto M, Yamada T, Kimbara K, Horner J, Newcomb M, Gupta TK, Chakrabarty AM. 2003. Induction of apoptosis in macrophages by *Pseudomonas aeruginosa* azurin: tumour-suppressor protein p53 and reactive oxygen species, but not redox activity, as critical elements in cytotoxicity. *Mol Microbiol* **47**(2): 549-559.

Gou Y, Miao D, Zhou M, Wang L, Zhou H, Su G. 2018. Bio-Inspired Protein-Based Nanoformulations for Cancer Theranostics. *Front Pharmacol* **9**: 1-19.

Green MR, Manikhas GM, Orlov S, Afanasyev B, Makhson AM, Bhar P, Hawkins MJ. 2006. Abraxane, a novel Cremophor-free, albumin-bound particle form of paclitaxel for the treatment of advanced non-small-cell lung cancer. *Ann Oncol* **17**(8): 1263-1268.

Groot PM, Wu CC, Carter BW, Munden RF. 2018. The epidemiology of lung cancer. *Transl Lung Cancer Res* **7**(3): 220-233.

Guaglianone P, Chan K, Delaflor-weiss E, Hanisch R, Jeffers S. 1994. Phase I and pharmacologic study of liposomal daunorubicin (DaunoXome). *Invest New Drugs* **12**: 103-110.

Guan J, Qian J, Zhan C. 2019. Preparation of Cholera Toxin Subunit B Functionalized Nanoparticles for Targeted Therapy of Glioblastoma. *Methods Mol Biol* **2059**: 207-212.

Gurunathan S, Kang M, Qasim M. 2018. Nanoparticle-Mediated Combination Therapy:

Two-in-One Approach for Cancer. *Int J Mol Sci* **19**(10). pii: E3264.

Habault J, Poyet JL. 2019. Recent Advances in Cell Penetrating Peptide-Based Anticancer Therapies. *Molecules* **24**(5): 927.

Hao G, Xu ZP, Li L. 2018. Manipulating extracellular tumour pH: an effective target for cancer therapy. *RSC Adv* **8**: 22182.

Harris F, Dennison SR, Singh J, Phoenix DA. 2013. On the Selectivity and Efficacy of Defense Peptides with Respect to Cancer Cells. *Med Res Rev* **33**: 190-234.

Haug BE, Camilio KA, Eliassen LT, Stensen W, Svendsen JS, Berg K, Mortensen B, Serin G, Mirjolet J-F, Bichat F, Rekdal Ø. 2016. Discovery of a 9-Mer Cationic Peptide (LTX-315) as a Potential First in Class Oncolytic Peptide. *J Med Chem* **59**: 2918-2927.

Hetz C, Bono MR, Barros LF, Lagos R. 2002. Microcin E492, a Channel-Forming Bacteriocin from *Klebsiella Pneumoniae*, Induces Apoptosis in Some Human Cell Lines. *Proc Natl Acad Sci* **99**: 2696-2701.

Hey T, Fiedler E, Rudolph R, Fiedler M. 2005. Artificial, non-antibody binding proteins for pharmaceutical and industrial applications. *Trends Biotechnol* **23**(10): 514-22.

Hilchie A, Doucette C, Pinto D, Patrzykat A, Douglas S, Hoskin D. 2011. Pleurocidinfamily cationic antimicrobial peptides are cytolytic for breast carcinoma cells and prevent growth of tumor xenografts. *Breast Cancer Res* **13**: R102.

Hilchie AL, Hoskin DW. 2010. Application of cationic antimicrobial peptides in cancer treatment: laboratory investigations and clinical potential. In: Emerging cancer therapy: microbial approaches and biotechnological tools. Wiley, Hoboken, pp. 309-332.

Hilchie AL, Hoskin DW. 2019. Power Coombs MR, Anticancer activities of natural and synthetic peptides. In Antimicrobial Peptides: Basics for Clinical Application. Matsuzaki K, Ed, Springer: Singapore, pp. 131-147.

Hoffmann K, Milech N, Juraja SM, Cunningham PT, Stone SR, Francis RW, Anastasas M, Hall CM, Heinrich T, Bogdawa HM, Winslow S, Scobie MN, Dewhurst RE, Florez L, Ong F, Kerfoot M, Champain D, Adams AM, Fletcher S, Viola HM, Hool LC, Connor T, Longville BAC, Tan YF, Kroeger K, Morath V, Weiss GA, Skerra A, Hopkins RM, Watt PM. 2018. A platform for discovery of functional cell-penetrating peptides for efficient multi-cargo intracellular delivery. *Sci Rep* **8**(1):12538.

Hojjat-Farsangi M. 2014. Small-molecule inhibitors of the receptor tyrosine kinases: promising tools for targeted Cancer therapies. *Int J Mol Sci* **15**(8): 13768-13801.

Hong CS, Yamada T, Fialho AM, Das Gupta TK, Chakrabarty AM inventors; The Board of Trustees of the University of Illinois, assignee. Transport agents for crossing the blood-brain barrier and into brain cancer cells, and methods of use thereof. US patent 8,188,251. October 4, 2010.

Hoskin DW, Ramamoorthy A. 2008. Studies on Anticancer Activities of Antimicrobial Peptides. *Biochim Biophys Acta - Biomembr* **1778**: 357-375.

Howard MD, Jay M, Dziubla TD, Lu X. 2008. PEGylation of nanocarrier drug delivery systems: State of the art. *J Biomed Nanotechnol* **4**: 133-148.

Hrkach J, Von Hoff D, Mukkaram Ali M, Andrianova E, Auer J, Campbell T, De Witt D, Figa M, Figueiredo M, Horhota A, Low S, McDonnell K, Peeke E, Retnarajan B, Sabnis A, Schnipper E, Song JJ, Song YH, Summa J, Tompsett D, Troiano G, Van Geen Hoven T, Wright J, LoRusso P, Kantoff PW, Bander NH, Sweeney C, Farokhzad OC, Langer R, Zale S. 2012. Preclinical development and clinical translation of a PSMA-targeted docetaxel nanoparticle with a differentiated pharmacological profile. *Sci Transl Med* **4**(128): 128ra39.

Hubert A, Lyass O, Pode D, Gabizon A. 2000. Doxil (Caelyx): An exploratory study with pharmacokinetics in patients with hormone-refractory prostate cancer. *Anticancer Drugs* **11**: 23-127.

Ichikawa N, Iwabuchi K, Kurihara H, Ishii K, Kobayashi T, Sasaki T, Hattori N, Mizuno Y, Hozumi K, Yamada Y, Arikawa-Hirasawa E. 2009. Binding of laminin-1 to monosialoganglioside GM1 in lipid rafts is crucial for neurite outgrowth. *J Cell Sci* **122**(Pt 2): 289-299.

Immordino ML, Cattel L. 2006. Stealth liposomes : review of the basic science , rationale , and clinical applications , existing and potential. *Int J Nanomedicine* **3**: 297-315.

Inoue A, Saijo Y, Maemondo M, Gomi K, Tokue Y, Kimura Y, Ebina M, Kikuchi T, Moriya T, Nukiwa T. 2003. Severe acute interstitial pneumonia and gefitinib. *Lancet* **361**(9352): 137-139.

Inthagard J, Edwards J, Roseweir AK. 2019. Immunotherapy: enhancing the efficacy of this promising therapeutic in multiple cancers. *Clin Sci (Lond)* **133(2)**: 181-193.

Iqbal J, Abbasi BA, Ahmad R, Mahmood T, Ali B, Khalil AT, Kanwal S, Shah SA, Alam MM, Badshah H, Munir A. 2018. Nanomedicines for developing cancer nanotherapeutics: from benchtop to bedside and beyond. *Appl Microbiol Biotechnol* **102**(22): 9449-9470.

Irwin ME, Mueller KL, Bohin N, Ge Y, Boerner JL. 2011. Lipid raft localization of EGFR alters the response of cancer cells to the EGFR tyrosine kinase inhibitor gefitinib. *J Cell Physiol* **226**: 2316-2328.

Ishii H, Azuma K, Sakai K, Kawahara A, Yamada K, Tokito T, Okamoto I, Nishio K, Hoshino T. 2015. Digital PCR analysis of plasma cell-free DNA for non-invasive detection of drug resistance mechanisms in EGFR mutant NSCLC: correlation with paired tumor samples. *Oncotarget* **6**(31): 30850-30858.

Jaeckle KA, Batchelor T, O'Day SJ, Phuphanich S, New P, Lesser G, Cohn A, Gilbert M, Aiken R, Heros D, Rogers L, Wong E, Fulton D, Gutheil JC, Baidas S, Kennedy JM, Mason W, Moots P, Russell C, Swinnen LJ, Howell SB. 2002. An open label trial of sustained-release cytarabine (DepoCyt) for the intrathecal treatment of solid tumor neoplastic meningitis. *J Neurooncol* **57**: 231-239.

Jahan ST, Sadat SMA, Walliser M, Haddadi A. 2017. Targeted Therapeutic NPs: An Immense Promise to Fight against Cancer. *J Drug Deliv* **2017**: 1-24.

Jeannot V, Gauche C, Mazzaferro S, Couvet M, Vanwonterghem L, Henry M, Didier C, Vollaire J, Josserand V, Coll JL, Schatz C, Lecommandoux S, Hurbin A. 2018. Anti-tumor efficacy of hyaluronan-based nanoparticles for the co-delivery of drugs in lung cancer. *J Control Release* **275**: 117-128.

Jia L, Gorman GS, Coward LU, Noker PE, McCormick D, Horn TL, Harder JB, Muzzio M, Prabhakar B, Ganesh B, Das Gupta TK, Beattie CW. 2011. Preclinical pharmacokinetics, metabolism, and toxicity of azurin-p28 (NSC745104) a peptide inhibitor of p53 ubiquitination. *Cancer Chemother Pharmacol* **68**(2): 513-524.

Jin C, Bai L, Lin L, Wang S, Yin X. 2018. Paclitaxel-loaded nanoparticles decorated with bivalent fragment HAb18 F(ab')2 and cell penetrating peptide for improved therapeutic effect on hepatocellular carcinoma. *Artif Cells Nanomed Biotechnol* **46**(5): 1076-1084.

Johansson HJ, El-Andaloussi S, Holm T, Mäe M, Jänes J, Maimets T, Langel U. 2008. Characterization of a novel cytotoxic cell-penetrating peptide derived from p14ARF protein. *Mol Ther* **16**(1): 115-123.

Judson I, Radford JA, Harris M, Blay J, Hoesel Q Van. 2001. Randomised phase II trial of pegylated liposomal doxorubicin (DOXIL/CAELYX) versus doxorubicin in the treatment of advanced or metastatic soft tissue sarcoma : a study by the EORTC Soft Tissue and Bone Sarcoma Group. *Eur J Cancer* **37**: 870-877.

Kabary DM, Helmy MW, Abdelfattah EA, Fang JY, Elkhodairy KA, Elzoghby AO. 2018. Inhalable multi-compartmental phospholipid enveloped lipid core nanocomposites for localized mTOR inhibitor/herbal combined therapy of lung carcinoma. *Eur J Pharm Biopharm* **130**: 152-164.

Kahraman E, Güngör S, Özsoy Y. 2017. Potential enhancement and targeting strategies of polymeric and lipid-based nanocarriers in dermal drug delivery. *Ther Deliv* **8**: 967-985.

Kalmouni M, Al-Hosani S, Magzoub M. 2019. Cancer targeting peptides. *Cell Mol Life Sci* **76**(11): 2171-2183.

Kamaly N, Yameen B, Wu J, Farokhzad OC. 2016. Degradable Controlled-Release Polymers and Polymeric NPs: Mechanisms of Controlling Drug Release. *Chem Rev* **116**: 2602-63.

Kato T, Seto T, Nishio M, Goto K, Yamamoto N, Okamoto I, Tao L, Yu W, Khaznadar T, Tajima K, Shibata M, Seki A, Yamamoto N. 2018. Erlotinib plus bevacizumab phase Il study in patients with advanced non-small-cell lung cancer (JO25567): updated safety results. *Drug Saf* **41**: 229-237.

Kaur J, Tikoo K. 2013. p300/CBP dependent hyperacetylation of histone potentiates anticancer activity of gefitinib nanoparticles. *Biochim Biophys Acta* **1833**(5): 1028-1040.

Kim K, Lee J, Kim D, Yoon I. 2019. Recent Progress in the Development of Poly (lactic-co-glycolic acid)-Based Nanostructures for Cancer Imaging and Therapy. *Pharmaceutics* **11**: 280-308.

Kim KY. 2007. Nanotechnology platforms and physiological challenges for cancer

therapeutics. *Nanomedicine* **3**(2): 103-110.

Kopeckova K, Eckschlager T, Sirc J, Hobzova R, Plch J, Hrabeta J, Michalek J. 2019. Nanodrugs used in cancer therapy. *Biomed Pap Med Fac Univ Palacky Olomouc Czech Repub* **163**: 122-131.

Kumar A, Dixit CK. 2017. Methods for characterization of nanoparticles. *Adv Nanomed Delivery Ther Nucleic Acids* 43-58.

Kurrikoff K, Vunk B, Langel Ü. 2021. Status update in the use of cell-penetrating peptides for the delivery of macromolecular therapeutics. *Expert Opin Biol Ther* **21**:3: 361-370.

Lakowicz JR. 2006. Principles of fluorescence spectroscopy. Joseph R. Lakowicz, editor. 3rd ed., Springer US.

Lavie Y, Fiucci G, Liscovitch M. 2001. Upregulation of caveolin in multidrug resistant cancer cells: functional implications. *Adv Drug Deliv Rev* **49**(3): 317-323.

Leamon CP, Low PS. 2001. Folate-mediated targeting: from diagnostics to drug and gene delivery. *Drug Discov Today* **6**: 44-51.

Lee EJ, Yun UJ, Koo KH, Sung JY, Shim J, Ye SK, Hong KM, Kim YN. 2014. Down-regulation of lipid raft-associated onco-proteins via cholesterol-dependent lipid raft internalization in docosahexaenoic acid-induced apoptosis. *Biochim Biophys Acta* **1841**(1): 190-203.

Lee SW, Reimer CL, Oh P, Campbell DB, Schnitzer JE. 1998. Tumor cell growth inhibition by caveolin re-expression in human breast cancer cells. *Oncogene* **16**(11): 1391-1397.

Leuschner C, Hansel W. 2005. Targeting Breast and Prostate Cancers Through Their Hormone Receptors. *Biol Reprod* **73**: 860-865.

Liang J, Lu F, Li B, Liu L, Zeng G, Zhou Q, Chen L. 2019. IRF8 induces senescence of lung cancer cells to exert its tumor suppressive function. *Cell Cycle* **18**(23): 3300-3312.

Libutti SK, Paciotti GF, Byrnes AA, Alexander HR Jr, Gannon WE, Walker M, Seidel GD, Yuldasheva N, Tamarkin L. 2010. Phase I and pharmacokinetic studies of CYT-6091, a novel PEGylated colloidal gold-rhTNF nanomedicine. *Clin Cancer Res* **16**(24): 6139-6149.

Li J, Feng L, Fan L, Zha Y, Guo L, Zhang Q, Chen J, Pang Z, Wang Y, Jiang X, Yang VC, Wen L. 2011. Targeting the brain with PEG-PLGA NPs modified with phage-displayed peptides. *Biomaterials* **32**: 4943-4950.

Lin C, Zhang X, Chen H, Bian Z, Zhang G, Riaz MK, Tyagi D, Lin G, Zhang Y, Wang J, Lu A, Yang Z. 2018. Dual-ligand modified liposomes provide effective local targeted delivery of lung-cancer drug by antibody and tumor lineage-homing cell-penetrating peptide. *Drug Deliv* **25**(1): 256-266.

Lingwood D, Simons K. 2010. Lipid rafts as a membraneorganizing principle. *Science* **327**: 46-50.

Liu Y, Yang G, Jin S, Xu L, Zhao CX. 2020. Development of High-Drug-Loading Nanoparticles. *Chempluschem* **85**(9): 2143-2157.

Li X, Wang J, Li S, Liu Z, Zheng Z, Zhang Y. 2019. Development and Evaluation of Multifunctional Poly(Lactic-co-glycolic acid) Nanoparticles Embedded in Carboxymethyl β-Glucan Porous Microcapsules as a Novel Drug Delivery System for Gefitinib. *Pharmaceutics* **11**(9): 469.

Li YF, Wang DD, Zhao BW, Wang W, Huang CY, Chen YM, Zheng Y, Keshari RP, Xia JC, Zhou ZW. 2012. High level of COP1 expression is associated with poor prognosis in primary gastric cancer. *Int J Biol Sci* **8**: 1168-1177.

Li Y, Li N, Pan W, Yu Z, Yang L, Tang B. 2017. Hollow mesoporous silica NPs with tunable structures for controlled drug delivery. *ACS Appl Mater Interfaces* **9**: 2123-2129.

Li Y, Zhang H. 2019. Nanoparticle-Based Drug Delivery Systems for Enhanced Tumor-Targeting Treatment. *J Biomed Nanotechnol* **15**(1): 1-27.

Li Z, Shu J, Yang B, Zhang Z, Huang J, Chen Y. 2020. Emerging non-invasive detection methodologies for lung cancer. *Oncol Lett* **19**(5): 3389-3399.

Logozzi M, De Milito A, Lugini L, Borghi M, Calabrò L, Spada M, Perdicchio M, Marino ML, Federici C, Iessi E, Brambilla D, Venturi G, Lozupone F, Santinami M, Huber V, Maio M, Rivoltini L, Fais S. 2009. High levels of exosomes expressing CD63 and caveolin-1 in plasma of melanoma patients. *PLoS One* **4**(4): e5219.

Lulla RR, Goldman S, Yamada T, Beattie CW, Bressler L, Pacini M, Pollack IF, Fisher PG, Packer RJ, Dunkel IJ, Dhall G, Wu S, Onar A, Boyett JM, Fouladi M. 2016. Phase 1 trial of p28 (NSC745104), a non-HDM2-mediated peptide inhibitor of p53 ubiquitination in pediatric patients with recurrent or progressive central nervous system tumors: A Pediatric Brain Tumor Consortium Study. *Neuro Oncol* **28**: 1319-1325.

Lundberg P, Langel U. 2003. A brief introduction to cell-penetrating peptides. *J Mol Recognit* **16**: 227-233.

Luo X, Yang Y, Kong F, Zhang L, Wei K. 2019. CD30 aptamer-functionalized PEG-PLGA nanoparticles for the superior delivery of doxorubicin to anaplastic large cell lymphoma cells. *Int J Pharm* **564**: 340-349.

MacKenzie MJ, Hirte HW, Siu LL, Gelmon K, Ptaszynski M, Fisher B, Eisenhauer E. 2004. A phase I study of OSI-211 and cisplatin as intravenous infusions given on days 1, 2 and 3 every 3 weeks in patients with solid cancers. *Ann Oncol* **15**(4): 665-670.

Madani SY, Naderi N, Dissanayake O, Tan A, Seifalian AM. 2011. A new era of cancer treatment: carbon nanotubes as drug delivery tools. *Int J Nanomedicine* **6**: 2963-2979.

Mahmoudi M, Sant S, Wang B, Laurent S, Sen T. 2011. Superparamagnetic iron oxide NPs (SPIONs): Development, surface modification and applications in chemotherapy. *Adv Drug Deliv Rev* **63**: 24-46.

Martínez-Jothar L, Doulkeridou S, Schiffelers RM, Sastre Torano J, Oliveira S, van Nostrum CF, Hennink WE. 2018. Insights into maleimide-thiol conjugation chemistry: Conditions for efficient surface functionalization of nanoparticles for receptor targeting. *J Control Release* **282**: 101-109.

Martínez-Montiel N, Rosas-Murrieta NH, Martínez-Montiel M, Gaspariano-Cholula MP, Martínez-Contreras RD. 2016. Microbial and Natural Metabolites That Inhibit Splicing: A Powerful Alternative for Cancer Treatment. *Biomed Res Int* **2016**: 3681094.

Martinez-Outschoorn UE, Sotgia F, Lisanti MP. 2015. *Caveolae* and signalling in cancer. *Nat Rev Cancer* **15**(4): 225-237.

Martins C, Sousa F, Araújo F, Sarmento B. 2018. Functionalizing PLGA and PLGA Derivatives for Drug Delivery and Tissue Regeneration Applications. *Adv Healthc Mater* **7**: 1-24.

Martins JP, das Neves J, de la Fuente M, Celia C, Florindo H, Günday-Türeli N, Popat A, Santos JL, Sousa F, Schmid R, Wolfram J, Sarmento B, Santos HA. 2020. The solid progress of nanomedicine. *Drug Deliv Transl Res* **10**(3): 726-729.

Masood F. 2016. Polymeric NPs for targeted drug delivery system for cancer therapy. *Mater Sci Eng C* **60**: 569-578.

Matsumura Y, Maeda H. 1986. A New Concept for Macromolecular Therapeutics in Cancer Chemotherapy : Mechanism of Tumoritropic Accumulation of Proteins and the Antitumor Agent Smancs1. *Cancer Res* **46**: 6387-6392.

McNeil S. 2016. Evaluation of nanomedicines: stick to the basics. *Nat Rev Mater* **1**: 16073.

Meel R, Sulheim E, Shi Y, Kiessling F, Mulder WJM, Lammers T. 2019. Smart cancer nanomedicine. *Nat Nanotechnol* **14**(11): 1007-1017.

Menon GK. 2002. New insights into skin structure: scratching the surface. *Adv Drug Deliv Rev* **54**: S3-17.

Mehta RR, Yamada T, Taylor BN, Christov K, King ML, Majumdar D, Lekmine F, Tiruppathi C, Shilkaitis A, Bratescu L, Green A, Beattie CW, Das Gupta TK. 2011. A cell penetrating peptide derived from azurin inhibits angiogenesis and tumor growth by inhibiting phosphorylation of VEGFR-2, FAK and Akt. *Angiogenesis* **14**: 355-369.

Micewicz ED, Jung C, Shaue D, Ewa D, Luong H, McBride WH, Ruchala P. 2011. Small Azurin Derived Peptide Targets Ephrin Receptors for Radiotherapy. *Int J Pept Res Ther* **17**: 247-257.

Mir M, Ahmed N, Rehman AU. Recent applications of PLGA based nanostructures in drug delivery. 2017. *Colloids Surf B Biointerfaces* **159**: 217-231.

Mitchell MJ, Billingsley MM, Haley RM, Wechsler ME, Peppas NA, Langer R. 2020. Engineering precision nanoparticles for drug delivery. *Nat Rev Drug Discov* **4**: 1-24.

Molino NM, Wang SW. 2014. Caged protein NPs for drug delivery. *Curr Opin Biotechnol* **28**: 75-82.

Mollinedo F, Gajate C. 2015. Lipid rafts as major platforms for signaling regulation in cancer. *Adv Biol Regul* **57**: 130-146.

Mondal L, Mukherjee B, Das K, Bhattacharya S, Dutta D, Chakraborty S, Pal MM, Gaonkar RH, Debnath MC. 2019. CD-340 functionalized doxorubicin-loaded nanoparticle induces

apoptosis and reduces tumor volume along with drug-related cardiotoxicity in mice. *Int J Nanomedicine* **14**: 8073-8094.

Montané X, Bajek A, Roszkowski K, Montornés JM, Giamberini M, Roszkowski S, Kowalczyk O, Garcia-Valls R, Tylkowski B. 2020. Encapsulation for Cancer Therapy. *Molecules* **25**(7): 1605-1630.

Moore TL, Rodriguez-Lorenzo L, Hirsch V, Balog S, Urban D, Jud C, Rothen-Rutishauser B, Lattuada M, Petri-Fink A. 2015. Nanoparticle colloidal stability in cell culture media and impact on cellular interactions. *Chem Soc Rev* **44**(17): 6287-6305.

Mout R, Moyano DF, Rana S, Rotello VM. 2012. Surface functionalization of nanoparticles for nanomedicine. *Chem Soc Rev* **41**(7): 2539-2544.

Murai T. 2015. Cholesterol lowering: role in cancer prevention and treatment. *Biol Chem* **396**: 1-11.

Muralidharan R, Panneerselvam J, Chen A, Zhao YD, Munshi A, Ramesh R. HuR-targeted nanotherapy in combination with AMD3100 suppresses CXCR4 expression, cell growth, migration and invasion in lung cancer. 2015. *Cancer Gene Ther* **22**: 581-590.

Nakamura H, Kawasaki N, Taguchi M, Kabasawa K. 2006. Survival impact of epidermal growth factor receptor overexpression in patients with non-small cell lung cancer: a meta-analysis. *Thorax* **61**(2): 140-145.

Nam KH, Lee BL, Park JH, Kim J, Han N, Lee HE, Kim MA, Lee HS, Kim WH. 2013. Caveolin 1 expression correlates with poor prognosis and focal adhesion kinase expression in gastric cancer. *Pathobiology* **80**(2): 87-94.

NATIONAL CANCER INSTITUTE, 2020. Drugs Approved for Lung Cancer. Available: https://www.cancer.gov/about-cancer/treatment/drugs/lung. Accessed on: 6th May 2020.

Neubert RH. 2011. Potentials of new nanocarriers for dermal and transdermal drug delivery. *Eur J Pharm Biopharm* **77**(1): 1-2.

Ng CM, Loh H-S, Muthoosamy K, Sridewi N, Manickam S. 2016. Conjugation of insulin onto the sidewalls of single-walled carbon nanotubes through functionalization and diimide-activated amidation. *Int J Nanomedicine* **11**: 1607-1614.

Nie X, Liu Y, Li M, Yu X, Yuan W, Huang S, Ren D, Wang Y, Wang Y. 2020. SP94 Peptide-Functionalized PEG-PLGA Nanoparticle Loading with Cryptotanshinone for Targeting Therapy of Hepatocellular Carcinoma. *AAPS PharmSciTech* **21**(4): 124.

Nishant T, Sathish Kumar D, Kumar A, Phaneendra M. 2011. Role of Pharmacokinetic Studies in Drug Discovery. *J Bioequiv Availab* **3**: 263-267.

Niu K, Li N, Yao Y, Guo C, Ge Y, Wang J. 2019. Polypeptide Nanogels With Different Functional Cores Promote Chemotherapy of Lung Carcinoma. *Front Pharmacol* **10**: 37.

Ni XL, Chen LX, Zhang H, Yang B, Xu S, Wu M, Liu J, Yang LL, Chen Y, Fu SZ, Wu JB. 2017. *In vitro* and *in vivo* antitumor effect of gefitinib nanoparticles on human lung cancer. *Drug Deliv* **24**(1): 1501-1512.

Noei A, Nili-Ahmadabadi A, Soleimani M. 2019. The Enhanced Cytotoxic Effects of the p28-Apoptin Chimeric Protein As A Novel Anti-Cancer Agent on Breast Cancer Cell Lines. *Drug Res (Stuttg)* **69**(3): 144-150.

Norambuena A, Schwartz MA. 2011. Effects of integrin-mediated cell adhesion on plasma membrane lipid raft components and signaling. *Mol Biol Cell* **22**(18): 3456-3464.

Numico G, Castiglione F, Granetto C, Garrone O, Mariani G, Costanzo G, Ciura P, Gasco M, Ostellino O, Porcile G, Merlano M. 2002. Single-agent pegylated liposomal doxorubicin (Caelix) in chemotherapy pretreated non-small cell lung cancer patients: a pilot trial. Lung Cancer **35**(1): 59-64.

Otsuka H, Nagasaki Y, Kataoka K. 2012. PEGylated NPs for biological and pharmaceutical applications. *Adv Drug Deliv Rev* **64**: 246-255.

Owen DM, Rentero C, Magenau A, Abu-Siniyeh A, Gaus K. 2011. Quantitative imaging of membrane lipid order in cells and organisms. *Nat Protoc* **7**(1): 24-35.

Owens DE, Peppas NA. 2006. Opsonization, biodistribution, and pharmacokinetics of polymeric NPs. *Int J Pharm* **307**: 93-102.

Padmalatha M, Prakash V, Kusum S, Kumar RV, Wilson K, Vivekananda V. 2011. Development and Validation of High Performance Liquid Chromatographic Method for the Determination of Erlotinib. *J Pharm Res* **4**: 637-638.

Pang H, Le PU, Nabi IR. 2004. Ganglioside GM1 levels are a determinant of the extent of *caveolae*/raft-dependent endocytosis of cholera toxin to the Golgi apparatus. *J Cell Sci* **117**(Pt 8): 1421-1430.

Pang J, Xing H, Sun Y, Feng S, Wang S. 2020. Non-small cell lung cancer combination therapy: Hyaluronic acid modified, epidermal growth factor receptor targeted, pH sensitive lipid-polymer hybrid nanoparticles for the delivery of erlotinib plus bevacizumab. *Biomed Pharmacother* **125**: 109861.

Panyam J, Zhou WZ, Prabha S, Sahoo SK, Labhasetwar V. 2002. Rapid endolysosomal escape of poly(DL-lactide-co-glycolide) nanoparticles: implications for drug and gene delivery. *Faseb J* **16**(10): 1217-1226.

Paranjpe M, Müller-Goymann CC. 2014. Nanoparticle-mediated pulmonary drug delivery: a review. *Int J Mol Sci* **15**(4): 5852-5873.

Parasassi T, De Stasio G, Ravagnan G, Rusch RM, Gratton E. 1991. Quantitation of lipid phases in phospholipid vesicles by the generalized polarization of Laurdan fluorescence. *Biophys J* **60**(1): 179-189.

Parasassi T, Krasnowska EK. 1998. Laurdan and Prodan as polarity-sensitive fluorescent membrane probes. *J Fluoresc* **8**: 365-373.

Parashar P, Tripathi CB, Arya M, Kanoujia J, Singh M, Yadav A, Kaithwas G, Saraf SA. 2019. A synergistic approach for management of lung carcinoma through folic acid functionalized co-therapy of capsaicin and gefitinib nanoparticles: Enhanced apoptosis and metalloproteinase-9 down-regulation. *Phytomedicine* **53**: 107-123.

Park JW, Benz CC, Martin FJ. 2004. Future Directions of Liposome- and Immunoliposome-Based Cancer Therapeutics. *Semin Oncol* **31**: 196-205.

Parton RG. 2018. *Caveolae*: Structure, Function, and Relationship to Disease. *Annu Rev Cell Dev Biol* **34**: 111-136.

Parton RG, Richards AA. 2003. Lipid rafts and *caveolae* as portals for endocytosis: new insights and common mechanisms. *Traffic* **4**: 724-738.

Peetla C, Vijayaraghavalu S, Labhasetwar V. 2013. Biophysics of cell membrane lipids in cancer drug resistance: Implications for drug transport and drug delivery with nanoparticles. *Adv Drug Deliv Rev* **65**(13-14): 1686-1698.

Peng F, Li R, Zhang F, Qin L, Ling G, Zhang P. 2020. Potential drug delivery nanosystems for improving tumor penetration. *Eur J Pharm Biopharm* pii: S0939-6411(20)30103-X.

Pillai G, 2014. Nanomedicines for Cancer Therapy: An Update of FDA Approved and Those under Various Stages of Development. *SOJ Pharm Pharm Sci* **1**(2): 1-13.

Ping Z, Niebert M, Porazik K, Walker TL, Cooper HM, Middelberg APJ, Gray PP, Bartlett PF, Qing G, Lu M. 2008. Subcellular compartment targeting of layered double hydroxide NPs. *J. Control Release* **130**: 86-94.

Pinto SN, Fernandes F, Fedorov A, Futerman AH, Silva LC, Prieto M. 2013. A Combined Fluorescence Spectroscopy, Confocal and 2-Photon Microscopy Approach to Re-Evaluate the Properties of Sphingolipid Domains. *BBA - Biomembr* **1828**: 2099-2110.

Pinto SN, Silva LC, de Almeida RFM, Prieto M. 2008. Membrane Domain Formation, Interdigitation, and Morphological Alterations Induced by the Very Long Chain Asymmetric C24:1 Ceramide. *Biophys J* **95**: 2867-2879.

Pirker R. 2020. Conquering lung cancer: current status and prospects for the future. *Pulmonology* pii: S2531-0437(20)30031-3.

Prasad M, Lambe UP, Brar B, Shah I, Manimegalai J, Ranjan K, Rao R, Kumar S, Mahant S, Kumar S, Iqbal MN, Dhama K, Misri J, Prasad G. 2018. Nanotherapeutics: An insight into healthcare and multi-dimensional applications in medical sector of the modern world. *Biomedicine & Pharmacotherapy* **97**: 1521-1537.

Pubmed, Cancer nanomedicine. 2021a. Available: https://pubmed.ncbi.nlm.nih.gov/?term=cancer+nanomedicine. Accessed on: 7th February 2021.

Pubmed, search keyword: Anticancer peptides in Clinical Trials. 2021b. Available: https://pubmed.ncbi.nlm.nih.gov/?term=anticancer+peptide&filter=pubt.clinicaltrial&filter=years.2000-2021&sort=date. Accessed on: 13th March 2021.

Punj V, Bhattacharyya S, Saint-dic D, Vasu C, Cunningham EA, Graves J. 2004. Bacterial cupredoxin azurin as an inducer of apoptosis and regression in human breast cancer. *Oncogene* **23**: 2367-2378.

Punj V, Gupta TK Das, Chakrabarty AM. 2003. Bacterial cupredoxin azurin and its

interactions with the tumor suppressor protein p53. *Oncogene* **312**: 109-114.

Qaddoumi MG, Ueda H, Yang J, Davda J, Labhasetwar V, Lee VH. 2004. The characteristics and mechanisms of uptake of PLGA nanoparticles in rabbit conjunctival epithelial cell layers. *Pharm Res* **21**(4): 641-648.

Quest AF, Lobos-González L, Nuñez S, Sanhueza C, Fernández JG, Aguirre A, Rodríguez D, Leyton L, Torres V. 2013. The caveolin-1 connection to cell death and survival. *Curr Mol Med* **13**(2): 266-281.

Raber HF, Heerde T, Din SNE, Flaig C, Hilgers F, Bitzenhofer N, Jäger K, Drepper T, Gottschalk K, Bodenberger NE, Weil T, Kubiczek DH, Rosenau F. 2020. Azulitox-A *Pseudomonas aeruginosa* P28-Derived Cancer-Cell-Specific Protein Photosensitizer. *Biomacromolecules* **21**(12): 5067-5076.

Reissmann S. 2014. Cell penetration: scope and limitations by the application of cell-penetrating peptides. *J Pept Sci* **20**(10): 760-784.

Rezvantalab S, Drude NI, Moraveji MK, Güvener N, Koons EK, Shi Y, Lammers T, Kiessling F. 2018. PLGA-Based Nanoparticles in Cancer Treatment. *Front Pharmacol* **9**: 1260.

Rivas CJM, Tarhini M, Badri W, Miladi K, Greige-gerges H, Agha Q, Arturo S, Rodríguez G, Álvarez R, Fessi H, Elaissari A. 2017. Nanoprecipitation process: From encapsulation to drug delivery. *Int J Pharm* **532**: 66-81.

Rizvi SAA, Saleh AM. 2018. Applications of nanoparticle systems in drug delivery technology. *Saudi Pharm J* **26**: 64-70.

Roger E, Lagarce F, Garcion E, Benoit JP. 2010. Biopharmaceutical parameters to consider in order to alter the fate of nanocarriers after oral delivery. *Nanomedicine* **5**: 287-306.

Sadat F, Mirakabad T, Nejati-koshki K, Yamchi MR, Milani M, Zeighamian V, Rahimzadeh A. 2014. PLGA-Based NPs as Cancer Drug Delivery Systems. *Asian Pac J Cancer Prev* **15**: 517-535.

Sahin A, Esendagli G, Yerlikaya F, Caban-Toktas S, Yoyen-Ermis D, Horzum U, Aktas Y, Khan M, Couvreur P, Capan Y. 2017. A small variation in average particle size of PLGA nanoparticles prepared by nanoprecipitation leads to considerable change in nanoparticles' characteristics and efficacy of intracellular delivery. *Artif Cells Nanomed Biotechnol* **45**(8): 1657-1664.

Santini S, Bizzarri AR, Cannistraro S. 2011. Modelling the interaction between the p53 DNA-binding domain and the p28 peptide fragment of Azurin. *J Mol Recognit* **24**: 1043-1055.

Saravanakumar K, Hu X, Shanmugam S, Chelliah R, Sekar P, Oh DH, Vijayakumar S, Kathiresan K, Wang MH. 2019. Enhanced cancer therapy with pH-dependent and aptamer functionalized doxorubicin loaded polymeric (poly D, L-lactic-co-glycolic acid) nanoparticles. *Arch Biochem Biophys* **671**: 143-151.

Sarkar S, Horn G, Moulton K, Oza A, Byler S, Kokolus S, Longacre M. 2013. Cancer development, progression, and therapy: an epigenetic overview. *Int J Mol Sci* **14**(10): 21087-21113.

Sausville EA, Garbo LE, Weiss GJ, Shkolny D, Yurkovetskiy AV, Bethune C, Ramanathan RK, Fram RJ. 2010. Phase I study of XMT-1001 given IV every 3 weeks to patients with advanced solid tumors. *JCO* **28**: e13121-e13121.

Senapati S, Mahanta AK, Kumar S, Maiti P. 2018. Controlled drug delivery vehicles for cancer treatment and their performance. *Signal Transduct Target Ther* **16**: 1-19.

Sengupta P, Baird B, Holowka D. 2007. Lipid rafts, fluid/fluid phase separation, and their relevance to plasma membrane structure and function. *Semin Cell Dev Biol* **18**(5): 583-590.

Seto T, Kato T, Nishio M, Goto K, Atagi S, Hosomi Y, Yamamoto N, Hida T, Maemondo M, Nakagawa K, Nagase S, Okamoto I, Yamanaka T, Tajima K, Harada R, Fukuoka M, Yamamoto N. 2014. Erlotinib alone or with bevacizumab as firstline therapy in patients with advanced non-squamous non-small-cell lung cancer harbouring EGFR mutations (JO25567): an open-label, randomised, multicentre, phase 2 study. *Lancet Oncol* **15**: 1236-1244.

Sevastre AS, Horescu C, Baloi SC, Cioc CE, Vatu BI, Tuta C, Artene SA, Danciulescu MM, Tudorache S, Dricu A. 2019. Benefits of Nanomedicine for Therapeutic Intervention in Malignant Diseases. *Coatings* **9**: 628.

Sezgin E, Levental I, Mayor S, Eggeling C. 2017. The mystery of membrane organization: composition, regulation and roles of lipid rafts. *Nat Rev Mol Cell Biol* **18**(6): 361-374.

Shahbazi S, Bolhassani A. 2018. Comparison of six cell penetrating peptides with different properties for *in vitro* and *in vivo* delivery of HPV16 E7 antigen in therapeutic vaccines. *Int Immunopharmacol* **62**: 170-180.

Shen Y, TanTai J. 2020. Co-Delivery Anticancer Drug Nanoparticles for Synergistic Therapy Against Lung Cancer Cells. *Drug Des Devel Ther* **14**: 4503-4510.

Sher T, Dy GK, Adjei AA. 2008. Small cell lung cancer. *Mayo Clin Proc* **83**(3): 355-367.

Shi Y. 2020. Clinical Translation of Nanomedicine and Biomaterials for Cancer Immunotherapy: Progress and Perspectives. *Adv Therap* **3**: 1900215.

Shi Y, Tan SH, Ng S, Zhou J, Yang ND, Koo GB, McMahon KA, Parton RG, Hill MM, Del Pozo MA, Kim YS, Shen HM. 2015. Critical role of CAV1/caveolin-1 in cell stress responses in human breast cancer cells via modulation of lysosomal function and autophagy. *Autophagy* **11**(5): 769-784.

Sibata CH, Colussi VC, Oleinick NL, Kinsella TJ. 2000. Photodynamic therapy: a new concept in medical treatment. *Braz J Med Biol Res* **33**(8): 869-880.

Signorelli S, Santini S, Yamada T, Bizzarri AR, Beattie CW, Cannistraro S. 2017. Binding of amphipathic cell penetrating peptide p28 to wild type and mutated p53 as studied by Raman, atomic force and surface plasmon resonance spectroscopies. *Biochim Biophys Acta* **1861**: 910-921.

Silva ATCR, Cardoso BCO, Silva MESR, Freitas RFS, Sousa RG. 2015. Synthesis, characterization, and study of PLGA copolymer *in vitro* degradation. *J Biomater Nanobiotechnol* **6**: 8-19.

Silva S, Almeida AJ, Vale N. 2018. Combination of Cell-Penetrating Peptides with NPs for Therapeutic Application: A Review. *Biomolecules* **9**: 1-24.

Silva S, Almeida AJ, Vale N. 2019. Combination of Cell-Penetrating Peptides with Nanoparticles for Therapeutic Application: A Review. *Biomolecules* **10**: pii: E22.

Simons K, Toomre D. 2000. Lipid rafts and signal transduction. *Nat Rev Mol Cell Biol* **1**: 31-39.

Sims LB, Curry KC, Parupalli S, Horner G, Frieboes HB, Steinbach-Rankins JM. 2019. Efficacy of Surface-Modified PLGA NPs as a Function of Cervical Cancer Type. *Pharm Res* **5**: 36-66.

Sindhwani S, Syed AM, Ngai J, Kingston BR, Maiorino L, Rothschild J, MacMillan P, Zhang Y, Rajesh NU, Hoang T, Wu JLY, Wilhelm S, Zilman A, Gadde S, Sulaiman A, Ouyang B, Lin Z, Wang L, Egeblad M, Chan WCW. 2020. The entry of nanoparticles into solid tumours. *Nat Mater* **19**(5): 566-575.

Singh P, Pandit S, Mokkapati VRSS, Garg A, Ravikumar V, Mijakovic I. 2018. Gold Nanoparticles in Diagnostics and Therapeutics for Human Cancer. *Int J Mol Sci* **19**(7): pii: E1979.

Škrlec K, Štrukelj B, Berlec A. 2015. Non-immunoglobulin scaffolds: a focus on their targets. *Trends Biotechnol* **33**(7): 408-418.

Slowing II, Vivero-Escoto JL, Wu C-W, Lin VSY. 2008. Mesoporous silica NPs as controlled release drug delivery and gene transfection carriers. *Adv Drug Deliv Rev* **60**: 1278-1288.

Soares S, Sousa J, Pais A, Vitorino C. 2018. Nanomedicine: Principles, Properties, and Regulatory Issues. *Front Chem* **6**: 360-375.

Soleimani M, Sadeghi HM, Jahanian-Najafabadi A. 2019. A Bi-Functional Targeted P28-NRC Chimeric Protein with Enhanced Cytotoxic Effects on Breast Cancer Cell Lines. *Iran J Pharm Res* **18**(2): 735-744.

Song Y, Zhou B, Du X, Wang Y, Zhang J, Ai Y, Xia Z, Zhao G. 2020. Folic acid (FA)-conjugated mesoporous silica nanoparticles combined with MRP-1 siRNA improves the suppressive effects of myricetin on non-small cell lung cancer (NSCLC). *Biomed Pharmacother* **125**: 109561.

Sousa AR, Oliveira MJ, Sarmento B. 2019. Impact of CEA-targeting Nanoparticles for Drug

Delivery in Colorectal Cancer. *J Pharmacol Exp Ther* **370**(3): 657-670.

Sree KSN, Pai KG, Verma R, Ananthakrishna P, Kumar L. 2017. Validation of hplc method for quantitative determination of gefitinib in polymeric nanoformulation. *Pharm Chem J*+ **51**: 159-163.

Srivastava S, Gupta S, Mohammad S, Ahmad I. 2019. Development of α-tocopherol surface-modified targeted delivery of 5-fluorouracil-loaded poly-D, L-lactic-co-glycolic acid nanoparticles against oral squamous cell carcinoma. *J Cancer Res Ther* **15**(3): 480-490.

Stathopoulos GP, Antoniou D, Dimitroulis J, Michalopoulou P, Bastas A, Marosis K, Stathopoulos J, Provata A, Yiamboudakis P, Veldekis D, Lolis N, Georgatou N, Toubis M, Pappas Ch, Tsoukalas G. 2010. Liposomal cisplatin combined with paclitaxel versus cisplatin and paclitaxel in non-small-cell lung cancer: a randomized phase III multicenter trial. *Ann Oncol* **21**(11): 2227-2232.

Stathopoulos GP, Antoniou D, Dimitroulis J, Stathopoulos J, Marosis K, Michalopoulou P. 2011. Comparison of liposomal cisplatin versus cisplatin in non-squamous cell non-small-cell lung cancer. *Cancer Chemother Pharmacol* **68**(4): 945-950.

Strebhardt K, Ullrich A. 2008. Paul Ehrlich's magic bullet concept: 100 years of progress. *Nat Rev Cancer* **8**(6): 473-480.

Su H, Wang Y, Gu Y, Bowman L, Zhao J, Ding M. 2018. Potential applications and human biosafety of nanomaterials used in nanomedicine. *J Appl Toxicol* **38**(1): 3-24.

Suresh D, Zambre A, Mukherjee S, Ghoshdastidar S, Jiang Y, Joshi T, Upendran A, Kannan R. 2019. Silencing AXL by covalent siRNA-gelatin-antibody nanoconjugate inactivates mTOR/EMT pathway and stimulates p53 for TKI sensitization in NSCLC. *Nanomedicine* **20**: 102007.

Swider E, Koshkina O, Tel J, Cruz LJ, de Vries IJM, Srinivas M. 2018. Customizing poly(lactic-co-glycolic acid) particles for biomedical applications. *Acta Biomater* **73**: 38-51.

Tan M, Lan KH, Yao J, Lu CH, Sun M, Neal CL, Lu J, Yu D. 2006. Selective inhibition of ErbB2-overexpressing breast cancer *in vivo* by a novel TAT-based ErbB2-targeting signal transducers and activators of transcription 3-blocking peptide. *Cancer Res* **66**(7): 3764-3772.

Tao J, Fung S, Zheng Y. 2019. Application of flash nanoprecipitation to fabricate poorly water-soluble drug nanoparticles. *Acta Pharm Sin B* **9**: 4-18.

Taranta M, Bizzarri AR, Cannistraro S. 2009. Modeling the interaction between the N-terminal domain of the tumor suppressor p53 and azurin. *J Mol Recogni* **22**: 215-222.

Tavassoli M, Guelen L, Luxon BA, Gäken J. 2005. Apoptin: specific killer of tumor cells? *Apoptosis* **10**(4): 717-724

Taylor BN, Mehta RR, Yamada T, Lekmine F, Christov K, Chakrabarty AM, Green A, Bratescu L, Shilkaitis A, Beattie CW, Das Gupta TK. 2009. Noncationic peptides obtained from azurin preferentially enter cancer cells. *Cancer Res* **69**: 537-546.

Teixeira V, Feio MJ, Bastos M. 2012. Role of Lipids in the Interaction of Antimicrobial Peptides with Membranes. *Prog Lipid Res* **51**: 149-177.

Thalhauser S, Breunig M. 2020. Considerations for efficient surface functionalization of nanoparticles with a high molecular weight protein as targeting ligand. *Eur J Pharm Sci* **155**: 105520.

Tomalia DA, Baker H, Dewald J, Hall M, Kallos G, Martin S, Roeck J, Ryder J, Smith P. 1985. A New Class of Polymers : Starburst-Dendritic. *Polym J* **17**: 117-132.

Travis WD, Brambilla E, Nicholson AG, Yatabe Y, Austin JHM, Beasley MB, Chirieac LR, Dacic S, Duhig E, Flieder DB, Geisinger K, Hirsch FR, Ishikawa Y, Kerr KM, Noguchi M, Pelosi G, Powell CA, Tsao MS, Wistuba I. 2015. The 2015 World Health Organization Classification of Lung Tumors: Impact of Genetic, Clinical and Radiologic Advances Since the 2004 Classification. *J Thorac Oncol* **10**(9): 1243-1260.

Vale N, Duarte D, Silva S, Correia AS, Costa B, Gouveia MJ, Ferreira A. 2020. Cell-penetrating peptides in oncologic pharmacotherapy: A review. *Pharmacol Res* **162**: 105231.

Van de Kamp M, Silvestrini MC, Brunori M, Van Beeumen J, Hali FC, Canters GW. 1990. Involvement of the hydrophobic patch of azurin in the electron-transfer reactions with cytochrome C551 and nitrite reductase. *Eur J Biochem* **194**(1): 109-118.

Ventola CL. 2017. Progress in Nanomedicine: Approved and Investigational Nanodrugs. *PT* **42**: 742-755.

Vihanto MM, Vindis C, Djonov V, Cerretti DP, Huynh-Do U. 2006. Caveolin-1 is required for signaling and membrane targeting of EphB1 receptor tyrosine kinase. *J Cell Sci* **119**(Pt 11):2299-2309.

Wakabayashi M, Matsuzaki K. 2009. Ganglioside-induced amyloid formation by human islet amyloid polypeptide in lipid rafts. *FEBS Lett* **583**(17): 2854-2858.

Wali AF, Majid S, Rasool S, Shehada SB, Abdulkareem SK, Firdous A, Beigh, S, Shakeel S, Mushtaq S, Akbar I, Madhkali H, Rehman MU. 2019. Natural products against cancer: review on phytochemicals from marine sources in preventing cancer. *Saudi Pharm J* **27**: 767-777.

Wang H, Zhao Y, Wang H, Gong J, He H, Cheol M, Yang VC, Huang Y. 2014. Low-molecular-weight protamine-modified PLGA NPs for overcoming drug-resistant breast cancer. *J Control Release* **192**: 47-56.

Warso MA, Richards JM, Mehta D, Christov K, Schaeffer C, Rae Bressler L, Yamada T, Majumdar D, Kennedy SA, Beattie CW, Das Gupta TK. 2013. A first-in-class, first-in-human, phase I trial of p28, a non-HDM2-mediated peptide inhibitor of p53 ubiquitination in patients with advanced solid tumours. *Br J Cancer* **108**: 1061-1070.

Weiss GJ, Chao J, Neidhart JD, Ramanathan RK, Bassett D, Neidhart JA, Choi CHJ, Chow W, Chung V, Forman SJ, Garmey E, Hwang J, Kalinoski DL, Koczywas M, Longmate J,

Melton RJ, Morgan R, Oliver J, Peterkin JJ, Ryan JL, Schluep T, Synold TW, Twardowski P, Davis ME, Yen Y. 2013. First-in-human phase 1/2a trial of CRLX101, a cyclodextrin-containing polymer-camptothecin nanopharmaceutical in patients with advanced solid tumor malignancies. *Invest New Drugs* **31**(4): 986-1000.

Weissig V, Pettinger TK, Murdock N. 2014. Nanopharmaceuticals (part 1): products on the market. *Int J Nanomedicine* **9**: 4357-4373.

Werengowska-CieTwierz K, WiVniewski M, Terzyk AP, Furmaniak S. 2015. The Chemistry of Bioconjugation in Nanoparticles-Based Drug Delivery System. *Adv Cond Matter Phys* **2015**: 198175.

West H, McCleod M, Hussein M, Morabito A, Rittmeyer A, Conter HJ, Kopp HG, Daniel D, McCune S, Mekhail T, Zer A, Reinmuth N, Sadiq A, Sandler A, Lin W, Lohmann TO, Archer V, Wang L, Kowanetz M, Cappuzzo F. 2019. Atezolizumab in combination with carboplatin plus nab-paclitaxel chemotherapy compared with chemotherapy alone as first-line treatment for metastatic non-squamous non-small-cell lung cancer (IMpower130): a multicentre, randomised, open-label, phase 3 trial. *Lancet Oncol* **20**: 924.

Whitmore L, Wallace BA. 2004. DICHROWEB, an Online Server for Protein Secondary Structure Analyses from Circular Dichroism Spectroscopic Data. *Nucleic Acids Res* **32**: W668-W673.

Wild CP. 2019. The global cancer burden: necessity is the mother of prevention. *Nat Rev Cancer* **19**(3): 123-124.

Wild CP, Weiderpass E, Stewart BW. 2020. World Cancer Report: Cancer Research for Cancer Prevention. Lyon, France: International Agency for Research on Cancer. Available from: http://publications.iarc.fr/586. Licence: CC BY-NC-ND 3.0 IGO.

Wilhelm S, Tavares AJ, Dai Q, Ohta S, Audet J, Dvorak HF, Chan WCW. 2016. Analysis of nanoparticle delivery to tumours. *Nat Rev Mater* **1**: 16014.

Woodman C, Vundu G, George A, Wilson CM. 2020. Applications and strategies in nanodiagnosis and nanotherapy in lung cancer. *Semin Cancer Biol* pii: S1044-579X(20)30042-0.

Wu J, Xu F, Li S, Ma P, Zhang X, Liu Q, Fu R. 2019. Porous Polymers as Multifunctional Material Platforms toward Task-Specific Applications. *Adv Mater* **31**: 1-45.

Wu P, Zhou Q, Zhu H, Zhuang Y, Bao J. 2020. Enhanced antitumor efficacy in colon cancer using EGF functionalized PLGA nanoparticles loaded with 5-Fluorouracil and perfluorocarbon. *BMC Cancer* **20**(1): 354.

Wurz GT, Kao CJ, Wolf M, DeGregorio MW. 2014. Tecemotide: an antigen-specific cancer immunotherapy. *Hum Vaccin Immunother* **10**(11): 3383-3393.

Xie J, Bi Y, Zhang H, Dong S, Teng L, Lee RJ, Yang Z. 2020a. Cell-Penetrating Peptides in Diagnosis and Treatment of Human Diseases: From Preclinical Research to Clinical Application. *Front Pharmacol* 11: 697.

Xie M, Liu D, Yang Y. 2020b. Anti-cancer peptides: classification, mechanism of action,

reconstruction and modification. *Open Biol* **10**: 200004.

Xiong S, Zhao X, Heng BC, Ng KW, Loo JS. 2011. Cellular uptake of Poly-(D,L-lactide-co-glycolide) (PLGA) nanoparticles synthesized through solvent emulsion evaporation and nanoprecipitation method. *Biotechnol J* **6**(5): 501-508.

Yamada T, Christov K, Shilkaitis A, Bratescu L, Green A, Santini S, Bizzarri AR, Cannistraro S, Gupta TK, Beattie CW. 2013a. p28, a first in class peptide inhibitor of cop1 binding to p53. *Br J Cancer* **108**: 2495-2504.

Yamada T, Das Gupta TK, Beattie CW. 2013b. p28, an anionic cell-penetrating peptide, increases the activity of wild type and mutated p53 without altering its conformation. *Mol Pharm* **10**: 3375-3383.

Yamada T, Fialho AM, Punj V, Bratescu L, Gupta TK, Chakrabarty AM. 2005. Internalization of bacterial redox protein azurin in mammalian cells: entry domain and specificity. *Cell Microbiol* **7**: 1418-1431.

Yamada T, Goto M, Punj V, Zaborina O, Chen ML, Kimbara K, Majumdar D, Cunningham E, Das Gupta TK, Chakrabarty AM. 2002a. Bacterial redox protein azurin, tumor supressor protein p53, and regression of cancer. *Proc Natl Acad Sci USA* **99**: 14098-14103.

Yamada T, Goto M, Punj V, Zaborina O, Kimbara K, Das Gupta TK, Chakrabarty AM. 2002b. The Bacterial Redox Protein Azurin Induces Apoptosis in J774 Macrophages through Complex Formation and Stabilization of the Tumor Suppressor Protein p53 The Bacterial Redox Protein Azurin Induces Apoptosis in J774 Macrophages through Complex Formation and Stabilization of the Tumor Suppressor Protein p53. *Infect Immun* **70**: 7054-7062.

Yamada T, Gupta TK Das, Beattie CW. 2016. p28-mediated activation of p53 in G2/M phase of the cell cycle enhances the efficacy of DNA damaging and antimitotic chemotherapy. *Cancer Res* **76**: 2354-2365.

Yamada T, Hiraoka Y, Ikehata M, Kimbara K, Avner BS, Gupta TK Das, Chakrabarty AM. 2004. Apoptosis or growth arrest: modulation of tumor suppressor p53 specificity by bacterial redox protein azurin. *Proc PNAS* **101**: 4770-4775.

Yamada T, Mehta RR, Lekmine F, Christov K, King ML, Majumdar D, Shilkaitis A, Green A, Bratescu L, Beattie CW, Das Gupta TK. 2009. A peptide fragment of azurin induces a p53-mediated cell cycle arrest in human breast cancer cells. *Mol Cancer Ther* **8**: 2947-2958.

Yamada T, Signorelli S, Cannistraro S, Beattie CW, Bizarri AR. 2015. Chirality switching within an anionic cell-penetrating peptide inhibits translocation without affecting preferential entry. *Mol Pharm* **12**: 140-149.

Yamamoto N, Matsubara T, Sato T, Yanagisawa K. 2008. Age-dependent high-density clustering of GM1 ganglioside at presynaptic neuritic terminals promotes amyloid beta-protein fibrillogenesis. *Biochim Biophys Acta* **1778**(12): 2717-2726.

Yanagisawa S, Banfield MJ, Dennison C. 2006. The role of hydrogen bonding at the active

site of a cupredoxin: the Phe114Pro azurin variant. *Biochemistry* **45**: 8812-8822.

Yang A, Farmer E, Wu TC, Hung CF. 2016a. Perspectives for therapeutic HPV vaccine development. *J Biomed Sci* **23**(1): 75.

Yang K, Feng L, Liu Z. 2016b. Stimuli responsive drug delivery systems based on nano-graphene for cancer therapy. *Adv Drug Deliv Rev* **105**: 228-241.

Yang P, Gai S, Lin J. 2012. Functionalized mesoporous silica materials for controlled drug delivery. *Chem Soc Rev* **41**: 3679-3698.

Yildiz I, Shukla S, Steinmetz NF. 2011. Applications of viral NPs in medicine. *Curr Opin Biotechnol* **22**: 901-908.

Yu HA, Arcila ME, Rekhtman N, Sima CS, Zakowski MF, Pao W, Kris MG, Miller VA, Ladanyi M, Riely GJ. 2013. Analysis of tumor specimens at the time of acquired resistance to EGFR-TKI therapy in 155 patients with EGFR-mutant lung cancers. *Clin Cancer Res* **19**(8): 2240-2247.

Zaborina O, Dhiman N, Chen ML, Kostal J, Holder IA, Chakrabarty AM. 2000. Secreted products of a nonmucoid *Pseudomonas aeruginosa* strain induce two modes of macrophage killing: external-ATP- dependent , P2Z-receptor-mediated necrosis apoptosis. *Microbiology* **146**: 2521-2530.

Zanganeh S, Hutter G, Spitler R, Lenkov O, Mahmoudi M, Shaw A, Pajarinen JS, Nejadnik H, Goodman S, Moseley M, Coussens LM, Daldrup-Link HE. 2016. Iron oxide nanoparticles inhibit tumour growth by inducing pro-inflammatory macrophage polarization in tumour tissues. *Nat Nanotechnol* **11**(11): 986-994.

Zhang C, Ji X, Zhang Y, Zhou G, Ke X, Wang H, Tinnefeld P, He Z. 2013. One-pot synthesized aptamer-functionalized CdTe:Zn2+ quantum dots for tumor-targeted fluorescence imaging *in vitro* and *in vivo*. *Anal Chem* **85**: 5843-5849.

Zhang H. 2016. Onivyde for the therapy of multiple solid tumors. *Onco Targets Ther* **9**: 3001-3007.

Zhang H, Yee D, Wang C. 2008. Quantum dots for cancer diagnosis and therapy: biological and clinical perspectives. *Nanomedicine (Lond)* **3**: 83-91.

Zhang L, Liu F, Li G, Zhou Y, Yang Y. 2015. Twin-Arginine Translocation Peptide Conjugated Epirubicin-Loaded NPs for Enhanced Tumor Penetrating and Targeting. *J Pharm Sci* **104**: 4185-4196.

Zhang S, Wang L, Liu H, Zhao G, Ming L. 2014. Enhancement of recombinant myricetin on the radiosensitivity of lung cancer A549 and H1299 cells. *Diagn Pathol* **9**(1): 68.

Zhang T, Bao J, Zhang M, Ge Y, Wei J, Li Y, Wang W, Li M, Jin Y. 2020. Chemo-photodynamic therapy by pulmonary delivery of gefitinib nanoparticles and 5-aminolevulinic acid for treatment of primary lung cancer of rats. *Photodiagnosis Photodyn Ther* **31**: 101807.

Zhao M, Li H, Fan L, Ma Y, Gong H, Lai W, Fang Q, Hu Z. 2018. Quantitative proteomic

analysis to the first commercialized liposomal paclitaxel nano-platform Lipusu revealed the molecular mechanism of the enhanced anti-tumor effect. *Artif Cells Nanomed Biotechnol* **46**: S147-S155.

Zu M, Ma L, Zhang X, Xie D, Kang Y, Xiao B. 2019. Chondroitin sulfate-functionalized polymeric nanoparticles for colon cancer-targeted chemotherapy. *Colloids Surf B Biointerfaces* **177**: 399-406.

VIII. APPENDIX

VIII.1. AZURIN INTERACTION WITH THE LIPID RAFT COMPONENTS GANGLIOSIDE GM-1 AND CAVEOLIN-1 INCREASES MEMBRANE FLUIDITY AND SENSITIVITY TO ANTI-CANCER DRUGS (Supplementary information of Chapter II)

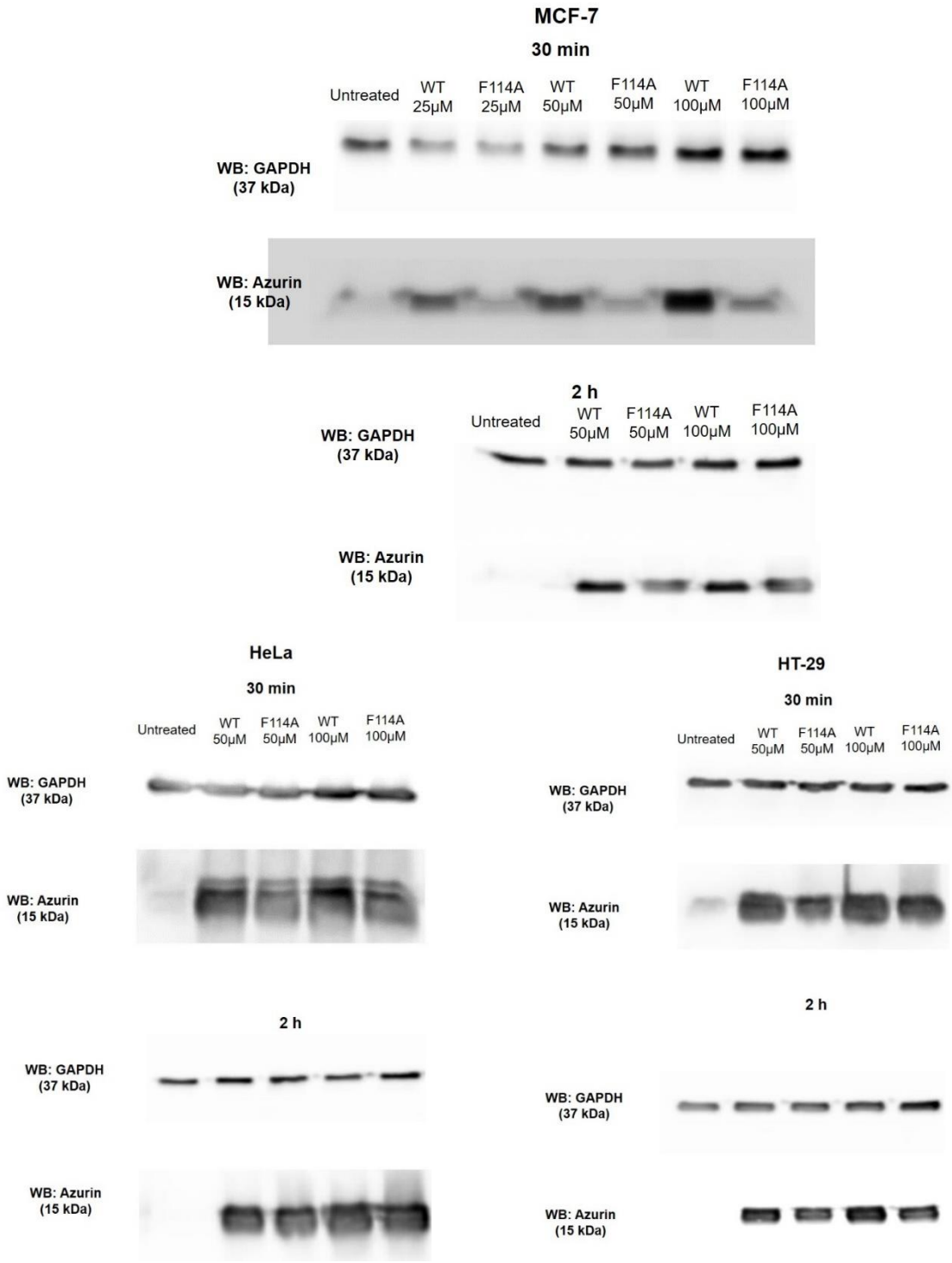

Figure VIII.1-1: Full-length western blot images. Conditions described in main text.

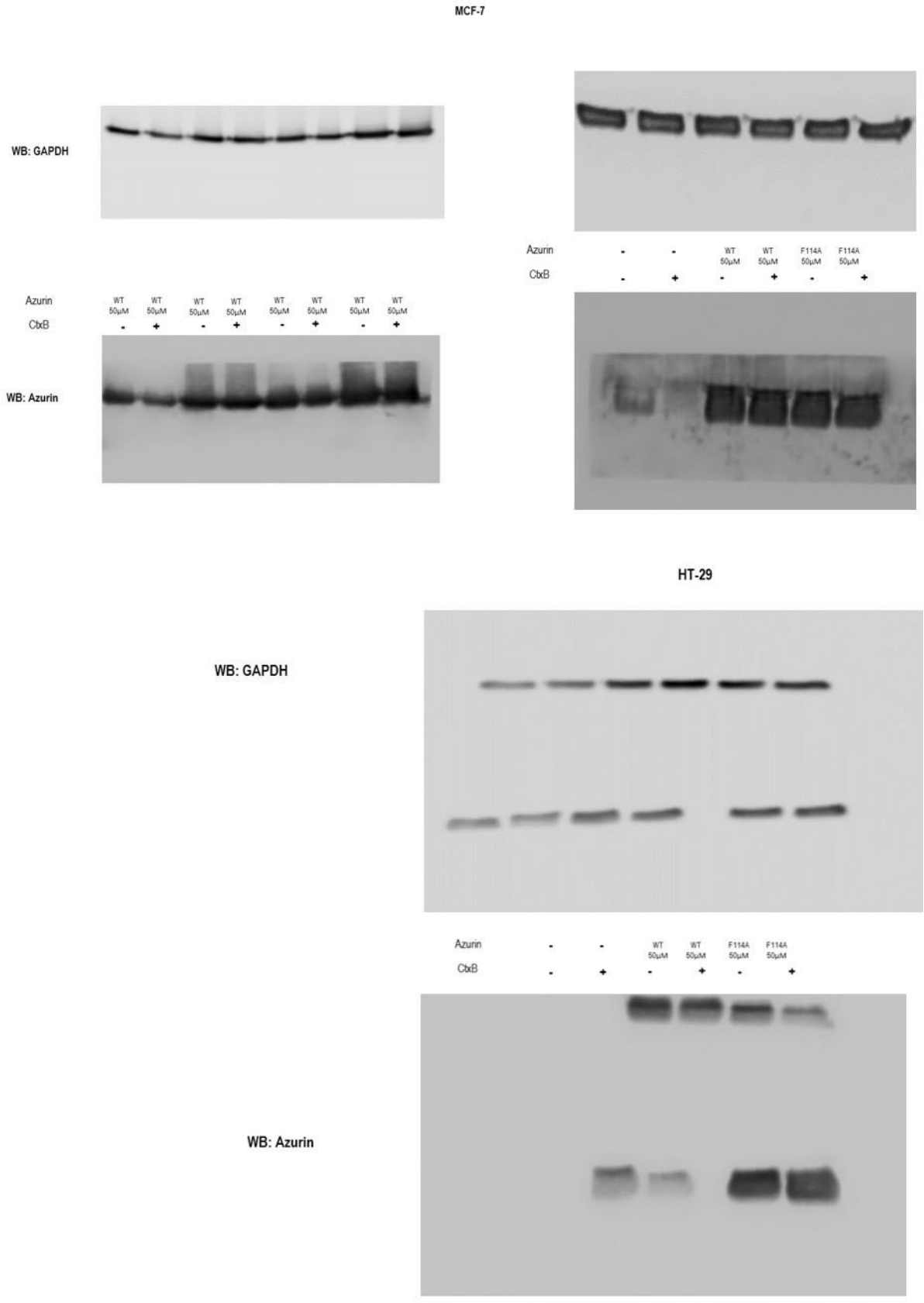

Figure VIII.1-2: Full-length western blot images. Conditions described in main text.

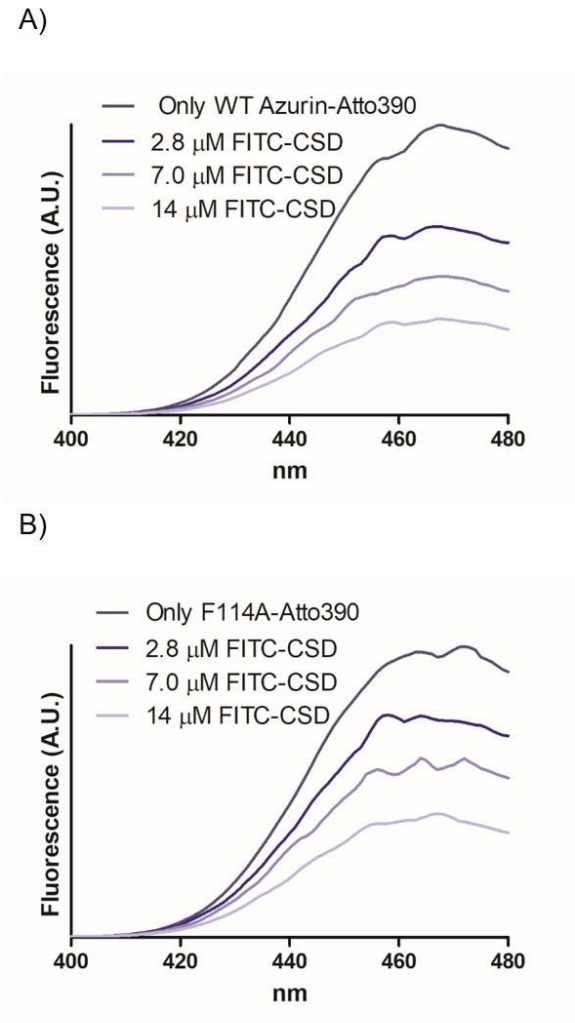

Figure VIII.1-3: Fluorescence spectra of the donors Atto390-WT **A)** or Atto390-F114A **B)** acquired with 390 nm excitation and measured over the emission wavelength range of 400 to 470 nm, since no acceptor (FITC-labeled CSD peptide) emits there. The FITC-labeled CSD peptide was titrated from 0 to 14 µM. Fluorescence measurements were carried out with a SLMAminco 8100 Series 2 spectrofluorimeter (Rochester) with double excitation and emission monochromators (MC-400), in a right-angle geometry. The light source was a 450-W Xe arc lamp and the reference a Rhodamine B quantum counter solution. Quartz cuvettes (1×1 cm) from Hellma Analytics were used.

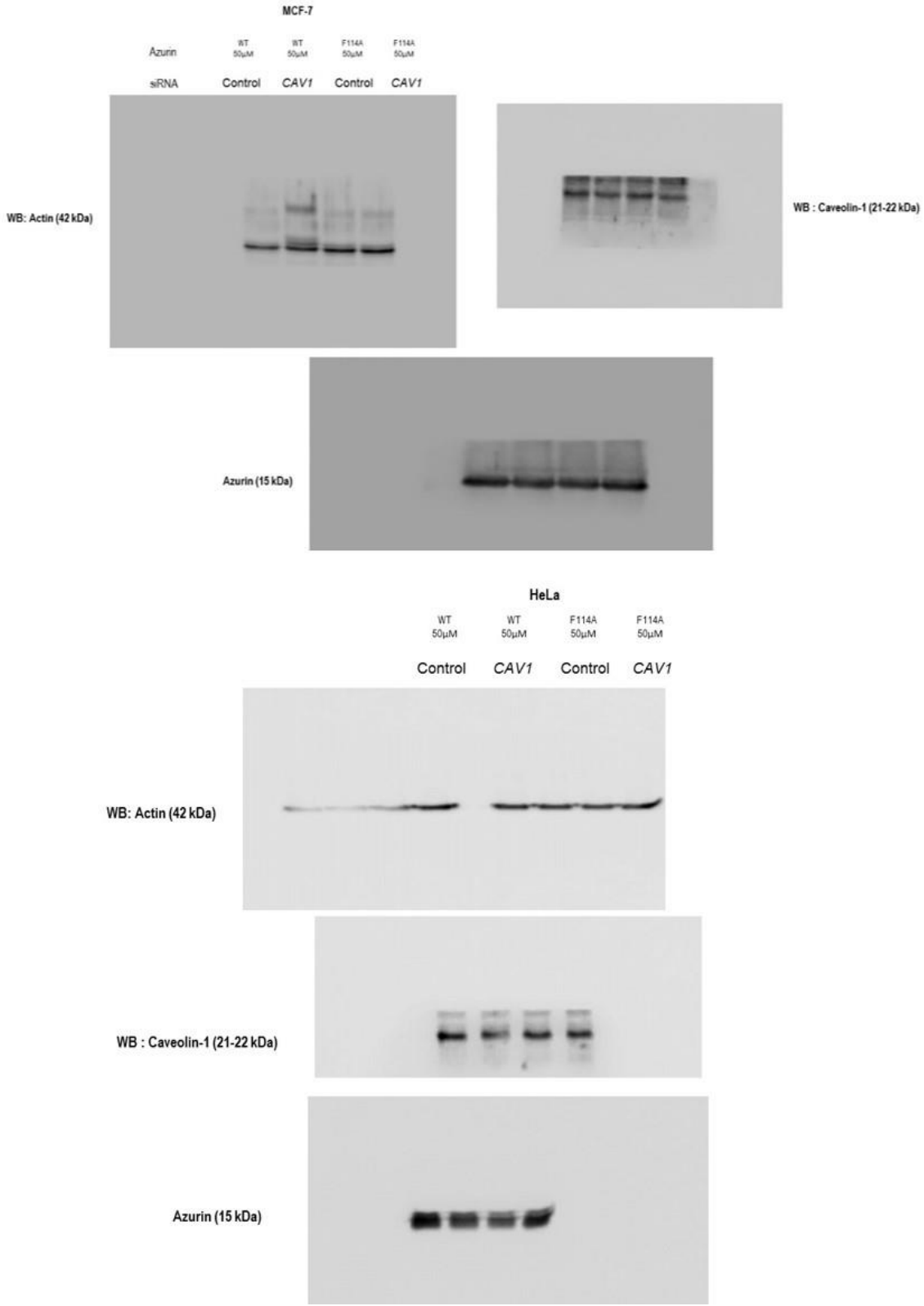

Figure VIII.1-4: Full-length western blot images. Conditions described in main text.

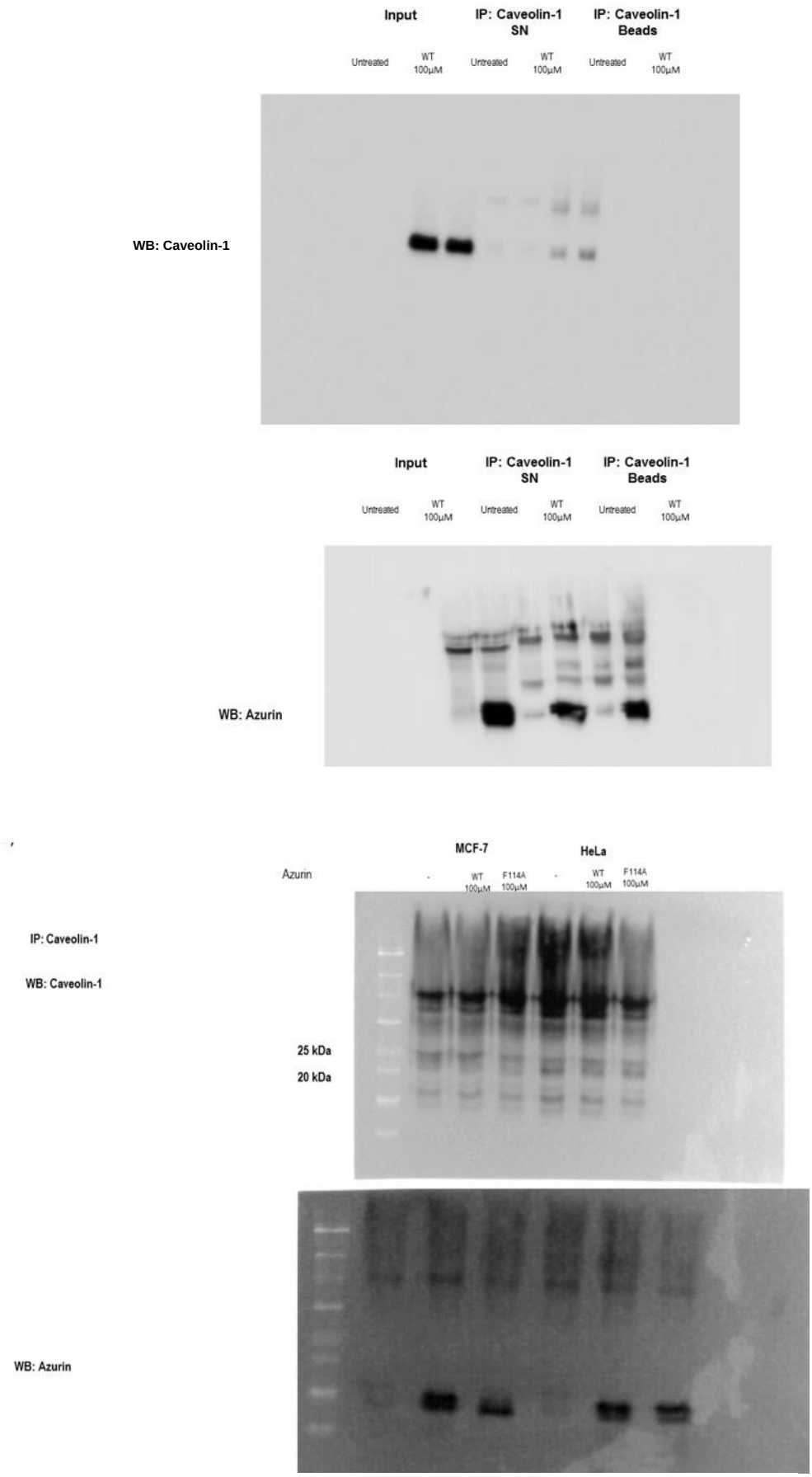

Figure VIII.1-5: Full-length western blot images. Conditions described in main text.

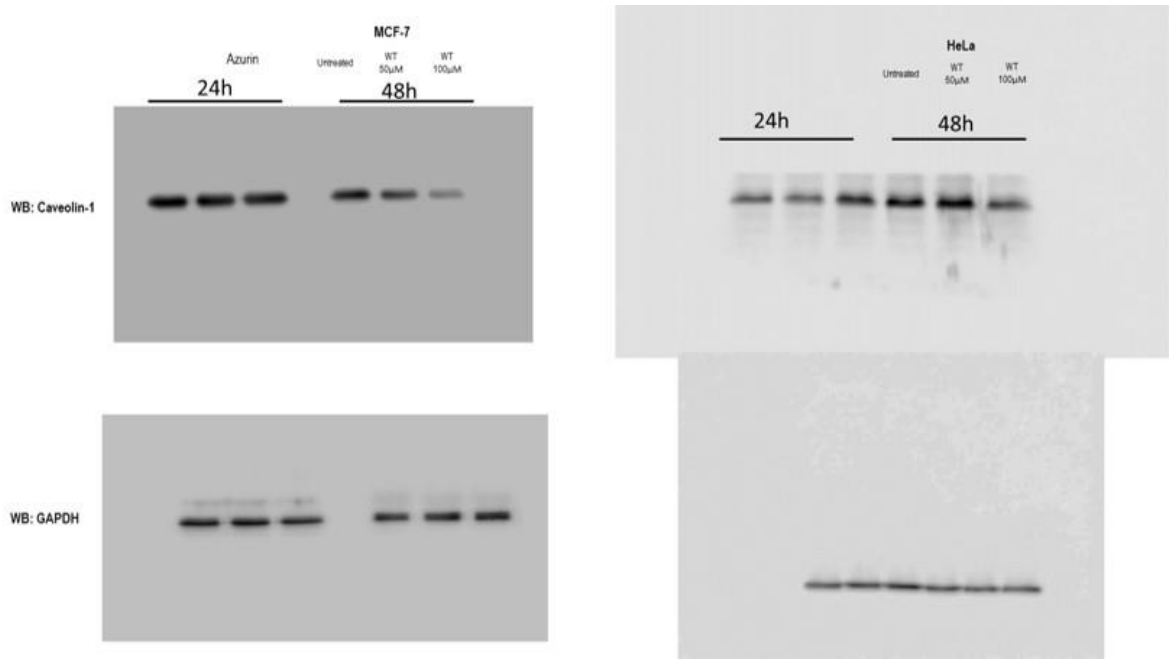

Figure VIII.1-6: Full-length western blot images. Conditions described in main text.

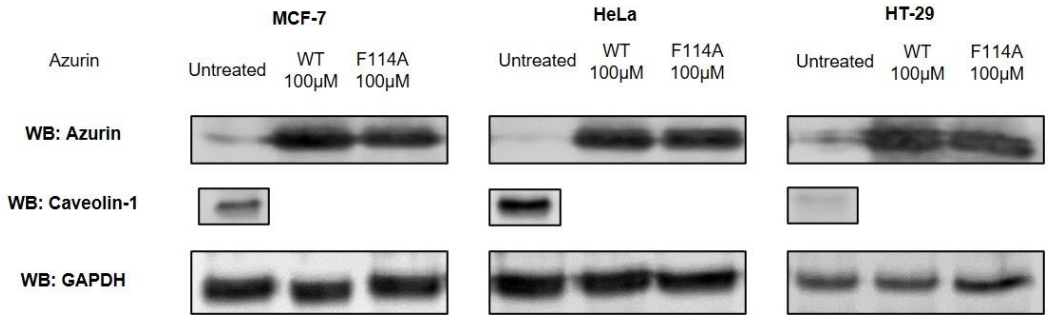

Figure VIII.1-7: Entry of azurin WT and F114A mutant in MCF-7, HeLa and HT-29 cells. Cells were exposed to 50-100 μM of both proteins for 48 h, after which cells were lysed and protein entry inside cells was determined by western blot (top panel). Endogenous levels of caveolin-1 in each cell line (middle panel).

VIII.2. P28-FUNCTIONALIZED PLGA NANOPARTICLES LOADED WITH GEFITINIB REDUCE TUMOR BURDEN AND METASTASES FORMATION ON LUNG CANCER (Supplementary information of Chapter IV)

Table VIII.2-1: Physico-chemical properties of nf-NPs and p28-NPs with different percentages of PLGA-PEG and PLGA-PEG-Mal polymers, their conjugation efficiency (CE) and energy-dispersive X-ray spectra (EDS) analysis (average atomic). Results are presented as mean ± SD (n=3).

Amount of PLGA-PEG	Amount of PLGA-PEG-Mal	Sample	Z-average (nm)	PDI	ζ-Potential (mV)	CE (%)	S average atomic (%)
10%	-	nf-NPs	80±6	0.17±0.01	-12.5±1.9	-	-
10%	-	p28-NPs	81±7	0.19±0.01	-12.0±2.1	51±6	0.19±0.02
20%	-	nf-NPs	76±7	0.18±0.07	-11.1±1.4	-	-
20%	-	p28-NPs	78±7	0.21±0.02	-10.2±2.3	58±4	0.14±0.02
-	10%	nf-NPs	76±5	0.23±0.04	-12.7±1.8	-	-
-	10%	p28-NPs	71±5	0.20±0.02	-11.7±1.3	37±9	0.24±0.06
-	20%	nf-NPs	77±4	0.18±0.05	-11.5±1.5	-	-
-	20%	p28-NPs	76±6	0.17±0.07	-11.3±1.8	49±1	0.10±0.01

Z-average: average size; PDI: polydispersity index; ζ-Potential: zeta-potential; CE: conjugation efficiency; nf-NPs: non-functionalized nanoparticles; p28-NPs: p28-functionalized nanoparticles; S: sulfur

Table VIII.2-2: Gefitinib (GEF) loaded PLGA NPs (NPs-GEF) production design.

Formulation code	Mass of PLGA polymer (mg)	Theoretical gefitinib loading (%)	Type of organic solvent	Volume of organic phase (mL)	Type of surfactant (w/v)	Volume of aqueous phase (mL)
GEF-NPs 1	20	10	DMSO	1	0.5% Kolliphor® p407	20; pH 7.4
GEF-NPs 2	20	**2.5**	DMSO	1	0.5% Kolliphor® p407	20; pH 7.4
GEF-NPs 3	20	10	DMSO	**4**	0.5% Kolliphor® p407	20; pH 7.4
GEF-NPs 4	20	10	DMSO	4	**2% Kolliphor® p407**	20; pH 7.4
GEF-NPs 5	20	10	DMSO	4	0.5% Kolliphor® p407	**20; pH 3.5**
GEF-NPs 6	20	10	DMSO	1	**2% Tween® 80**	20; pH 7.4
GEF-NPs 7	20	10	**Acetone**	4	0.5% Kolliphor® p407	20; pH 3.5
GEF-NPs 8	20	10	Acetone	4	**2% Tween® 80**	20; pH 3.5
GEF-NPs 9	20	10	Acetone	4	2% Tween® 80	**20; pH 7.4**
GEF-NPs 10	20	10	Acetone	4	**1% Tween® 80**	20; pH 7.4
GEF-NPs 11	20	10	Acetone	4	**0.5% Tween® 80**	20; pH 7.4
GEF-NPs 12	20	10	Acetone	**3**	0.5% Tween® 80	20; pH 7.4
GEF-NPs 13	20	10	Acetone	**2**	0.5% Tween® 80	20; pH 7.4
GEF-NPs 14	20	10	Acetone	3	0.5% Tween® 80	**40; pH 7.4**
GEF-NPs 15	20	10	Acetone	3	0.5% Tween® 80	**15; pH 7.4**
GEF-NPs 16	20	10	**Acetonitrile**	3	0.5% Tween® 80	15; pH 7.4
GEF-NPs 17	20	10	**THF**	3	0.5% Tween® 80	15; pH 7.4
GEF-NPs 18	20	10	**DMF**	3	0.5% Tween® 80	15; pH 7.4
GEF-NPs 19	20	10	DMF	3	**1% Tween® 80**	15; pH 7.4
GEF-NPs 20	20	10	DMF	3	**2% Tween® 80**	15; pH 7.4
GEF-NPs 21	20	10	DMF	3	**1% Kolliphor® p407**	15; pH 7.4
GEF-NPs 22	20	10	DMF	3	1% Tween® 80	**10; pH 7.4**
GEF-NPs 23	20	**5**	DMF	3	1% Tween® 80	10; pH 7.4

PLGA: poly(lactic-co-glycolic acid); **GEF-NPs:** Gefitinib loaded PLGA NPs; **DMSO:** Dimethyl sulfoxide; **THF:** Tetrahydrofuran; **DMF:** Dimethylformamide; Bold parameters correspond to the optimization performed.

Table VIII.2-3: Physico-chemical characteristics, association efficiency (AE) and practical gefitinib (GEF) loading of GEF-NPs based on the established production design. The values are represented as mean values ± SD (n=3).

Formulation code	Z-average (nm)	PDI	ζ-Potential (mV)	Practical gefitinib loading (%)	AE (%)	Optimization
GEF-NPs 1	Non-homogeneous formulation with visible precipitate					-
GEF-NPs 2	Non-homogeneous formulation with visible precipitate					TGL decrease
GEF-NPs 3	Non-homogeneous formulation with visible precipitate					Increased organic phase volume considering GEF-NPs 1
GEF-NPs 4	Non-homogeneous formulation with visible precipitate					% of surfactant increase
GEF-NPs 5	Non-homogeneous formulation with visible precipitate					Decrease of pH of the aqueous phase considering GEF-NPs 3
GEF-NPs 6	Non-homogeneous formulation with visible precipitate					Change of surfactant type considering GEF-NPs 1
GEF-NPs 7	172±19	0.28±0.05	-7.4±0.7	-	-	Change of organic solvent type considering GEF-NPs 5
GEF-NPs 8	96±7	0.18±0.04	-8.9±1.7	-	-	Change of surfactant type
GEF-NPs 9	96±4	0.14±0.01	-9.2±1.3	1±1	8±5	pH of aqueous phase increase
GEF-NPs 10	106±5	0.23±0.03	-10.7± 1.1	4±1	36±6	% of surfactant decrease
GEF-NPs 11	100±2	0.18±0.02	-7.4±0.7	4±0	37±2	
GEF-NPs 12	128±5	0.32±0.04	-17.9±1.2	4±1	33±29	Organic phase volume decrease
GEF-NPs 13	Non-homogeneous formulation with visible precipitate					
GEF-NPs 14	112±9	0.17±0.04	-18.1±3.7	5±0	49±4	Increased aqueous phase volume considering GEF-NPs 13
GEF-NPs 15	115±5	0.30±0.06	-18.1±1.5	7±1	71±10	Aqueous phase volume decrease
GEF-NPs 16	Non-homogeneous formulation with visible precipitate					Change of type of organic solvent
GEF-NPs 17	Non-homogeneous formulation with visible precipitate					
GEF-NPs 18	62±1	0.14±0.03	-14.5±1.3	6±0	60±5	
GEF-NPs 19	62±0	0.10±0.02	-8.4±1.1	6±1	62±5	% of surfactant increase
GEF-NPs 20	63±1	0.09±0.01	-11.0±0.1	5±1	54±3	
GEF-NPs 21	Non-homogeneous formulation with visible precipitate					Change of surfactant type considering GEF-NPs 20
GEF-NPs 22	68±7	0.19±0.01	-6.5±0.8	6±0	56±2	Aqueous phase volume decrease
GEF-NPs 23	67±2	0.14±0.02	-8.2±1.1	3±0	61±3	TGL decrease

GEF-NPs: Gefitinib loaded PLGA NPs; **Z-average:** average size; **PDI:** polydispersity index; **ζ-Potential:** zeta-potential; **AE:** association efficiency; **TGL:** Theoretical gefitinib loading.

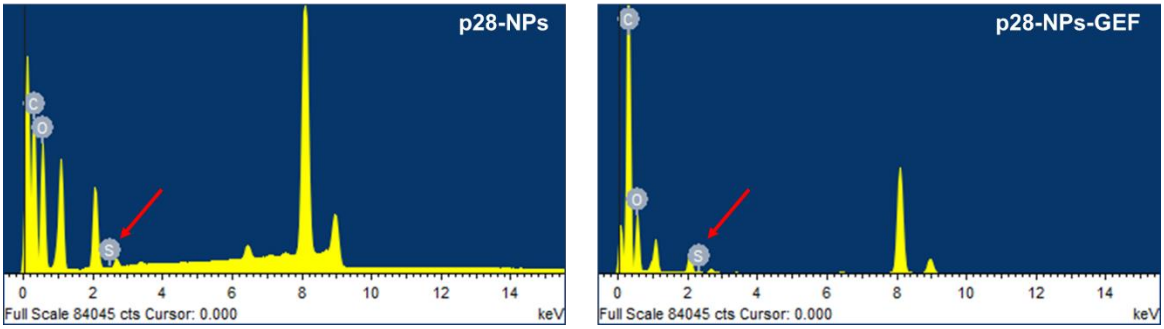

Figure VIII.2-1: Elementary analysis of functionalized unloaded NPs (p28-NPs) and p28-functionalized GEF-loaded NPs (p28-NPs-GEF).

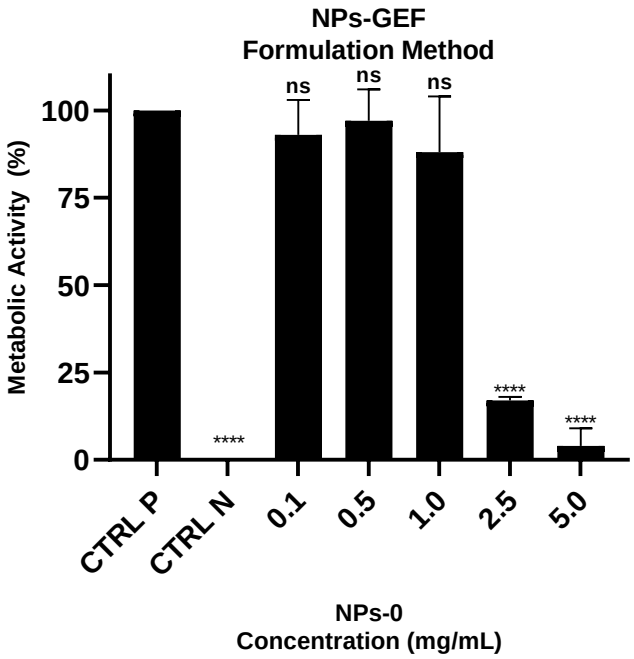

Figure VIII.2-2: Metabolic activity of A549 cancer cells upon treatment with different empty nanoparticles (NPs-0) concentrations for 72 h. Data was expressed as mean ± SD (n=3; ns: not significative; *p<0.1; **p<0.01; ***p<0.001; ****p＜0.0001).

VIII.3. P28-FUNCTIONALIZED PLGA NANOPARTICLES LOADED WITH ERLOTINIB: DEVELOPMENT, CHARACTERIZATION AND *IN VITRO* EVALUATION OF THEIR LUNG ANTICANCER ACTIVITY

VIII.3.1. Material and methods

VIII.3.1.1. Preparation of p28-functionalized PLGA nanoparticles loaded with erlotinib

p28-functionalized erlotinib (ERL; APExBIO®)-loaded PLGA NPs (p28-NPs-ERL) were prepared by nanoprecipitation as previously described in **IV.3.2.2. section**, but with small changes, namely in the composition of the organic phase. The same amount of PLGA and PLGA-PEG-Mal-p28 were used and dissolved in 1.5 mL of acetone (VWR™) and 1.1 mg of ERL were dissolved in 0.5 mL of methanol (CARLO ERBA). Then, they were mixed to form the organic phase. The following steps are the same as those described in the section mentioned above.

VIII.3.1.2. Characterization of nanoparticles

VIII.3.1.2.1. Average particle size, size distribution and surface charge

Described in **IV.3.2.3.1. section**.

VIII.3.1.2.2. Erlotinib association efficiency and drug loading

The quantification of ERL was performed with the same method described in **IV.3.2.3.2. section**, but the composition of the mobile phase, as well as the detection wavelength were adjusted to this compound. The mobile phase was composed of ACN:30mM of potassium dihydrogen orthophosphate buffer (KH_2PO_4; MERCK®) (45:55, v/v; pH 3.2 adjusted with orthophosphoric acid, MERCK®) at a flow rate of 0.8 mL/min. The sample detection was performed at 246 nm (Padmalatha *et al.*, 2011).

VIII.3.1.2.3. Morphology screening

Described in **IV.3.2.3.3. section**.

VIII.3.1.2.4. Colloidal stability of nanoparticles

Described in **IV.3.2.3.4. section**.

VIII.3.1.3. Erlotonib *in vitro* release study

Described in **IV.3.2.4. section**.

VIII.3.1.4. Human cell lines and cell culture

Described in **IV.3.2.5. section**.

VIII.3.1.5. Cell viability assay

Described in **IV.3.2.8. section**.

VIII.3.2. Results

VIII.3.2.1. Preparation and characterization of p28-functionalized PLGA nanoparticles loaded with erlotinib

Initially, a NPs-ERL production design (logP value of ERL: 3.2) was performed to achieve the best possible AE and DL values with appropriate physico-chemical characteristics (Tables VIII.3.2-1 and -2). Upon this optimization process, the p28-NPs-ERL were formulated (Figure VIII.3.2-1A), and their physico-chemical properties, AE and DL were evaluated (Table VIII.3.2-3), and their morphology was analyzed (Figure VIII.3.2-1B).

VIII.3.2.2. Colloidal stability of nanoparticles in cell culture medium

Colloidal stability evaluation showed that when the NPs were added to medium, in all types the Z-average size persisted constant and PDI demonstrated small variations over time (Figure VIII.3.2-1C). The ζ-potential of p28-NPs-ERL was -9.6 ± 0.8 mV at the beginning of the assay (t=0), and after 72 h was -12.7 ± 1.0 mV.

VIII.3.2.3. Payload release profile

In vitro ERL release study reported a biphasic pattern consisting of an initial burst release (60-80% in the first hour) followed by a sustained release phase over 72 h in both cases, similar to the GEF release profile (Figure VIII.3.2-1D). Regardless of the pH used, no important differences in the ERL release were also detected.

Table VIII.3.2-1: Erlotinib loaded PLGA NPs (NPs-ERL) production design.

Formulation code	Mass of PLGA polymer (mg)	Theoretical erlotinib loading (%)	Type of organic solvent	Volume of organic phase (mL)	Type of surfactant (w/v)	Volume of aqueous phase (mL)
ERL-NPs 1	20	10	DMF	3.0	1% Tween® 80	20; pH 7.4
ERL-NPs 2	20	**5**	**Acetone for PLGA** **DMF for ERL**	**1.5** **1.5**	1% Tween® 80	20; pH 7.4
ERL-NPs 3	20	5	Acetone for PLGA DMF for ERL	**2.0** **1.0**	1% Tween® 80	20; pH 7.4
ERL-NPs 4	20	5	Acetone for PLGA DMF for ERL	**0.5** **2.5**	1% Tween® 80	20; pH 7.4
ERL-NPs 5	20	5	**Acetone for PLGA** **Methanol for ERL**	**1.5** **1.5**	1% Tween® 80	20; pH 7.4
ERL-NPs 6	20	5	Acetone for PLGA Methanol for ERL	**1.5** **0.5**	1% Tween® 80	20; pH 7.4
ERL-NPs 7	20	5	Acetone for PLGA Methanol for ERL	1.5 0.5	1% Tween® 80	**40; pH 7.4**
ERL-NPs 8	20	5	Acetone for PLGA Methanol for ERL	1.5 0.5	1% Tween® 80	**15; pH 7.4**
ERL-NPs 9	20	5	Acetone for PLGA Methanol for ERL	1.5 0.5	1% Tween® 80	**10; pH 7.4**

PLGA: poly(lactic-co-glycolic acid); **ERL:** Erlotinib; **ERL-NPs:** ERL loaded PLGA NPs; **DMF:** Dimethylformamide; Bold parameters correspond to the optimization performed.

Table VIII.3.2-2: Physico-chemical characteristics, association efficiency (AE) and practical erlotinib loading of ERL-NPs based on the established production design. The values are represented as mean values ± SD (n=3).

Formulation code	Z-average (nm)	PDI	ζ-Potential (mV)	Practical erlotinib loading (%)	AE (%)	Optimization
ERL-NPs 1	208±6	0.19±0.02	-26.4±0.7	-	-	-
ERL-NPs 2	168±9	0.10±0.01	-29.1±1.4	1±0	13±0	Change of organic phase and TEL decrease
ERL-NPs 3	170±1	0.09±0.02	-29.3±0.1	1±0	22±1	Acetone volume increase and consequent DMF volume decrease
ERL-NPs 4	203±2	0.12±0.02	-28.9±1.2	1±0	17±0	Acetone volume decrease and consequent DMF volume increase
ERL-NPs 5	Non-homogeneous formulation with visible precipitate					DMF alteration by methanol considering ERL-NPs 2
ERL-NPs 6	194±1	0.11±0.00	-29.9±1.6	1±0	22±0	Methanol volume decrease
ERL-NPs 7	144±1	0.09±0.01	-9.4±0.7	0±0	3±0	Aqueous phase volume increase
ERL-NPs 8	138±2	0.09±0.02	-9.5±0.2	2±0	28±2	Aqueous phase volume decrease
ERL-NPs 9	138±1	0.09±0.02	-9.6±0.7	2±0	30±3	

ERL-NPs: Erlotinib loaded PLGA NPs; **Z-average:** average size; **PDI:** polydispersity index; **ζ-Potential:** zeta-potential; **AE:** association efficiency; **TEL:** Theoretical erlotinib loading.

Table VIII.3.2-3: Physico-chemical properties of empty nanoparticles (NPs-0), functionalized unloaded NPs (p28-NPs), erlotinib (ERL) loaded NPs (NPs-ERL), and p28-functionalized ERL-loaded NPs (p28-NPs-ERL) and their association efficiency (AE) and drug loading (DL). Values are presented as mean ± SD (n=3), na: not applicable.

Sample	Z-average (nm)	PDI	ζ-Potential (mV)	AE (%)	DL (%)
NPs-0	105 ± 8	0.14 ± 0.03	-15.4 ± 4.1	na	na
p28-NPs	107 ± 3	0.19 ± 0.03	-13.1 ± 1.1	na	na
NPs-ERL	116 ± 8	0.12 ± 0.02	-12.7 ± 3.3	54 ± 7	3 ± 0
p28-NPs-ERL	96 ± 3	0.16 ± 0.03	-11.3 ± 0.8	31 ± 1	2 ± 0

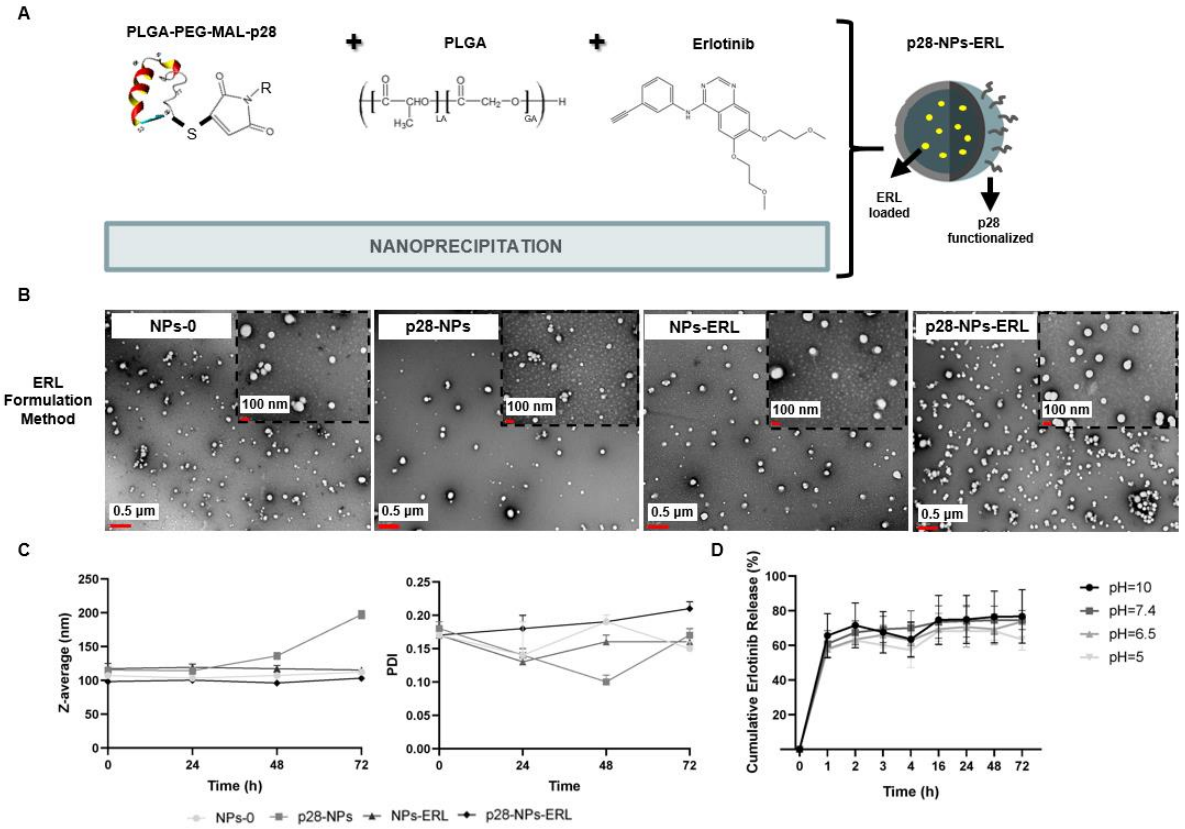

Figure VIII.3.2-1: Physico-chemical characterization and in vitro release of p28-NPs-ERL. **A)** Compounds of p28-NPs-ERL produced by nanoprecipitation. **B)** TEM images of empty nanoparticles (NPs-0), functionalized unloaded NPs (p28-NPs), ERL loaded NPs (NPs-ERL), and p28-functionalized ERL-loaded NPs (p28-NPs-ERL). Scale bars represent 0.5 µm and 100 nm **C)** Stability of empty nanoparticles (NPs-0), functionalized unloaded NPs (p28-NPs), ERL-loaded NPs (NPs-ERL), and p28-functionalized ERL-loaded NPs (p28-NPs-ERL) in cell culture medium at 37 ºC for 72 h. The size and PDI of the nanosystems were measured over time. **D)** *in vitro* release profile of ERL from PLGA NPs in PBS pH 5, pH 6.5, pH 7.4 and pH 10 added with 0.1% Tween® 80 (v/v) at 37 ºC during 72 h. All measurements were done in triplicate and results are presented as mean ± SD.

VIII.3.2.4. Effect of p28-functionalized PLGA nanoparticles loaded with erlotinib on metabolic activity

In vitro cell viability was evaluated through a Resazurin assay in A549 cancer cell line and 16HBE14o- non-cancer cell line (Figure VIII.3.2-2). A range of concentrations, in relation to the drug, from 2.5 µM to 17.5 µM of free ERL, NPs-0, p28-NPs, NPs-ERL and p28-NPs-ERL were tested (in the case of NPs concentration, cells were treated with a maximum of 0.06 mg/mL, below the cytotoxicity limit of 1mg/mL obtained after treatment of A549 cells for 72 h with increasing concentrations of NPs-0; Figure VIII.3.2-3). The results demonstrated that none of the treatments in 16HBE14o- non-cancer cells had an effect on their metabolic activity. On the other hand, the treatment in A549 cancer cells exhibited a decrease in metabolic activity with increasing concentrations of free ERL. The treatments with 6.2 µM of free p28 (concentration corresponding to that obtained in the

functionalization process), NPs-0 and p28-NPs did not alter the metabolic activity in these cancer cells. The results achieved from the treatment of the mixture with the free drug and peptide (free p28+ERL) compared to the condition of only free drug, reveal similar values of metabolic activity, which again showed that the treatment with 6.2 μM of free p28 has no influence on this parameter. Regarding the value of the metabolic activity obtained after treatment with the highest concentration of free ERL with NPs-0, it was found that this was similar to that obtained in the highest concentration of encapsulated drug, without functionalization. Comparing the values of metabolic activity of the treatment with free and encapsulated ERL, it was observed that in the case of the drug being encapsulated, a more controlled decrease in this parameter occurred. Lastly, when comparing the p28-NPs-ERL functional nanosystem treatment with NPs-ERL treatment, a significant decrease in metabolic activity (p<0.05) occurred in most cases (Figure VIII.3.2-2)

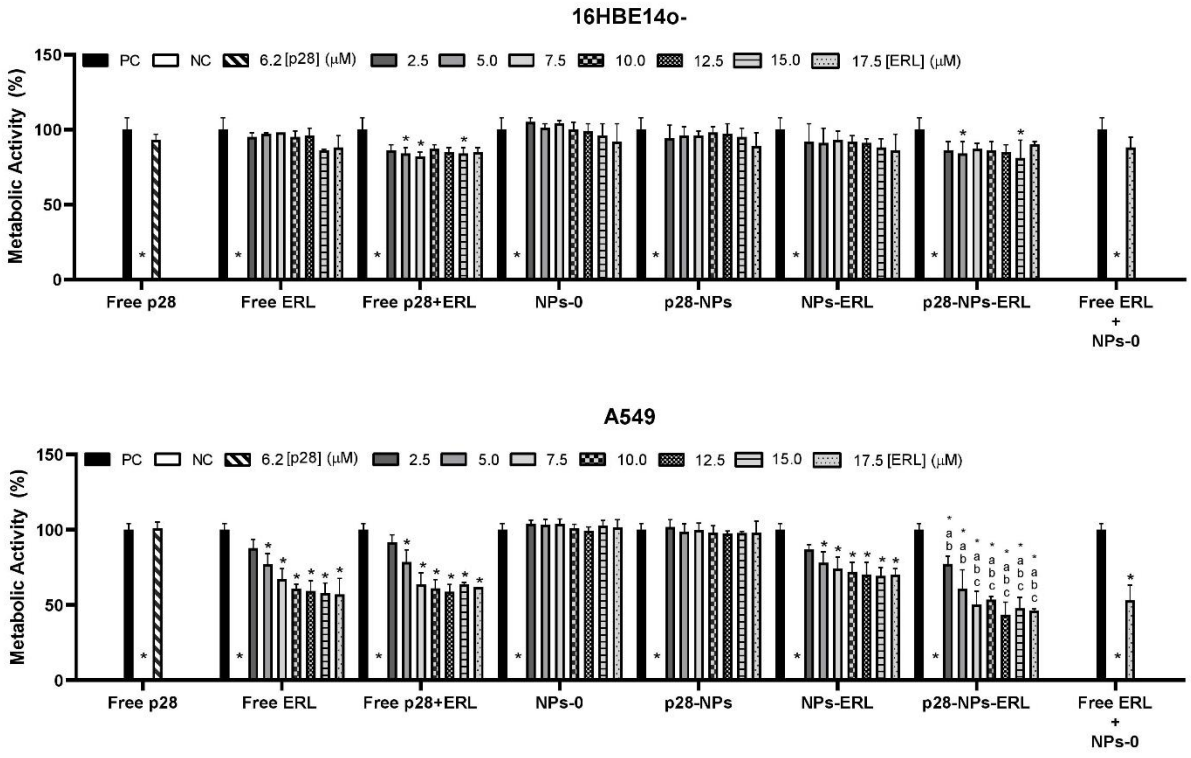

Figure VIII.3.2-2: Metabolic activity of 16HBE14o- non-cancer cells and A549 cancer cells when incubated with different concentrations of free ERL, empty nanoparticles (NPs-0), functionalized unloaded NPs (p28-NPs), ERL loaded NPs (NPs-ERL), and p28-functionalized ERL-loaded NPs (p28-NPs-ERL) during 72h. Negative Control (NC) and Positive Control (PC) consisted on cells incubated with 1% of Triton X-100 in medium, and only with medium, respectively. Values represent the mean ± SD, and each condition has at least an n=3. * denotes a significant difference of p<0.05 between each condition and PC; a, b, c and d represent a significant difference of p<0.05 between p28-NPs-ERL treatment vs empty NPs, p28-NPs, NPs-ERL and Free p28+ERL treatments, respectively.

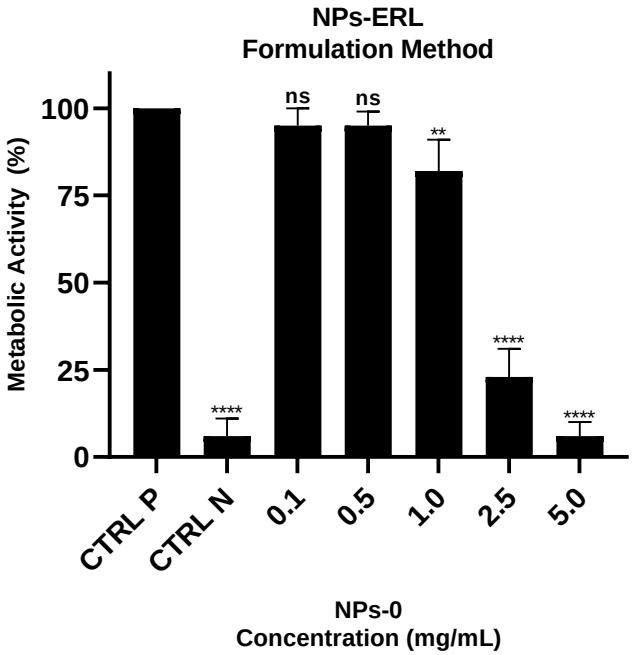

Figure VIII.3.2-3: Metabolic activity of A549 cancer cells upon treatment with different empty nanoparticles (NPs-0) concentrations for 72 h. Data was expressed as mean ± SD (n=3; ns: not significative; **p*<0.1; ***p*<0.01; ****p*<0.001; *****p*＜0.0001).